$\mu \to e$ conversion in nuclei: EFT description, charge densities, and pseudo-scalar decays

Inaugural dissertation
of the Faculty of Science,
University of Bern

presented by

Frederic Noël

from Germany

Supervisor of the doctoral thesis:
Prof. Dr. Martin Hoferichter

Institute for Theoretical Physics
Albert Einstein Center for Fundamental Physics
University of Bern

$\mu \to e$ conversion in nuclei: EFT description, charge densities, and pseudo-scalar decays

Inaugural dissertation
of the Faculty of Science,
University of Bern

presented by

Frederic Noël

from Germany

Supervisor of the doctoral thesis:
Prof. Dr. Martin Hoferichter

Institute for Theoretical Physics
Albert Einstein Center for Fundamental Physics
University of Bern

Accepted by the Faculty of Science.

Bern, 18.09.2024

The Dean
Prof. Dr. Jean-Louis Reymond

Abstract

The description of LFV $\mu \to e$ conversion in nuclei proves challenging due to the various energy scales involved, ranging from the BSM scale via chiral scales down all the way to nuclear and bound-state physics scales. Nevertheless, this is a pressing matter in light of the upcoming experiments Mu2e and COMET, which will improve the experimental limits by four orders of magnitude. This can be done in a model-independent way using an effective field theory framework in terms of effective BSM operators, which however crucially depends on hadronic and nuclear matrix elements. In this work, we present the comprehensive EFT formalism we developed, which describes bound-state physics and nuclear responses at the same time, and discuss the related hadronic and nuclear uncertainties. In particular, the uncertainties inherent in these non-perturbative inputs limit the discriminating power among different BSM scenarios that can be achieved. In order to quantify the associated uncertainties, we revisit nuclear charge densities and propagate uncertainties from elastic electron scattering experiments. These charge densities, parameterized in terms of Fourier-Bessel series, are crucial ingredients, in combination with EFT and nuclear-structure techniques, for the evaluation of general $\mu \to e$ conversion rates with quantified uncertainties. Using this framework, we could also transfer the very strong experimental limits for $\mu \to e$ conversion onto LFV decays of light pseudo-scalars, resulting in indirect limits surpassing the direct experimental ones by several orders of magnitude.

Part of this work has been published in:

[1] M. Hoferichter, J. Menéndez and F. Noël, *Improved Limits on Lepton-Flavor-Violating Decays of Light Pseudoscalars via Spin-Dependent $\mu \to e$ Conversion in Nuclei*, *Phys. Rev. Lett.* **130** (4, 2023) 131902, [2204.06005]

[2] F. Noël and M. Hoferichter, *Uncertainty quantification for $\mu \to e$ conversion in nuclei: charge distributions*, *JHEP* **08** (2024) 052, [2406.06677]

Contents

Chapter 1

Introduction

The Standard Model (SM) of particle physics [3] classifies the known elementary particles and the interactions between them via three of the four fundamental forces: electromagnetic, strong, and weak interactions. The SM particles are listed in Fig. 1.1 and are categorized as either fermions (half-integer spin) or bosons (integer spin). Quarks and leptons have spin 1/2 and are fermions, while the gauge bosons have spin 1 and the Higgs boson has spin 0. The symmetry group of the SM is realized as a

$$SU(3)_c \times SU(2)_L \times U(1)_Y, \tag{1.1}$$

which describes the strong interactions via the non-Abelian $SU(3)_c$ [4–6], and electromagnetic and weak interactions are unified in the $SU(2)_L \times U(1)_Y$ [7,8]. Below the electroweak scale the $SU(2)_L \times U(1)_Y$ symmetry breaks spontaneously into Abelian $U(1)_{\text{em}}$ describing electromagnetic interactions, and gives rise to a vacuum expectation value of the Higgs field [9–11], which generates masses for the quarks and leptons via the Yukawa couplings. The interactions between the particles in the SM are mediated by the gauge bosons. Strong interactions are mediated by the gluon, electromagnetic interactions via the photon, and weak interactions via the $W^{\pm}$- and Z-boson. The latter ones are the remaining degrees of freedom for weak interactions after the spontaneous symmetry breaking and also become massive in the process. In the context of this thesis, the leptons play a predominant role. Within the SM, leptons interact only weakly or electromagnetically. Based on the symmetry group of $SU(2)_L$ and their weak interactions, we can categorize the leptons into three flavors, grouping each charged lepton e, μ, τ with its corresponding neutrino ν_e, ν_μ, ν_τ, as illustrated in Fig. 1.1. For every process in the SM, the lepton flavor (LF) is a conserved quantity, which however is an accidental property and not demanded by construction.

The SM in its current form has been proven to have high predictive power and to be extremely precise. For example, the SM predicted top quark, tau neutrino, and the Higgs boson significantly in advance of their experimental discovery [12–16]. Furthermore, quantities like the magnetic moment of the electron could be calculated using the SM up to a relative accuracy of $\approx 10^{-12}$ [17,18], which makes this one of the most precisely verified

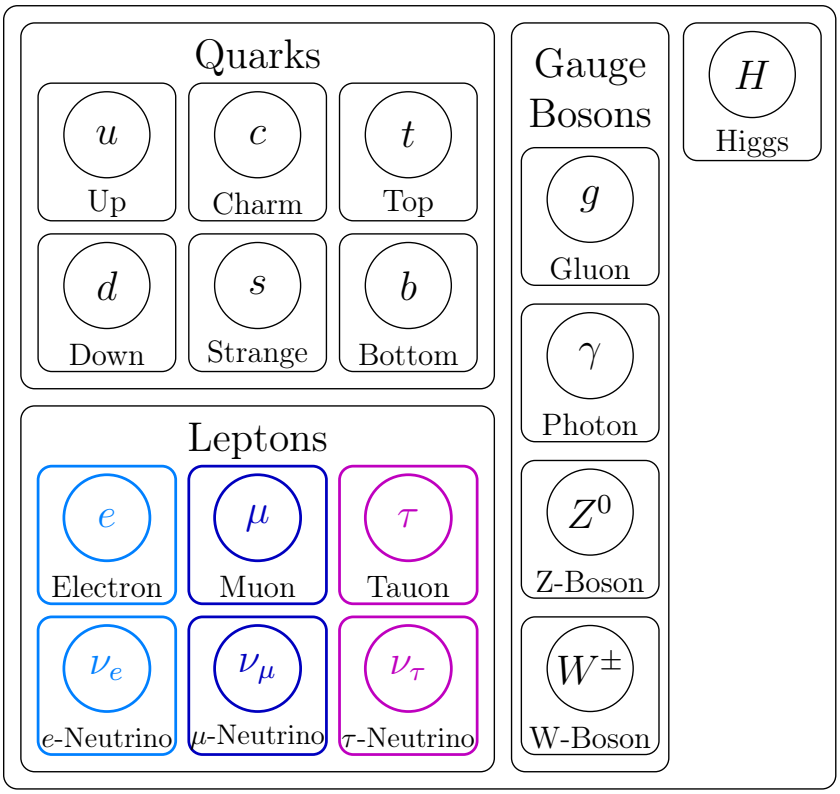

Figure 1.1: The SM of particle physics, highlighting the three different Lepton Flavors, which are the focus of this work.

predictions in physics. Despite these impressive achievements, we know that the SM is incomplete. First of all, on cosmological scales, a lot of observations are not described within the SM. Primarily, there is no gravity in the SM and no unification with general relativity. Secondly, we have strong observational claims for dark matter [19–22] and dark energy [23–27]. These cosmological observations require an extension of the SM. Further, the matter anti-matter asymmetry in the universe requires sizable CP violation [28]. In the SM the complex phases of the CKM-matrix can generate CP violation [29], which can be quantified by the rephrasing invariant Jarlskog invariant [30], which, however, is too small to explain the observed matter anti-matter asymmetry [31–33]. Furthermore, there are lots of precision experiments that test the predictions of the SM on measurable quantities. In some of these experiments, like for example the magnetic moment of the muon [34, 35], we have seen slight tensions to the SM prediction, where it remains to be seen if these persist. Moreover, the observation of neutrino oscillations [36], requires non-zero neutrino masses, which is not possible without an extension of the SM. In particular, neutrino oscillations also violate LF by converting between different neutrino flavors.

All these indications for physics beyond the SM (BSM) motivate a systematic study of possible BSM physics. As already elaborated, LF is an accidental property of the SM and is furthermore violated by the experimentally observed neutrino oscillations. This makes the study of other potential processes that violate LF a prominent probe for BSM physics. One of the most stringent bounds on LF violation (LFV) comes from $\mu \to e$ conversion in nuclei, which is the focus of this thesis.

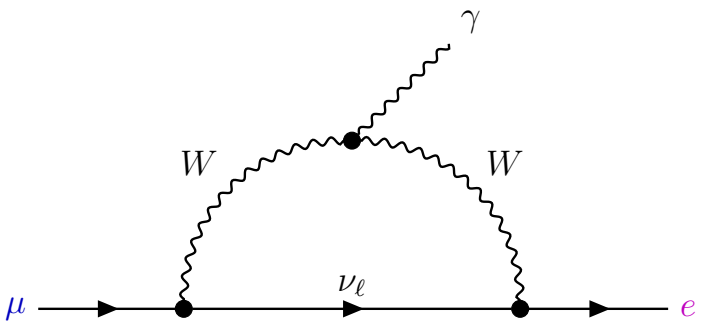

Figure 1.2: The LFV process $\mu \to e\gamma$ via rotation to the mass basis of the neutrino.

1.1 Lepton Flavor Violation

LF is a quantum number related to the three families of leptons (e, ν_e), (μ, ν_μ) and (τ, ν_τ), which exist within the SM (see Fig. 1.1). Within the SM individual LF is conserved, which means each particle of each family appears in the same amount on each side of a process (with anti-particles counted negatively). For example, a muon decays within the SM via $\mu^- \to e^- \bar{\nu}_e \nu_\mu$ and fulfills LF conservation, which necessitates the two neutrinos. A similar process without the neutrinos on the other hand would violate LF and is not allowed within the SM. If LFV interactions exist, they need to be described by going beyond the SM. As already elaborated earlier, there are good motivations to investigate potential BSM physics. In particular, neutrino oscillations are experimentally observed [36] and not described within the SM, as these would break LF conservation. Thus, the investigation of potential other sources of LFV is very attractive. This is further reinforced by the fact that LF conservation is an accidental property of the SM. Writing down the most general dimension four Lagrangian containing the SM fields, one can only construct interactions that fulfill LF conservation. However, it is not necessary to demand this condition explicitly, and extending the SM Lagrangian beyond dimension four naturally generates LFV interactions. Hence, it comes naturally to expect that BSM physics might violate LF. In fact, as already pointed out, neutrino oscillations break LF and are thus a kind of neutral LFV (NLFV), between the different neutrino flavors. This kind of LFV is extremely inefficient and requires the neutrinos to travel long distances to oscillate. In principle, the same mechanism could be used to mediate charged LFV (CLFV) between the charged leptons e, μ, and τ. For example, one could generate the LFV process $\mu \to e\gamma$ with a diagram as shown in Fig. 1.2, where the intermediate neutrino propagates in its mass basis and thus can change between coupling as a muon neutrino at the first vertex to coupling as an electron neutrino at the second vertex. However, the decay rate of this process scales with $(\frac{\Delta m_\nu}{m_W})^4$, which, dependent on the input for the neutrino mass difference Δm_ν, results in a decay rate $\lesssim 10^{-50}$, which is hence suppressed beyond anything that can be expected to be measured [37–41]. Thus, this kind of indirect CLFV via neutrino mixing does not play a role on normal particle physics scales. However, this means any positive observation of CLFV would be a clear signal of BSM physics, and since there are no directly competing SM processes, this would result in a very clean probe of BSM physics.

LFV process	current limit	(planned) experiments
$\mu \to e\gamma$	$< 4.2 \cdot 10^{-13}$ [43]	MEG II [45]
$\mu \to 3e$	$< 1.0 \cdot 10^{-12}$ [44]	Mu3e [46]
$\tau \to \ell\gamma, 3\ell, \ell P, \ldots$	$\lesssim 10^{-8}$ [52–59]	Belle II [60], ...
$K \to \mu e, \mu e\pi, \mu e\pi\pi$	$\lesssim 10^{-11}$ [61–64]	KOTO [65], LHCb [66]
$\pi^0 \to \mu e$	$< 3.6 \cdot 10^{-10}$ [63, 64, 67, 68]	JEF [50], REDTOP [51]
$\eta \to \mu e$	$< 6 \cdot 10^{-6}$ [69]	
$\eta' \to \mu e$	$< 4.7 \cdot 10^{-4}$ [70]	
$\mathrm{Au}\,\mu^- \to \mathrm{Au}\,e^-$	$< 7 \cdot 10^{-13}$ [71]	
$\mathrm{Ti}\,\mu^- \to \mathrm{Ti}\,e^-$	$< 6.1 \cdot 10^{-13}$ [72]	
$\mathrm{Al}\,\mu^- \to \mathrm{Al}\,e^-$	$\lesssim 10^{-17}$ (projected)	Mu2e [48], COMET [49]

Table 1.1: A selection of LFV processes and limits on their branching ratios given at 90% confidence level. The conversion rate is, based on historical conventions, normalized to the muon capture rate [73].

There are plenty of potential LFV processes. The most stringent bounds are on the one hand from the leptonic processes of $\mu \to e\gamma$ [43] and $\mu \to 3e$ [44], which will further improve via the experiments MEG2 [45] and Mu3e [46] (and potentially beyond [47]) and on the other hand from the semi-leptonic process of $\mu \to e$ conversion in nuclei, where significant improvements of up to four orders of magnitude to the current limits are projected for the experiments Mu2e [48] and COMET [49]. These three processes probe quite the complementary set of LFV operators, where $\mu \to e$ conversion in particular, due to the interaction with the nucleus, also covers interactions with quarks and gluons. Furthermore, the LFV decays of $P \to \bar{\mu}e$ for the light pseudo-scalars $P = \pi^0, \eta, \eta'$ can be an independent constraint on LFV interactions between electrons and muons. These are less stringent. In particular, for η and η' these limits are quite weak, which could be improved substantially from the proposed JEF or REDTOP experiments [50, 51]. In Tab. 1.1 an overview of the experimental limits of some of the most important LFV processes and the ones that will be of importance for this work, as well as the related experiments is given. With all these experiments continuing to improve the experimental limits on LFV processes, this also necessitates improvements on the theoretical side, on the one hand to project sensitivities of specific channels and on the other hand to assess potential BSM physics, once measured.

1.2 The Process of $\mu \to e$ Conversion

The process of $\mu \to e$ conversion occurs when a muon bound to a nucleus converts into an electron, without any neutrinos. At the initial state of this process, a muonic atom is formed. The muon can be generated by hitting a proton beam onto a production target and then extracting out the muons among the generated particles. These are then focused onto the target material, where the muon quickly cascades down into the ground state

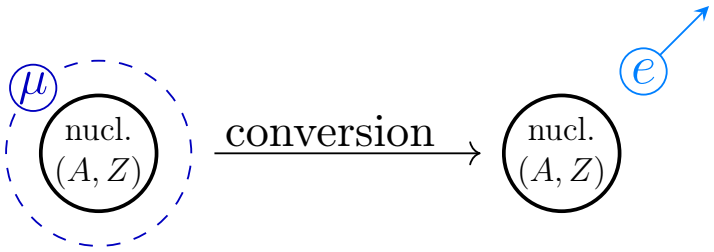

Figure 1.3: Schematic representation of $\mu \to e$ conversion in nuclei

of the nucleus. If now $\mu \to e$ conversion occurs, apart from a small recoil correction, all energy of the mass of the muon is translated into the momentum of the generated electron. Consequently, the electron is ejected from the nucleus and can be experimentally observed as a very clean experimental response of an electron with a fixed momentum. In Fig. 1.3 a schematic representation of the process is shown.

Competing processes in this scenario are, on the one hand, the muon capture [73], namely ${}^{A}_{Z}M + \mu \to {}^{A}_{Z-1}M' + \nu_\mu$, with M, M' the corresponding nucleus, which will not be visible in the experimental setup, as neutrinos will not be detected. This process is however nevertheless for historical reasons the normalization for the $\mu \to e$ conversion rates as shown in Tab. 1.1, though there have been recently some suggestions to change these conventions [75]. On the other hand, the muon can decay via the SM with two neutrinos also called the decay in orbit (DIO). In this process, however, also the two neutrinos may carry away energy and the probability of all the energy just going towards the electron is very small. Fig. 1.4 shows a schematic representation of the DIO spectrum loosely adapted from Ref. [76], where $\mu \to e$ conversion sits at the very end of the phase space spectrum. A third source of background comes from cosmic radiation, which mainly consists of cosmic muons interacting with the detector setup and producing electrons, which can end up in the detector. All other sources are even smaller and well under control. In total all these backgrounds are quite small and are well below a single observation for the initial stages of Mu2e and COMET [76, 77].

From the theoretical point of view, $\mu \to e$ conversion has been an attractive process to study for quite some time [78, 79] due to its quite stringent bounds, which are at the same time difficult to interpret due to the involved nucleus and the related nuclear and bound-state effects. The involved scales reach from the BSM scales $\gtrsim$ TeV, where the LFV operators live, via hadronic scales $\sim 100\,\text{MeV}$, which is roughly the transferred momentum, down to the muon bound-state energies and recoil onto the nucleus at $\lesssim 1\,\text{MeV}$. Thus, for a systematic study of $\mu \to e$ conversion, the most sensible choice is an effective field theory (EFT) framework, which combines different effective descriptions at different scales. Various works have studied EFT descriptions of $\mu \to e$ conversion and the complementarity of $\mu \to e$ conversion in combination with other LFV proves like $\mu \to e\gamma$ or $\mu \to 3e$ [80–87]. The groundwork for the modern descriptions of $\mu \to e$ conversion were laid in Ref. [88], where the conversion rate was calculated for scalar, vector and dipole interactions including bound-state effects for the leading nuclear responses. Subleading nuclear responses, which go with the spin of the nucleus, were studied in Refs. [89, 90] using a simplified description of the lepton physics in terms of plane waves, also discussing Renormalization Group (RG) evolution of the LFV operators. At the same time, a detailed study on the RG evolution for

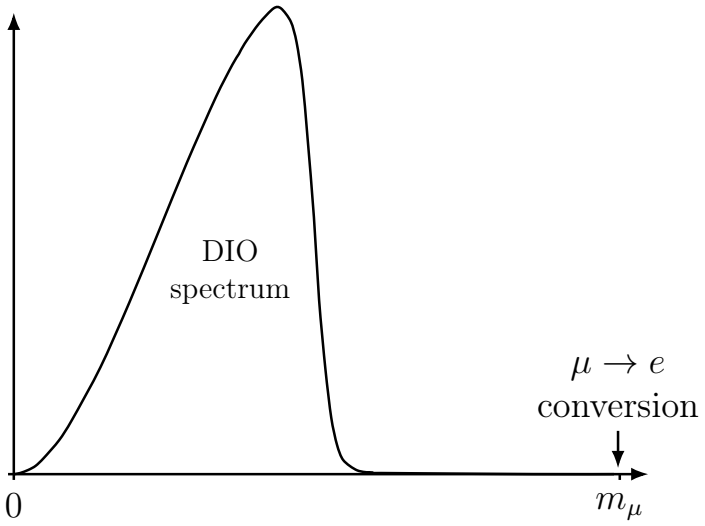

Figure 1.4: Conceptional DIO spectrum, reconstructed after Ref. [76]

LFV processes including electrons and muons was also performed in Ref. [91]. Furthermore, two-nucleon interactions were studied in Refs. [92, 93]. More recently, a nuclear-level EFT was developed in Refs. [94–96], which includes the charged lepton bound-state physics in terms of adjusted plane waves, but otherwise neglects Coulomb corrections.

The aim of this thesis is to construct an EFT framework, which includes all LFV operators up to dimension 6 and describes also subleading nuclear responses at the same time with bound-state effects. In this way, in particular, Coulomb effects are completely taken into account. We further, discuss and collect the necessary hadronic inputs for such a framework and extract in that context nuclear charge densities from elastic electron-nucleus scattering.

1.3 Outline of the Thesis

For such an EFT framework for $\mu \to e$ conversion, we need to combine inputs at very different scales, starting from the EFT operators at high energies, via hadronic scales down to nuclear and bound-state physics. The theoretical groundwork for such a framework is laid in Chap. 2, where the different aspects are introduced and discussed individually. In Chap. 3 these concepts are then combined into a comprehensive EFT framework describing $\mu \to e$ conversion in nuclei, as schematically shown in Fig. 1.5. We then demonstrate based on two commonly considered scenarios, either focusing on the charged lepton bound-state physics or the nuclear responses, how this general framework can describe $\mu \to e$ conversion including bound-state physics and nuclear responses at the same time[1].

Such a framework facilitates a quantitative study of the appearing LFV interactions, also in the light of the upcoming Mu2e and COMET experiments, and in combination with

[1]From here on we will use the term bound-state physics to refer to the bound-state physics of the charged leptons, while bound-state effects of the nucleons are considered via the term of nuclear response.

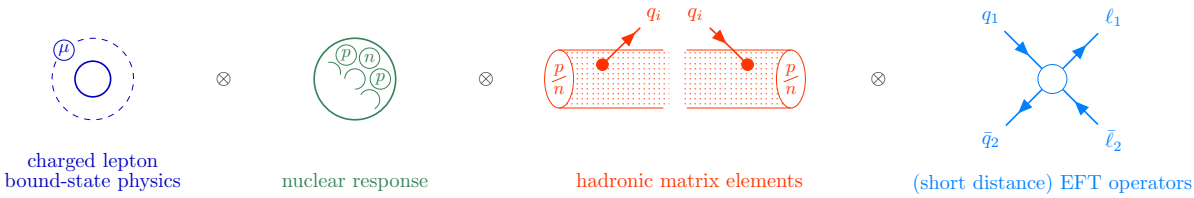

Figure 1.5: Schematic representation of the components of the EFT framework for $\mu \to e$ conversion

complementary LFV processes like $\mu \to 3e$ or $\mu \to e\gamma$. As a first exercise, we can display this in the context of LFV decays of light pseudo-scalars, as done in Chap. 4. As these decays are mediated by LFV operators which can also mediate $\mu \to e$ conversion, the limits on these processes act as complementary constraints on the underlying operators. Since in practice the limits on $\mu \to e$ conversion are a lot more stringent than the LFV pseudo-scalar decays, we are able to derive indirect limits, which improve upon directly measured ones by several orders of magnitude.

For a quantitative description of $\mu \to e$ conversion, robust inputs for the different components illustrated in Fig. 1.5 are crucial. In particular, the non-perturbative inputs from hadronic and nuclear physics, are hard to predict precisely and a precise treatment of the bound-state physics also requires numerical calculations. While the common hadronic matrix elements are usually available from either phenomenological considerations or from LatticeQCD [97], calculating nuclear responses model independently is more complicated. Historically, only very light nuclei could be calculated directly from first principles, and for anything heavier empirical models, like the nuclear shell model [98, 99], needed to be employed. Only recently a new strategy of ab-initio calculations was developed, which are able to calculate nuclear responses also for comparably heavy nuclei, while still being built upon QCD principles [100–102].

While the correlations among different quantities for these nuclear models are empirically shown to be quite consistent, the central value predictions still vary a lot between different models. Hence, it is advantageous to calibrate these based on quantities that are easily accessible experimentally. The charge density and the related charge radius are such quantities, which can be extracted from elastic electron-nucleus scattering. These charge densities are also of interest for $\mu \to e$ conversion in two other ways. Foremost, the calculation of the bound-state physics requires input for the nucleus electric potential given directly by the electric charge distribution of the nucleus and is thus crucial for a quantitative description of these bound-state effects. Furthermore, if $\mu \to e$ conversion happens via a one-photon exchange, the interaction is analogous to elastic electron-nucleus scattering, and the matrix element will be directly proportional to the charge form factor, which is directly given as the Fourier transform of the charge density. Hence, for this kind of interaction, the charge density can be directly employed, without additional input from nuclear theory calculations.

For all these reasons, quantitative input for the charge density is crucial. Unfortunately, the historically available model-independent extractions of the charge densities do not provide proper uncertainty estimations. Thus, we first review the groundwork for calculating general elastic electron-nucleus scattering in Chap. 5, and then extract in Chap. 6

charge densities for a set of nuclei most relevant for $\mu \to e$ conversion, directly from elastic electron nucleon scattering data. These results are also fully documented and conveniently provided to the community, for use in other projects, like for example for neutrino-nucleus scattering or parity-violating electron scattering (PVES).

Finally, in Chap. 7 we demonstrate how these results can be used to generate quantitative inputs for the nuclear and bound-state physics in terms of so-called overlap integrals. For dipole interactions, these overlap integrals are straightforward to calculate, as these directly depend on the charge density. This lets us showcase how uncertainties from the charge densities can be systematically propagated onto the overlap integrals. For scalar and vector interactions the overlap integrals depend on the proton and neutron densities, which are not directly accessible experimentally. This challenge can be addressed by correlating modern ab-initio calculations for the proton, neutron, and charge densities, which can be calibrated based on the experimentally extracted charge densities. We take the first steps in executing such a strategy and discuss the necessary procedure to obtain quantitative overlap integrals for scalar and vector interactions.

In Chap. 8 we conclude the thesis and give a brief outlook on related and future projects.

Chapter 2

Theoretical Framework

The description of $\mu \to e$ conversion requires lots of different scales, starting from BSM and weak scales, via hadronic and nucleon scales all the way down to nucleus-level and lepton-bound-state scales. EFTs make it possible to systematically combine inputs from all these different scales. The physical scale of $\mu \to e$ conversion is given on one side by the momentum of the electron which is pretty close to the mass of the muon $m_\mu \sim 100\,\text{MeV}$, and on the other hand by the binding energy of the muon and the recoil onto the nucleus which is $\lesssim 1\,\text{MeV}$. The BSM physics generating the necessary operators, however, sit somewhere above 1 TeV. To bridge this gap of several orders of magnitude, a tower of effective field theories can be employed.

Since we do not know the UV complete theory above the SM, we can only construct the most general EFT extending the SM, covering all possible BSM theories sitting above the SM. This strategy falls under the name of the SM effective field theory (SMEFT) [103–105], which adds all possible higher dimensional operators fulfilling the same symmetries as the SM and only using SM field. These infinitely many operators are then ordered by inverse powers of the cutoff scale Λ, which denotes at which point the effective theory breaks down. At energies of around 100 GeV the SM experiences the spontaneous symmetry breaking of the Higgs field, generating mass terms for the fermions and weak bosons. In turn, once we are below this scale, the heavy degrees of freedom of the SM can be integrated out resulting in a low-energy effective theory of the SM(EFT) also called the Low-energy effective field theory below the electroweak scale (LEFT) [105]. This theory now only contains the light quarks [1] u, d, s, the leptons, photons, and gluons, and everything else is integrated out. In particular, weak interactions are point interactions and handled as in Fermi's theory of weak interactions [106, 107], and the BSM operators have similar shapes. At this level, in the following called the quark-level, we construct our effective field theory containing all possible LFV operators contributing to $\mu \to e$ conversion up to dimension 7, as further explained in Sec. 2.1. To now deduce the influence of these operators sitting just below the electroweak scale on the process happening at $\lesssim 1 - 100\,\text{MeV}$, we need to

[1] Depending on the considered energy scale the c, b quarks are also part of the LEFT, but are integrated out at the corresponding thresholds for our application.

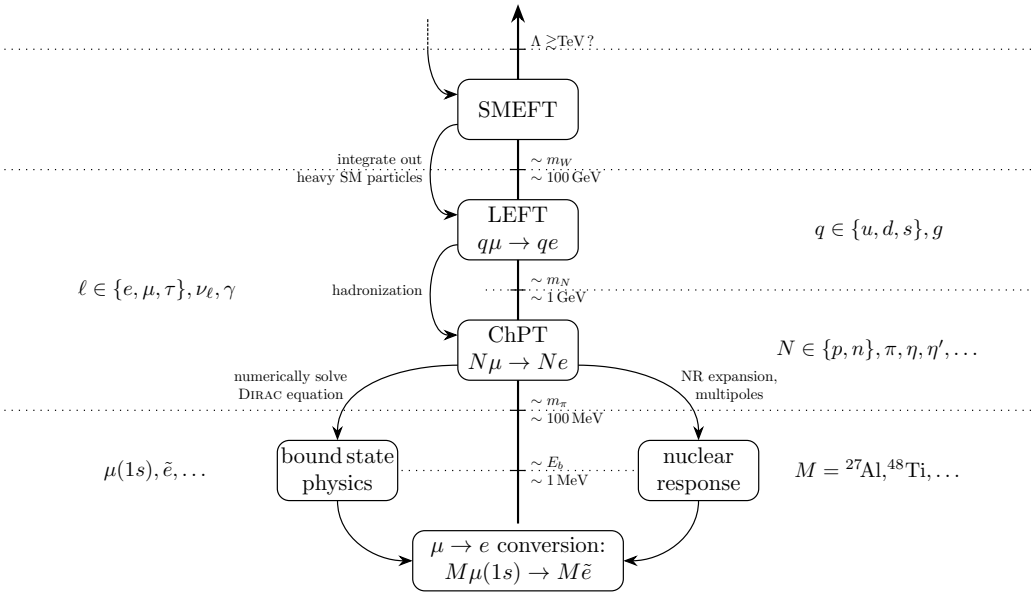

Figure 2.1: Schematic representation of the EFT scales for $\mu \to e$ conversion

further descend on the effective field theory ladder. Below $\sim 1\,\text{GeV}$ quarks and gluons confine to mesons and baryons, necessitating a non-perturbative description of QCD. This comes in the form of chiral perturbation theory (ChPT) [108], a low-energy effective theory based on the approximate chiral symmetry of QCD, directly containing the meson and baryon fields, as well as their interactions with external fields. These operators can then be matched to the quark-level operators, where the relative coupling strengths of these interactions can either be fixed by phenomenological considerations based on experimental input or by LatticeQCD calculations. The resulting structures are the so-called hadronic matrix elements, which are explained in more detail in Sec. 2.2. To incorporate the nuclear physics, presented by the fact that the lepton is interacting with a whole nucleus and not a single nucleon, we need to consider nuclear interactions below 100 MeV. First of all, this means, that the nucleons are non-relativistic and their interactions can be expanded in their momenta, resulting in corresponding non-relativistic nucleon operators. Now based on these non-relativistic operators, and after a multipole decomposition, the response of the whole nucleus is classified. More details on this can be found in Sec. 2.4. At this level, also the bound-state physics on the side of the leptons starts to matter. As the muon starts in a bound state of the nucleus and the outgoing electron is distorted by the nucleus, we also need to consider these effects, which also happen at an energy level of $\lesssim 1\,\text{MeV}$. For more details on how these effects can be included rigorously, we refer to Chap. 5. Fig. 2.1 shows schematically how the different energy scales and effective theories are related.

2.1 Effective Field Theory Description

We may describe Lepton Flavor violating processes under the premise of SMEFT [105]. This is a model-independent effective field theory extension of the SM, which simply

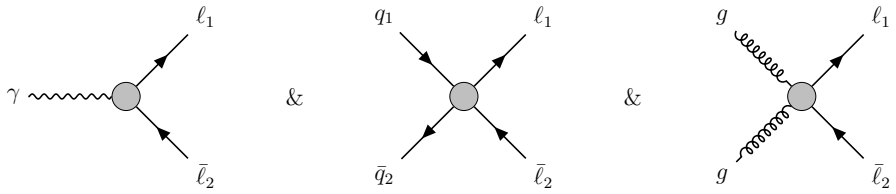

Figure 2.2: Some LF violating vertices relevant for $\mu \to e$ conversion

contains all possible interactions with all SM fields while fulfilling the same symmetries as the SM. This promotes the SM to being the leading terms of a low-energy effective theory to an unknown high-energy ultra-violet (UV) complete theory. Constructing the next terms in the effective theory constitutes a systematic approach to investigating potential BSM physics, without limiting ourselves to a specific UV theory. Since the overlying theory, which would generate the effective theory by integrating out the new physics degrees of freedom, is not known, the coupling strengths of the effective operators, also called Wilson coefficients, are unknown. Nevertheless, experimental limits on BSM physics can give limits on the size of these Wilson coefficients and thus limit in turn potential UV theories that could generate the effective operators. As already pointed out earlier, since LF is an accidental property of the SM, taking this approach naturally generates LFV operators, as shown in Fig. 2.2. As we consider a low-energy process, we directly integrate out heavy SM fields and consider the so-called LEFT Lagrangian, below the electro-weak scale. The effective Lagrangian can be written as

$$\mathcal{L}^{\text{LEFT}} = \mathcal{L}_{\text{QED}} + \mathcal{L}_{\text{QCD}} + \mathcal{L}^{(5)} + \mathcal{L}^{(6)} + \dots, \qquad \mathcal{L}^{(d)} = \sum_{i=1}^{n_d} \frac{\tilde{C}_i^{(d)}}{\Lambda^{d-4}} \tilde{O}_i^{(d)}, \tag{2.1}$$

where the upper index refers to the dimension of the contained operators. Here Λ is the BSM scale, which makes the Wilson coefficients $C_i^{(d)}$ dimensionless and may serve as a scale at which the effective field theory breaks down. For example, in a simple UV extension of the SM, this could refer to the lightest mass of the introduced BSM particles, whose propagator contracts to a point and generates a $1/M \sim 1/\Lambda$ when integrated out.

To describe $\mu \to e$ conversion, in particular, the following operators are relevant up to dimension seven

$$\begin{aligned}
\mathcal{L}^{(5)} &\supset \sum_{Y=L,R} \frac{\tilde{C}_{D,Y}^{(5)}}{\Lambda} \tilde{O}_{D,Y}^{(5)} && := \sum_{Y=L,R} C_Y^D O_Y^D, \\
\mathcal{L}^{(6)} &\supset \sum_{Y=L,R} \sum_{\substack{X=S,P,\\V,A,T}} \sum_{q=u,d,s} \frac{\tilde{C}_{X,Y,q}^{(6)}}{\Lambda^2} \tilde{O}_{X,Y,q}^{(6)} && := \sum_{Y=L,R} \sum_{\substack{X=S,P,\\V,A,T}} \sum_{q=u,d,s} C_Y^{X,q} O_Y^{X,q}, \\
\mathcal{L}^{(7)} &\supset \sum_{Y=L,R} \sum_{X=GG,G\tilde{G}} \frac{\tilde{C}_{X,Y}^{(7)}}{\Lambda^3} \tilde{O}_{X,Y}^{(7)} && := \sum_{Y=L,R} \sum_{X=GG,G\tilde{G}} C_Y^X O_Y^X,
\end{aligned} \tag{2.2}$$

where D stands for dipole, S for scalar, P for pseudo-scalar, V for vector, A for axial vector, T for tensor, and GG and $G\tilde{G}$ stand for the symmetric and antisymmetric gluonic

contributions, respectively, all referring to the hadronic part of the interaction. We can write these as

$$\mathcal{L}_{\text{eff}}^{\mu\to e} = \sum_{Y=L,R} \left(\sum_{q=u,d,s} \sum_{\substack{X=S,P,\\ V,A,T}} C_Y^{X,q}\ O_Y^{X,q} + \sum_{\substack{X=D,\\ GG,G\tilde{G}}} C_Y^X\ O_Y^X \ + \text{ h.c.} \right), \tag{2.3}$$

with

$$O_Y^{X(,q)} = L_Y^{X,(n)}\ Q_{(n)}^{X(,q)}, \tag{2.4}$$

where $(n) \in \{\emptyset, \mu, \mu\nu\}$ denotes the contraction of the Lorentz indices and[2]

$$\begin{aligned}
L_Y^S &= \Lambda^{-2}\ \overline{e_Y}\mu, & Q^{S,q} &= \bar{q}q, \\
L_Y^P &= L_Y^S, & Q^{P,q} &= \bar{q}\gamma^5 q, \\
L_Y^{V,\mu} &= \Lambda^{-2}\ \overline{e_Y}\gamma^\mu\mu, & Q_\mu^{V,q} &= \bar{q}\gamma_\mu q, \\
L_Y^{A,\mu} &= L_Y^{V,\mu}, & Q_\mu^{A,q} &= \bar{q}\gamma_\mu\gamma^5 q, \\
L_Y^{T,\mu\nu} &= \Lambda^{-2}\ \overline{e_Y}\sigma^{\mu\nu}\mu, & Q_{\mu\nu}^{T,q} &= \bar{q}\sigma_{\mu\nu}q, \\
L_Y^{GG} &= \Lambda^{-1}\ L_Y^S, & Q^{GG} &= \alpha_s G_{\alpha\beta}^a G_a^{\alpha\beta}, \\
L_Y^{G\tilde{G}} &= \Lambda^{-1}\ L_Y^S, & Q^{G\tilde{G}} &= i\alpha_s G_{\alpha\beta}^a \tilde{G}_a^{\alpha\beta}, \\
L_Y^{D,\mu\nu} &= \Lambda\ L_Y^{T,\mu\nu}, & Q_{\mu\nu}^D &= F_{\mu\nu},
\end{aligned} \tag{2.5}$$

where we use $\overline{e_Y} = \overline{eP_Y} = \bar{e}P_{\bar{Y}}$ and $Y \in \{L, R\}$[3] with $P_{L/R} = (\mathbb{1} \mp \gamma^5)/2$. This chiral basis for the electron spinors makes explicit, that for $m_e \to 0$ the left-handed component e_L and right-handed component e_R decouple, which we assume in the following. The BSM scale Λ is here absorbed into the L_Y^X structures.

2.2 Quantum Chromo Dynamics and the Chiral Scale

The interactions between quarks and gluons are given in the SM via Quantum Chromo Dynamics (QCD) [4–6, 109]. QCD at low energy is non-perturbative [110, 111] as the strong coupling constant α_s grows exponentially as can be seen in Fig. 2.3. At low energies, only integer and half-integer bound states of quarks and gluons exist, called baryons and mesons, respectively. These bound states are confined to be color-neutral. In $\mu \to e$ conversion the appearing states are the protons and neutrons inside the nucleus. Their interactions need to be described non-perturbatively in terms of effective field theories. Interactions between mesons and baryons at low energies can be characterized in the framework of ChPT. For our application the matching of the LFV operators at quark level, to the hadronic operator at nucleon level is quite straightforward, using the well-known

[2] We use $\sigma^{\mu\nu} = \frac{i}{2}[\gamma^\mu, \gamma^\nu] = \frac{i}{2}(\gamma^\mu\gamma^\nu - \gamma^\nu\gamma^\mu)$ and $\tilde{G}_a^{\mu\nu} = \frac{1}{2}\epsilon^{\mu\nu\alpha\beta}G_{\alpha\beta}^a$ with $\epsilon^{0123} = +1$.

[3] With $\bar{Y}$ we mean: $\bar{L} = R$, $\bar{R} = L$

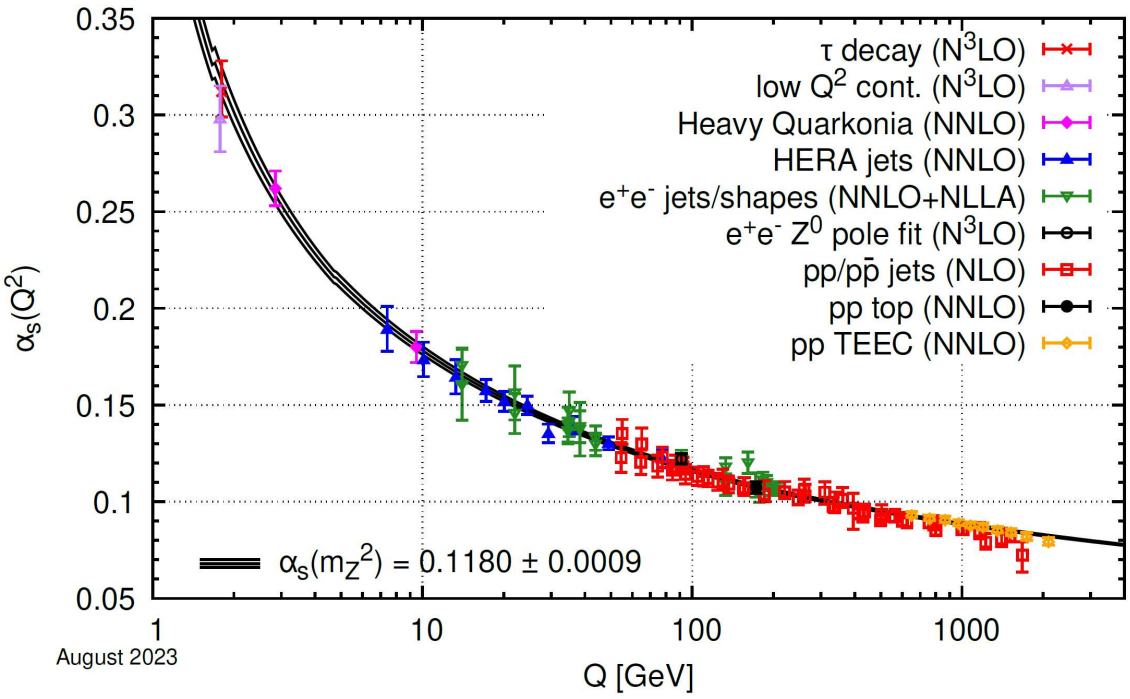

Figure 2.3: QCD running coupling, taken from Ref. [112]

hadronic matrix elements for the quark currents. We can find the contributing operators on nucleon level by writing down all possible structures with the same Lorentz structure as well as individual symmetry under C, P, and T as the quark-level operators. The prefactors of the nucleon-level structures are then called hadronic matrix elements or form factors. These quantities can then either be measured and phenomenologically deduced or calculated numerically from LatticeQCD.

2.2.1 Hadronic Matrix Elements

The allowed Hermitian building blocks for a spin 1/2 field ψ, are

$$\bar{\psi}\psi, \quad \bar{\psi}i\gamma^5\psi, \quad \bar{\psi}\gamma^\mu\psi, \quad \bar{\psi}\gamma^\mu\gamma^5\psi, \quad \bar{\psi}\sigma^{\mu\nu}\psi, \tag{2.6}$$

with γ^μ the Dirac gamma matrices. These structures can be contracted or combined with the following Lorentz structures inside the Lagrangian

$$\partial_\mu, \quad g^{\mu\nu}, \quad \epsilon^{\mu\nu\alpha\beta} \ . \tag{2.7}$$

If external photons or other particles with polarizations exist, they can also be used here, which however will not be the case in our application. Higher structures with more gamma

	scalar $\bar{\psi}\psi$	pseudo-scalar $i\bar{\psi}\gamma^5\psi$	vector $\bar{\psi}\gamma^\mu\psi$	axial-vector $\bar{\psi}\gamma^\mu\gamma^5\psi$	tensor $\bar{\psi}\sigma^{\mu\nu}\psi$	∂_μ
P	$+1$	-1	$(-1)^\mu$	$-(-1)^\mu$	$(-1)^\mu(-1)^\nu$	$(-1)^\mu$
C	$+1$	$+1$	-1	$+1$	-1	$+1$
T	$+1$	-1	$(-1)^\mu$	$(-1)^\mu$	$-(-1)^\mu(-1)^\nu$	$-(-1)^\mu$
CPT	$+1$	$+1$	-1	-1	$+1$	-1

Table 2.1: Transformation properties under C, P, T [113]. Here $(-1)^\mu = +1$ for $\mu = 0$ and $(-1)^\mu = -1$ for $\mu = 1, 2, 3$. Note that the gluon field A^μ in the gluon field strength tensor $G^a_{\mu\nu}$ transforms as a vector and the pseudo-scalar field $\hat{P}$ transforms as a pseudo-scalar.

matrices can always be reduced to these structures by using the identities

$$\begin{aligned}\gamma^\mu\gamma^\nu\gamma^\rho &= g^{\mu\nu}\gamma^\rho + g^{\nu\rho}\gamma^\mu - g^{\mu\rho}\gamma^\nu - i\epsilon^{\sigma\mu\nu\rho}\gamma_\sigma\gamma^5,\\ \sigma_{\mu\nu}\gamma^5 &= +i\sigma_{\alpha\beta}\frac{1}{2}\epsilon^{\alpha\beta\mu\nu},\end{aligned} \tag{2.8}$$

as well as the basic properties of the Clifford algebra $\{\gamma^\mu, \gamma^\nu\} = 2g^{\mu\nu}\mathbb{1}_4$ and $\gamma_\mu\gamma^\mu = 4\mathbb{1}_4$. Hence, there is no higher independent gamma matrix structure than $\sigma^{\mu\nu}$.

Using these possible structures we can relate the quark-level interactions to the nucleon-level interactions by matching operators with the same symmetry behavior. The structures of Eq. (2.6) possess under C, P, T the behavior of Tab. 2.1. Hence, we find based on these symmetry properties the following association between quark and gluon structures and nucleon structures

$$\begin{aligned}\text{scalar:} \quad & G^{\mu\nu}_a G^a_{\mu\nu},\ \bar{q}q \ \rightarrow\ \bar{N}N,\\ \text{pseudo-scalar:} \quad & G^{\mu\nu}_a \tilde{G}^a_{\mu\nu},\ i\bar{q}\gamma^5 q \rightarrow\ i\bar{N}\gamma^5 N,\ \partial_\mu\bar{N}\gamma^5\gamma^\mu N,\\ \text{vector:} \quad & \bar{q}\gamma^\mu q \ \rightarrow\ \bar{N}\gamma^\mu N,\ \partial^\mu\partial_\nu\bar{N}\gamma^\nu N,\ \partial_\nu\bar{N}\sigma^{\mu\nu}N,\\ \text{axial-vector:} \quad & \bar{q}\gamma^5\gamma^\mu q \ \rightarrow\ \bar{N}\gamma^5\gamma^\mu N,\ i\partial^\mu\bar{N}\gamma^5 N,\ \partial_\mu\partial_\nu\bar{N}\gamma^5\gamma^\nu N,\\ \text{tensor:} \quad & \bar{q}\sigma^{\mu\nu}q \ \rightarrow\ \bar{N}\sigma^{\mu\nu}N,\ \partial^{[\mu}\bar{N}\gamma^{\nu]}N,\ \gamma^{[\mu}\gamma_\alpha\bar{N}\sigma^{\nu]\alpha}N,\end{aligned} \tag{2.9}$$

where we used the notation $A^{[\mu}B^{\nu]} = \frac{1}{2}(A^\mu B^\nu - A^\nu B^\mu)$ for the tensor terms. When evaluating matrix elements with these operators, the partial derivatives become momenta $\partial_\mu \rightarrow -i(p^\mu - p'^\mu) := -iq^\mu$ and the momenta acting on the free states become $\not{p}u_N(p) = m_N u_N(p)$, which simplifies and combines a few structures. Based on this association the hadronic matrix elements are defined to be

$$\begin{aligned}\langle N|\,\bar{q}q\,|N\rangle &= \bar{u}_N(p',s')\left(\frac{m_N}{m_q}f_q^N(q)\right)u_N(p,s),\\ \langle N|\,\bar{q}i\gamma^5 q\,|N\rangle &= \bar{u}_N(p',s')\left(\frac{m_N}{m_q}G_5^{q,N}(q)i\gamma^5\right)u_N(p,s),\\ \langle N|\,\bar{q}\gamma^\mu q\,|N\rangle &= \bar{u}_N(p',s')\left(\gamma^\mu F_1^{q,N}(q) - \frac{i\sigma^{\mu\nu}q_\nu}{2m_N}F_2^{q,N}(q)\right)u_N(p,s),\end{aligned}$$

$$
\begin{aligned}
\langle N|\,\bar{q}\gamma^\mu\gamma^5 q\,|N\rangle &= \bar{u}_N(p',s')\left(\gamma^\mu\gamma^5 G_A^{q,N}(q) - \gamma^5\frac{q^\mu}{2m_N}G_P^{q,N}(q)\right)u_N(p,s),\\
\langle N|\,\bar{q}\sigma^{\mu\nu} q\,|N\rangle &= \bar{u}_N(p',s')\left(\sigma^{\mu\nu}F_{1,T}^{q,N}(q) - 2\gamma^{[\mu}\frac{iq^{\nu]}}{m_N}F_{2,T}^{q,N}(q) - 4p^{[\mu}\frac{iq^{\nu]}}{m_N^2}F_{3,T}^{q,N}(q)\right)u_N(p,s),\\
\langle N|\,G^a_{\mu\nu}G_a^{\mu\nu}\,|N\rangle &= \bar{u}_N(p',s')\left(\frac{4\pi}{\alpha_s}a_N(q)\right)u_N(p,s),\\
\langle N|\,G^a_{\mu\nu}\tilde{G}_a^{\mu\nu}\,|N\rangle &= \bar{u}_N(p',s')\left(i\frac{4\pi}{\alpha_s}\tilde{a}_N(q)\gamma^5\right)u_N(p,s).
\end{aligned}
\tag{2.10}
$$

In Chap. 4 we will also consider the LFV decays of light pseudo-scalars. Hence, it makes sense to also introduce the appearing hadronic matrix elements for light pseudo-scalars $\hat{P}$. For a single pseudo-scalar meson decaying, the only existing structures are $\mathbb{1}\hat{P}$ and $\partial_\mu\hat{P}$ such that based on the symmetry properties the existing structures are

$$
\begin{aligned}
\text{scalar:} \quad & G_a^{\mu\nu}G^a_{\mu\nu},\ \bar{q}q \ \to\ 0,\\
\text{pseudo-scalar:} \quad & G_a^{\mu\nu}\tilde{G}^a_{\mu\nu},\ i\bar{q}\gamma^5 q \to\ \hat{P},\\
\text{vector:} \quad & \bar{q}\gamma^\mu q \ \to\ 0,\\
\text{axial-vector:} \quad & \bar{q}\gamma^5\gamma^\mu q \ \to\ \partial^\mu\hat{P},\\
\text{tensor:} \quad & \bar{q}\sigma^{\mu\nu} q \ \to\ 0.
\end{aligned}
\tag{2.11}
$$

As shown scalar, vector, and tensor contributions vanish due to parity, where for the tensor even the parity breaking $\partial^{[\mu}\partial^{\nu]}\hat{P} = 0$ vanishes due to the anti-symmetry of the tensor. The non-zero pseudo-scalar matrix elements become

$$
\begin{aligned}
\langle 0|\,m_q\bar{q}i\gamma^5 q\,|P(q)\rangle &= \frac{b_q}{2}h_P^q(q),\\
\langle 0|\,\bar{q}\gamma^\mu\gamma^5 q\,|P(q)\rangle &= ib_q f_P^q(q)q^\mu,\\
\langle 0|\,\frac{\alpha_s}{4\pi}G^{a\mu\nu}\tilde{G}^a_{\mu\nu}\,|P(q)\rangle &= a_P(q),
\end{aligned}
\tag{2.12}
$$

with $b_{u,d} = \frac{1}{\sqrt{2}}$ and $b_q = 1$ else.

The axial vector current has the special property of fulfilling the (anomalous) Ward identity given by

$$
\partial_\mu(\bar{q}\gamma^\mu\gamma^5 q) = 2m_q\bar{q}i\gamma^5 q - \frac{\alpha_s}{4\pi}G^a_{\mu\nu}\tilde{G}_a^{\mu\nu}. \tag{2.13}
$$

This results in the following Ward identity for the hadronic matrix element for the nucleons

$$
G_A^{q,N} + \frac{q_\mu q^\mu}{4m_N^2}G_P^{q,N} = G_5^{q,N} - \frac{\tilde{a}_N}{2m_N} \quad\to\quad G_A^{q,N} = G_5^{q,N} - \frac{\tilde{a}_N}{2m_N}, \tag{2.14}
$$

if we consider $q^\mu q_\mu \approx -\vec{q}^2 \ll m_N^2$. And for the pseudo-scalars we have

$$
b_q f_P^q q_\mu q^\mu = b_q h_P^q - a_P \quad\to\quad b_q f_P^q m_P^2 = b_q h_P^q - a_P, \tag{2.15}
$$

since q^μ is here just the energy and momentum of the pseudo-scalar meson. These properties enable, in either case, the elimination of one of the hadronic matrix elements. We typically write G_5 and h_P in terms of the other hadronic matrix elements.

For the pseudo-scalar form factors of π, η, and η' we can further reduce the number of independent operators using isospin symmetry and neglecting strangeness and gluonic contributions to the pion matrix elements. The remaining free parameters are the pion decay constant F_π, the singlet and octet decay constants F^0, F^8 with the corresponding mixing angles θ_0, θ_8 as well as the gluon parameters a_0, θ_y. The parameters defined via Eq. (2.12) are then given in terms of these parameters via

$$\begin{aligned}
f_\pi^u &= -f_\pi^d = \sqrt{2}\, F_\pi, & f_\pi^s &= 0, & a_\pi &= 0, \\
f_\eta^u &= f_\eta^d = \sqrt{\frac{2}{3}} F^8 \cos\theta_8 - \frac{2}{\sqrt{3}} F^0 \sin\theta_0, & f_\eta^s &= -\frac{2}{\sqrt{3}} F^8 \cos\theta_8 - \sqrt{\frac{2}{3}} F^0 \sin\theta_0, \\
f_{\eta'}^u &= f_{\eta'}^d = \sqrt{\frac{2}{3}} F^8 \sin\theta_8 + \frac{2}{\sqrt{3}} F^0 \cos\theta_0, & f_{\eta'}^s &= -\frac{2}{\sqrt{3}} F^8 \sin\theta_8 + \sqrt{\frac{2}{3}} F^0 \cos\theta_0, \\
a_\eta &= -a_0 \sin\theta_y, & a_{\eta'} &= a_0 \cos\theta_y,
\end{aligned} \tag{2.16}$$

and the pseudo-scalar matrix elements h_P^q are then given via (2.15).

2.3 Non-relativistic Nucleon Currents

The relativistic nucleon currents $\bar{u}_N(p', s')\Gamma^{X'}_{(m)} u_N(p, s)$, as appearing in Eq. (2.10), with $X' = S, P, V, A, T$ and

$$\Gamma^S = \mathbb{1}, \qquad \Gamma^P = \gamma_5, \qquad \Gamma^V_\mu = \gamma_\mu, \qquad \Gamma^A_\mu = \gamma_\mu\gamma_5, \qquad \Gamma^T_{\mu\nu} = \sigma_{\mu\nu}, \tag{2.17}$$

can be expanded non-relativistically, as for our application the nucleons are bound to the nucleus and the transferred momentum onto the nucleons is small. The non-relativistic spinors are given by[4]

$$u_N(p,s) = \sqrt{\frac{E_N + m_N}{2E_N}} \begin{pmatrix} \mathbb{1}\chi_s \\ \frac{(\vec{p}\cdot\vec{\sigma})}{E_N + m_N}\chi_s \end{pmatrix} = \begin{pmatrix} \left(1 - \frac{\vec{p}^2}{8m_N^2}\right)\mathbb{1}\chi_s \\ \left(\frac{1}{2m_N}\right)(\vec{p}\cdot\vec{\sigma})\chi_s \end{pmatrix} + \mathcal{O}\left(\frac{|\vec{p}|^3}{m_N^3}\right), \tag{2.18}$$

[4]We use the non-relativistic spinor normalization $u^\dagger u = 1$.

with χ_s the two component Pauli spinor and $\vec{\sigma}$ the three-vector of pauli-matrices. A non-relativistic expansion in the momenta up to $\mathcal{O}(m_N^{-2})$ results in

$$\begin{aligned}
\bar{u}_{N'}\mathbb{1}u_N &= \chi^\dagger_{s'}\left(\mathbb{1} + \frac{-\vec{q}^2 - 4\vec{p}^2 + 4(\vec{q}\cdot\vec{p}) - 2i(\vec{q}\cdot(\vec{\sigma}\times\vec{p}))}{8m_N^2}\right)\chi_s,\\
\bar{u}_{N'}\gamma^5 u_N &= \chi^\dagger_{s'}\left(\frac{(\vec{q}\cdot\vec{\sigma})}{2m_N}\right)\chi_s,\\
\bar{u}_{N'}\gamma^0 u_N &= \chi^\dagger_{s'}\left(\mathbb{1} + \frac{-\vec{q}^2 + 2i(\vec{q}\cdot(\vec{\sigma}\times\vec{p}))}{8m_N^2}\right)\chi_s,\\
\bar{u}_{N'}\gamma^i u_N &= \chi^\dagger_{s'}\left(\frac{-q_i + 2p_i + i(\vec{q}\times\vec{\sigma})_i}{2m_N}\right)\chi_s,\\
\bar{u}_{N'}\gamma^0\gamma^5 u_N &= \chi^\dagger_{s'}\left(\frac{-(\vec{q}\cdot\vec{\sigma}) + 2(\vec{\sigma}\cdot\vec{p})}{2m_N}\right)\chi_s,\\
\bar{u}_{N'}\gamma^i\gamma^5 u_N &= \chi^\dagger_{s'}\left(\sigma_i + \frac{-\vec{q}^2\sigma_i + 2i(\vec{q}\times\vec{p})_i + 2(\vec{q}\times(\vec{\sigma}\times\vec{p}))_i}{8m_N^2}\right.\\
&\qquad\left. + \frac{-4\vec{p}^2\sigma_i - 2q_i(\vec{\sigma}\vec{p}) + 2(\vec{q}\cdot\vec{p})\sigma_i + 4(\vec{\sigma}\cdot\vec{p})p_i}{8m_N^2}\right)\chi_s,\\
\bar{u}_{N'}\sigma^{0i}u_N &= \chi^\dagger_{s'}\left(\frac{iq_i + (\vec{q}\times\vec{\sigma})_i + 2(\vec{\sigma}\times\vec{p})_i}{2m_N}\right)\chi_s,\\
\epsilon_{ijk}\ \bar{u}_{N'}\sigma^{ij}u_N &= 2\ \chi^\dagger_{s'}\left(\sigma_k + \frac{-\vec{q}^2\sigma_k - 2i(\vec{q}\times\vec{p})_k - 2(\vec{q}\times(\vec{\sigma}\times\vec{p}))_k}{8m_N^2}\right.\\
&\qquad\left. + \frac{+2q_k(\vec{\sigma}\cdot\vec{p}) + 2(\vec{q}\cdot\vec{p})\sigma_k - 4(\vec{\sigma}\cdot\vec{p})p_k}{8m_N^2}\right)\chi_s.
\end{aligned} \tag{2.19}$$

We may identify the following structures

$$\begin{aligned}
&h^M = \mathbb{1}, && h^\Sigma = \sigma_i, &&\\
&h_i^\Delta = \frac{ip_i}{q}, && h^\Omega = \frac{i(\vec{\sigma}\cdot\vec{p})}{q}, && h_i^\Phi = \frac{-(\vec{\sigma}\times\vec{p})_i}{q},\\
&h^{\Omega'} = \frac{i(\vec{q}\cdot\vec{\sigma})(\vec{\sigma}\cdot\vec{p})}{q^2}, && h^{\Omega''} = \frac{-\vec{p}^2}{q^2}, && h_i^\Theta = \frac{-\sigma_i\vec{p}^2}{q^2},\\
&h_i^\Pi = \frac{-(\vec{\sigma}\cdot\vec{p})p_i}{q^2}, && h_i^\Xi = \frac{-(\vec{q}\cdot\vec{\sigma})p_i}{q^2}, && h_i^\Gamma = \frac{i(\vec{q}\cdot\vec{p})\sigma_i}{q^2},
\end{aligned} \tag{2.20}$$

where we introduced the from here on used convention $q = |\vec{q}|$. We choose these labels in association with the nuclear responses these structures will generate in a whole nucleus. Some structures like h^M experience a coherent enhancement in the nucleus, which is, why it makes sense to include terms up to a higher order for these structures. However, as there are no enhancement mechanisms for the Ω', Ω'', Θ, Π, Ξ, and Γ structures, we will

drop them in the following, resulting in an incomplete expansion at order $\mathcal{O}(m_N^{-2})$ given by

$$\begin{aligned}
\bar{u}_{N'}\mathbb{1}u_N &= \chi_{s'}^\dagger\left(\left(1-\frac{q^2}{8m_N^2}\right)h^M + \frac{-iqq_i}{2m_N^2}h^\Delta + \frac{iqq_i}{4m_N^2}h_i^\Phi\right)\chi_s,\\
\bar{u}_{N'}\gamma^5 u_N &= \chi_{s'}^\dagger\left(\frac{q_i}{2m_N}h_i^\Sigma\right)\chi_s,\\
\bar{u}_{N'}\gamma^0 u_N &= \chi_{s'}^\dagger\left(\left(1-\frac{q^2}{8m_N^2}\right)h^M + \frac{-iqq_i}{4m_N^2}h_i^\Phi\right)\chi_s,\\
\bar{u}_{N'}\gamma^i u_N &= \chi_{s'}^\dagger\left(\frac{-q_i}{2m_N}h^M + \frac{-iq}{m_N}h_i^\Delta + \frac{i\epsilon_{ijk}q_j}{2m_N}h_k^\Sigma\right)\chi_s,\\
\bar{u}_{N'}\gamma^0\gamma^5 u_N &= \chi_{s'}^\dagger\left(\frac{-q_i}{2m_N}h_i^\Sigma + \frac{-iq}{m_N}h^\Omega\right)\chi_s,\\
\bar{u}_{N'}\gamma^i\gamma^5 u_N &= \chi_{s'}^\dagger\left(\left(1-\frac{q^2}{8m_N^2}\right)h_i^\Sigma + \frac{q\epsilon_{ijk}q_j}{4m_N^2}h_k^\Delta + \frac{-q\epsilon_{ijk}q_j}{4m_N^2}h_k^\Phi + \frac{iqq_i}{4m_N^2}h^\Omega\right)\chi_s,\\
\bar{u}_{N'}\sigma^{0i}u_N &= \chi_{s'}^\dagger\left(\frac{iq_i}{2m_N}h^M + \frac{\epsilon_{ijk}q_j}{2m_N}h_k^\Sigma + \frac{-q}{m_N}h_i^\Phi\right)\chi_s,\\
\epsilon_{ijk}\ \bar{u}_{N'}\sigma^{ij}u_N &= 2\ \chi_{s'}^\dagger\left(\left(1-\frac{q^2}{8m_N^2}\right)h_k^\Sigma + \frac{-\epsilon_{klm}qq_l}{4m_N^2}h_m^\Delta + \frac{\epsilon_{klm}qq_l}{4m_N^2}h_m^\Phi\right)\chi_s.
\end{aligned} \tag{2.21}$$

2.4 Nuclear Response

While the muon interacts with the nucleus, it becomes relevant how the interaction with a free proton or neutron differs from the interaction inside a bound nucleus. This falls under the name of nuclear response as the individual interactions with protons and neutrons can be pooled together into different responses of the whole nucleus. The following derivation largely follows Ref. [114], where some adjustments for a more modern notation were made [115–117].

We have already seen in the previous section, how the non-relativistic expansion for the interactions with a single nucleon results in different non-relativistic structures $h_{(m)}^S$. These can be transformed into non-relativistic operators via

$$\hat{h}_{(m)}^S = N^+\ h_{(m)}^S[p_i \to -i\vec{\nabla}_i]\ N^-, \tag{2.22}$$

such that the derivative acting on the initial nucleon state generates the initial nucleon momentum p in the matrix element (see also Sec. 3.4). Interactions to the whole nucleus now result as a sum over these interactions with all individual nucleons. As this derivation is independent of the chosen one-nucleon current, we may generally consider a semi-leptonic process with a leptonic and a hadronic current interacting according to

$$\mathcal{L} = \int \mathrm{d}^3x\ \hat{L}^\mu(x)\hat{H}_\mu(x). \tag{2.23}$$

We now consider the generic semi-leptonic process $L^i M^i \to L^f M^f$ with some initial (final) lepton states L^i (L^f) with momentum k_μ (k'_μ) and spin s (s') and initial (final) nucleon states M^i (M^f) with total spin J_i (J_f), spin component M_i (M_f) and momentum p (p'), written as

$$\begin{aligned} \left|L^i(k,t)\right\rangle \left|M^i(p,J_i,M_i)\right\rangle &=: \left|L^i\right\rangle \left|M^i(J_i,M_i)\right\rangle, \\ \left\langle L^f(k',t')\right| \left\langle M^f(p',J_f,M_f)\right| &=: \left\langle L^f\right| \left\langle M^f(J_f,M_f)\right|. \end{aligned} \tag{2.24}$$

The matrix element for this process becomes

$$\begin{aligned} i\mathcal{M} &= i \left\langle L^f\right| \left\langle M^f(J_f,M_f)\right| \mathcal{L} \left|L^i\right\rangle \left|M^i(J_i,M_i)\right\rangle \\ &= i \int \mathrm{d}^3x \left\langle L^f\right| \hat{L}^\mu \left|L_i\right\rangle \left\langle M^f(J_f,M_f)\right| \hat{H}_\mu \left|M^i(J_i,M_i)\right\rangle, \end{aligned} \tag{2.25}$$

where we may consider

$$\left\langle L^f\right| \hat{L}^\mu \left|L^i\right\rangle = l^\mu e^{-i\vec{q}\cdot\vec{x}}. \tag{2.26}$$

This makes sense in particular for free initial and final lepton states. For example, if the leptonic interaction for this process is given between two lepton spinors $\Psi_{1,2}$ by

$$\hat{L} = \bar{\Psi}_2 \Gamma^\mu \Psi_1, \tag{2.27}$$

with Γ^μ some arbitrary Lorentz structure. Then the free field quantization of the spinors, given by

$$\Psi(x) = \int \frac{\mathrm{d}^3k}{(2\pi)^3} \frac{1}{\sqrt{2E_k}} \sum_s \left(a_\Psi(k,s) u_\Psi(k,s) e^{-i\vec{k}\cdot\vec{x}} + b_\Psi(k,s) v_\Psi(k,s) e^{i\vec{k}\cdot\vec{x}} \right) \tag{2.28}$$

$$\bar{\Psi}(x) = \int \frac{\mathrm{d}^3k'}{(2\pi)^3} \frac{1}{\sqrt{2E_{k'}}} \sum_s \left(a^\dagger_\Psi(k',s) \bar{u}_\Psi(k',s) e^{i\vec{k}'\cdot\vec{x}} + b^\dagger_\Psi(k',s) \bar{v}_\Psi(k',s) e^{-i\vec{k}'\cdot\vec{x}} \right), \tag{2.29}$$

dictates

$$\begin{aligned} \left\langle L^f\right| \hat{L}^\mu \left|L^i\right\rangle = \left\langle L^f\right| \bar{\Psi}_2 \Gamma^\mu \Psi_1 \left|L^i\right\rangle &= \bar{u}_2(k',t') e^{i\vec{k}'\cdot\vec{x}} \Gamma^\mu u_1(k,t) e^{-i\vec{k}\cdot\vec{x}} \\ &= \bar{u}_2(k',t') \Gamma^\mu u_1(k,t) e^{-i(\vec{k}-\vec{k}')\cdot\vec{x}}, \end{aligned} \tag{2.30}$$

Hence, we find in fact a structure like Eq. (2.26). The assumption of Eq. (2.26) is however more general and can also be applied in a more general setting as we will see later. It follows

$$\begin{aligned} i\mathcal{M} &= i \int \mathrm{d}^3x \, l^\mu e^{-i\vec{q}\cdot\vec{x}} \left\langle M^f(J_f,M_f)\right| \hat{H}_\mu \left|M^i(J_i,M_i)\right\rangle \\ &= i \int \mathrm{d}^3x \left\langle M^f(J_f,M_f)\right| l^\mu e^{-i\vec{q}\cdot\vec{x}} \hat{H}_\mu \left|M^i(J_i,M_i)\right\rangle. \end{aligned} \tag{2.31}$$

This description can now be further developed to give rise to the different nuclear responses. This happens in a so-called multipole decomposition.

2.4.1 Multipole Decomposition

The structure $l^\mu e^{-i\vec{q}\cdot\vec{x}}\hat{H}_\mu$ of Eq. (2.31) can be expanded in a multipole decomposition, which separates the different kinds of nuclear responses. For this, we first write out the Lorentz contraction

$$l^\mu e^{-i\vec{q}\cdot\vec{x}}\hat{H}_\mu = l^0\hat{H}_0 e^{-i\vec{q}\cdot\vec{x}} - \vec{l}\hat{\vec{H}}e^{-i\vec{q}\cdot\vec{x}}, \tag{2.32}$$

and then change to a system of spherical coordinates orientated around $\vec{q}$ in z-direction. This defines

$$\vec{l} = \sum_{\lambda=\pm,3} l_\lambda \vec{e}^\dagger_\lambda, \qquad\qquad l_0 = l_0, \tag{2.33}$$

which are given as

$$\begin{aligned} \vec{e}_\pm &= \mp\frac{1}{\sqrt{2}}(\vec{e}_1 \pm i\vec{e}_2), & \vec{e}_3 &= \vec{q}/q, \\ l_\pm &= \mp\frac{1}{\sqrt{2}}(l_1 \pm i l_2), & l_3 &= l_3. \end{aligned} \tag{2.34}$$

Here the longitudinal component is labeled with 3 instead of 0, to prevent confusion with the time-like component which has also the index 0, however we still consider the angular momentum of $\lambda = 3$ to be 0. With this follows

$$\vec{l}\hat{\vec{H}}e^{-i\vec{q}\cdot\vec{x}} = \sum_\lambda l_\lambda \vec{e}^\dagger_\lambda \hat{\vec{H}} e^{-i\vec{q}\cdot\vec{x}}. \tag{2.35}$$

Expanding $e^{i\vec{q}\vec{x}}$ in terms of spherical harmonics $Y_{L,M}$ and spherical Bessel functions j_l via

$$e^{i\vec{q}\cdot\vec{x}} = \sum_{l=0}^{\infty}\sqrt{4\pi(2l+1)}i^l j_l(\vec{q}\cdot\vec{x})Y_{l,0}(\hat{x}), \tag{2.36}$$

results in[5]

$$\begin{aligned} \vec{e}_\lambda e^{i\vec{q}\cdot\vec{x}} &= \vec{e}_\lambda \sum_{l=0}^{\infty}\sqrt{4\pi(2l+1)}i^l j_l(\vec{q}\cdot\vec{x})Y_{l,0}(\hat{x}) \\ &= \sum_{lLM}\sqrt{4\pi(2l+1)}i^l j_l(\vec{q}\cdot\vec{x})\,\langle l01\lambda|l1LM\rangle\,\vec{Y}_{L,l,M}(\hat{x}), \end{aligned} \tag{2.37}$$

where we introduced the vector spherical harmonics [118]

$$\vec{Y}_{L,L',M} = \sum_{m\lambda}\langle L'm1\lambda|LM\rangle\, Y_{L'm}\vec{e}_\lambda, \qquad Y_{lm}\vec{e}_\lambda = \sum_{LM}\langle lm1\lambda|LM\rangle\,\vec{Y}_{L,l,M}. \tag{2.38}$$

[5]The λ inside the Clebsch-Gordan coefficient is interpreted as an angular momentum of $0, \pm 1$, according to $\lambda = \pm \to \pm 1$, $\lambda = 3 \to 0$

The Clebsch-Gordan coefficient force $M = \lambda$ and $l = L, L \pm 1$. Evaluating these explicitly for the different λ one finds

$$\begin{aligned}\vec{e}_{\pm} e^{i\vec{q}\cdot\vec{x}} &= \sum_{L\geq 1} \sqrt{2\pi(2L+1)} i^L \left[\mp j_L(\vec{q}\cdot\vec{x}) \vec{Y}_{\pm,L,L} - \frac{1}{q}\vec{\nabla} \times j_L(\vec{q}\cdot\vec{x}) \vec{Y}_{\pm,L,L} \right], \\ \vec{e}_3 e^{i\vec{q}\cdot\vec{x}} &= \frac{-i}{q} \sum_{L\geq 0} \sqrt{4\pi(2L+1)} i^L \vec{\nabla} j_L(\vec{q}\cdot\vec{x}) Y_{L,0}. \end{aligned} \tag{2.39}$$

Using these conditions we find[6]

$$\begin{aligned}\sum_{\lambda} l_\lambda \vec{e}_\lambda^\dagger \hat{\vec{H}} e^{-i\vec{q}\cdot\vec{x}} = &\sum_{L\geq 0} \sqrt{4\pi(2L+1)} (-i)^L (l_0 \mathcal{M}_{L,0} - l_3 \mathcal{L}_{L,0}) \\ &+ \sum_{L\geq 1} \sqrt{4\pi(2L+1)} (-i)^L \frac{1}{\sqrt{2}} \sum_{\lambda=\pm} l_\lambda \big(\lambda \mathcal{T}^{\text{mag}}_{L,-\lambda} + \mathcal{T}^{\text{el}}_{L,-\lambda} \big), \end{aligned} \tag{2.40}$$

with[7]

$$\begin{aligned} \mathcal{M}_{L,M} &= j_J(qr) Y_{JM}(\hat{r}) H_0, & \mathcal{L}_{L,M} &= \frac{i}{q} \Big(\vec{\nabla} j_J(qr) Y_{JM}(\hat{r}) \Big) \vec{H}, \\ \mathcal{T}^{\text{el}}_{L,M} &= \frac{1}{q} \Big(\vec{\nabla} \times j_J(qr) \vec{Y}_{JJM}(\hat{r}) \Big) \vec{H}, & \mathcal{T}^{\text{mag}}_{L,M} &= \Big(j_J(qr) \vec{Y}_{JJM}(\hat{r}) \Big) \vec{H}. \end{aligned} \tag{2.41}$$

These are called the Coulomb, electric longitudinal, electric transverse, and magnetic transverse multipole, where these names are of historical nature. Note that in general for each hadronic current H_μ a different set of these four multipoles exist.

Inserting this in Eq. (2.31), means now we need to evaluate the following matrix elements

$$\left\langle M^f(J_f, M_f) \right| \mathcal{S}_{LM} \left| M^i(J_i, M_i) \right\rangle, \tag{2.42}$$

for $\mathcal{S} \in \{\mathcal{M}, \mathcal{L}, \mathcal{T}^{\text{el}}, \mathcal{T}^{\text{mag}}\}$. We can simplify this calculation by using the Wigner-Eckart theorem, resulting in

$$\begin{aligned} &\left\langle M^f(J_f, M_f) \right| \mathcal{S}_{LM} \left| M^i(J_i, M_i) \right\rangle \\ &\quad = (-1)^{J_f - M_f} \begin{pmatrix} J_f & L & J_i \\ -M_f & M & M_i \end{pmatrix} \left\langle M^f(J_f) \right\| \mathcal{S}_L \left\| M^i(J_i) \right\rangle \\ &\quad = \frac{1}{\sqrt{2J_f+1}} \left\langle J_i M_i, JM | J_f M_f \right\rangle \left\langle M^f(J_f) \right\| \mathcal{S}_L \left\| M^i(J_i) \right\rangle, \end{aligned} \tag{2.43}$$

where we used the Wigner $3j$-symbol, for which further applies

$$\sum_{M_i, M_f} \begin{pmatrix} J_f & L & J_i \\ -M_f & M & M_i \end{pmatrix} \begin{pmatrix} J_f & L' & J_i \\ -M_f & M' & M_i \end{pmatrix} = \frac{1}{2L+1} \delta_{LL'} \delta_{MM'}. \tag{2.44}$$

[6]Mind that here the hadronic current got contracted with $\vec{e}_\lambda^\dagger$ instead of $\vec{e}_\lambda$. Hence, $\vec{e}_\lambda e^{i\vec{q}\cdot\vec{x}}$ needs to be complex conjugated, where also the identity $\vec{Y}^\dagger_{L,L,M} = -(-1)^l \vec{Y}_{L,L,-M}$ was used.

[7]We deviate from the classic convention of including the $\int \mathrm{d}^3x$ integral here, for easier association with the explicit structures of Eq. (2.45).

The structures $\langle M^f(J_f)||\mathcal{S}_L||M^i(J_i)\rangle$ can now be calculated with nuclear physics methods, as explained in more detail in the next section. For just a single kind of interaction like in Eq. (2.23) and for free external lepton states, one can find a general expression for the spin averaged absolute value of the matrix element squared of Eq. (2.31), just in terms of these reduced matrix elements, and the analytically calculable lepton spin sums. However, as for our application both of these conditions are not met, we refer for any further considerations in this special case to Ref. [114]. For our case, it is more advantageous to calculate matrix elements for all spin combinations explicitly on this level and then calculate the spin averaged absolute value squared afterwards.

2.4.2 Typical Nuclear Responses

As already mentioned, for each hadronic current H_μ in Eq. (2.23) a different set of the four multipole structures of Eq. (2.41) exists. In addition, the derivation of $\mathcal{M}_{L,M}$ based on H_0 and the derivation of $\mathcal{L}_{L,M}$, $\mathcal{T}^{\text{el}}_{L,M}$, and $\mathcal{T}^{\text{mag}}_{L,M}$ based on H_i are independent. Hence, the multipole decomposition for any scalar current can be done via H_0, and for any Euclidean vector can be done via H_i, even if they are physically not part of the same Lorentz vector H_μ. Thus we can construct the multipole structures directly based on the scalar and vector currents of Eq. (2.20), whose naming directly deduces from the name of the nucleonic structure $\hat{h}^{S,N_i}_{(m)}$ from Eq. (2.22) according to

$$\begin{aligned}
\mathcal{M}_{L,M}(\hat{h}^{S,N_i}) &:= S^i_{L,M}, & \mathcal{L}_{L,M}(\hat{h}^{S,N_i}_j) &:= iS''^{\,i}_{L,M},\\
\mathcal{T}^{\text{el}}_{L,M}(\hat{h}^{S,N_i}_j) &:= iS'^{\,i}_{L,M}, & \mathcal{T}^{\text{mag}}_{L,M}(\hat{h}^{S,N_i}_j) &:= S^i_{L,M},
\end{aligned} \tag{2.45}$$

which is also illustrated in Tab. 2.2. For these structures, we follow the conventions of Ref. [119] which means

$$\begin{aligned}
M^i_{JM} &= j_J(qr_i)Y_{JM}(\hat{r}_i), & \Omega^i_{JM} &= j_J(qr_i)Y_{JM}(\hat{r}_i)\left(\vec{\sigma}\cdot\frac{\vec{\nabla}_i}{q}\right),\\
\Delta^i_{JM} &= j_J(qr_i)\vec{Y}_{JJM}(\hat{r}_i)\cdot\frac{\vec{\nabla}_i}{q}, & \Delta'^{\,i}_{JM} &= -i\left(\frac{\vec{\nabla}_i}{q}\times j_J(qr_i)\vec{Y}_{JJM}(\hat{r}_i)\right)\cdot\frac{\vec{\nabla}_i}{q},\\
\Delta''^{\,i}_{JM} &= \left(\frac{\vec{\nabla}_i}{q}j_J(qr_i)Y_{JM}(\hat{r}_i)\right)\cdot\frac{\vec{\nabla}_i}{q}, & \Sigma^i_{JM} &= j_J(qr_i)\vec{Y}_{JJM}(\hat{r}_i)\cdot\vec{\sigma},\\
\Sigma'^{\,i}_{JM} &= -i\left(\frac{\vec{\nabla}_i}{q}\times j_J(qr_i)\vec{Y}_{JJM}(\hat{r}_i)\right)\cdot\vec{\sigma}, & \Sigma''^{\,i}_{JM} &= \left(\frac{\vec{\nabla}_i}{q}j_J(qr_i)Y_{JM}(\hat{r}_i)\right)\cdot\vec{\sigma},\\
\Phi^i_{JM} &= i\ j_J(qr_i)\vec{Y}_{JJM}(\hat{r}_i)\cdot\left(\vec{\sigma}\times\frac{\vec{\nabla}_i}{q}\right), & \Phi'^{\,i}_{JM} &= \left(\frac{\vec{\nabla}_i}{q}\times j_J(qr_i)\vec{Y}_{JJM}(\hat{r}_i)\right)\cdot\left(\vec{\sigma}\times\frac{\vec{\nabla}_i}{q}\right),\\
\Phi''^{\,i}_{JM} &= i\left(\frac{\vec{\nabla}_i}{q}j_J(qr_i)Y_{JM}(\hat{r}_i)\right)\cdot\left(\vec{\sigma}\times\frac{\vec{\nabla}_i}{q}\right),
\end{aligned} \tag{2.46}$$

	$\mathbb{1}$	$\vec{\sigma}\vec{\nabla}$	$\vec{\nabla}$	$\vec{\sigma}$	$\vec{\sigma}\times\vec{\nabla}$
$\mathcal{M}$	M	Ω			
$\mathcal{T}^{\text{mag}}$			Δ	Σ	Φ
$\mathcal{T}^{\text{el}}$			Δ'	Σ'	Φ'
$\mathcal{L}$			Δ''	Σ''	Φ''

Table 2.2: Overview of the names of the used multipoles

which is consistent with Eq. (2.20).

These nuclear structures are still abstract objects. The observable quantities are the so-called structure functions, which we define as[8]

$$\mathcal{F}_N^{\mathcal{S}_L}(\vec{q}) = \sqrt{\frac{4\pi}{2J+1}} \int \mathrm{d}^3x \sum_{i=1}^{A} \delta_{NN_i} \left\langle M^f(J_f) \middle|\middle| \mathcal{S}_L^i(\vec{q},\vec{x}) \middle|\middle| M^i(J_i) \right\rangle , \tag{2.47}$$

with $N = n, p$. These are thus directly related to the reduced matrix elements. For an exact calculation of these objects, one would need to calculate all $\langle M||\mathcal{S}_L^i(\vec{q},\vec{x})||M\rangle$ explicitly, which generally is different for every proton and neutron inside the nucleus. As these can generally be part of several states of the nucleus, a with the number of nucleons exponentially growing number of off-diagonal single-nucleon matrix elements would need to be calculated. To also be able to calculate nuclei with more than just a few nucleons, different numerical methods were developed to calculate these quantities, ranging from empirical methods like the shell model up to modern ab-initio calculations, which are based on QCD principles.

For a shell-model calculation, the numerically determined structure functions can be parameterized in an oscillator basis as

$$\mathcal{F}(\vec{q}) = e^{-\frac{u(q)}{2}} \sum_{i=0}^{n} c_i u(q)^i, \tag{2.48}$$

where n is finite and $u(q) = q^2b^2/2$ with b the harmonic oscillator length, which is empirically chosen to be

$$b = \frac{197.327\,\text{MeV fm}}{\sqrt{938.919\,\text{MeV}(45\,\text{MeV}A^{-1/3} - 25\,\text{MeV}A^{-2/3})}}, \tag{2.49}$$

and c_i the parameters.

The multipoles in Eq. (2.46) can be separated into so-called spin-independent (SI) and spin-dependent (SD) responses. Such a distinction makes sense as the SI multipoles show a coherent enhancement with the number of nucleons as the response of the nucleus is simply a coherent combination of the individual responses of the nucleons. This is, in particular, the case for the M multipole, having no nucleon-specific structure, which is why $\mathcal{F}_N^{M_0}(0) = \sum_N = \#N$ and this multipole is coherently enhanced. The Φ'' multipole

[8] We pull out a factor of $\sqrt{\frac{2J+1}{4\pi}}$ for a normalization according to $F_p^{M_0}(0) = Z$

also shows a partial enhancement due to its relation to the orbit angular momentum. For this reason, the contributions from the M and Φ'' multipoles are commonly denoted to be the SI response. On the other hand, multipoles like Σ' and Σ'', depend on the spin of the nucleons, which mostly cancel out in the nucleus, and are thus considered to be SD responses, which are not coherently enhanced. In particular, SD responses only exist for nuclei with total spin $J > 0$.

Furthermore, due to their behavior under time reversal, certain operator combinations vanish for elastic processes ($|M\rangle = |M^i(J_i)\rangle = \left|M^f(J_f)\right\rangle$). In particular [117]

$$\begin{aligned}
&\langle M||\Sigma||M\rangle = 0, && \langle M||\Delta'||M\rangle = 0,\\
&\langle M||\Omega||M\rangle = -\frac{1}{2}\langle M||\Sigma''||M\rangle, && \langle M||\Delta''||M\rangle = +\frac{1}{2}\langle M||M||M\rangle,\\
&\langle M||\Phi||M\rangle = +\frac{1}{2}\langle M||\Sigma'||M\rangle. &&
\end{aligned} \tag{2.50}$$

These conditions can be used to reduce the number of independent structures that may emerge down to M, Δ, Σ', Σ'', Φ'', and Φ'. Moreover, Parity conservation arrogates that for elastic processes only multipoles with even L contribute for M and Φ'', and only odd multipoles contribute for Δ, Σ', Σ''. The number of multipoles L is always limited by the spin of the nucleus, with $L \leq 2J$ for the elastic process.

2.4.3 Normalization

To fix the applied conventions for the structure functions, it makes sense to document the used normalization. We normalize the M-response to the charge $Z = \mathcal{F}_p^{M_0}(0)$ and neutron number $N = \mathcal{F}_n^{M_0}(0)$, respectively. Similarly, the normalizations $\mathcal{F}_N^{\Phi''_0}(0)$ can be related to spin-orbit corrections to nuclear charge radii [116, 120]

$$\langle r^2\rangle_{\rm so} = -\frac{3}{2m_N^2 Z}\Big(\big(1+2\kappa_p\big)\mathcal{F}_p^{\Phi''_0}(0) + 2\kappa_n\mathcal{F}_n^{\Phi''_0}(0)\Big), \tag{2.51}$$

the ones for Σ' to spin-expectation values $\langle \mathbf{S}_N\rangle$[9]

$$\mathcal{F}_N^{\Sigma'_1}(0) = 2\sqrt{\frac{2}{3}}\sqrt{\frac{J+1}{J}}\langle \mathbf{S}_N\rangle, \tag{2.52}$$

and the Δ response is related to the reduced matrix element of the angular-momentum operator

$$\mathcal{F}_N^{\Delta_1}(0) = -\frac{1}{\sqrt{6}}\sqrt{\frac{J+1}{J}}\langle \mathbf{L}_N\rangle. \tag{2.53}$$

[9] $\langle \mathbf{S}_N\rangle = 1/2$ for a free proton or neutron. This normalization for the Σ' response differs from Ref. [116] according to $\mathcal{F}_N^{\Sigma'_L}\big|_{\text{this work}} = 2\sqrt{\frac{4\pi}{2J+1}}\mathcal{F}_N^{\Sigma'_L}\big|_{\text{[116]}}$.

Dependent on the context it makes sense to think about the structure-function in a nucleon basis with $N = n, p$ or in an isospin basis $\tau = 0, 1$. One can always change between the two representations via

$$C_{0,1} = \frac{C_p \pm C_n}{2}, \qquad \mathcal{F}_{0,1} = \mathcal{F}_p \pm \mathcal{F}_n, \tag{2.54}$$

such that

$$\sum_{N=p,n} C_N \mathcal{F}_N = \sum_{\tau=0,1} C_\tau \mathcal{F}_\tau. \tag{2.55}$$

Chapter 3

EFT Description of $\mu \to e$ Conversion

In the following chapter, we will develop a comprehensive framework for $\mu \to e$ conversion, built upon the methods outlined in the previous chapter. As already illustrated in Fig. 2.1, the description of $\mu \to e$ conversion is challenging due to the various energy scales involved, ranging from the BSM scale via chiral scales down all the way to nuclear and bound-state physics scales. In particular, the different kinds of non-perturbative inputs, need to be combined self-consistently for a comprehensive description of the whole $\mu \to e$ conversion process. This is a pressing matter in light of the upcoming experiments of Mu2e and COMET, which will improve the experimental limits by four orders of magnitude.

The key motivation in this kind of analysis is to what extent different BSM scenarios can be distinguished, either from $\mu \to e$ conversion alone or in combination with inputs from the purely leptonic processes of $\mu \to e\gamma$ or $\mu \to 3e$. A systematic approach to these questions is to describe LFV processes in terms of effective operators for the underlying LFV interaction. As already elaborated in Sec. 1.2, there have been various detailed studies focusing on different individual aspects, like particular effective operators, particular multipoles, or particular simplifications to the nuclear or bound-state physics. To assess the discriminatory power between the different operators robustly, all of these aspects need to be quantitatively controlled at the same time. Therefore we will set up such a framework in this chapter, and thereby lay the groundwork for a full comprehensive description of $\mu \to e$ conversion, with maximized discriminatory power.

After a brief introduction of the kinematic conventions for $\mu \to e$ conversion in nuclei, we will follow the schematics of Fig. 2.1 to work our way from the quark level, via the nucleon level, all the way to the nucleus level and even including bound-state effects. Consequently, this framework is ultimately able to combine all the just mentioned aspects into a comprehensive description of $\mu \to e$ conversion, directly dependent on the Wilson coefficients of the effective Lagrangian, as illustrated schematically in Fig. 1.5.

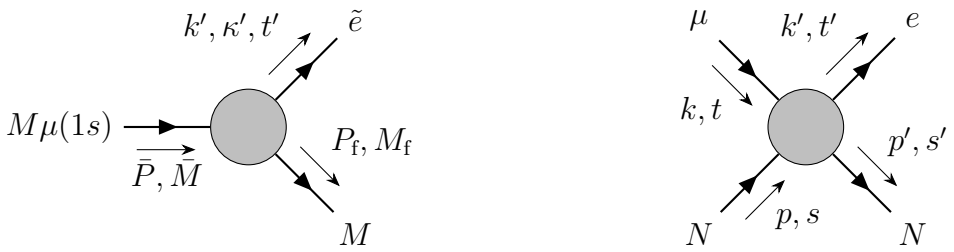

Figure 3.1: Feynman graphs for $\mu \to e$ conversion in nuclei and the internal one-nucleon interaction. The momentum of the bound states is composed of the momentum of the nucleus and muon according to $\bar{P}_\mu = P_{\mathrm{i}\,\mu} + k_\mu$, and the spin $\bar{M}$ of the bound state is a combination of the spin of the nucleus J_i, M_i, the spin of the muon $t = \pm\frac{1}{2}$ and the orbital angular momentum l, where the combination of the latter two quantities is denoted by κ according to Eq. (5.41). κ' is analogously defined for the spin of the electron $t' = \pm\frac{1}{2}$ and the orbital angular momentum l'. Since the muon is in the $1s$ ground state, we have $l = 0$, $\kappa = -1$. The total spin of the nucleus is the same for the initial and final state with $J = J_i = J_f$.

3.1 Kinematics

The kinematics of $\mu \to e$ conversion in nuclei can be considered on the nucleus level as a two-body decay, starting with a muonic nucleus at rest in the initial state and the ejected electron as well as the remaining nucleus in the final state. Inside the nucleus, this interaction is mediated by interactions with the individual nucleons inside the nucleus. Here, for now, we focus on one-nucleon interactions, but in the larger scope would like to extend this framework to also include corrections from two- or more-nucleon interactions. The kinematics and assigned spin and momenta labels for the $\mu \to e$ process, as well as the internal one-nucleon interactions, are presented in Fig. 3.1, where we use the notation that M refers to a nucleus (i.e. $M = {}^{27}\mathrm{Al}, {}^{48}\mathrm{Ti}, \dots$) and N refers to the nucleons (i.e. either proton or neutron: $N = p, n$). The notation $M\mu(1s)$ means the muon is bound in the $1s$-orbital, so the ground state of the nucleus and $\tilde{e}$ refers to the fact, that the outgoing electron is altered by the potential of the nucleus.

In the rest frame of the bound state, namely for $\bar{P} = (m_{\bar{P}}, \vec{0})$ with $m_{\bar{P}} = m_M + m_\mu + E_b^{\mu(1s)}$, where m_M is the nucleus mass, m_μ the muon mass and $E_b^{\mu(1s)} < 0$ the binding energy of the muon in the ground state of the nucleus, the four-momenta are given by

$$\begin{aligned} P_\mathrm{i} &= (m_{\bar{P}} - E, -\vec{k}), & P_\mathrm{f} &= (m_{\bar{P}} - E', -\vec{k'}), \\ k &= (E, \vec{k}), & k' &= (E', \vec{k}'), \\ p &= (p_0, \vec{p}), & p' &= (E + p_0 - E', \vec{k} + \vec{p} - \vec{k}'). \end{aligned} \tag{3.1}$$

Since the kinematics of the two-body decay are entirely fixed, we find

$$E' = \frac{m_{\bar{P}}^2 - m_M^2 + m_e^2}{2m_{\bar{P}}}, \qquad |\vec{k}'| = \frac{1}{2m_{\bar{P}}}\sqrt{\lambda(m_{\bar{P}}^2, m_M^2, m_e^2)}, \tag{3.2}$$

with the Källén function $\lambda(a,b,c) = a^2 + b^2 + c^2 - 2ab - 2bc - 2ac$. Thus, we have up to small corrections from recoil and the binding energy at leading order

$$E' \approx |\vec{k'}| \approx m_\mu. \tag{3.3}$$

Hence, at leading order, all of the energy of the mass of the muon is converted into kinetic energy for the electron.

While the muons as well as the nucleons are not in momentum eigenstates and thus all values for the momenta should in principle be considered, the fact that they are bound to the rest of the nucleus limits the range of the momentum they can in practice attain, without breaking loose from the nucleus. We further define the transferred momentum

$$q_\mu = k'_\mu - k_\mu = p_\mu - p'_\mu = P_{\mathrm{i}\,\mu} - P_{\mathrm{f}\,\mu}, \tag{3.4}$$

which remains a well-defined quantity at the same time for the full process as well as for the internal one, as long as we only consider one-nucleon interactions.

For easier reference of the here introduced kinematics we also refer to the lookup table of App. A.2.

3.2 Quark-level Lagrangian and Hadronic Matrix Elements

To describe $\mu \to e$ conversion, all operators of the Lagrangian of Eq. (2.3) are relevant, namely again

$$\mathcal{L}_{\mathrm{eff}}^{\mu\to e} = \sum_{Y=L,R} \left(\sum_{q=u,d,s} \sum_{\substack{X=S,P,\\ V,A,T}} C_Y^{X,q}\ L_Y^{X,(n)}\ Q_{(n)}^{X,q} + \sum_{\substack{X=D,\\ GG,G\tilde{G}}} C_Y^X\ L_Y^{X,(n)}\ Q_{(n)}^X \ + \ \mathrm{h.c.} \right), \tag{3.5}$$

with

$$\begin{aligned}
L_Y^S &= \Lambda^{-2}\ \overline{e_Y}\mu, & Q^{S,q} &= \bar{q}q,\\
L_Y^P &= L_Y^S, & Q^{P,q} &= \bar{q}\gamma^5 q,\\
L_Y^{V,\mu} &= \Lambda^{-2}\ \overline{e_Y}\gamma^\mu\mu, & Q_\mu^{V,q} &= \bar{q}\gamma_\mu q,\\
L_Y^{A,\mu} &= L_Y^{V,\mu}, & Q_\mu^{A,q} &= \bar{q}\gamma_\mu\gamma^5 q,\\
L_Y^{T,\mu\nu} &= \Lambda^{-2}\ \overline{e_Y}\sigma^{\mu\nu}\mu, & Q_{\mu\nu}^{T,q} &= \bar{q}\sigma_{\mu\nu}q,\\
L_Y^{GG} &= \Lambda^{-3}\ L_Y^S, & Q^{GG} &= \alpha_s G^a_{\alpha\beta}G_a^{\alpha\beta},\\
L_Y^{G\tilde{G}} &= \Lambda^{-3}\ L_Y^S, & Q^{G\tilde{G}} &= i\alpha_s G^a_{\alpha\beta}\tilde{G}_a^{\alpha\beta},\\
L_Y^{D,\mu\nu} &= \Lambda\ L_Y^{T,\mu\nu}, & Q_{\mu\nu}^D &= F_{\mu\nu}.
\end{aligned} \tag{3.6}$$

These quark-currents couple to the nucleons via hadronic matrix elements. The relevant hadronic matrix elements are given by Eq. (2.10), namely

$$\begin{aligned}
\langle N|\,\bar{q}q\,|N\rangle &= \bar{u}_N(p',s')\left(\frac{m_N}{m_q}f_q^N(q)\right)u_N(p,s),\\
\langle N|\,\bar{q}i\gamma^5 q\,|N\rangle &= \bar{u}_N(p',s')\left(\frac{m_N}{m_q}G_5^{q,N}(q)i\gamma^5\right)u_N(p,s),\\
\langle N|\,\bar{q}\gamma^\mu q\,|N\rangle &= \bar{u}_N(p',s')\left(\gamma^\mu F_1^{q,N}(q)-\frac{i\sigma^{\mu\nu}q_\nu}{2m_N}F_2^{q,N}(q)\right)u_N(p,s),\\
\langle N|\,\bar{q}\gamma^\mu\gamma^5 q\,|N\rangle &= \bar{u}_N(p',s')\left(\gamma^\mu\gamma^5 G_A^{q,N}(q)-\gamma^5\frac{q^\mu}{2m_N}G_P^{q,N}(q)\right)u_N(p,s),\\
\langle N|\,\bar{q}\sigma^{\mu\nu}q\,|N\rangle &= \bar{u}_N(p',s')\left(\sigma^{\mu\nu}F_{1,T}^{q,N}(q)-2\gamma^{[\mu}\frac{iq^{\nu]}}{m_N}F_{2,T}^{q,N}(q)-4p^{[\mu}\frac{iq^{\nu]}}{m_N^2}F_{3,T}^{q,N}(q)\right)u_N(p,s),\\
\langle N|\,G^a_{\mu\nu}G_a^{\mu\nu}\,|N\rangle &= \bar{u}_N(p',s')\left(\frac{4\pi}{\alpha_s}a_N(q)\right)u_N(p,s),\\
\langle N|\,G^a_{\mu\nu}\tilde{G}_a^{\mu\nu}\,|N\rangle &= \bar{u}_N(p',s')\left(i\frac{4\pi}{\alpha_s}\tilde{a}_N(q)\gamma^5\right)u_N(p,s).
\end{aligned}\tag{3.7}$$

We may write all these relations generally as

$$\langle N|\,Q_{(n)}^{X(,q)}\,|N\rangle = \sum_{\substack{X'=S,P,\\ V,A,T}} F_{X,X'}^{(q,)N}\ \mathcal{Q}_{X,X'}^{(n,m)}\ \bar{u}_{N'}\Gamma_{(m)}^{X'}u_N,\tag{3.8}$$

with

$$\begin{aligned}
F_{S,S}^{q,N} &= \frac{m_N}{m_q}f_q^{q,N}, & \mathcal{Q}_{S,S} &= 1,\\
F_{P,P}^{q,N} &= \frac{m_N}{m_q}G_5^{q,N}, & \mathcal{Q}_{P,P} &= 1,\\
F_{V,V}^{q,N} &= F_1^{q,N}, & \mathcal{Q}_{V,V}^{\mu,\nu} &= g^{\mu\nu},\\
F_{V,T}^{q,N} &= -\frac{1}{2}F_2^{q,N}, & \mathcal{Q}_{V,T}^{\mu',\mu\nu} &= \tfrac{ig^{\mu'\mu}q^\nu}{m_N},\\
F_{A,A}^{q,N} &= G_A^{q,N}, & \mathcal{Q}_{A,A}^{\mu,\nu} &= g^{\mu\nu},\\
F_{A,P}^{q,N} &= i\frac{1}{2}F_2^{q,N}, & \mathcal{Q}_{A,P}^{\mu} &= \tfrac{iq^\mu}{m_N},\\
F_{T,T}^{q,N} &= F_{1,T}^{q,N}, & \mathcal{Q}_{T,T}^{\mu\nu,\mu'\nu'} &= g^{\mu\mu'}g^{\nu\nu'},\\
F_{T,V}^{q,N} &= -2F_{2,T}^{q,N}, & \mathcal{Q}_{T,V}^{\mu\nu,\mu'} &= \tfrac{iq^{[\nu}g^{\mu]\mu'}}{m_N},\\
F_{T,S}^{q,N} &= -4F_{3,T}^{q,N}, & \mathcal{Q}_{T,S}^{\mu\nu} &= \tfrac{iq^{[\nu}p^{\mu]}}{m_N^2},\\
F_{GG,S}^{N} &= 4\pi a_N, & \mathcal{Q}_{GG,S} &= 1,\\
F_{G\tilde{G},P}^{N} &= -4\pi\tilde{a}_N, & \mathcal{Q}_{GG,S} &= 1,
\end{aligned}\tag{3.9}$$

and all other $F_{X,X'}^{(q,)N}$ and $\mathcal{Q}_{X,X'}^{(n,m)}$ are zero.

3.3 Matrix Element for free $N\mu \to Ne$

To match our Lagrangian on the quark level to the nucleon-level description, we calculate the matrix element for free $N\mu \to Ne$ using the hadronic matrix elements. We find

$$i\mathcal{M}_{X,Y}^{N(,q)} = iC_Y^{X(,q)} \langle N, e| L_Y^{X,(n)} Q_{(n)}^{X(,q)} |N, \mu\rangle = iC_Y^{X(,q)} \langle e| L_Y^{X,(n)} |\mu\rangle \langle N| Q_{(n)}^{X(,q)} |N\rangle , \quad (3.10)$$

with $X \in \{S, P, V, A, T, GG, G\tilde{G}\}$, where we excluded the dipole term $X = D$, which will be discussed in more detail separately in Sec. 3.7. Inserting the matrix elements of Eq. (3.8) results in

$$i\mathcal{M}_{X,Y}^{N(,q)} = iC_Y^{X(,q)} \sum_{X'} F_{X,X'}^{(q,)N} \ \langle e| L_Y^{X,(n)} |\mu\rangle \ \mathcal{Q}_{X,X'}^{(n,m)} \ \bar{u}_{N'} \Gamma_{(m)}^{X'} u_N. \quad (3.11)$$

We may further combine the same Lorentz structures on the leptonic side according to

$$L^S = L^P = \Lambda L^{GG} = \Lambda L^{G\tilde{G}}, \qquad L^V = L^A, \quad (3.12)$$

and may thus write

$$\begin{aligned} i\mathcal{M}_Y^N &= \sum_{q=u,d,s} \sum_{\substack{X=S,P,\\V,A,T}} i\mathcal{M}_{X,Y}^{N,q} + \sum_{X=GG,G\tilde{G}} i\mathcal{M}_{X,Y}^N \\ &:= i \sum_{X\in S,V,T} \sum_{\substack{X'=S,P,\\V,A,T}} C_Y^{X,X'} \ \langle e| L_Y^{X,(n)} |\mu\rangle \ \mathcal{P}_{X,X'}^{(n,m)} \ \bar{u}_{N'} \Gamma_{(m)}^{X'} u_N, \end{aligned} \quad (3.13)$$

defining

$$\begin{aligned}
C_Y^{S,S} &= \sum_q C_Y^{S,q} F_{S,S}^{q,N} + \Lambda^{-1} C_Y^{GG} F_{GG,S}^N, & \mathcal{P}_{S,S} &= 1 \\
C_Y^{S,P} &= \sum_q C_Y^{P,q} F_{P,P}^{q,N} + \Lambda^{-1} C_Y^{G\tilde{G}} F_{G\tilde{G},P}^N, & \mathcal{P}_{S,P} &= 1 \\
C_Y^{V,V} &= \sum_q C_Y^{V,q} F_{V,V}^{q,N}, & \mathcal{P}_{V,V}^{\mu,\mu'} &= g^{\mu\mu'} \\
C_Y^{V,A} &= \sum_q C_Y^{A,q} F_{A,A}^{q,N}, & \mathcal{P}_{V,A}^{\mu,\mu'} &= g^{\mu\mu'} \\
C_Y^{V,P} &= \sum_q C_Y^{A,q} F_{A,P}^{q,N}, & \mathcal{P}_{V,P}^{\mu} &= \tfrac{iq^\mu}{m_N} \\
C_Y^{V,T} &= \sum_q C_Y^{V,q} F_{V,T}^{q,N}, & \mathcal{P}_{V,T}^{\mu',\mu\nu} &= \tfrac{ig^{\mu'\mu}q^\nu}{m_N} \\
C_Y^{T,T} &= \sum_q C_Y^{T,q} F_{T,T}^{q,N}, & \mathcal{P}_{T,T}^{\mu\nu,\mu'\nu'} &= g^{\mu\mu'}g^{\nu\nu'} \\
C_Y^{T,S} &= \sum_q C_Y^{T,q} F_{T,S}^{q,N}, & \mathcal{P}_{T,S}^{\mu\nu} &= \tfrac{iq^{[\nu}p^{\mu]}}{m_N^2}
\end{aligned}$$

$$C_Y^{T,V} = \sum_q C_Y^{T,q} F_{T,V}^{q,N}, \qquad \mathcal{P}_{T,V}^{\mu\nu,\mu'} = \tfrac{iq^{[\nu}g^{\mu]\mu'}}{m_N} \tag{3.14}$$

To find the appearing non-relativistic structures, we need to expand the nucleon spinors in this expression non-relativistically, as given in Eq. (2.19). For this, we first need to separate the Lorentz contractions in terms of temporal and spatial components. We use the following notation

$$\begin{aligned} A_\mu^X B_X^\mu &= A_0^X B_X^0 - A_i^X A_X^i := A^{X^0} B_{X^0} + A_i^{\vec{X}} B_{\vec{X}}^i, \\ A_{\mu\nu}^X B_X^{\mu\nu} &= -A_{0i}^X B_X^{0i} - A_{i0}^X B_X^{i0} + A_{ij}^X B_X^{ij} \\ &= -2A_{[0i]}^X B_X^{[0i]} + \frac{1}{2}(\epsilon_{i'j'k} A_{i'j'}^X)(\epsilon_{ijk} B_X^{ij}) := A_i^{\vec{X}} B_{\vec{X}}^i + A_i^{\vec{\vec{X}}} B_{\vec{\vec{X}}}^i, \end{aligned} \tag{3.15}$$

which is valid if at least one out of $A_{\mu\nu}^X$ and $B_X^{\mu\nu}$ is antisymmetric. Note that here $\Gamma_{\mu\nu}^T$ as well as $L_{\mu\nu}^T$ are antisymmetric, so this will be true for any tensor contraction that appears. This results in

$$i\mathcal{M}_Y^N = i \sum_{\substack{X\in S,V^0,\vec{V},\\ \vec{T},\vec{\vec{T}}}} \sum_{\substack{X'=S,P,\\ V^0,\vec{V},A^0,\vec{A},\vec{T},\vec{\vec{T}}}} C_Y^{X,X'} \ \langle e|\, L_Y^{X,(n)} \,|\mu\rangle \ \mathcal{P}_{X,X'}^{(n,m)} \ \bar{u}_{N'} \Gamma_{(m)}^{X'} u_N, \tag{3.16}$$

where $(n) \in \{\emptyset, i\}$, now denotes the contractions of Euclidean indices and

$$C_Y^{X^0,X^0} = C_Y^{\vec{X},\vec{X}'} = C_Y^{\vec{\vec{X}},\vec{\vec{X}}'} = C_Y^{X,X'}, \tag{3.17}$$

stays the same, as we absorb any factors of -1, 2, $\frac{1}{2}$ into the kinematic prefactors $\mathcal{P}_{X,X'}$, which become

$$\begin{aligned} &\mathcal{P}_{S,S} = 1, && \mathcal{P}_{S,P} = 1, && \mathcal{P}_{V^0,V^0} = 1 \\ &\mathcal{P}_{\vec{V},\vec{V}}^{i,j} = -\delta^{ij}, && \mathcal{P}_{V^0,A^0} = 1, && \mathcal{P}_{\vec{V},\vec{A}}^{i,j} = -\delta^{ij} \\ &\mathcal{P}_{V^0,P} = \frac{iq^0}{m_N}, && \mathcal{P}_{\vec{V},P}^{i} = \frac{-iq^i}{m_N}, && \mathcal{P}_{V^0,\vec{T}}^{j} = \frac{-iq^j}{m_N} \\ &\mathcal{P}_{\vec{V},\vec{T}}^{ij} = \frac{iq^0}{m_N}\delta^{ij}, && \mathcal{P}_{\vec{V},\vec{\vec{T}}}^{i,j} = \frac{i\epsilon_{imj}q^m}{2m_N}, && \mathcal{P}_{\vec{T},\vec{T}}^{ij} = -2\delta^{ij} \\ &\mathcal{P}_{\vec{\vec{T}},\vec{\vec{T}}}^{ij} = \frac{1}{2}\delta^{ij}, && \mathcal{P}_{\vec{T},S}^{i} = -2\frac{iq^{[0}p^{i]}}{m_N^2}, && \mathcal{P}_{\vec{\vec{T}},S}^{k} = \frac{iq^i p^j}{2m_N^2}\epsilon_{ijk} \\ &\mathcal{P}_{\vec{T},V^0}^{i} = \frac{iq^i}{m_N}, && \mathcal{P}_{\vec{T},\vec{V}}^{i,j} = \frac{-iq^0\delta^{ij}}{m_N}, && \mathcal{P}_{\vec{\vec{T}},\vec{V}}^{i,j} = \frac{iq^k}{2m_N}\epsilon_{ikj}. \end{aligned} \tag{3.18}$$

Now expanding $\bar{u}_{N'}\Gamma_{(m)}^{X'}u_N$ for the different structures non-relativistically in terms of the nucleon momenta leads to Eq. (2.21), which we may write generally as

$$\bar{u}_{N'}\Gamma_{X'}^{(n)}u_N = \sum_{\substack{S\in M,\Sigma,\\ \Delta,\Omega,\Phi}} \mathcal{K}_{X',S}^{(n,m)} \ \chi_{s'}^\dagger h_{(m)}^S \chi_s, \tag{3.19}$$

with

$$\begin{aligned}
\mathcal{K}_{S,M} &= 1 - \frac{\vec{q}^2}{8m_N^2}, & \mathcal{K}^i_{S,\Delta} &= \frac{-iqq^i}{2m_N^2}, & \mathcal{K}^i_{S,\Phi} &= \frac{iqq^i}{4m_N^2},\\
\mathcal{K}^i_{P,\Sigma} &= \frac{q^i}{2m_N}, & \mathcal{K}_{V^0,M} &= 1 - \frac{\vec{q}^2}{8m_N^2}, & \mathcal{K}^i_{V^0,\Phi} &= \frac{-iqq^i}{4m_N^2},\\
\mathcal{K}^i_{\vec{V},M} &= \frac{-q^i}{2m_N}, & \mathcal{K}^{i,j}_{\vec{V},\Delta} &= \delta^{ij}\frac{-iq}{m_N}, & \mathcal{K}^{i,j}_{\vec{V},\Sigma} &= \frac{i\epsilon^{ikj}q_k}{2m_N},\\
\mathcal{K}^i_{A^0,\Sigma} &= \frac{-q^i}{2m_N}, & \mathcal{K}_{A^0,\Omega} &= \frac{-iq}{m_N}, & \mathcal{K}^{i,j}_{\vec{A},\Sigma} &= \left(1 - \frac{\vec{q}^2}{8m_N^2}\right)\delta^{ij},\\
\mathcal{K}^{i,j}_{\vec{A},\Delta} &= \frac{q\epsilon^{ikj}q_k}{4m_N^2}, & \mathcal{K}^{i,j}_{\vec{A},\Phi} &= \frac{-q\epsilon^{ikj}q_k}{4m_N^2}, & \mathcal{K}^i_{\vec{A},\Omega} &= \frac{iqq^i}{4m_N^2},\\
\mathcal{K}^i_{\vec{T},M} &= \frac{iq^i}{2m_N}, & \mathcal{K}^{i,j}_{\vec{T},\Sigma} &= \frac{\epsilon_{ikj}q_k}{2m_N}, & \mathcal{K}^{i,j}_{\vec{T},\Phi} &= \frac{-q}{m_N}\delta^{ij},\\
\mathcal{K}^{i,j}_{\vec{T},\Sigma} &= 2\left(1 - \frac{\vec{q}^2}{8m_N^2}\right)\delta^{ij}, & \mathcal{K}^{i,j}_{\vec{T},\Delta} &= 2\frac{-qq_k\epsilon^{ikj}}{4m_N^2}, & \mathcal{K}^{i,j}_{\vec{T},\Phi} &= 2\frac{qq_k\epsilon^{ikj}}{4m_N^2},
\end{aligned} \tag{3.20}$$

and all others zero. Inserting these now in Eq. (3.16), we find that the kinematic prefactors $\mathcal{P}_{X,X'}$, still contain some p_i as well as p_0 and q_0 dependence. These can alter the nuclear structure as only q_i remains a well-defined quantity also for the whole nucleus. First we can get rid of the p_0, q_0, as for free nucleons, we have

$$\frac{p_0}{m_N} = 1 + \frac{\vec{p}^2}{2m_N^2} + \mathcal{O}(m_N^{-4}), \qquad \frac{q_0}{m_N} = \frac{p_0 - p_0'}{m_N} = \frac{2\vec{q}\vec{p} - \vec{q}^2}{2m_N^2} + \mathcal{O}(m_N^{-4}). \tag{3.21}$$

Note in particular, that in this interpretation hence q_0/m_N should be considered of order $\mathcal{O}(m_N^{-2})$ and thus most terms including q_0 drop out. However, as already denoted in Ref. [119], there arises some ambiguity in the treatment of q_0, once we go from the free one-nucleon interaction to a whole nucleus, since these free nucleon kinematics will not be valid anymore, while bound to a nucleus. In particular, q_0 could also be interpreted as the energy difference on the leptonic side of the process, which could be calculated based on the bound-state energy of the muon. Ref. [119] finds the effects of these ambiguities to be small, in particular, if only one-nucleon interactions are considered. And since in our application these terms are already sub-leading, we find it sufficient to choose these free nucleon kinematics here, though alternatives could be investigated in the future. Recently, these ambiguities in the treatment of q_0 have also been discussed in Ref. [121] in the context of β decays.

The now remaining p_i dependencies can be combined into the non-relativistic structures using

$$\frac{p_i}{m_N}h^M = \frac{-iq}{m_N}h_i^\Delta, \qquad \frac{p_i}{m_N}h_i^\Sigma = \frac{-iq}{m_N}h^\Omega, \qquad \frac{\epsilon_{ijk}p_j}{m_N}h_k^\Sigma = -\frac{q}{m_N}h_i^\Phi, \tag{3.22}$$

	S	V^0	$\vec{V}$	$\vec{T}$	$\overleftrightarrow{T}$	all
M	S	V^0,$\vec{T}$	$\vec{V}$,$\vec{T}$	S, $\vec{T}$,V^0,$\vec{V}$	(S),($\vec{V}$)	S,$\vec{T}$,V^0,$\vec{V}$
Σ	P	($\vec{T}$),P,A^0	$\vec{T}$,$\overleftrightarrow{T}$,$\vec{V}$,P,$\vec{A}$	$\vec{T}$,$\vec{V}$	$\overleftrightarrow{T}$,$\vec{V}$	$\vec{T}$,$\overleftrightarrow{T}$,$\vec{V}$,P,A^0,$\vec{A}$
Δ	S	-	$\overleftrightarrow{T}$,$\vec{V}$,$\vec{A}$	S,$\vec{V}$	S,$\overleftrightarrow{T}$,$\vec{V}$	S,$\overleftrightarrow{T}$,$\vec{V}$,$\vec{A}$
Ω	-	A^0	$\vec{A}$	-	-	$\vec{A}$,A^0
Φ	S	$\vec{T}$,V^0	$\vec{T}$,$\overleftrightarrow{T}$,$\vec{A}$	S,$\vec{T}$,V^0	S,$\overleftrightarrow{T}$	S,$\vec{T}$,$\overleftrightarrow{T}$,V^0,$\vec{A}$
all	S,P	$\vec{T}$,V^0,P,A^0	$\vec{T}$,$\overleftrightarrow{T}$,$\vec{V}$,P,$\vec{A}$	S,$\vec{T}$,V^0,$\vec{V}$	S,$\overleftrightarrow{T}$,$\vec{V}$	all

Table 3.1: List of existing intermediate X' for each X, S combination

and all other structures that could be constructed in this way were already excluded. Using these rules we can write

$$\begin{aligned} i\mathcal{M}_Y^N &= i \sum_{\substack{X\in S,V^0,\vec{V},\\ \vec{T},\overleftrightarrow{T}}} \sum_{\substack{X'=S,P,\\ V^0,\vec{V},A^0,\vec{A},\vec{T},\overleftrightarrow{T}}} C_Y^{X,X'} \ \langle e|\, L_Y^{X,(n)}\, |\mu\rangle \ \mathcal{P}_{X,X'}^{(n,m)} \ \bar{u}_{N'}\Gamma_{(m)}^{X'} u_N \\ &= i \sum_{\substack{X\in S,V^0,\vec{V},\\ \vec{T},\overleftrightarrow{T}}} \sum_{\substack{X'=S,P,\\ V^0,\vec{V},A^0,\vec{A},\vec{T},\overleftrightarrow{T}}} \sum_{\substack{S\in M,\Sigma,\\ \Delta,\Omega,\Phi}} C_Y^{X,X'} \ \langle e|\, L_Y^{X,(n)}\, |\mu\rangle \ \mathcal{P}_{X,X'}^{(n,m)} \ \mathcal{K}_{X',S}^{(m,l)} \ \chi_{s'}^\dagger h_{(l)}^S \chi_s \\ &:= i \sum_{\substack{X\in S,V^0,\vec{V},\\ \vec{T},\overleftrightarrow{T}}} \sum_{\substack{S\in M,\Sigma,\\ \Delta,\Omega,\Phi}} \langle e|\, L_Y^{X,(n)}\, |\mu\rangle \ C_{Y,X,S}^{(n,m)} \ \chi_{s'}^\dagger h_{(m)}^S \chi_s, \end{aligned} \tag{3.23}$$

where in the last step we also applied Eqs. (3.21) and (3.22). To find the prefactors $C_{Y,X,S}^{(n,m)}$ we need to consider

$$\sum_{\substack{X'=S,P,\\ V^0,\vec{V},A^0,\vec{A},\vec{T},\overleftrightarrow{T}}} \tilde{C}_Y^{X,X'} \tilde{\mathcal{P}}_{X,X'}^{(n,l)} \mathcal{K}_{X',S}^{(l,m)} \tag{3.24}$$

and collect all non-zero summands. The existing combinations based on Eq. (3.18) and (3.20) can be seen in Tab. 3.1. We find, again only keeping terms up to $\mathcal{O}(m_N^{-2})$,

$$\begin{aligned} C_{Y,S,M} &= \left(1 - \frac{\vec{q}^2}{8m_N^2}\right) C_Y^{S,S}, & C_{Y,S,\Sigma}^i &= \frac{q^i}{2m_N} C_Y^{S,P}, \\ C_{Y,S,\Delta}^i &= \frac{-iqq^i}{2m_N^2} C_Y^{S,S}, & C_{Y,S,\Phi}^i &= \frac{iqq^i}{4m_N^2} C_Y^{S,S}, \\ C_{Y,V^0,M} &= C_Y^{V,V} + \frac{\vec{q}^2}{8m_N^2}\Big(4C_Y^{V,T} - C_Y^{V,V}\Big), & C_{Y,V^0,\Sigma}^i &= \frac{-q^i}{2m_N} C_Y^{V,A}, \\ C_{Y,V^0,\Phi}^i &= \frac{iqq^i}{4m_N^2}\Big(4C_Y^{V,T} - C_Y^{V,V}\Big), & C_{Y,V^0,\Omega} &= \frac{-iq}{m_N} C_Y^{V,A}, \\ C_{Y,\vec{V},\Delta}^{i,j} &= \delta^{ij}\frac{iq}{m_N} C_Y^{V,V} + \frac{-q\epsilon^{ilj}q_l}{4m_N^2} C_Y^{V,A}, & C_{Y,\vec{V},M}^i &= \frac{q^i}{2m_N} C_Y^{V,V}, \end{aligned}$$

$$
\begin{aligned}
C^{i,j}_{Y,\vec{V},\Phi} &= \frac{q\epsilon^{ilj}q_l}{4m_N^2}C_Y^{V,A}, & C^{i}_{Y,\vec{V},\Omega} &= \frac{-iqq^i}{4m_N^2}C_Y^{V,A},\\
C^{i,j}_{Y,\vec{V},\Sigma} &= (-\delta^{ij})\left(1-\frac{\vec{q}^2}{8m_N^2}\right)C_Y^{V,A} + \frac{i\epsilon^{ilj}q_l}{2m_N}\left(2C_Y^{V,T}-C_Y^{V,V}\right) + \frac{-iq^iq^j}{2m_N^2}C_Y^{V,P},\\
C^{i}_{Y,\vec{T},M} &= \frac{iq^i}{m_N}\left(C_Y^{T,S}-C_Y^{T,T}+C_Y^{T,V}\right), & C^{i,j}_{Y,\vec{T},\Sigma} &= \frac{-\epsilon_{ilj}q_l}{m_N}C_Y^{T,T},\\
C^{i,j}_{Y,\vec{T},\Phi} &= \frac{2q}{m_N}\delta^{ij}C_Y^{T,T},\\
C^{i,j}_{Y,\vec{\tilde{T}},\Sigma} &= \delta^{ij}\left(1-\frac{\vec{q}^2}{8m_N^2}\right)C_Y^{T,T} + \frac{\delta^{ij}\vec{q}^2-q^iq^j}{4m_N^2}C_Y^{T,V}, & C^{i,j}_{Y,\vec{\tilde{T}},\Phi} &= \frac{qq_l\epsilon^{ilj}}{4m_N^2}C_Y^{T,T}\\
C^{i,j}_{Y,\vec{\tilde{T}},\Delta} &= \frac{q\epsilon_{ilj}q^l}{2m_N^2}\left(C_Y^{T,S}-C_Y^{T,T}+C_Y^{T,V}\right).
\end{aligned}
\tag{3.25}
$$

Note that the combinations $(X, X', S) = (V^0, \vec{T}, \Sigma)$ and $(\vec{\tilde{T}}, \vec{V}, M)$ vanished as they go with $q_iq_j\epsilon_{ijk} = 0$ and thus for $C^i_{Y,\vec{\tilde{T}},M}$ only one term remains, which has a remaining p_i dependence and thus becomes a part of the $C^i_{Y,\vec{\tilde{T}},\Delta}$ term using Eq. (3.22). With these prefactors, Eq. (3.23) is now the full matrix element for free non-relativistic $N\mu \to Ne$.

3.4 Nucleon-level Lagrangian

To construct what happens on the nucleus level, we need to construct the non-relativistic nucleon-level Lagrangian, which can reproduce the same matrix element as calculated for free non-relativistic $N\mu \to Ne$ in the previous section. Fortunately, this is quite straightforward to construct. One finds

$$
\mathcal{L}^{\text{non-rel.}}_{Y,N} = \sum_{\substack{X\in S,V^0,\vec{V},\\ \vec{T},\vec{\tilde{T}}}} \sum_{\substack{S\in M,\Sigma,\\ \Delta,\Omega,\Phi}} L_Y^{X,(n)}\ \hat{C}^{(n,m)}_{Y,X,S}\ \hat{h}^{S,N}_{(m)}, \tag{3.26}
$$

where

$$
\hat{C}^{(n,m)}_{Y,X,S} = C^{(n,m)}_{Y,X,S}\ [q_i \to -i\vec{\nabla}_i], \qquad \hat{h}^{S,N}_{(m)} = N^+\ h^S_{(m)}[p_i \to -i\vec{\nabla}_i]\ N^-, \tag{3.27}
$$

such that in combination with the non-relativistic spinors, defined via

$$
N^-(x)\,|N(p,s)\rangle = \chi_s e^{i\vec{p}\cdot\vec{x}}, \qquad \langle N(p',s')|\,N^+(x) = \chi^\dagger_{s'}e^{-i\vec{p}'\cdot\vec{x}}, \tag{3.28}
$$

the same dependencies in the matrix element are reproduced via

$$
\langle N(p',s')|\,N^+(x)\vec{\nabla}N^-(x)\,|N(p,s)\rangle = i\vec{p}\ \chi^\dagger_{s'}\chi_s e^{i\vec{q}\cdot\vec{x}}, \tag{3.29}
$$

$$
\vec{\nabla}\,\langle N(p',s')|\,N^+(x)N^-(x)\,|N(p,s)\rangle = i\vec{q}\ \chi^\dagger_{s'}\chi_s e^{i\vec{q}\cdot\vec{x}}. \tag{3.30}
$$

This Lagrangian can now be utilized more generally to calculate the interactions with a whole nucleus.

For a nucleus M with $A = Z + N$ nucleons $N_i \in \{n, p\}$, we may copy the Lagrangian A times to describe the one-particle interactions with each nucleon according to

$$\mathcal{L}_Y^M = \sum_{i=1}^{A} \mathcal{L}_{Y,N_i}^{\text{non-rel.}}. \tag{3.31}$$

3.5 Matrix element for $\mu \to e$ Conversion

To calculate the matrix element for the whole $\mu \to e$ conversion process according to $M\mu(1s) \to M + \tilde{e}$, we need to employ the Lagrangian of Eq. (3.26) for a whole nucleus and deduce the nuclear response on the hadronic side of the interaction and include the bound-state physics on the leptonic side. Fortunately, these two aspects party decouple, as our interaction also separates into a leptonic and a hadronic part. Since the nucleus is markedly heavier than the muon or the electron, from the perspective of the leptons, the nucleus can be considered as a static potential and we may consider the bound-state physics solely by adjusting the muon and electron states. Hence, the in-state of the process separates into the incoming nucleus M and a bound muon $\mu(1s)$ and the out-state separates into a perturbed electron $\tilde{e}$ and the outgoing nucleus M. Namely, we may write

$$\begin{aligned} \left|M\mu(1s)(\bar{P}, \bar{M})\right\rangle = |\mu(k, \kappa = -1, t)\rangle \, |M(P_i, J, M_i)\rangle \qquad &:= |\mu(1s)\rangle \, |M\rangle \,, \\ \langle M(P_f, J, M_f); \tilde{e}(k', \kappa', t')| = \langle M(P_f, J, M_f)| \, \langle \tilde{e}(k', \kappa', t')| \qquad &:= \langle M| \, \langle \tilde{e}| \,, \end{aligned} \tag{3.32}$$

where the spin and momentum labels are according to Fig. 1.3. Hence, the matrix element for this process becomes

$$\begin{aligned} i\mathcal{M}_Y &= \int \mathrm{d}^3x \sum_{i=1}^{A} \langle M; \tilde{e}| \, \mathcal{L}_{Y,N_i}^{\text{non-rel.}}(x) \, |M\mu(1s)\rangle \,, \\ &= \int \mathrm{d}^3x \sum_{i=1}^{A} \langle M| \, \langle \tilde{e}| \, \mathcal{L}_{Y,N_i}^{\text{non-rel.}}(x) \, |\mu(1s)\rangle \, |M\rangle \,, \\ &= \int \mathrm{d}^3x \sum_{i=1}^{A} \sum_{X,S} \langle M| \, \langle \tilde{e}| \, L_Y^{X,(n)} \, \hat{C}_{Y,X,S}^{(n,m)} \, \hat{h}_{(m)}^{S,N_i} \, |\mu(1s)\rangle \, |M\rangle \,, \\ &= \int \mathrm{d}^3x \sum_{i=1}^{A} \sum_{X,S} \langle \tilde{e}| \, L_Y^{X,(n)} \, |\mu(1s)\rangle \, \langle M| \, \hat{C}_{Y,X,S}^{(n,m)} \, \hat{h}_{(m)}^{S,N_i} \, |M\rangle \,. \end{aligned} \tag{3.33}$$

We can now evaluate the leptonic side via

$$\mu(x) \, |\mu(1s)\rangle = \psi_\mu^{(1s),t}(x), \qquad e_Y(x) \, |\tilde{e}\rangle = \psi_{e_Y}^{\kappa',t'}(x) = P_Y \psi_e^{\kappa',t'}(x), \tag{3.34}$$

where the $\psi(x)$ are the full four-component position space solutions of the Dirac equation in the presence of the nucleus potential. These can be separated into radial and angular components and calculated numerically as explained in great detail in Chap. 5. The wave

functions are given in Eq. (5.43), which we reveal in advance to be

$$\psi^{\mu}_{\kappa}(\vec{r}) = \frac{1}{r}\begin{pmatrix} g_{\kappa}(r)\phi^{\mu}_{\kappa}(\hat{r}) \\ i f_{\kappa}(r)\phi^{\mu}_{-\kappa}(\hat{r}) \end{pmatrix}. \tag{3.35}$$

Applying this parameterization, we find

$$\langle \tilde{e}|\, L_Y^{X,(n)}\, |\mu(1s)\rangle = \Lambda^{-2}\ \overline{\Psi^{\kappa',t'}_{e_Y}}\Gamma^{(n)}_X \Psi^{(1s),t}_{\mu}, \tag{3.36}$$

such that the amplitude becomes

$$i\mathcal{M}_Y = \int \mathrm{d}^3x \sum_{i=1}^{A}\sum_{X,S} \overline{\Psi^{\kappa',t'}_{e_Y}}\Gamma^{(n)}_X \Psi^{(1s),t}_{\mu}\, \langle M|\, \hat{C}^{(n,m)}_{Y,X,S}\ \hat{h}^{S,N_i}_{(m)}\, |M\rangle\,. \tag{3.37}$$

To perform the common multipole decomposition as explained in Sec. 2.4 we rewrite the leptonic side in terms of its Fourier transformation via

$$\begin{aligned} \overline{\Psi^{\kappa',t'}_{e_Y}(x)}\Gamma^{(n)}_X \Psi^{(1s),t}_{\mu}(x) &= \int \frac{\mathrm{d}^3q}{(2\pi)^3}\, \widetilde{\overline{\Psi^{\kappa',t'}_{e_Y}}\Gamma^{(n)}_X \Psi^{(1s),t}_{\mu}}(\vec{q})\ e^{-i\vec{q}\cdot\vec{x}}, \\ \widetilde{\overline{\Psi^{\kappa',t'}_{e_Y}}\Gamma^{(n)}_X \Psi^{(1s),t}_{\mu}}(\vec{q}) &= \int \mathrm{d}^3x'\, \overline{\Psi^{\kappa',t'}_{e_Y}(x')}\Gamma^{(n)}_X \Psi^{(1s),t}_{\mu}(x')\ e^{i\vec{q}\cdot\vec{x}'}, \end{aligned} \tag{3.38}$$

such that we get

$$\begin{aligned} i\mathcal{M}_Y &= \int \mathrm{d}^3x \int \frac{\mathrm{d}^3q}{(2\pi)^3} \sum_{i=1}^{A}\sum_{X,S} \widetilde{\overline{\Psi^{\kappa',t'}_{e_Y}}\Gamma^{(n)}_X \Psi^{(1s),t}_{\mu}}(\vec{q})\ e^{-i\vec{q}\vec{x}}\, \langle M|\, \hat{C}^{(n,m)}_{Y,X,S}\ \hat{h}^{S,N_i}_{(m)}\, |M\rangle\,, \\ &= \int \mathrm{d}^3x \int \frac{\mathrm{d}^3q}{(2\pi)^3} \sum_{i=1}^{A}\sum_{X,S} C^{(n,m)}_{Y,X,S}\ \widetilde{\overline{\Psi^{\kappa',t'}_{e_Y}}\Gamma^{(n)}_X \Psi^{(1s),t}_{\mu}}(\vec{q})\ e^{-i\vec{q}\vec{x}}\, \langle M|\, \hat{h}^{S,N_i}_{(m)}\, |M\rangle\,, \end{aligned} \tag{3.39}$$

where in the second step we are able to transform the $-i\vec{\nabla}$ inside the $\hat{C}^{(n,m)}_{Y,X,S}$ back to $\vec{q}$, giving back the $C^{(n,m)}_{Y,X,S}$. This happens in the following way: Partial integration moves the derivative onto the leptonic side (picking up a minus sign), where it acts on $e^{-i\vec{q}\vec{x}}$, giving exactly $\vec{q}$ back. We define the leptonic current as

$$\tilde{l}^{(m)}_{S,Y}(\vec{q}) = \sum_X C^{(n,m)}_{Y,X,S}\ \widetilde{\overline{\Psi^{\kappa',t'}_{e_Y}}\Gamma^{(n)}_X \Psi^{(1s),t}_{\mu}}(\vec{q}), \tag{3.40}$$

where the tilde reflects the fact, that this is the Fourier transform of the leptonic current

$$l^{(m)}_{S,Y} = \sum_X \tilde{C}^{(n,m)}_{Y,X,S}\ \overline{\Psi^{\kappa',t'}_{e_Y}}\Gamma^{(n)}_X \Psi^{(1s),t}_{\mu}. \tag{3.41}$$

We use this notation to write

$$
\begin{aligned}
i\mathcal{M}_Y &= \int \mathrm{d}^3x \int \frac{\mathrm{d}^3q}{(2\pi)^3} \sum_{i=1}^{A} \sum_{S} \tilde{l}^{(m)}_{S,Y}(\vec{q})\; e^{-i\vec{q}\cdot\vec{x}} \,\langle M|\, \hat{h}^{S,N_i}_{(m)} \,|M\rangle \\
&= \int \frac{\mathrm{d}^3q}{(2\pi)^3} \sum_{i=1}^{A} \sum_{S=M,\Omega} \tilde{l}_{S,Y}(\vec{q}) \;\int \mathrm{d}^3x\, e^{-i\vec{q}\cdot\vec{x}} \,\langle M|\, \hat{h}^{S,N_i} \,|M\rangle \\
&\quad + \int \frac{\mathrm{d}^3q}{(2\pi)^3} \sum_{i=1}^{A} \sum_{S=\Sigma,\Delta,\Phi} \tilde{l}^{j}_{S,Y}(\vec{q}) \;\int \mathrm{d}^3x\, e^{-i\vec{q}\cdot\vec{x}} \,\langle M|\, \hat{h}^{S,N_i}_{j} \,|M\rangle \,, \qquad (3.42)
\end{aligned}
$$

separating the scalar and vector multipole structures. Carrying out the multipole decomposition according to Eq. (2.40) and inserting the definitions of Eq. (2.45), we find

$$
\begin{aligned}
i\mathcal{M}_Y = \int \frac{\mathrm{d}^3q}{(2\pi)^3} \sum_{i=1}^{A} \Bigg[& \sum_{S=M,\Omega} \int \mathrm{d}^3x \sum_{L\geq 0} \sqrt{4\pi(2L+1)}(-i)^L \tilde{l}_{S,Y}(\vec{q}) \,\langle M|\, S^i_{L,0} \,|M\rangle \\
& + \sum_{S=\Sigma,\Delta,\Phi} \int \mathrm{d}^3x \sum_{L\geq 0} \sqrt{4\pi(2L+1)}(-i)^L \tilde{l}^3_{S,Y} i \,\langle M|\, S''^{\,i}_{L,0} \,|M\rangle \\
& + \sum_{S=\Sigma,\Delta,\Phi} \int \mathrm{d}^3x \sum_{L\geq 1} \sqrt{4\pi(2L+1)}(-i)^L \\
& \quad \times \frac{1}{\sqrt{2}} \sum_{\lambda=\pm} \tilde{l}^{\lambda}_{S,Y}\big(-\lambda \,\langle M|\, S^i_{L,-\lambda} \,|M\rangle - i \,\langle M|\, S'^{\,i}_{L,-\lambda} \,|M\rangle\big) \Bigg] . \qquad (3.43)
\end{aligned}
$$

Reducing the matrix elements via the Wigner-Eckart theorem as given in Eq. (2.43), results in

$$
\begin{aligned}
i\mathcal{M}_Y = & \int \frac{\mathrm{d}^3q}{(2\pi)^3} \sum_{i=1}^{A} \int \mathrm{d}^3x \sum_{L\geq 0} \sqrt{\frac{4\pi(2L+1)}{2J+1}}(-i)^L \,\langle JM_i, L0|JM_f\rangle \\
& \quad \times \left[\sum_{S=M,\Omega} \tilde{l}_{S,Y}(\vec{q}) \,\langle M||S^i_{L,0}||M\rangle + \sum_{S=\Sigma,\Delta,\Phi} \tilde{l}^3_{S,Y} i \,\langle M||S''^{\,i}_{L}||M\rangle \right] \\
& + \int \frac{\mathrm{d}^3q}{(2\pi)^3} \sum_{i=1}^{A} \int \mathrm{d}^3x \sum_{L\geq 1} \sqrt{\frac{4\pi(2L+1)}{2J+1}}(-i)^L \frac{1}{\sqrt{2}} \sum_{\lambda=\pm} \langle JM_i, L-\lambda|JM_f\rangle \\
& \quad \times \left[\sum_{S=\Sigma,\Delta,\Phi} \tilde{l}^{\lambda}_{S,Y}\big(-\lambda \,\langle M||S^i_{L}||M\rangle - i \,\langle M||S'^{\,i}_{L}||M\rangle\big) \right] , \qquad (3.44)
\end{aligned}
$$

and inserting the structure functions according to Eq. (2.47) gives

$$
\begin{aligned}
i\mathcal{M}_Y = &\int \frac{\mathrm{d}^3q}{(2\pi)^3} \sum_{N=n,p} \sum_{L\geq 0} \sqrt{2L+1}(-i)^L \langle JM_i, L0|JM_f\rangle \\
&\times \left[\sum_{S=M,\Omega} \tilde{l}_{S,Y}(\vec{q}) \mathcal{F}_N^{S_L}(\vec{q}) + \sum_{S=\Sigma,\Delta,\Phi} \tilde{l}^3_{S,Y}(\vec{q}) i\mathcal{F}_N^{S''_L}(\vec{q}) \right] \\
&+ \int \frac{\mathrm{d}^3q}{(2\pi)^3} \sum_{N=n,p} \sum_{L\geq 1} \sqrt{2L+1}(-i)^L \frac{1}{\sqrt{2}} \sum_{\lambda=\pm} \langle JM_i, L-\lambda|JM_f\rangle \\
&\times \left[\sum_{S=\Sigma,\Delta,\Phi} \tilde{l}^{\lambda}_{S,Y}(\vec{q}) \Big(-\lambda \mathcal{F}_N^{S_L}(\vec{q}) - i\mathcal{F}_N^{S'_L}(\vec{q}) \Big) \right] . \qquad (3.45)
\end{aligned}
$$

The conditions of Eq. (2.50) for an elastic process can be used to further reduce the number of independent structures down to M, Δ, Σ', Σ'', Φ'' and Φ'. Moreover, Parity conservation dictates that for elastic processes only multipoles with even L contribute for M and Φ'', and only odd multipoles contribute for Δ, Σ', Σ''. For simplicity, we keep the current notation, but keep these conditions in mind, for explicit calculations later down the line.

To now further progress in calculating the decay rate of $\mu \to e$ conversion, we calculate the reduced matrix element squared according to

$$
\overline{|\mathcal{M}_Y|}^2 = \frac{1}{2(2J+1)} \sum_{M_i,M_f,t,t'} \mathcal{M}_Y^\dagger \mathcal{M}_Y, \qquad (3.46)
$$

averaging over initial spins and summing over final spins. The sums over the nucleon spins can be carried out via (2.44) and in the scenario of free leptons standard spin-sum techniques could be used to calculate the sum over the lepton spins. However, as our lepton spinors are bound or distorted by the nucleus and thus only given as numerical solutions, this will not be possible. Hence, it is more advantageous to simply calculate the matrix elements for every spin combination and then do the spin sums in the end. Nevertheless, in some special cases, it might still make sense to evaluate the spin sums with the standard techniques, which we will examine later.

3.6 Power Counting

Due to the cascading definitions of the prefactor, which is on the one hand necessary for clarity, but on the other hand very concealing, we will investigate which EFT operator contributes via which multipole at which order. For this purpose the whole carried out derivation is shown again schematically in Fig. 3.2, denoting between each step the separation into different contributions and the combination of terms that have the same structure. In particular, the terms at the level of the nucleon structures, and their connections to the previous nodes, denote the composition of each term in Eq. (3.25) in

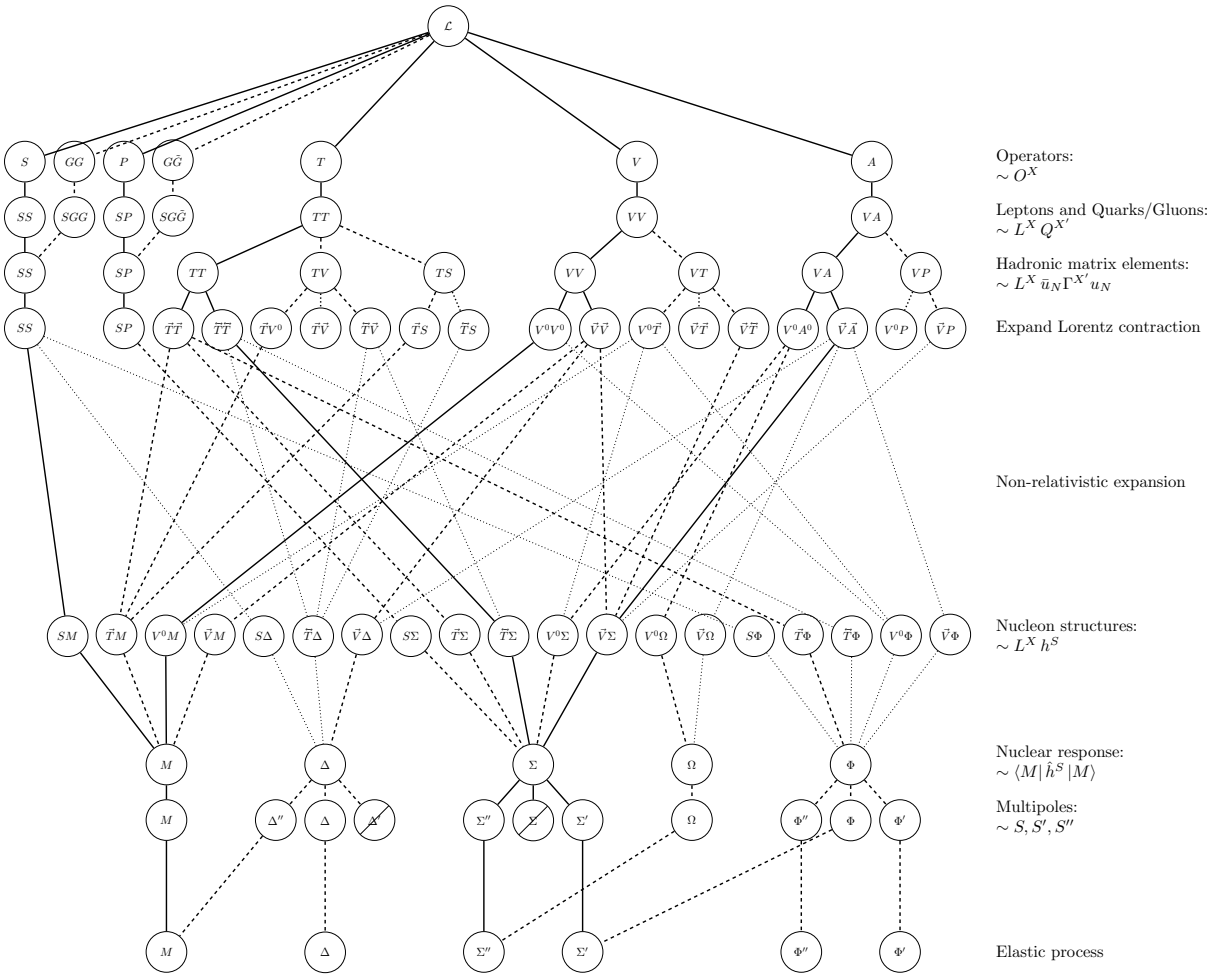

Figure 3.2: Schematic tree of which Wilson coefficients contribute at which order to which multipole, following the derivation of this chapter. Solid lines are $\mathcal{O}(1)$, dashed lines $\mathcal{O}(m_N^{-1})$, dotted lines $\mathcal{O}(m_N^{-2})$, and anything going beyond that was dropped.

	$\sim \#N \cdot \frac{m_N}{m_q}$	$\sim \#N$	$\sim \frac{m_N}{m_q}$	~ 1
$\mathcal{O}(1)$	$(S \to M)$	$(V \to M)$	-	$(A, T \to \Sigma^{\prime,\prime\prime})$
$\mathcal{O}(\frac{q}{m_N})$	-	$(GG, V, T \to M)$ $(T \to \Phi'')$	$(P \to \Sigma^{\prime,\prime\prime})$	$(V \to \Delta)$ $(T \to \Phi')$ $(V, A, T \to \Sigma^{\prime,\prime\prime})$
$\mathcal{O}(\frac{q^2}{m_N^2})$	$(S \to M, \Phi'')$	$(V, A, T \to M, \Phi'')$	-	$\ddots$

Table 3.2: Power counting of the different LFV operators. We denote with $(X \to S)$ the initial quark-level operators O^X as well as the ultimately resulting nuclear responses S with that power counting.

terms of its power counting. In fact, most of the power counting of the final matrix element can be read off directly of the $\tilde{l}_S$ and thus the $C_{Y,X,S}$ of Eq. (3.25).

On top of this, we have different enhancements for specific multipoles. In particular, the M-response is coherently enhanced as $\mathcal{F}_N^{M_0} \sim \mathcal{F}_N^{\Delta''_0} \sim \#N$ gives an enhancement scaling with the number of nucleons in the nucleus. Furthermore, $\mathcal{F}_N^{\Phi''_0}$ shows a similar partial enhancement, being related to the orbital angular momentum, which we will count in the same way. Furthermore, scalar and pseudo-scalar nuclear matrix elements come with a factor of $\frac{m_N}{m_q}$ inside the F_{SS}, F_{PP}. There is no clear consensus, on what the natural scale of these matrix elements is and if this should be considered as an enhancement or not. Since it is easier to disregard than to reinsert, we will also consider this enhancement. Finally, the gluonic contributions come with a suppression of $1/\Lambda$, which we counted as $\mathcal{O}(m_N^{-1})$, but in practice could of course also be a lot more suppressed, dependent on the value of Λ. Combining these effects we have a (partial) enhancement with $\#N$ in terms that go with $C_{M,X}, C^3_{\Delta,X}, C^3_{\Phi,X}$ and an enhancement with $\frac{m_N}{m_q}$ for terms that go with $C^{S,q}$ and $C^{P,q}$. We can now use Fig. 3.2 and Eq. (3.25) to easily collect all terms up to a specific order resulting in Tab. 3.2, where we dropped any pure $\mathcal{O}(m_N^{-2})$ terms as these are incomplete anyways since we disregarded the non-enhanced $\mathcal{O}(m_N^{-2})$ nuclear structures. We denote for each contribution the initial quark-level operators and the ultimately resulting nuclear response, classifying possible paths in Fig. 3.2. Note that this table is just a result of the power counting and some of these terms might cancel to zero. As expected, we see that at leading order scalar and vector terms dominate, where the rest starts to contribute at effective $\mathcal{O}(1)$.

3.7 Dipole Contribution

The dipole operator couples to the nucleus via photon exchange, as can be seen in Fig. 3.3. Due to the photon propagator and the higher order in Λ, in a pure LEFT-based power counting this term is quite enhanced in comparison to the other terms and would most definitely dominate $\mu \to e$ conversion. Albeit, considering its origination from SMEFT a coupling to the Higgs field (with vacuum expectation value v) is required and the dipole operator actually goes with $v\Lambda^{-2}$ instead of Λ^{-1}, which results in C^D being suppressed with $\frac{v}{\Lambda}$ in comparison to the other Wilson coefficients. This can be substantial if new physics are above the EW scale and $\Lambda \gg v$. Furthermore, while 4-point vertices can be easily motivated by the insertion of the propagator of a new massive particle, 3-point vertices require a loop (or they would mix directly with the SM particles), which can further suppress this kind of interaction. For these reasons, the power counting of this operator in comparison to the other interactions is not trivial and we handle this calculation separately, as a discussion of the different mechanisms, how potential BSM models could generate the considered LEFT operators, and in which power counting this would result, is beyond the scope of this work. Furthermore, to constraint this operator we do not solely need to rely on $\mu \to e$ conversion as it is independently and without competition by other operators constrained by the limits on $\mu \to e\gamma$. For simplicity, we carry out the following calculation with pure LEFT-based power counting.

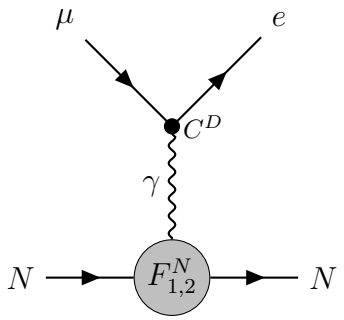

Figure 3.3: Dipole coupling to nucleons

To calculate the process of Fig. 3.3, the necessary coupling of the photon to the nucleus is given in the SM via

$$\mathcal{L}_{q\bar{q}\gamma} = -Q_q \eta_e \sqrt{4\pi\alpha_{\rm el}} A^\mu \bar{q}\gamma_\mu q = -Q_q \eta_e \sqrt{4\pi\alpha_{\rm el}} A^\mu Q_\mu^{V,q}, \tag{3.47}$$

where η_e refers to the sign convention for the charge.[1] We thus consider

$$\begin{aligned}\langle N|\, Q^D_{\mu\nu}\,|N\rangle = \langle N|\, F_{\mu\nu}\,|N\rangle &= \sum_q \sqrt{4\pi\alpha_{\rm el}}(-\eta_e)Q_q \frac{(-i)}{q^2} 2iq_{[\mu}\,\langle N|\, Q^{V,q}_{\nu]}\,|N\rangle \\ &= -2\eta_e\sqrt{4\pi\alpha_{\rm el}}\frac{q^{[\mu}}{q^2}\,\langle N|\, j^{\nu]}_{\rm em}\,|N\rangle\,,\end{aligned} \tag{3.48}$$

with $j^\mu_{\rm em}$ the electromagnetic current, which couples to the nucleons via the well-known proton and neutron form factors

$$\begin{aligned}\langle N(p')|\, j^\mu_{\rm em}\,|N(p)\rangle &= \bar{u}_{N'}\left(F_1^N\gamma^\mu - F_2^N\frac{i\sigma^{\mu\nu}q_\nu}{2m_N}\right)u_N \\ &= \bar{u}_{N'}\left(F_1^N\gamma^\mu + F_2^N\frac{i\sigma^{\mu j}q_j}{2m_N}\right)u_N + \mathcal{O}(m_N^{-3}).\end{aligned} \tag{3.49}$$

We thus may write the matrix element using

$$\Gamma^\mu_D = F_1^N\gamma^\mu - F_2^N\frac{i\sigma^{\mu\nu}q_\nu}{2m_N}, \tag{3.50}$$

in the same notation as before as

$$i\mathcal{M}^{N,D}_Y = iC^{T,D}_Y\ \ \langle e|\, L^{T,\mu\nu}_Y\,|\mu\rangle\ \ \mathcal{P}^{\mu\nu,\nu'}_{X,D}\ \ \bar{u}_{N'}\Gamma^D_{\nu'}u_N, \tag{3.51}$$

with

$$C^{T,D}_Y = -2\eta_e i\Lambda C^D_Y\frac{\sqrt{4\pi\alpha_{\rm el}}m_N}{q^2}, \qquad \mathcal{P}^{\mu\nu,\nu'}_{T,D} = \frac{-iq^{[\mu}g^{\nu]\nu'}}{m_N} = P^{\mu\nu,\nu'}_{T,V}. \tag{3.52}$$

[1] This refers to a minimal coupling of $\mathrm{D}_\mu = \partial_\mu + i\eta_e\sqrt{4\pi\alpha_{\rm el}}A^\mu$ [122]

Expanding the Lorentz contractions to Euclidean contractions gets us

$$i\mathcal{M}_Y^{N,D} = i \sum_{X\in\vec{T},\vec{\mathbb{T}}} \sum_{X'\in D^0,\vec{D}} C_Y^{X,D} \ \langle e|\, L_Y^{X,(n)}\,|\mu\rangle \ \mathcal{P}_{X,X'}^{(n,m)} \ \bar{u}_{N'}\Gamma_{(m)}^{X'} u_N, \tag{3.53}$$

where the prefactors are directly given from $\mathcal{P}_{X,D}^{(n,m)} = \mathcal{P}_{X,V}^{(n,m)}$. Carrying out the non-relativistic expansion for the electromagnetic current (up to $\mathcal{O}(m_N^{-2})$) we end up with

$$\begin{aligned}
&\langle N(p')|\, j_{\text{em}}^0\,|N(p)\rangle \\
&\quad = \chi_{s'}^\dagger \left(\left(F_1^N + \frac{-q^2(F_1^N+2F_2^N)}{8m_N^2} \right) h^M + \left(\frac{-iqq_j(F_1^N+2F_2^N)}{4m_N^2} \right) h_j^\Phi \right) \chi_s, \\
&\langle N(p')|\, j_{\text{em}}^i\,|N(p)\rangle \\
&\quad = \chi_{s'}^\dagger \left(\left(\frac{-q_i F_1^N}{2m_N} \right) h^M + \left(\frac{-iqF_1^N}{m_N} \right) h_i^\Delta + \left(\frac{i\epsilon_{ijk}q_j\big(F_1^N+F_2^N\big)}{2m_N} \right) h_k^\Sigma \right) \chi_s.
\end{aligned} \tag{3.54}$$

We may write again

$$\bar{u}_{N'}\Gamma_D^{(n)} u_N = \sum_{\substack{S\in M,\Sigma,\\ \Delta,\Phi}} \mathcal{K}_{D,S}^{(n,m)} \ \chi_{s'}^\dagger h_{(m)}^S \chi_s, \tag{3.55}$$

with

$$\begin{aligned}
\mathcal{K}_{D^0,M} &= F_1^N + \frac{-q^2(F_1^N+2F_2^N)}{8m_N^2}, & \mathcal{K}_{D^0,\Phi}^j &= \frac{-iqq_j(F_1^N+2F_2^N)}{4m_N^2}, \\
\mathcal{K}_{\vec{D},M}^i &= \frac{-q_iF_1^N}{2m_N}, \quad \mathcal{K}_{\vec{D},\Delta}^{i,j} = \delta_{ij}\frac{-iqF_1^N}{m_N}, & \mathcal{K}_{\vec{D},\Sigma}^{i,j} &= \frac{i\epsilon_{ikj}q_k\big(F_1^N+F_2^N\big)}{2m_N},
\end{aligned} \tag{3.56}$$

and all others zero. We can combine this again to write

$$i\mathcal{M}_Y^{N,D} := i \sum_{X\in\vec{T},\vec{\mathbb{T}}} \sum_{\substack{S\in M,\Sigma,\\ \Delta,\Phi}} \langle e|\, L_Y^{X,(n)}\,|\mu\rangle \ C_{Y,X,S}^{(n,m),D} \ \chi_{s'}^\dagger h_{(m)}^S \chi_s, \tag{3.57}$$

with

$$\begin{aligned}
C_{Y,\vec{T},M}^{i,D} &= C_Y^{T,D} F_1^N \frac{iq^i}{m_N}, & C_{Y,\vec{T},\Delta}^{i,j,D} &= C_Y^{T,D} F_1^N \frac{\epsilon_{ikj}q^kq}{2m_N^2}, \\
C_{Y,\vec{T},\Sigma}^{i,j,D} &= C_Y^{T,D} \frac{(q^2\delta_{ij}-q_iq_j)\big(F_1^N+F_2^N\big)}{4m_N^2}.
\end{aligned} \tag{3.58}$$

These could be added normally to the terms of Eq. (3.25) and combined in the calculation. However, due to the enhancement of $\frac{\Lambda m_N}{q^2}$ in $C^{T,D}$ based on a purely LEFT-based power counting, we would need to calculate these up to $\mathcal{O}(m_N^{-4})$ to consider interference terms with the other operators at the same order. On the one hand, if this power counting is genuine, the dipole will strongly dominate anything else anyway, which makes considering interference redundant, on the other hand, we have already discussed that considering the

SMEFT matching and potential mechanisms to generate the dipole operators introduce further suppressions, which can compensate the enhancement. In either way, it should be sufficient to stay at the currently considered order. Following the derivation from above

$$\begin{aligned}
i\mathcal{M}_Y^D = &\int \frac{\mathrm{d}^3q}{(2\pi)^3} \sum_{N=n,p} \sum_{L\geq 0} \sqrt{2L+1}(-i)^L \langle JM_i, L0|JM_f\rangle \\
&\times \left[\tilde{l}^D_{M,Y}(\vec{q})\mathcal{F}_N^{M_L}(\vec{q}) + i\tilde{l}^{3,D}_{\Sigma,Y}(\vec{q})\mathcal{F}_N^{\Sigma''_L}(\vec{q})\right] \\
&+ \int \frac{\mathrm{d}^3q}{(2\pi)^3} \sum_{N=n,p} \sum_{L\geq 1} \sqrt{2L+1}(-i)^L \frac{1}{\sqrt{2}} \sum_{\lambda=\pm} \langle JM_i, L-\lambda|JM_f\rangle \\
&\times \left[-\lambda\tilde{l}^{\lambda,D}_{\Delta,Y}(\vec{q})\mathcal{F}_N^{\Delta_L}(\vec{q}) - i\tilde{l}^{\lambda,D}_{\Sigma,Y}(\vec{q})\mathcal{F}_N^{\Sigma'_L}(\vec{q})\right],
\end{aligned} \tag{3.59}$$

with

$$\begin{aligned}
\tilde{l}_{M,Y}(\vec{q}) &= iC_Y^{T,D} F_1^N \frac{iq_i}{m_N} \widetilde{\overline{\Psi_{e_Y}^{\kappa',t'}} \sigma^{0i} \Psi_\mu^{(1s),t}}(\vec{q}) \\
\tilde{l}^{\pm}_{\Delta,Y}(\vec{q}) &= iC_Y^{T,D} F_1^N \frac{q_i q}{m_N^2} \widetilde{\overline{\Psi_{e_Y}^{\kappa',t'}} \sigma^{i\pm} \Psi_\mu^{(1s),t}}(\vec{q}) \\
\tilde{l}^{\pm}_{\Sigma,Y}(\vec{q}) &= iC_Y^{T,D} \frac{q_i q_k \big(F_1^N + F_2^N\big)}{2m_N^2} \epsilon_{kj\pm} \widetilde{\overline{\Psi_{e_Y}^{\kappa',t'}} \sigma^{ij} \Psi_\mu^{(1s),t}}(\vec{q}) \\
\tilde{l}^{3}_{\Sigma,Y}(\vec{q}) &= iC_Y^{T,D} \frac{q_i q_k \big(F_1^N + F_2^N\big)}{2m_N^2} \epsilon_{kj3} \widetilde{\overline{\Psi_{e_Y}^{\kappa',t'}} \sigma^{ij} \Psi_\mu^{(1s),t}}(\vec{q}),
\end{aligned} \tag{3.60}$$

where we used

$$\begin{aligned}
\big(q^2\delta_{kl} - q_k q_l\big)\epsilon_{ijk}\sigma^{ij} &= q_n q_m \epsilon_{nkk'}\epsilon_{mlk'}\epsilon_{ijk}\sigma^{ij} = q_n q_m \epsilon_{mlk'}(\delta_{k'i}\delta_{nj} - \delta_{nj}\delta_{k'i})\sigma^{ij} \\
&= 2q_n q_m \epsilon_{mlk'}\sigma^{k'n} = -2q_i q_k \epsilon_{jkl}\sigma^{ij}.
\end{aligned} \tag{3.61}$$

We find

$$\begin{aligned}
&\langle JM_i, L0|JM_f\rangle \left[\tilde{l}^D_{M,Y}\mathcal{F}_N^{M_L} + i\tilde{l}^{3,D}_{\Sigma,Y}\mathcal{F}_N^{\Sigma''_L}\right] \\
&= iC_Y^{T,D}\frac{iq_i}{m_N}\langle JM_i, L0|JM_f\rangle \\
&\quad\times\left[\widetilde{\overline{\Psi_{e_Y}^{\kappa',t'}}\sigma^{0i}\Psi_\mu^{(1s),t}}\; F_1^N\mathcal{F}_N^{M_L} + \frac{q_k\epsilon_{kj3}}{m_N}\widetilde{\overline{\Psi_{e_Y}^{\kappa',t'}}\sigma^{ij}\Psi_\mu^{(1s),t}}\;\tfrac{1}{2}\big(F_1^N+F_2^N\big)\mathcal{F}_N^{\Sigma''_L}\right],
\end{aligned} \tag{3.62}$$

and

$$\begin{aligned}
&\sum_{\lambda=\pm}\langle JM_i, L-\lambda|JM_f\rangle \left[-\lambda\tilde{l}^{\lambda,D}_{\Delta,Y}\mathcal{F}_N^{\Delta_L} - i\tilde{l}^{\lambda,D}_{\Sigma,Y}\mathcal{F}_N^{\Sigma'_L}\right] \\
&= iC_Y^{T,D}\frac{iq_i}{m_N}\sum_{\lambda=\pm}\langle JM_i, L-\lambda|JM_f\rangle \\
&\quad\times\left[\frac{i\lambda q}{m_N}\widetilde{\overline{\Psi_{e_Y}^{\kappa',t'}}\sigma^{i\lambda}\Psi_\mu^{(1s),t}}\,F_1^N\mathcal{F}_N^{\Delta_L} - \frac{q_k\epsilon_{kj\lambda}}{m_N}\widetilde{\overline{\Psi_{e_Y}^{\kappa',t'}}\sigma^{ij}\Psi_\mu^{(1s),t}}\;\tfrac{1}{2}\big(F_1^N+F_2^N\big)\mathcal{F}_N^{\Sigma'_L}\right]
\end{aligned}$$

$$
\begin{aligned}
&= iC_Y^{T,D}\frac{iq_i}{m_N}\sum_{\lambda=\pm}\langle JM_i, L{-}\lambda|JM_f\rangle\ \widetilde{\overline{\Psi_{e_Y}^{\kappa',t'}}\sigma^{ij}\Psi_\mu^{(1s),t}}\\
&\quad\times\left[\frac{q\epsilon_{3j-\lambda}}{m_N}F_1^N\mathcal{F}_N^{\Delta_L}-\frac{q_k\epsilon_{kj\lambda}}{m_N}\tfrac{1}{2}\big(F_1^N+F_2^N\big)\mathcal{F}_N^{\Sigma'_L}\right]\\
&= iC_Y^{T,D}\frac{iq_i}{m_N}\sum_{\lambda=\pm}\epsilon_{kj-\lambda}\,\widetilde{\overline{\Psi_{e_Y}^{\kappa',t'}}\sigma^{ij}\Psi_\mu^{(1s),t}}\,\frac{q}{m_N} \qquad (3.63)\\
&\quad\times\Big[\langle JM_i, L{-}\lambda|JM_f\rangle\,\delta_{k3}F_1^N\mathcal{F}_N^{\Delta_L}+\langle J-M_i, L{-}\lambda|J-M_f\rangle\,\tfrac{q_k}{q}\tfrac{1}{2}\big(F_1^N+F_2^N\big)\mathcal{F}_N^{\Sigma'_L}\Big],
\end{aligned}
$$

where we used that $\langle JM_i, L{-}\lambda|JM_f\rangle = (-1)^L\langle J{-}M_i, L\lambda|J{-}M_f\rangle$ and for the elastic process Σ'_L is only non-zero for odd L. Notably for all terms a factor of $\frac{q_i}{m_N}$ factors out. The reduced matrix element squared (considering only the dipole contribution) becomes

$$
\begin{aligned}
\overline{|\mathcal{M}_Y^D|}^2 &= \int\frac{\mathrm{d}^3q}{(2\pi)^3}\int\frac{\mathrm{d}^3q'}{(2\pi)^3}\frac{1}{2}\sum_{t,t'}\\
&\quad\times\left(\sum_{L\geq 0}\Big(\tilde{l}_{0,Y}^D(q)h_0^D(q)+\tilde{l}_{3,Y}^D(q)h_3^D(q)\Big)\Big(\tilde{l}_{0,Y}^D(q')h_0^D(q')+\tilde{l}_{3,Y}^D(q')h_3^D(q')\Big)^*\right.\\
&\qquad\left.+\frac{1}{2}\sum_{\lambda=\pm}\tilde{l}_{\lambda,Y}^{D,k}(q)\tilde{l}_{\lambda,Y}^{D,k'*}(q')\sum_{L\geq 1}h_\lambda^{D,k}(q)h_\lambda^{D,k'*}(q')\right), \qquad (3.64)
\end{aligned}
$$

with

$$
\begin{aligned}
\tilde{l}_{0,Y}^D(\vec{q}) &= \frac{iq_i}{m_N}\widetilde{\overline{\Psi_{e_Y}^{\kappa',t'}}\sigma^{0i}\Psi_\mu^{(1s),t}}(\vec{q}), \qquad & \tilde{l}_{3,Y}^D(\vec{q}) &= \frac{iq_i}{m_N}\frac{q_k}{q}i\epsilon_{kj3}\widetilde{\overline{\Psi_{e_Y}^{\kappa',t'}}\sigma^{ij}\Psi_\mu^{(1s),t}}(\vec{q}),\\
\tilde{l}_{\pm,Y}^{D,k}(\vec{q}) &= \frac{iq_i}{m_N}i\epsilon_{kj\mp}\widetilde{\overline{\Psi_{e_Y}^{\kappa',t'}}\sigma^{ij}\Psi_\mu^{(1s),t}}(\vec{q}), \qquad (3.65)
\end{aligned}
$$

and

$$
\begin{aligned}
h_0^D(\vec{q}) &= \frac{iC_Y^{T,D}}{\Lambda^2}\sum_{N=n,p}F_1^N\mathcal{F}_N^{M_L}, \qquad & h_3^D(\vec{q}) &= \frac{iC_Y^{T,D}}{\Lambda^2}\sum_{N=n,p}\frac{-iq}{m_N}\tfrac{1}{2}\big(F_1^N(\vec{q})+F_2^N(\vec{q})\big)\mathcal{F}_N^{\Sigma''_L},\\
h_\pm^{D,k}(\vec{q}) &= \frac{iC_Y^{T,D}}{\Lambda^2}\sum_{N=n,p}\frac{-iq}{m_N}\Big(\delta_{k3}F_1^N\mathcal{F}_N^{\Delta_L}+\tfrac{q_k}{q}\tfrac{1}{2}\big(F_1^N+F_2^N\big)\mathcal{F}_N^{\Sigma'_L}\Big). \qquad (3.66)
\end{aligned}
$$

Looking at these terms we find

$$
\begin{aligned}
\sum_{N=n,p}F_1^N\mathcal{F}_N^{M_L} &= ZF_{\mathrm{ch}}^L|_{\mathcal{O}(m_N^{-1})},\\
\sum_{N=n,p}\frac{-iq}{m_N}\Big(F_1^N\mathcal{F}_N^{\Delta_L}+\tfrac{q_3}{q}\tfrac{1}{2}\big(F_1^N+F_2^N\big)\mathcal{F}_N^{\Sigma'_L}\Big) &= F_{\mathrm{mag}}^L|_{q_3=-q,\mathcal{O}(m_N^{-1})}, \qquad (3.67)
\end{aligned}
$$

such that we may write

$$h_0^D(\vec{q}) = \frac{iC_Y^{T,D}}{\Lambda^2} Z F_{\text{ch}}, \qquad h_\lambda^{D,k}(\vec{q}) = \frac{iC_Y^{T,D}}{\Lambda^2} \delta_{k3} F_{\text{mag}} + \mathcal{O}(q - |q_3|). \tag{3.68}$$

We note further

$$\tilde{l}_{3,Y}^D(\vec{q}) = \mathcal{O}(q - |q_3|). \tag{3.69}$$

The $\mathcal{O}(q-|q_3|)$ terms are generally speaking still relevant and one still needs to integrate over these. However, one expects that the lepton integral peaks at $\vec{q} \approx \vec{k'}$, since the momentum of the muon k inside the nucleus is limited. And we may choose $\vec{k'}$ without loss of generality pointing in $-\hat{e}_3$ direction, which then results in these terms being the most important ones for $q \approx |q_3|$. Hence, we may write an equivalent amplitude

$$\begin{aligned} i\mathcal{M}_Y^D = \frac{2\eta_e C_Y^D \sqrt{4\pi\alpha_{\text{el}}}}{\Lambda} \int \frac{\mathrm{d}^3 q}{(2\pi)^3} \frac{m_N}{q^2} \Bigg(& \sum_{L\geq 0} \sqrt{2L+1} (-i)^L \langle JM_i, L0 | JM_f \rangle \, \tilde{l}_{0,Y}^D(\vec{q}) Z \mathcal{F}_{\text{ch}}^L(\vec{q}) \\ & + \sum_{L\geq 1} \sqrt{2L+1} (-i)^L \frac{1}{\sqrt{2}} \sum_{\lambda=\pm} \langle JM_i, L-\lambda | JM_f \rangle \, (-\lambda) \tilde{l}_{\lambda,Y}^{D,3}(\vec{q}) \mathcal{F}_{\text{mag}}^L(\vec{q}) \\ & + \mathcal{O}(q - |q_3|) \Bigg), \end{aligned} \tag{3.70}$$

which shows that for $q = |q_3|$, the amplitude simply depends on the same elastic and magnetic form factors, which appear for any one-photon exchange with a nucleus. Looking at the general power counting we have predominantly two kinds of terms

$$\begin{aligned} \mathcal{O}(\tfrac{m_N}{q}) \cdot \frac{\Lambda}{m_N} \cdot \#N : & \qquad (D \to F_{\text{ch}}(M, \Phi'', \dots)), \\ \mathcal{O}(\tfrac{m_N}{q}) \cdot \frac{\Lambda}{m_N} : & \qquad (D \to F_{\text{mag}}(\Delta, \Sigma', \dots)). \end{aligned} \tag{3.71}$$

It remains generally true, even with $q \neq |q_3|$, that at leading order and for $L = 0$ we have only have

$$i\mathcal{M}_Y^D = \frac{2\eta_e C_Y^D \sqrt{4\pi\alpha_{\text{el}}}}{\Lambda} \int \frac{\mathrm{d}^3 q}{(2\pi)^3} \delta_{M_i, M_f} \frac{iq_i}{q^2} \overbrace{\overline{\Psi_{e_Y}^{\kappa',t'}} \sigma^{0i} \Psi_\mu^{(1s),t}}(\vec{q}) Z \mathcal{F}_{\text{ch}}^0(\vec{q}). \tag{3.72}$$

Since we are on amplitude level, the amplitude for the dipole interaction can be added to the matrix element of Eq. 3.45, for a complete $\mu \to e$ conversion amplitude, which however, depending on the power counting, is incomplete regarding higher order corrections to the dipole. In Sec. 3.8.1 we will show how these terms will combine if just the leading order terms from both descriptions are considered. The calculated cross section then also shows how the dipole will interfere with the scalar and vector interactions.

3.8 Special Cases

We demonstrate the capabilities of the full solution of Eq. (3.45) in two commonly considered scenarios. First, we consider the leading nuclear response, with the full bound-state physics, showcasing the proper treatment of the latter in the form of overlap integrals [88] as well as how the numerical solutions of the Dirac equation can be included consistently. Secondly, we consider Eq. (3.45) with a simplified treatment of the bound-state physics, but discussing different kinds of nuclear responses, in particular demonstrating the separation into SI and SD $\mu \to e$ conversion. Both scenarios are not only a good consistency check but also showcase how the general framework developed here includes both nuclear response and bound-state physics at the same time.

3.8.1 Coherently enhanced Multipoles

We consider the leading terms in q/m_N in the limit where only the $\#N$ enhanced terms contribute. These are all terms that go with M^0, where only $L = 0$ and only scalar, vector, and dipole operators contribute (see Tab. 3.2). On the amplitude level, the dipole contribution of Eq. (3.72) is simply added to the leading terms of the full solution of Eq. (3.45) and we find

$$i\mathcal{M}_Y = \int \frac{\mathrm{d}^3 q}{(2\pi)^3} \delta_{M_i,M_f} \left[\sum_{N=n,p} \tilde{l}_{M,Y}(\vec{q}) \mathcal{F}_N^{M_0}(\vec{q}) + 2\eta_e \frac{Z C_Y^D}{\Lambda} \frac{m_N}{q^2} \tilde{l}_{0,Y}^D(\vec{q}) \sqrt{4\pi\alpha_{\mathrm{el}}} \mathcal{F}_{\mathrm{ch}}^0(\vec{q}) \right], \quad (3.73)$$

where at this order

$$\begin{aligned} \tilde{l}_{M,Y}(\vec{q}) &= \frac{1}{\Lambda^2} \int \mathrm{d}^3 x \left(C_Y^{S,S} \ \overline{\Psi_{e_Y}^{\kappa',t'}} \Psi_\mu^{(1s),t} \ + \ C_Y^{V,V} \ \overline{\Psi_{e_Y}^{\kappa',t'}} \gamma^0 \Psi_\mu^{(1s),t} \right) e^{i\vec{q}\cdot\vec{x}} \\ \tilde{l}_{0,Y}^D(\vec{q}) &= \int \mathrm{d}^3 x \, \frac{i q_i}{m_N} \overline{\Psi_{e_Y}^{\kappa',t'}} \sigma^{0i} \Psi_\mu^{(1s),t} e^{i\vec{q}\cdot\vec{x}}. \end{aligned} \quad (3.74)$$

The matrix element becomes[2]

$$\begin{aligned} i\mathcal{M}_Y &= \frac{\delta_{M_i,M_f}}{\Lambda^2} \int \frac{\mathrm{d}^3 q}{(2\pi)^3} \left[2\eta_e \int \mathrm{d}^3 x \, \Lambda C_Y^D \overline{\Psi_{e_Y}^{\kappa',t'}} \sigma^{0i} \Psi_\mu^{(1s),t} e^{i\vec{q}\cdot\vec{x}} \frac{i q_i}{q^2} \sqrt{4\pi\alpha_{\mathrm{el}}} Z \mathcal{F}_{\mathrm{ch}}^0(\vec{q}) \right. \\ &\quad \left. + \sum_{N=n,p} \int \mathrm{d}^3 x \left(C_Y^{S,S} \overline{\Psi_{e_Y}^{\kappa',t'}} \Psi_\mu^{(1s),t} + C_Y^{V,V} \overline{\Psi_{e_Y}^{\kappa',t'}} \gamma^0 \Psi_\mu^{(1s),t} \right) e^{i\vec{q}\cdot\vec{x}} \mathcal{F}_N^{M_L}(\vec{q}) \right] \\ &= \frac{\delta_{M_i,M_f}}{\Lambda^2} \left[2\eta_e \int \mathrm{d}^3 x \, \Lambda C_Y^D \overline{\Psi_{e_Y}^{\kappa',t'}} \sigma^{0i} \Psi_\mu^{(1s),t} (-E(\vec{x}) \hat{x}_i) \right. \\ &\quad \left. + \sum_{N=n,p} \int \mathrm{d}^3 x \left(C_Y^{S,S} \overline{\Psi_{e_Y}^{\kappa',t'}} \Psi_\mu^{(1s),t} + C_Y^{V,V} \overline{\Psi_{e_Y}^{\kappa',t'}} \gamma^0 \Psi_\mu^{(1s),t} \right) (\#N) \rho_N(x) \right], \end{aligned} \quad (3.75)$$

[2] We neglected here higher order q-dependent corrections to the hadronic matrix elements inside $C^{S,S}$ and $C^{V,V}$, which generally would need to be integrated as well.

where we used that the nucleon density is given by the Fourier-Transform of the respective M_0 structure function and the Fourier Transformation of $\frac{q_i}{q^2}F_{\rm ch}(\vec{q})$ is given by the electric field $E(r)\hat{x}_i$ according to

$$\begin{aligned}\int \frac{\mathrm{d}^3q}{(2\pi)^3}\frac{iq_i}{q^2}ZF^0_{\rm ch}(q)e^{i\vec{q}\cdot\vec{x}} &= \frac{\mathrm{d}}{\mathrm{d}x_i}\int\frac{\mathrm{d}^3q}{(2\pi)^3}\frac{ZF^0_{\rm ch}(q)}{q^2}e^{i\vec{q}\cdot\vec{x}} = \frac{\mathrm{d}}{\mathrm{d}x_i}\int\frac{\mathrm{d}q}{2\pi^2}ZF^0_{\rm ch}(q)j_0(qr)\\ &= \int\frac{\mathrm{d}q}{2\pi^2}ZF^0_{\rm ch}(q)\frac{1}{q}j_0'(qr)\frac{\mathrm{d}}{\mathrm{d}x_i}r = -\int\frac{\mathrm{d}q}{2\pi^2}ZF^0_{\rm ch}(q)qj_1(qr)\hat{x}_i\\ &= -\frac{4\pi}{\sqrt{4\pi\alpha_{\rm el}}}\int\frac{\mathrm{d}q}{2\pi^2}\int\mathrm{d}r'\,q^2j_1(qr')j_1(qr)r^2E(r)\hat{x}_i\\ &= -\frac{4\pi}{\sqrt{4\pi\alpha_{\rm el}}}\frac{1}{2\pi^2}\int\mathrm{d}r'\,\frac{\pi}{2r^2}\delta(r-r')r^2E(r)\hat{x}_i = \frac{-E(r)}{\sqrt{4\pi\alpha_{\rm el}}}\hat{x}_i, \quad (3.76)\end{aligned}$$

where we used (see also Eq. (5.6))

$$\begin{aligned}&ZF^0_{\rm ch}(q) = 4\pi\int\mathrm{d}r\,r^2j_0(qr)\rho_0(r), \qquad \rho_0(r) = \frac{1}{\sqrt{4\pi\alpha_{\rm el}}}\frac{1}{r^2}\frac{\mathrm{d}}{\mathrm{d}r}\big[r^2E(r)\big],\\ &ZF^0_{\rm ch}(q) = \frac{4\pi}{\sqrt{4\pi\alpha_{\rm el}}}\int\mathrm{d}r\,j_0(qr)\frac{\mathrm{d}}{\mathrm{d}r}\big[r^2E(r)\big] \overset{\text{P.I.}}{=} -\frac{4\pi}{\sqrt{4\pi\alpha_{\rm el}}}\int\mathrm{d}r\,q\,\underbrace{j_0'(qr)}_{=-j_1(qr)}\,r^2E(r). \quad (3.77)\end{aligned}$$

Inserting the representation of Eq. (3.35) in Eq. (3.75) we get for the scalar and vector contractions

$$\begin{aligned}\overline{\Psi_e^{\kappa',t'}}\Psi_\mu^{(1s),t} &= \frac{1}{r^2}\Big(g^{(e)}_{\kappa'}g^{(\mu)}_{-1}\;\phi^{t'\dagger}_{\kappa'}\phi^t_{-1} - f^{(e)}_{\kappa'}f^{(\mu)}_{-1}\;\phi^{t'\dagger}_{-\kappa'}\phi^t_{+1}\Big),\\ \overline{\Psi_e^{\kappa',t'}}\gamma^5\Psi_\mu^{(1s),t} &= \frac{i}{r^2}\Big(f^{(e)}_{\kappa'}g^{(\mu)}_{-1}\;\phi^{t'\dagger}_{-\kappa'}\phi^t_{-1} + g^{(e)}_{\kappa'}f^{(\mu)}_{-1}\;\phi^{t'\dagger}_{\kappa'}\phi^t_{+1}\Big),\\ \overline{\Psi_e^{\kappa',t'}}\gamma^0\Psi_\mu^{(1s),t} &= \frac{1}{r^2}\Big(g^{(e)}_{\kappa'}g^{(\mu)}_{-1}\;\phi^{t'\dagger}_{\kappa'}\phi^t_{-1} + f^{(e)}_{\kappa'}f^{(\mu)}_{-1}\phi^{t'\dagger}_{-\kappa'}\phi^t_{+1}\Big),\\ \overline{\Psi_e^{\kappa',t'}}\gamma^5\gamma^0\Psi_\mu^{(1s),t} &= \frac{i}{r^2}\Big(f^{(e)}_{\kappa'}g^{(\mu)}_{-1}\;\phi^{t'\dagger}_{-\kappa'}\phi^t_{-1} - g^{(e)}_{\kappa'}f^{(\mu)}_{-1}\;\phi^{t'\dagger}_{\kappa'}\phi^t_{+1}\Big). \quad (3.78)\end{aligned}$$

For the dipole terms, we can use the properties of Eq. (5.39), in particular

$$(\hat{x}\cdot\vec{\sigma})\phi^\mu_\kappa(\hat{x}) = -\phi^\mu_{-\kappa}(\hat{x}), \quad (3.79)$$

and find

$$\begin{aligned}\overline{\Psi_e^{\kappa',t'}}\hat{x}_i\sigma^{0i}\Psi_\mu^{(1s),t} &= \frac{-1}{r^2}\Big(f^{(e)}_{\kappa'}g^{(\mu)}_{-1}\;\phi^{t'\dagger}_{-\kappa'}(\hat{x}\cdot\vec{\sigma})\phi^t_{-1} + g^{(e)}_{\kappa'}f^{(\mu)}_{-1}\;\phi^{t'\dagger}_{\kappa'}(\hat{x}\cdot\vec{\sigma})\phi^t_{+1}\Big)\\ &= \frac{+1}{r^2}\Big(f^{(e)}_{\kappa'}g^{(\mu)}_{-1}\;\phi^{t'\dagger}_{-\kappa'}\phi^t_{+1} + g^{(e)}_{\kappa'}f^{(\mu)}_{-1}\;\phi^{t'\dagger}_{\kappa'}\phi^t_{-1}\Big),\\ \overline{\Psi_e^{\kappa',t'}}\gamma^5\hat{x}_i\sigma^{0i}\Psi_\mu^{(1s),t} &= \frac{i}{r^2}\Big(g^{(e)}_{\kappa'}g^{(\mu)}_{-1}\;\phi^{t'\dagger}_{\kappa'}(\hat{x}\cdot\vec{\sigma})\phi^t_{-1} - f^{(e)}_{\kappa'}f^{(\mu)}_{-1}\;\phi^{t'\dagger}_{-\kappa'}(\hat{x}\cdot\vec{\sigma})\phi^t_{+1}\Big)\\ &= \frac{-i}{r^2}\Big(g^{(e)}_{\kappa'}g^{(\mu)}_{-1}\;\phi^{t'\dagger}_{\kappa'}\phi^t_{+1} - f^{(e)}_{\kappa'}f^{(\mu)}_{-1}\;\phi^{t'\dagger}_{-\kappa'}\phi^t_{-1}\Big). \quad (3.80)\end{aligned}$$

Using the orthogonality relation for the angular part (see also Eq. (5.42)) given as

$$\int \mathrm{d}\Omega\, \phi_\kappa^{t\dagger} \phi_{\kappa'}^{t'} = \delta_{\kappa\kappa'}\delta_{t't}, \tag{3.81}$$

we find

$$\begin{aligned}
\int \mathrm{d}\Omega\, \overline{\Psi_e^{\kappa',t'}} \Psi_\mu^{(1s),t} &= \frac{\delta_{tt'}}{r^2}\delta_{\kappa',-1}\Big(g_{-1}^{(e)} g_{-1}^{(\mu)} - f_{-1}^{(e)} f_{-1}^{(\mu)}\Big) &&=: \frac{\delta_{tt'}}{r^2}\delta_{\kappa',-1}\ s_1(r),\\
\int \mathrm{d}\Omega\, \overline{\Psi_e^{\kappa',t'}} \gamma^5 \Psi_\mu^{(1s),t} &= i\frac{\delta_{tt'}}{r^2}\delta_{\kappa',+1}\Big(f_{+1}^{(e)} g_{-1}^{(\mu)} + g_{+1}^{(e)} f_{-1}^{(\mu)}\Big) &&=: i\frac{\delta_{tt'}}{r^2}\delta_{\kappa',+1}\ s_2(r),\\
\int \mathrm{d}\Omega\, \overline{\Psi_e^{\kappa',t'}} \gamma^0 \Psi_\mu^{(1s),t} &= \frac{\delta_{tt'}}{r^2}\delta_{\kappa',-1}\Big(g_{-1}^{(e)} g_{-1}^{(\mu)} + f_{-1}^{(e)} f_{-1}^{(\mu)}\Big) &&=: \frac{\delta_{tt'}}{r^2}\delta_{\kappa',-1}\ v_1(r),\\
\int \mathrm{d}\Omega\, \overline{\Psi_e^{\kappa',t'}} \gamma^5\gamma^0 \Psi_\mu^{(1s),t} &= i\frac{\delta_{tt'}}{r^2}\delta_{\kappa',+1}\Big(f_{+1}^{(e)} g_{-1}^{(\mu)} - g_{+1}^{(e)} f_{-1}^{(\mu)}\Big) &&=: i\frac{\delta_{tt'}}{r^2}\delta_{\kappa',+1}\ v_2(r),\\
\int \mathrm{d}\Omega\, \overline{\Psi_e^{\kappa',t'}} \hat{x}_i\sigma^{0i} \Psi_\mu^{(1s),t} &= \frac{\delta_{tt'}}{r^2}\delta_{\kappa',-1}\Big(f_{-1}^{(e)} g_{-1}^{(\mu)} + g_{-1}^{(e)} f_{-1}^{(\mu)}\Big) &&=: \frac{\delta_{tt'}}{r^2}\delta_{\kappa',-1}\ d_1(r),\\
\int \mathrm{d}\Omega\, \overline{\Psi_e^{\kappa',t'}} \gamma^5\hat{x}_i\sigma^{0i} \Psi_\mu^{(1s),t} &= -i\frac{\delta_{tt'}}{r^2}\delta_{\kappa',+1}\Big(g_{+1}^{(e)} g_{-1}^{(\mu)} - f_{+1}^{(e)} f_{-1}^{(\mu)}\Big) &&=: i\frac{\delta_{tt'}}{r^2}\delta_{\kappa',+1}\ d_2(r).
\end{aligned} \tag{3.82}$$

Summing over all possible κ', the matrix element becomes

$$\begin{aligned}
i\mathcal{M}_Y &= \frac{\delta_{M_i,M_f}\delta_{tt'}}{2\Lambda^2}\int_0^\infty \mathrm{d}r\, \Bigg[2\eta_e\Lambda C_Y^D (d_1(r) \mp i d_2(r))(-E(r))\\
&\qquad + \sum_{N=n,p}\Big(C_Y^{S,S}(s_1(r) \mp i s_2(r)) + C_Y^{V,V}(v_1(r) \mp i v_2(r))\Big)(\#N)\rho_N(r)\Bigg]\\
&= \frac{\delta_{M_i,M_f}\delta_{tt'}}{\Lambda^2}\Bigg[\Lambda\eta_e C_Y^D (D_1 \mp i D_2)\\
&\qquad + \sum_{N=n,p}\Big(C_Y^{S,S}\Big(S_1^{(N)} \mp i S_2^{(N)}\Big) + C_Y^{V,V}\Big(V_1^{(N)} \mp i V_2^{(N)}\Big)\Big)\Bigg],
\end{aligned} \tag{3.83}$$

where the $\mp$ refers to $Y = L, R$ and we define for $i = 1, 2$

$$\begin{aligned}
S_i^{(N)} &= \frac{1}{2}\int_0^\infty \mathrm{d}r\ (\#N)\rho_N(r)\ s_i(r), \qquad V_i^{(N)} = \frac{1}{2}\int_0^\infty \mathrm{d}r\ (\#N)\rho_N(r)\ v_i(r),\\
D_i &= \int_0^\infty \mathrm{d}r\,(-E(r))\ d_i(r),
\end{aligned} \tag{3.84}$$

which are the so-called overlap integrals, as initially introduced in Ref. [88][3]. We can separate the amplitude in its real and imaginary part via $\mathcal{M}_Y = \mathcal{M}_{1,Y} \mp i\mathcal{M}_{2,Y}$ with

$$i\mathcal{M}_{i,Y} = \frac{\delta_{M_i,M_f}\delta_{tt'}}{\Lambda^2}\Bigg[\Lambda\eta_e C_Y^D D_i + \sum_{N=n,p}\Big(C_Y^{S,S} S_i^{(N)} + C_Y^{V,V} V_i^{(N)}\Big)\Bigg]. \tag{3.85}$$

[3]Note that we used a different normalization than Ref. [88]

For $m_e > 0$, the $Y = L, R$ can interfere and the reduced matrix element squared becomes

$$\begin{aligned}\overline{|\mathcal{M}|^2} &= \frac{1}{2(2J+1)} \sum_{t,t',M_i,M_f} |(\mathcal{M}_{1,L} + \mathcal{M}_{1,R}) - i(\mathcal{M}_{2,L} - \mathcal{M}_{2,R})|^2 \\ &= \sum_{i=1,2} \frac{1}{\Lambda^4} \left| \Lambda \eta_e C_i^D D_i + \sum_{N=n,p} \left(C_i^{S,S} S_i^{(N)} + C_i^{V,V} V_i^{(N)} \right) \right|^2 . \end{aligned} \tag{3.86}$$

with $C_{1,2}^{X(,X)} = C_L^{X(,X)} \pm C_R^{X(,X)}$. In the limit $m_e \to 0$ we can identify, according to Eq. (5.48),

$$g_{+1}^{(e)} = f_{-1}^{(e)}, \qquad f_{+1}^{(e)} = -g_{-1}^{(e)}. \tag{3.87}$$

From this follows immediately

$$s_1(r) = s_2(r), \qquad v_1(r) = v_2(r), \qquad d_1(r) = d_2(r), \tag{3.88}$$

and thus

$$S^{(N)} := S_1^{(N)} = S_2^{(N)}, \qquad V^{(N)} := V_1^{(N)} = V_2^{(N)}, \qquad D := D_1 = D_2, \tag{3.89}$$

with

$$\begin{aligned} D &= \int_0^\infty \mathrm{d}r \, (-E(r)) \Big(g_{-1}^{(e)}(r) f_{-1}^{(\mu)}(r) + f_{-1}^{(e)}(r) g_{-1}^{(\mu)}(r) \Big), \\ S^{(N)} &= \frac{1}{2} \int_0^\infty \mathrm{d}r \, (\#N) \rho_N(r) \Big(g_{-1}^{(e)}(r) g_{-1}^{(\mu)}(r) - f_{-1}^{(e)}(r) f_{-1}^{(\mu)}(r) \Big), \\ V^{(N)} &= \frac{1}{2} \int_0^\infty \mathrm{d}r \, (\#N) \rho_N(r) \Big(g_{-1}^{(e)}(r) g_{-1}^{(\mu)}(r) + f_{-1}^{(e)}(r) f_{-1}^{(\mu)}(r) \Big), \end{aligned} \tag{3.90}$$

Accordingly $\mathcal{M}_{1,Y} = \mathcal{M}_{2,Y}$ and the reduced matrix element squared becomes

$$\begin{aligned}\overline{|\mathcal{M}|^2} &= \frac{1}{2(2J+1)} \sum_{t,t',M_i,M_f} \sum_{\substack{Y=L,R \\ i=1,2}} |\mathcal{M}_{i,Y}|^2 \\ &= \sum_{Y=L,R} \frac{2}{\Lambda^4} \left| \Lambda \eta_e C_Y^D D + \sum_{N=n,p} \left(C_Y^{S,S} S^{(N)} + C_Y^{V,V} V^{(N)} \right) \right|^2 . \end{aligned} \tag{3.91}$$

Inserting the definition of Eq. (3.14) for the prefactors we find

$$\overline{|\mathcal{M}|^2} = \sum_{Y=L,R} \frac{2}{\Lambda^4} \left| \Lambda \eta_e C_Y^D D + \sum_{\substack{N=n,p \\ q=u,d,s}} \left(\frac{m_N}{m_q} C_Y^{S,q} f_q^N(0) S^{(N)} + C_Y^{V,q} F_1^{q,N}(0) V^{(N)} \right) \right|^2$$

$$\approx \sum_{Y=L,R} \frac{2}{\Lambda^4} \Bigg| \Lambda \eta_e C_Y^D D + \Big(2C_Y^{V,u} + C_Y^{V,d}\Big) V^{(p)} + \Big(C_Y^{V,u} + 2C_Y^{V,d}\Big) V^{(n)} + \sum_{\substack{N=n,p \\ q=u,d,s}} \frac{m_N}{m_q} C_Y^{S,q} f_q^N(0) S^{(N)} \Bigg|^2 , \tag{3.92}$$

where we inserted values for the vector form factors at $q^2 = 0$ in the second line. This result is consistent with what was calculated in Ref. [88][4], and condenses the numerical input from the bound-state physics into scalar quantities straightforwardly calculated by one-dimensional integrals.

3.8.2 Simplified Bound-State Physics

To make the discussion of subleading nuclear responses clearer, we can consider simplified wave functions for the leptons, where for simplicity we again drop the dipole term from this calculation. The simplest case for the bound-state physics that we can consider is the initial muon stationary at the center of the nucleus and the outgoing electron as a plane wave. In this case we have [84, 123]

$$\begin{aligned} \psi_\mu^{(1s),t}(\vec{x}) &\approx \frac{(m_\mu \alpha_{\rm el} Z)^{3/2}}{\sqrt{\pi}} e^{-Z\alpha_{\rm el} m_\mu r}\ u_\mu(k,t) e^{i\vec{k}\cdot\vec{x}} \approx \frac{(m_\mu \alpha_{\rm el} Z)^{3/2}}{\sqrt{\pi}}\ u_\mu(0,t), \\ \sum_{\kappa'} \psi_e^{\kappa',t'}(\vec{x}) &\approx u_e(k',t') e^{i\vec{k}'\cdot\vec{x}}. \end{aligned} \tag{3.93}$$

We can keep such a simple structure and improve our description, by calculating the average value of the muon in the nucleus given by

$$\left\langle \psi_\mu^{(1s)} \right\rangle^2 = 4\pi \int_0^\infty {\rm d}r\, r^2 \rho(r) \big(g_{(\mu)}^2 + f_{(\mu)}^2\big) := 4(m_\mu \alpha_{\rm el} Z)^3 \frac{Z_{\rm eff}^4}{Z^4}, \tag{3.94}$$

which defines the effective charge $Z_{\rm eff}$ [88], such that the initial muon wave function is

$$\psi_\mu^{(1s),t}(\vec{x}) \approx \left\langle \psi_\mu^{(1s)} \right\rangle\ u_\mu(0,t) = \frac{(m_\mu \alpha_{\rm el} Z)^{3/2}}{\sqrt{\pi}} \left(\frac{Z_{\rm eff}}{Z}\right)^2\ u_\mu(0,t). \tag{3.95}$$

[4]Note again, that the sign of $\eta_e = \pm 1$ is conventional and can be absorbed into the definition of the Wilson coefficient C_Y^D.

With these assumptions, we get

$$\begin{aligned}
\widetilde{\overline{\Psi_{e_Y}^{\kappa',t'}}\Gamma_X^{(n)}\Psi_\mu^{(1s),t}}(\vec{q}) &= \int \mathrm{d}^3x\, \overline{\Psi_{e_Y}^{\kappa',t'}}(\vec{x})\Gamma_X^{(n)}\Psi_\mu^{(1s),t}(\vec{x})\; e^{i\vec{q}\cdot\vec{x}} \\
&= \int \mathrm{d}^3x\, \frac{(m_\mu\alpha_{\mathrm{el}}Z)^{3/2}}{\sqrt{\pi}}\left(\frac{Z_{\mathrm{eff}}}{Z}\right)^2 \overline{u_{e_Y}(k',t')}\Gamma_X^{(n)}u_\mu(0,t)\; e^{i(\vec{q}-\vec{k'})\cdot\vec{x}} \\
&= \frac{(m_\mu\alpha_{\mathrm{el}}Z)^{3/2}}{\sqrt{\pi}}\left(\frac{Z_{\mathrm{eff}}}{Z}\right)^2 \overline{u_{e_Y}(k',t')}\Gamma_X^{(n)}u_\mu(0,t)\; (2\pi)^3\delta^{(3)}(\vec{q}-\vec{k'}), \quad (3.96)
\end{aligned}$$

and the transferred momentum $\vec{q}$ becomes equal to the momentum of the outgoing electron $\vec{k'}$ with $|\vec{k'}| \approx m_\mu$ fixed by Eq. (3.2). The matrix element becomes

$$\begin{aligned}
i\mathcal{M}_Y = &\sum_{N=n,p}\sum_{L\geq 0}\sqrt{2L+1}(-i)^L\,\langle JM_i, L0|JM_f\rangle \\
&\times\left[\sum_{S=M,\Omega} l_{S,Y}\mathcal{F}_N^{S_L}(m_\mu) + \sum_{S=\Sigma,\Delta,\Phi} l^3_{S,Y} i\mathcal{F}_N^{S''_L}(m_\mu)\right] \\
&+\sum_{N=n,p}\sum_{L\geq 1}\sqrt{2L+1}(-i)^L\frac{1}{\sqrt{2}}\sum_{\lambda=\pm}\langle JM_i, L-\lambda|JM_f\rangle \\
&\times\left[\sum_{S=\Sigma,\Delta,\Phi} l^\lambda_{S,Y}\Big(-\lambda\mathcal{F}_N^{S_L}(m_\mu) - i\mathcal{F}_N^{S'_L}(m_\mu)\Big)\right], \quad (3.97)
\end{aligned}$$

with

$$l_{S,Y}^{(m)} = \sum_X C_{Y,X,S}^{(n,m)}(\vec{k'})\;\frac{(m_\mu\alpha_{\mathrm{el}}Z)^{3/2}}{\sqrt{\pi}}\left(\frac{Z_{\mathrm{eff}}}{Z}\right)^2 \overline{u_{e_Y}(k',t')}\Gamma_X^{(n)}u_\mu(0,t). \quad (3.98)$$

We collect the prefactors $C_{Y,X,S}^{(n,m)}$ of Eq. (3.25) until $\mathcal{O}(1)$, keeping also the terms with $\mathcal{O}(\frac{m_N}{m_q})$ (see Tab. 3.2). We do not consider the $\#N$ enhancement explicitly, as we will see, that terms with this enhancement and without will separate into the SI and SD contributions in this calculation, which will not interfere. It remains from Eq. (3.25)

$$\begin{aligned}
C_{Y,S,M} = C_Y^{S,S} &= \sum_q C_Y^{S,q}\frac{m_N}{m_q}f_q^{q,N} + \Lambda^{-1}C_Y^{GG}4\pi a_N, \\
C_{Y,V^0,M} = C_Y^{V,V} &= \sum_q C_Y^{V,q}F_1^{q,N}, \\
C^i_{Y,S,\Sigma} &= \delta^{i3}\frac{m_\mu}{2m_N}C_Y^{S,P} = \delta^{i3}\frac{m_\mu}{2m_N}\left(\sum_q C_Y^{P,q}\frac{m_N}{m_q}G_5^{q,N} + \Lambda^{-1}C_Y^{G\tilde{G}}(-4\pi\tilde{a}_N)\right), \\
C^{i,j}_{Y,\vec{V},\Sigma} &= -\delta^{ij}C_Y^{V,A} = -\delta^{ij}\sum_q C_Y^{A,q}G_A^{q,N}, \\
C^{i,j}_{Y,\vec{T},\Sigma} &= \delta^{ij}C_Y^{T,T} = \delta^{ij}\sum_q C_Y^{T,q}F_{1,T}^{q,N}. \quad (3.99)
\end{aligned}$$

Hence, in this limit the matrix element only contains

$$i\mathcal{M}_Y = \sum_{N=n,p}\sum_{L\geq 0}\sqrt{2L+1}(-i)^L \langle JM_i, L0|JM_f\rangle \left[l_{M,Y}\mathcal{F}_N^{M_L}(m_\mu) + il^3_{\Sigma,Y}\mathcal{F}_N^{\Sigma''_L}(m_\mu)\right] + \sum_{N=n,p}\sum_{L\geq 1}\sqrt{2L+1}(-i)^L\frac{1}{\sqrt{2}}\sum_{\lambda=\pm}\langle JM_i, L-\lambda|JM_f\rangle\left[-il^\lambda_{\Sigma,Y}\mathcal{F}_N^{\Sigma'_L}(m_\mu)\right], \quad (3.100)$$

with

$$\begin{aligned}
l_{M,Y} &= \frac{(m_\mu\alpha_{\rm el}Z)^{3/2}}{\sqrt{\pi}}\left(\frac{Z_{\rm eff}}{Z}\right)^2\Big(C_Y^{S,S}\,\overline{u_{e_Y}(k',t')}u_\mu(0,t) + C_Y^{V,V}\,\overline{u_{e_Y}(k',t')}\gamma^0 u_\mu(0,t)\Big),\\
l^\lambda_{\Sigma,Y} &= \frac{(m_\mu\alpha_{\rm el}Z)^{3/2}}{\sqrt{\pi}}\left(\frac{Z_{\rm eff}}{Z}\right)^2\Big(-C_Y^{V,A}\,\overline{u_{e_Y}(k',t')}\gamma^\lambda u_\mu(0,t) + C_Y^{T,T}\,\overline{u_{e_Y}(k',t')}\epsilon^{\lambda ij}\sigma_{ij}u_\mu(0,t)\Big),\\
l^3_{\Sigma,Y} &= \frac{(m_\mu\alpha_{\rm el}Z)^{3/2}}{\sqrt{\pi}}\left(\frac{Z_{\rm eff}}{Z}\right)^2\Big(\frac{m_\mu}{2m_N}C_Y^{S,P}\,\overline{u_{e_Y}(k',t')}u_\mu(0,t) - C_Y^{V,A}\,\overline{u_{e_Y}(k',t')}\gamma^3 u_\mu(0,t)\\
&\qquad + C_Y^{T,T}\,\overline{u_{e_Y}(k',t')}\epsilon^{3ij}\sigma_{ij}u_\mu(0,t)\Big),
\end{aligned} \quad (3.101)$$

where we also used that for the elastic process $\mathcal{F}_N^{\Sigma_L}$ vanishes. We calculate the reduced matrix element squared as

$$\begin{aligned}
\overline{|\mathcal{M}|^2} &= \frac{1}{2(2J+1)}\sum_{t,t',M_i,M_f}\mathcal{M}^\dagger\mathcal{M}\\
&= \tfrac{1}{2}\sum_{L\geq 0}\left[\sum_{N=n,p} l_{M,Y}\mathcal{F}_N^{M_L} + il^3_{\Sigma,Y}\mathcal{F}_N^{\Sigma''_L}\right]^\dagger\left[\sum_{N=n,p} l_{M,Y}\mathcal{F}_N^{M_L} + il^3_{\Sigma,Y}\mathcal{F}_N^{\Sigma''_L}\right]\\
&\quad + \tfrac{1}{2}\sum_{L\geq 1}\tfrac{1}{2}\sum_{\lambda=\pm}\left[\sum_{N=n,p} l^\lambda_{\Sigma,Y}\mathcal{F}_N^{\Sigma'_L}\right]^\dagger\left[\sum_{N=n,p} l^\lambda_{\Sigma,Y}\mathcal{F}_N^{\Sigma'_L}\right]\\
&= \tfrac{1}{2}\sum_{L\text{ even}}\left[\sum_{N=n,p} l_{M,Y}\mathcal{F}_N^{M_L}\right]^\dagger\left[\sum_{N=n,p} l_{M,Y}\mathcal{F}_N^{M_L}\right] + \tfrac{1}{2}\sum_{L\text{ odd}}\left[\sum_{N=n,p} l^3_{\Sigma,Y}\mathcal{F}_N^{\Sigma''_L}\right]^\dagger\left[\sum_{N=n,p} l^3_{\Sigma,Y}\mathcal{F}_N^{\Sigma''_L}\right]\\
&\quad + \tfrac{1}{2}\sum_{L\text{ odd}}\tfrac{1}{2}\sum_{\lambda=\pm}\left[\sum_{N=n,p} l^\lambda_{\Sigma,Y}\mathcal{F}_N^{\Sigma'_L}\right]^\dagger\left[\sum_{N=n,p} l^\lambda_{\Sigma,Y}\mathcal{F}_N^{\Sigma'_L}\right],
\end{aligned} \quad (3.102)$$

where we used that only even L for M_L and odd L for $\Sigma'^{,''}_L$ contribute. For the calculation of the leptonic sums, we can use

$$\begin{aligned}
&\sum_{t,t'}\Big(\overline{u_{e_Y}(k',t')}\Gamma u_\mu(0,t)\Big)^\dagger\Big(\overline{u_{e_Y}(k',t')}\Gamma' u_\mu(0,t)\Big)\\
&\qquad = \frac{m_\mu^2}{4m_\mu m_\mu}\,\mathrm{Tr}\big(\bar\Gamma P_Y(\gamma^0-\gamma^3)\Gamma'(1+\gamma^0)\big),
\end{aligned} \quad (3.103)$$

$\Gamma\backslash\Gamma'$	$\mathbb{1}$	γ^0	$-\gamma^3$	$2\sigma^{12}$
$\mathbb{1}$	2	2	-2	∓ 4
γ^0	2	2	-2	∓ 4
$-\gamma^3$	-2	-2	2	± 4
$2\sigma^{12}$	∓ 4	∓ 4	± 4	8

$\Gamma\backslash\Gamma'$	$-\gamma^1$	$2\sigma^{23}$	$-\gamma^2$	$2\sigma^{31}$
$-\gamma^1$	2	± 4	$\mp 2i$	$-4i$
$2\sigma^{23}$	± 4	8	$-4i$	$\mp 8i$
$-\gamma^2$	$\pm 2i$	$4i$	2	± 4
$2\sigma^{31}$	$4i$	$\pm 8i$	± 4	8

Table 3.3: Trace calculations of $\mathrm{Tr}\big(\bar{\Gamma} P_Y(\gamma^0 - \gamma^3)\Gamma'(1+\gamma^0)\big)$

where we went to the limit of $m_e \to 0$ and $\vec{k'}$ oriented in $\hat{e}_3$ direction, such that $k_0 = k'_3 = m_\mu$. Further we define $\bar{\Gamma} = \gamma^0\Gamma^\dagger\gamma^0$ and used

$$\sum_s u(p,s)\overline{u(p,s)} = \frac{\not{p} + m}{2E}, \tag{3.104}$$

according to our normalization of the lepton spinors. The results for the trace of Eq. (3.103), are listed for all relevant combinations of Lorentz structures in Tab. 3.3. We may then use

$$\frac{1}{2}\sum_{\lambda=\pm} l^{\lambda\dagger}_{\Sigma,Y} l^{\lambda}_{\Sigma,Y} = \frac{1}{2}\sum_{j=1,2} l^{j\dagger}_{\Sigma,Y} l^{j}_{\Sigma,Y} \tag{3.105}$$

to find for the reduced matrix element squared

$$\begin{aligned}
\overline{|\mathcal{M}|^2} &= \frac{(m_\mu \alpha_{\mathrm{el}} Z)^3}{4\pi}\left(\frac{Z_{\mathrm{eff}}}{Z}\right)^2 \\
&\quad\times\left(\sum_{L\ \text{even}}\left|\sum_{N=n,p}\left(C^{S,S}_{N,Y} + C^{V,V}_{N,Y}\right)\mathcal{F}_N^{M_L}\right|^2 + \sum_{L\ \text{odd}}\left|\sum_{N=n,p}\left(-C^{V,A}_{N,Y} \mp 2C^{T,T}_{N,Y}\right)\mathcal{F}_N^{\Sigma'_L}\right|^2\right. \\
&\qquad\left. + \sum_{L\ \text{odd}}\left|\sum_{N=n,p}\left(\frac{m_\mu}{2m_N}C^{S,P}_{Y} - C^{V,A}_{N,Y} \mp 2C^{T,T}_{Y}\right)\mathcal{F}_N^{\Sigma''_L}\right|^2\right) \\
&= \frac{(m_\mu \alpha_{\mathrm{el}} Z)^3}{4\pi}\left(\frac{Z_{\mathrm{eff}}}{Z}\right)^2 \\
&\quad\times\left(\sum_{L\ \text{even}}\left|\sum_{i=0,1}\left(C^{S,S}_{i,Y} + C^{V,V}_{i,Y}\right)\mathcal{F}_i^{M_L}\right|^2 + \sum_{L\ \text{odd}}\left|\sum_{i=0,1}\left(-C^{V,A}_{i,Y} \mp 2C^{T,T}_{i,Y}\right)\mathcal{F}_i^{\Sigma'_L}\right|^2\right. \\
&\qquad\left. + \sum_{L\ \text{odd}}\left|\sum_{i=0,1}\left(\frac{m_\mu}{2m_N}C^{S,P}_{i,Y} - C^{V,A}_{i,Y} \mp 2C^{T,T}_{i,Y}\right)\mathcal{F}_i^{\Sigma''_L}\right|^2\right),
\end{aligned} \tag{3.106}$$

where we made the dependency of the prefactors on $N = n, p$ visible again and changed to a isospin basis $i = 0, 1$ according to Eq. (2.54). For the $C^{V,A}_{i,Y}$ interaction Ref. [116] calculated corrections from the induced pseudo-scalar form factor, the axial radius, and

two-body currents which we may add by writing

$$\overline{|\mathcal{M}|^2} = \frac{(m_\mu \alpha_{\rm el} Z)^3}{4\pi}\left(\frac{Z_{\rm eff}}{Z}\right)^2 \times \left(\sum_{L\ \text{even}}\left|\sum_{i=0,1}\left(C_{i,Y}^{S,S}+C_{i,Y}^{V,V}\right)\mathcal{F}_i^{M_L}\right|^2 + \sum_{L\ \text{odd}}\left|\sum_{i=0,1}\left(-C_{N,Y}^{V,A}(1+\delta')^i \mp 2C_{i,Y}^{T,T}\right)\mathcal{F}_i^{\Sigma'_L}\right|^2 + \sum_{L\ \text{odd}}\left|\sum_{i=0,1}\left(\frac{m_\mu}{2m_N}C_{i,Y}^{S,P} - C_{i,Y}^{V,A}(1+\delta'')^i \mp 2C_{i,Y}^{T,T}\right)\mathcal{F}_i^{\Sigma''_L}\right|^2\right). \quad (3.107)$$

At $q = m_\mu$ they take the values $\delta' = -0.28(5)$, $\delta'' = -0.44(4)$.

In this representation, we now also have a clear separation between SI and SD interactions. The first terms with even L are called SI, while the later ones for odd L are called SD. The total decay rate becomes

$$\Gamma = \frac{1}{32\pi^2}\frac{|k'|}{m_M^2}(2\bar{E})(2E_f)(2E')\int \mathrm{d}\Omega\,\overline{|\mathcal{M}|^2} = \frac{m_\mu^2}{\pi}\overline{|\mathcal{M}|^2} \quad (3.108)$$

$$= \frac{(\alpha_{\rm el} Z)^3 m_\mu^5}{4\pi^2}\left(\frac{Z_{\rm eff}}{Z}\right)^2 \times \left(\sum_{L\ \text{even}}\left|\sum_{i=0,1}\left(C_{i,Y}^{S,S}+C_{i,Y}^{V,V}\right)\mathcal{F}_i^{M_L}\right|^2 + \sum_{L\ \text{odd}}\left|\sum_{i=0,1}\left(-C_{i,Y}^{V,A}(1+\delta')^i \mp 2C_{i,Y}^{T,T}\right)\mathcal{F}_i^{\Sigma'_L}\right|^2 + \sum_{L\ \text{odd}}\left|\sum_{i=0,1}\left(\frac{m_\mu}{2m_N}C_{i,Y}^{S,P} - C_{i,Y}^{V,A}(1+\delta'')^i \mp 2C_{i,Y}^{T,T}\right)\mathcal{F}_i^{\Sigma''_L}\right|^2\right), \quad (3.109)$$

where the factors of $(2\bar{E})$, $(2E_f)$, $(2E')$ adjust for the non-relativistic normalization. We may write

$$\Gamma_{\rm SI} = \frac{(\alpha_{\rm el} Z)^3 m_\mu^5}{4\pi^2}\left(\frac{Z_{\rm eff}}{Z}\right)^2 \sum_{L\ \text{even}}\left|\sum_{i=0,1}\left(C_{i,Y}^{S,S}+C_{i,Y}^{V,V}\right)\mathcal{F}_i^{M_L}\right|^2,$$

$$\Gamma_{\rm SD} = \frac{(\alpha_{\rm el} Z)^3 m_\mu^5}{4\pi^2}\left(\frac{Z_{\rm eff}}{Z}\right)^2 \sum_{L\ \text{odd}}\left(\left|\sum_{i=0,1}\left(-C_{i,Y}^{V,A}(1+\delta')^i \mp 2C_{i,Y}^{T,T}\right)\mathcal{F}_i^{\Sigma'_L}\right|^2 + \left|\sum_{i=0,1}\left(\frac{m_\mu}{2m_N}C_{i,Y}^{S,P} - C_{i,Y}^{V,A}(1+\delta'')^i \mp 2C_{i,Y}^{T,T}\right)\mathcal{F}_i^{\Sigma''_L}\right|^2\right). \quad (3.110)$$

This illustrates how the master formulae from Ref. [1] emerge as a special case of the framework developed here.

Chapter 4

LFV Pseudo-scalar Decays[1]

We have seen that $\mu \to e$ conversion probes a multitude of different effective operators. Some of these operators also probe LFV decays of light pseudo-scalars $\pi^0, \eta, \eta' \to \mu e$ [124, 125]. This motivates a systematic comparison between limits from both of these processes. As shown in Tab. 1.1, the limits for $\mu \to e$ conversion are a lot more stringent than for the LFV pseudo-scalar decays. The current experimental limits for the light pseudo-scalars are in detail

$$\begin{aligned} \mathrm{Br}[\pi^0 \to \mu^+ e^-] &< 3.8 \times 10^{-10} && [67], \\ \mathrm{Br}[\pi^0 \to \mu^- e^+] &< 3.2 \times 10^{-10} && [64], \\ \mathrm{Br}[\pi^0 \to \mu^+ e^- + \mu^- e^+] &< 3.6 \times 10^{-10} && [63], \\ \mathrm{Br}[\eta \to \mu^+ e^- + \mu^- e^+] &< 6 \times 10^{-6} && [69], \\ \mathrm{Br}[\eta' \to \mu^+ e^- + \mu^- e^+] &< 4.7 \times 10^{-4} && [70], \end{aligned} \tag{4.1}$$

which are all given at a 90% confidence level. On the other hand the most stringent limits for $\mu \to e$ conversion are given by[2]

$$\begin{aligned} \mathrm{Br}[\mu \to e, \mathrm{Ti}] &< 6.1 \times 10^{-13} && [72], \\ \mathrm{Br}[\mu \to e, \mathrm{Au}] &< 7 \times 10^{-13} && [71]. \end{aligned} \tag{4.2}$$

Nevertheless, the contributing operators, which are according to Eq. (2.12) pseudo-scalar, axial vector, and gluonic operators, give rise to the SD response for $\mu \to e$ conversion [81, 89, 90]. In contrast to the SI response, these responses do not show a coherent enhancement and only contribute to nuclei with non-zero spin. As controlling the nuclear structure for nuclei as heavy as ^{197}Au is challenging, this leaves us with ^{47}Ti and ^{49}Ti, with relatively low natural abundances of 7.44% and 5.41%, respectively. Given both these circumstances,

[1] The results of this chapter have been published in Ref. [1].

[2] Reference [72] represents the final result by the SINDRUM-II experiment for $\mu \to e$ conversion in Ti, superseding the earlier limit $\mathrm{Br}[\mu \to e, \mathrm{Ti}] < 4.3 \times 10^{-12}$ [126]. We thank Peter Wintz for clarification on this point.

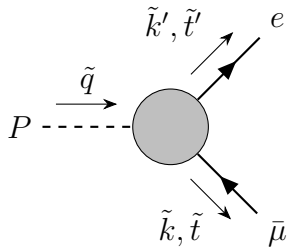

Figure 4.1: Feynman graph for $P \to \mu e$.

one might assume that inputs from $\mu \to e$ conversion and the pseudo-scalar decays could become competitive for these SD operators.

Nevertheless, we will find in practice that the limits from $\mu \to e$ conversion still surpass substantially, which then makes it possible to derive indirect limits on the pseudo-scalar decays from $\mu \to e$ conversion. In this chapter, we will discuss how we derived these limits.

4.1 Kinematics

We consider the LFV decays of light pseudo-scalars $P \to \mu e$ with $P = \pi^0, \eta, \eta'$ under the spin and momentum conventions of Fig. 4.1. In the rest frame of the pseudo-scalar P we have

$$\tilde{q} = (m_P, \vec{0}), \qquad \tilde{k}' = (\tilde{E}', \tilde{\vec{k}}'), \qquad \tilde{k} = (m_P - \tilde{E}', -\tilde{\vec{k}}') \tag{4.3}$$

with (in the limit of $m_e \to 0$)

$$\tilde{E}' = \left|\tilde{\vec{k}}'\right| = \frac{m_P^2 - m_\mu^2}{2m_P} \tag{4.4}$$

and in particular

$$(\tilde{k}' \cdot \tilde{k}) = \frac{1}{2}(m_P^2 - m_\mu^2) \tag{4.5}$$

	π	η		η'	
		Ref. [127]	Ref. [128]	Ref. [127]	Ref. [128]
$\frac{b_u f_P^u}{F_\pi}$	1	0.80	0.77	0.66	0.56
$\frac{b_d f_P^d}{F_\pi}$	-1	0.80	0.77	0.66	0.56
$\frac{b_s f_P^s}{F_\pi}$	0	-1.26	-1.17	1.45	1.50
$a_P\,[\mathrm{GeV}^3]$	0	–	-0.017	–	-0.038
$a_P^{\mathrm{FKS}}\,[\mathrm{GeV}^3]$	0	-0.022	-0.021	-0.056	-0.048

Table 4.1: Numerical values for the axial vector and gluonic matrix elements contributing to the $P \to \mu e$ decays, from a phenomenological extraction via η, η' transition form factors [127] and the recent lattice-QCD calculation [128] ($\overline{\mathrm{MS}}$ scale $\mu = 2$ GeV). The last line indicates the value of a_P extracted from f_P^u in the Feldmann–Kroll–Stech (FKS) scheme [129]. We use $F_\pi = 92.28\,\mathrm{MeV}$ [130].

4.2 Lagrangian and Hadronic Matrix Elements

We again employ the effective Lagrangian given by Eq. (2.3). The for $P \to \mu e$ relevant part of the Lagrangian simplifies to

$$\begin{aligned}\mathcal{L}_{\text{eff}}^{P\to\mu e} = \frac{1}{\Lambda^2}\sum_{\substack{Y=L,R\\ q=u,d,s}}\Big[C_Y^{P,q}(\overline{e_Y}\mu)(\bar{q}\gamma^5 q) + C_Y^{A,q}(\overline{e_Y}\gamma^\mu\mu)(\bar{q}\gamma_\mu\gamma^5 q)\Big] \\ + \frac{i\alpha_s}{\Lambda^3}\sum_{Y=L,R} C_Y^{G\tilde{G}}(\overline{e_Y}\mu)G^a_{\alpha\beta}\tilde{G}_a^{\alpha\beta} \;+\; \text{h.c.},\end{aligned} \tag{4.6}$$

as only pseudo-scalar, axial vector, and antisymmetric gluonic operators contribute. This is dictated by the hadronic matrix elements for the pseudo-scalars given via Eq. (2.12), namely again

$$\begin{aligned}\langle 0|\, m_q\bar{q}i\gamma^5 q\,|P(\tilde{q})\rangle &= \frac{b_q}{2}h_P^q(\tilde{q}),\\ \langle 0|\,\bar{q}\gamma^\mu\gamma^5 q\,|P(\tilde{q})\rangle &= ib_q f_P^q(\tilde{q})\tilde{q}^\mu,\\ \langle 0|\,\frac{\alpha_s}{4\pi}G^{a\mu\nu}\tilde{G}^a_{\mu\nu}\,|P(\tilde{q})\rangle &= a_P(\tilde{q}),\end{aligned} \tag{4.7}$$

which are related via the Ward identity of Eq. (2.15), namely

$$b_q f_P^q m_P^2 = b_q h_P^q - a_P. \tag{4.8}$$

In Tab. 4.1 we collect selected numerical values for the hadronic matrix elements.

4.3 The Decay Rate for $P \to \mu^{\mp} e^{\pm}$

Based on the Lagrangian of Eq. (4.6) the matrix elements for the decay $P \to \mu^- e^+$ become

$$\begin{aligned} i\mathcal{M}_Y^{P,q} &= i\frac{1}{\Lambda^2} C_Y^{P,q}\ \bar{u}_{e_Y} v_{\bar{\mu}}\ i\,\langle 0|\,\bar{q}\gamma^5 q\,|P(\tilde{q})\rangle\,, \\ i\mathcal{M}_Y^{A,q} &= i\frac{1}{\Lambda^2} C_Y^{A,q}\ \bar{u}_{e_Y}\gamma^\mu v_{\bar{\mu}}\ i\,\langle 0|\,\bar{q}\gamma_\mu\gamma^5 q\,|P(\tilde{q})\rangle\,, \\ i\mathcal{M}_Y^{G\tilde{G}} &= i\frac{i\alpha_s}{\Lambda^3}\ C_Y^{G\tilde{G}}\bar{u}_{e_Y} v_{\bar{\mu}}\ i\,\langle 0|\,G^a_{\mu\nu}\tilde{G}^{\mu\nu}_a\,|P(\tilde{q})\rangle\,, \end{aligned} \tag{4.9}$$

where we used for the outgoing electron $\bar{u}_{e_Y} := \bar{u}_{e_Y}(k', t')$ and for the outgoing anti-muon $v_{\bar{\mu}} := v_{\bar{\mu}}(k, t)$. Inserting the hadronic matrix elements of Eq. (4.7) we find

$$\begin{aligned} i\mathcal{M}_Y^{P,q} &= +i\frac{1}{\Lambda^2} C_Y^{P,q} b_q \frac{h_P^q}{2m_q}\bar{u}_{e_Y} v_{\bar{\mu}} \\ i\mathcal{M}_Y^{A,q} &= -i\frac{1}{\Lambda^2} C_Y^{A,q} b_q f_P^q \bar{u}_{e_Y} \not{q} v_{\bar{\mu}} \\ i\mathcal{M}_Y^{G\tilde{G}} &= -i\frac{1}{\Lambda^3} C_Y^{G\tilde{G}} 4\pi a_P \bar{u}_{e_Y} v_{\bar{\mu}}. \end{aligned} \tag{4.10}$$

With muon and electron on-shell, we further have

$$\bar{u}_{e_Y}\not{q} v_{\bar{\mu}} = \bar{u}_{e_Y}(\not{k}' + \not{k}) v_{\bar{\mu}} = \bar{u}_{e_Y}(m_{e_Y} - m_\mu) v_{\bar{\mu}} \approx -m_\mu \bar{u}_{e_Y} v_{\bar{\mu}}, \tag{4.11}$$

where we used momentum conservation as well as the free Dirac equation for muon and electron. Further, we neglected the electron mass compared to the muon mass. Adding all amplitudes we find

$$\begin{aligned} i\mathcal{M}_Y &= \sum_q (i\mathcal{M}_Y^{P,q} + i\mathcal{M}_Y^{A,q}) + i\mathcal{M}_Y^{G\tilde{G}} \\ &= i\frac{1}{\Lambda^2}\left(\sum_q \left(C_Y^{A,q} b_q f_P^q m_\mu + C_Y^{P,q} b_q \frac{h_P^q}{2m_q}\right) - C_Y^{G\tilde{G}}\frac{4\pi}{\Lambda} G_F a_P\right)\bar{u}_{e_Y} v_{\bar{\mu}}. \end{aligned} \tag{4.12}$$

The Hermitian conjugated process $P \to \mu^+ e^-$ is calculated analogously from the Hermitian conjugated part of the Lagrangian, such that the spin averaged matrix element squared becomes

$$\begin{aligned} \overline{|\mathcal{M}_Y|}^2 &= \frac{\left|C_Y^P\right|^2}{\Lambda^4}\,\mathrm{tr}\big((\not{k}' + m_e) P_{\bar{Y}} (\not{k} - m_\mu) P_Y\big) \approx \frac{\left|C_Y^P\right|^2}{\Lambda^4}\,\mathrm{tr}\big(P_Y^2 \not{k}'(\not{k} - m_\mu)\big) \\ &= \frac{\left|C_Y^P\right|^2}{\Lambda^4}\frac{1}{2} 4(k'\cdot k) = \frac{\left|C_Y^P\right|^2}{\Lambda^4}(m_P^2 - m_\mu^2), \end{aligned} \tag{4.13}$$

	p			n		
	[131]	[132]	[133]	[131]	[132]	[133]
$G_A^{u,N}$	0.842	0.777	0.847	−0.427	−0.438	−0.407
$G_A^{d,N}$	−0.427	−0.438	−0.407	0.842	0.777	0.847
$G_A^{s,N}$	−0.085	−0.053	−0.035	−0.085	−0.053	−0.035
$\tilde{a}_N$ [GeV]		-0.39(12)			-0.39(12)	

Table 4.2: Numerical values for the axial vector and gluonic matrix elements contributing to SD $\mu \to e$ conversion, from a phenomenological extraction via Ref. [131] and the recent lattice-QCD calculation ($\overline{\text{MS}}$ scale $\mu = 2$ GeV) [132, 133]. The last line indicates the value of $\tilde{a}_N$ extracted from a large N_c estimate which was derived in analogy to a_P^{FKS} in Ref. [1].

where we inserted Eq. (4.5) in the last line and introduced

$$C_Y^P = \sum_q \left(\pm C_Y^{A,q} b_q f_P^q m_\mu + C_Y^{P,q} b_q \frac{h_P^q}{2m_q} \right) - C_Y^{G\tilde{G}} \frac{4\pi}{\Lambda} G_F a_P, \tag{4.14}$$

where the $\pm$ refers to $P \to \mu^\mp e^\pm$. Adding the kinematic prefactors we find a decay rate of

$$\text{Br}[P \to \mu^\mp e^\pm] = \sum_{Y=L,R} \frac{1}{32\pi^2} \frac{|\vec{k}'|}{m_P^2} \int \overline{|\mathcal{M}_Y|}^2 \, \mathrm{d}\Omega = \frac{(m_P^2 - m_\mu^2)^2}{16\pi m_P^3 \Lambda^4} \sum_{Y=L,R} \left| C_Y^P \right|^2, \tag{4.15}$$

where the angular integral just gives a factor of 4π.

4.4 Spin Dependent $\mu \to e$ Conversion

Following the results of Eq. (3.110) the SD part of the $\mu \to e$ conversion rate follows as a special case from the general solution of Eq. (3.45) and can be written as

$$\begin{aligned} \Gamma_{\text{SD}} = \frac{(\alpha_{\text{el}} Z)^3 m_\mu^5}{4\pi^2} \left(\frac{Z_{\text{eff}}}{Z} \right)^2 \sum_{L \text{ odd}} \Bigg(& \left| \sum_{i=0,1} \left(-C_{i,Y}^{V,A} (1+\delta')^i \mp 2 C_{i,Y}^{T,T} \right) \mathcal{F}_i^{\Sigma'_L} \right|^2 \\ & + \left| \sum_{i=0,1} \left(\frac{m_\mu}{2m_N} C_{i,Y}^{S,P} - C_{i,Y}^{V,A} (1+\delta'')^i \mp 2 C_{i,Y}^{T,T} \right) \mathcal{F}_i^{\Sigma''_L} \right|^2 \Bigg), \end{aligned} \tag{4.16}$$

with

$$C_{0,Y}^{X,X'} = \frac{1}{2} \Big(C_{p,Y}^{X,X'} + C_{n,Y}^{X,X'} \Big) \qquad C_{1,Y}^{X,X'} = \frac{1}{2} \Big(C_{p,Y}^{X,X'} - C_{n,Y}^{X,X'} \Big), \tag{4.17}$$

	$S^{(p)}$	$V^{(p)}$	$S^{(n)}$	$V^{(n)}$
Ref. [88], method 1	0.0368	0.0396	0.0435	0.0468
Ref. [88], method 3	0.0371	0.0399	0.0462	0.0495
This work	0.039		0.044	

Table 4.3: Overlap integrals for ^{48}Ti compared to Ref. [88]. We find $Z_{\text{eff}} = 17.65$, using the charge distribution from Ref. [134] in the solution of the Dirac equation (for ^{27}Al we have $Z_{\text{eff}} = 11.64$). Methods 1 and 3 differ mainly in the estimate of the neutron distribution.

and for $N = p, n$

$$C_{N,Y}^{S,P} = \sum_q C_Y^{P,q} \frac{m_N}{m_q} G_5^{q,N} + \Lambda^{-1} C_Y^{G\tilde{G}} (-4\pi \tilde{a}_N),$$
$$C_{N,Y}^{V,A} = \sum_q C_Y^{A,q} G_A^{q,N}, \qquad C_{N,Y}^{T,T} = \sum_q C_Y^{T,q} F_{1,T}^{q,N}. \tag{4.18}$$

As input for the hadronic matrix elements, we can use the values from Tab. 4.2. For the bound-state corrections, we calculated the overlap integral values from Tab. 4.3, which in this limit condense into

$$Z_{\text{eff}}^{\text{Al}} = 11.64, \qquad Z_{\text{eff}}^{\text{Ti}} = 17.65. \tag{4.19}$$

The corrections from next-to-leading order and 2-body currents are given in Ref. [116] as

$$\delta' = -0.28(5), \qquad \delta'' = -0.44(4) \tag{4.20}$$

Finally, the nuclear structure functions are the results of a numerical analysis carried out in Ref. [1][3] using the nuclear shell model [98, 99] with the code ANTOINE [98, 135]. The calculations for Ti isotopes use the KB3G interaction [136] in a configuration space consisting of the $0f_{7/2}$, $1p_{3/2}$, $1p_{1/2}$ and $0f_{5/2}$ proton and neutron orbitals, with a ^{40}Ca core. For ^{27}Al the USDB interaction [137] and the $0d_{5/2}$, $0d_{3/2}$, $1s_{1/2}$ configuration space with an ^{16}O core was used. Tab. 4.4 summarizes the nuclear shell-model results for the M and Φ'' multipoles for all stable Ti and Al isotopes, while Tabs. 4.5 and 4.6 show the results for Σ', Σ'', following the conventions from Ref. [116].[4][5] In all cases proton/neutron and isoscalar/isovector components are related by $\mathcal{F}_\pm(q^2) = \mathcal{F}_p(q^2) \pm \mathcal{F}_n(q^2)$.

[3]The numerical shell-model calculations were carried out by Javier Menéndez and are not part of this thesis.

[4]Note that to arrive at the conventions of this work the Σ', Σ'' multipoles need to be multiplied with a factor of $2\sqrt{\frac{4\pi}{2J+1}}$.

[5]Note that the high number of digits presented here do not reflect the precision of the parameters, but is rather a measure to ensure reproducibility, since a systematic assessment of the uncertainty for these empirical shell-model results is difficult.

Isotope	^{46}Ti	^{47}Ti	^{48}Ti	^{49}Ti	^{50}Ti	^{27}Al
J^P	0^+	$5/2^-$	0^+	$7/2^-$	0^+	$5/2^+$
η [%]	8.25(3)	7.44(2)	73.72(3)	5.41(2)	5.18(2)	100
b [fm]	1.9769	1.9827	1.9884	1.9940	1.9995	1.8420
c_1^{M+}	−25.9987	−27.0005	−28.0021	−28.9986	−29.9991	−11.3343
c_2^{M+}	3.28239	3.49161	3.6798	3.85975	4.05453	0.837814
c_3^{M+}	−0.0685135	−0.0797877	−0.088061	−0.0939764	−0.102896	–
c_1^{M-}	1.99997	2.99993	4.00016	4.99982	5.99979	0.666696
c_2^{M-}	−0.406935	−0.617487	−0.830249	−1.03009	−1.2358	−0.0858552
c_3^{M-}	0.0200208	0.0310325	0.0424272	0.0518767	0.062231	–
$c_0^{\Phi''+}$	−4.73881	−5.91242	−6.77176	−7.96954	−8.91559	−4.98975
$c_1^{\Phi''+}$	1.8957	2.365	2.70879	3.18778	3.566129	0.997985
$c_2^{\Phi''+}$	−0.140202	−0.175856	−0.198666	−0.231598	−0.25760	–
$c_0^{\Phi''-}$	1.61434	2.67922	3.45274	4.5949	5.54649	0.303398
$c_1^{\Phi''-}$	−0.645785	−1.07173	−1.38116	−1.8379	−2.2185	−0.0606814
$c_2^{\Phi''-}$	0.0461341	0.0771383	0.100134	0.133188	0.160647	–

Table 4.4: Spin/parity J^P of the nuclear ground states, natural abundance η, harmonic-oscillator length b, and fit coefficients for the nuclear multipoles $\mathcal{F}_\pm^M$ and $\mathcal{F}_\pm^{\Phi''}$. The parameterizations $\mathcal{F}_\pm^M(u) = e^{-\frac{u}{2}} \sum_{i=0}^{3} c_i^{M\pm} u^i$ (with $c_0^{M+} = Z + N$ and $c_0^{M-} = Z - N$) and $\mathcal{F}_\pm^{\Phi''}(u) = e^{-\frac{u}{2}} \sum_{i=0}^{2} c_i^{\Phi''\pm} u^i$, with $u = \vec{q}^2 b^2/2$, correspond to the analytical form in the harmonic-oscillator basis [144]. This table is reproduced from Ref. [1].

Isotope	^{47}Ti			^{49}Ti			
L	1	3	5	1	3	5	7
$c_0^{\Sigma' p}$	0.0175579	–	–	0.0203333	–	–	–
$c_1^{\Sigma' p}$	−0.0179636	0.00453093	–	−0.0214563	−0.00759501	–	–
$c_2^{\Sigma' p}$	0.00314365	−0.00134858	−0.0000163753	0.00397767	0.00354166	−0.00043197	–
$c_3^{\Sigma' p}$	−0.0000982683	0.0000307488	0.0000216414	−0.000155929	−0.000272126	0.0000408714	-2.75178×10^{-6}
$c_0^{\Sigma' n}$	0.19529	–	–	0.271019	–	–	–
$c_1^{\Sigma' n}$	−0.245141	0.0279757	–	−0.357078	−0.129809	–	–
$c_2^{\Sigma' n}$	0.0551808	−0.0120502	−0.0298524	0.0813202	0.0399765	0.0179357	–
$c_3^{\Sigma' n}$	−0.00288588	0.0010701	0.00255996	−0.00432571	−0.00229466	−0.00108624	−0.00576536
$c_0^{\Sigma'' p}$	0.0124152	–	–	0.0143777	–	–	–
$c_1^{\Sigma'' p}$	−0.0118426	0.00392391	–	−0.0127874	−0.00657747	–	–
$c_2^{\Sigma'' p}$	0.00272966	−0.000701449	−0.0000149486	0.00252953	0.00196317	−0.000394335	–
$c_3^{\Sigma'' p}$	−0.000176902	0.0000103558	0.0000122962	−0.000122398	−0.000120552	0.0000438309	-2.57402×10^{-6}
$c_0^{\Sigma'' n}$	0.138089	–	–	0.191638	–	–	–
$c_1^{\Sigma'' n}$	−0.0676043	0.0242274	–	−0.0699121	−0.112418	–	–
$c_2^{\Sigma'' n}$	0.00783041	−0.00458878	−0.0272513	0.00435709	0.0179024	0.0163729	–
$c_3^{\Sigma'' n}$	−0.000298162	0.000464503	0.00168688	0.0000212473	−0.000600979	−0.000188205	−0.00539299

Table 4.5: Fit coefficients for the nuclear multipoles $\mathcal{F}_N^{\Sigma'_L}$ and $\mathcal{F}_N^{\Sigma''_L}$ of ^{47,49}Ti, using the fit function $\mathcal{F}(u) = e^{-\frac{u}{2}} \sum_{i=0}^{3} c_i u^i$. This table is reproduced from Ref. [1].

Isotope	^{27}Al		
L	1	3	5
$c_0^{\Sigma' p}$	0.217688	–	–
$c_1^{\Sigma' p}$	−0.199127	−0.0543796	–
$c_2^{\Sigma' p}$	0.0274599	0.00651646	0.0277341
$c_0^{\Sigma' n}$	0.0255784	–	–
$c_1^{\Sigma' n}$	−0.00985665	0.000280434	–
$c_2^{\Sigma' n}$	−0.00150251	−0.000488419	0.000128524
$c_0^{\Sigma'' p}$	0.153928	–	–
$c_1^{\Sigma'' p}$	−0.0262479	−0.0470943	–
$c_2^{\Sigma'' p}$	0.00103769	−0.00206298	0.0253177
$c_0^{\Sigma'' n}$	0.0180868	–	–
$c_1^{\Sigma'' n}$	−0.022234	0.000242867	–
$c_2^{\Sigma'' n}$	0.00278141	0.000103865	0.000117327

Table 4.6: Same as Tab. 4.5 for ^{27}Al. This table is reproduced from Ref. [1].

4.5 Indirect Limits

Using the two master formulas we may calculate an indirect limit for the pseudso-scalar decays. As the Wilson coefficients $C_Y^{P,q}$, $C_Y^{A,q}$, $C_Y^{\tilde{G}G}$ do not appear in the same linear combination in both processes there is no simple relation between the two processes. However, in the case where only one operator dominates, the transition is immediate and we can deduce indirect limits. Tab. 4.7 shows the limit if the triplet, octet, or singlet component of $C_Y^{P,q}$, $C_Y^{A,q}$, as well as the case where only $C_Y^{\tilde{G}G}$ is nonvanishing. The octet, singlet, and gluonic operators do not contribute to $\pi^0 \to \mu e$, nor do the triplet operators to $\eta, \eta' \to \mu e$. Combining all these flavor combinations should provide a realistic assessment of the sensitivities and results in a rough upper limit of

$$\mathrm{Br}[\pi^0 \to \mu e] \lesssim 4 \times 10^{-17}, \quad \mathrm{Br}[\eta \to \mu e] \lesssim 4 \times 10^{-12}, \quad \mathrm{Br}[\eta' \to \mu e] \lesssim 5 \times 10^{-13}. \quad (4.21)$$

To derive rigorous limits requires a scan over Wilson coefficients to minimize the effect in $\mu \to e$ conversion while retaining a sizable $P \to \mu e$ rate.[6] Moreover, theory uncertainties due to the hadronic and nuclear matrix elements need to be taken into account. To obtain robust limits, we take the meson matrix elements either from the phenomenological or the lattice-QCD determinations quoted in Tab. 4.1, similarly for the couplings $g_A^{q,N}$ from Refs. [131–133], and for $\tilde{a}_N$ as well δ', δ'' we include the uncertainties as given above. All quoted limits then refer to the worst limit obtained under this variation of the hadronic and nuclear input.

Equation (4.16) shows that each multipole in the transverse and longitudinal responses is squared separately, which in ^{47}Ti ($L = 1, 3, 5$) and ^{49}Ti ($L = 1, 3, 5, 7$) leads to a total of $2 \times 3 + 2 \times 4 = 14$ positive definite quantities. Accordingly, the only way to tune the rate to zero is to consider the couplings directly to protons and neutrons. Such a cancellation

[6] We set $C_L = C_R$ throughout, as left- and right-handed components do not interfere in either rate.

	π^0	η	η'
$C_Y^{A,3}$	1.1×10^{-17}	–	–
$C_Y^{A,8}$	–	1.5×10^{-17}	4.0×10^{-20}
$C_Y^{A,0}$	–	2.9×10^{-19}	2.1×10^{-19}
$C_Y^{P,3}$	4.1×10^{-17}	–	–
$C_Y^{P,8}$	–	3.2×10^{-13}	4.2×10^{-15}
$C_Y^{P,0}$	–	4.9×10^{-13}	6.6×10^{-14}
$C_Y^{G\tilde{G}}$	–	5.5×10^{-15}	4.5×10^{-16}

Table 4.7: Limits for $\mathrm{Br}[P \to \mu e] \equiv \mathrm{Br}[P \to \mu^+ e^- + \mu^- e^+]$ that follow from $\mathrm{Br}[\mu \to e, \mathrm{Ti}] < 6.1 \times 10^{-13}$ assuming the dominance of a single Wilson coefficient. $C_Y^{A,i}$, $C_Y^{P,i}$, $i = 3, 8, 0$, refer to triplet, octet, and singlet components, respectively. In all cases, we take $C_L = C_R$. We show the worst limits obtained when scanning over the two sets of matrix elements from Tab. 4.1, the couplings $g_A^{q,N}$ from Refs. [131–133], and $\tilde{a}_N$ including a 30% error.

occurs at

$$\begin{aligned} C_Y^{A,u} &= C_Y^{A,d}, & C_Y^{A,s} &= -\frac{2C_Y^{A,u} g_A^{u,0}}{G_A^{s,N}}, \\ \frac{C_Y^{P,u}}{m_u} &= \frac{C_Y^{P,d}}{m_d}, & \frac{C_Y^{P,s}}{m_s} &= \frac{4\pi}{\Lambda} C_Y^{G\tilde{G}} \frac{2G_A^{u,0}}{G_A^{u,0} - G_A^{s,N}}. \end{aligned} \tag{4.22}$$

Since the conditions not involving strangeness remove any isovector contribution, this implies that for this choice of Wilson coefficients $\mathrm{Br}[\pi^0 \to \mu e]$ vanishes as well. In this case, the limit is thus protected against accidental cancellation, and a scan over the parameter space establishes

$$\mathrm{Br}[\pi^0 \to \mu e] < 1.2 \times 10^{-13}, \tag{4.23}$$

as a rigorous limit. For η, η' a nonvanishing contribution

$$\begin{aligned} \mathrm{Br}[P \to \mu e] = \frac{(m_P^2 - m_\mu^2)^2}{2\pi \Gamma_P m_P^3 \Lambda^4} \left(b_u f_P^u G_A^{s,N} - b_s f_P^s G_A^{u,0}\right)^2 \\ \times \sum_{Y=L,R} \left(\left| \frac{m_\mu C_Y^{A,u}}{g_A^{s,N}} \right|^2 + \left| \frac{2\pi C_Y^{G\tilde{G}} m_P^2}{\Lambda (G_A^{u,0} - G_A^{s,N})} \right|^2 \right), \end{aligned} \tag{4.24}$$

remains, but such fine-tuned solutions are not viable due to RG corrections. As an example, we consider the dimension-6 contribution from $C_Y^{A,u} = C_Y^{A,d}$. If generated at a high scale Λ above the electroweak scale m_W, already the one-loop QED corrections below m_W produce a vector operator [89, 91]

$$C_Y^{V,q} \simeq -3Q_q \frac{\alpha_{\mathrm{el}}}{\pi} \log \frac{m_W}{m_N} C_Y^{A,q}, \tag{4.25}$$

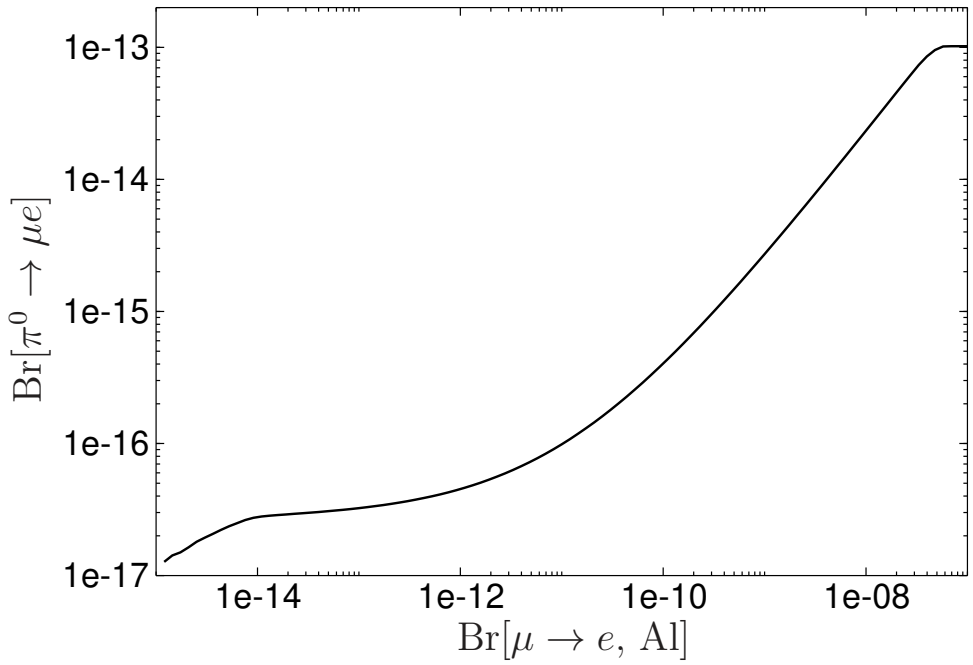

Figure 4.2: Limits on $\mathrm{Br}[\pi^0 \to \mu e]$ derived from $\mathrm{Br}[\mu \to e, \mathrm{Ti}]$ [72] in combination with a future limit on $\mathrm{Br}[\mu \to e, \mathrm{Al}]$. Already a moderate precision for the latter suffices to substantially reduce cancellations that otherwise dilute the limit from Eq. (4.21) to Eq. (4.23).

with quark charges $Q_u = 2/3$, $Q_d = -1/3$, and thus a contribution to the SI rate as given in Eq. (3.110). This indirect constraint gives

$$\mathrm{Br}[\eta \to \mu e] < 3.8 \times 10^{-18}, \qquad \mathrm{Br}[\eta' \to \mu e] < 9.1 \times 10^{-20}, \tag{4.26}$$

and thus excludes the solution via $C_Y^{A,q}$. Therefore, a fine-tuning of Wilson coefficients can relax the limits (4.21), but, realistically, only by a few orders of magnitude. Moreover, the cancellations that arise from the interference of isoscalar and isovector contributions can be substantially reduced by considering other $\mu \to e$ targets. Figure 4.2 illustrates this for $\mathrm{Br}[\pi^0 \to \mu e]$ as a function of a future limit for $\mu \to e$ conversion in Al in combination with the current Ti constraint. As nicely illustrated, a weak limit for Al of $\sim 10^{-8}$, leaves the combined limit basically unchanged, while already a limit at the same order as the current limits for Ti at $\sim 10^{-13}$, pushes the combined limit down to the values at the single-operator limit at $\sim 10^{-17}$.

Chapter 5

Charged Leptons in the Nucleus Potential

In the previous chapter, we have seen that a comprehensive description of $\mu \to e$ conversion requires numerical inputs for the wave functions of muon and electron in the nucleus potential as well as quantitative input for the nuclear structure functions. Both of these problems can be partly addressed by numerically solving the Dirac equation inside a nucleus potential. On the one hand, the resulting wave functions for the initial bound muon and outgoing electron can be used as direct input for the leptonic currents of Eq. (3.40), on the other hand, the solutions for continuum electrons can be used to calculate elastic electron-nucleus scattering, which directly relates to the charge form factor, which not only has high overlap with the M-response but also directly appears for the dipole interaction. To deduce these quantities thoroughly, quantitative input for the charge densities of the considered nuclei is necessary, these can be determined by comparing to elastic electron scattering data, as will be carried out in more detail in Chap. 6. In this chapter, we lay the groundwork for calculating the Dirac equation numerically for a given charge density and resulting charge potential, as well as computing elastic electron scattering based on it. We largely follow our discussions of Ref. [2].

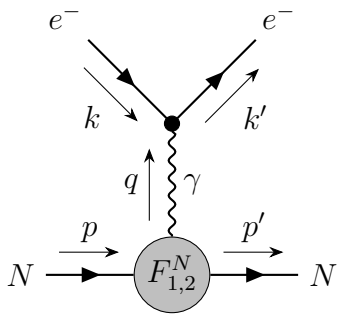

Figure 5.1: Elastic electron-nucleus scattering

5.1 Elastic Electron-Nucleus Scattering

Elastic electron-nucleus scattering happens at leading order via a simple one-photon exchange via the nucleus form factors as shown in Fig. 5.1, where also the used momentum labels are defined with momentum transfer $q_\mu = k'_\mu - k_\mu = p_\mu - p'_\mu$, where we still employ $q = |\vec{q}|$ in the following.[1] At leading order in Born approximation, this cross-section is given as

$$\frac{\mathrm{d}\sigma}{\mathrm{d}\Omega} = \left(\frac{\mathrm{d}\sigma}{\mathrm{d}\Omega}\right)_{\text{Mott}} \cdot \frac{E'}{E} \cdot \left|F(q,\theta)\right|^2, \tag{5.1}$$

with the Mott cross section [145, 146] given by

$$\left(\frac{\mathrm{d}\sigma}{\mathrm{d}\Omega}\right)_{\text{Mott}} = \frac{\alpha_{\text{el}}^2}{4E^2} \frac{\cos^2\frac{\theta}{2}}{\sin^4\frac{\theta}{2}}, \tag{5.2}$$

and the recoil factor is given as

$$\frac{E'}{E} = \left(1 + \frac{2E}{M}\sin^2\frac{\theta}{2} + \mathcal{O}\left(\frac{E^2}{M^2}\right)\right)^{-1}. \tag{5.3}$$

In the plane-wave Born approximation (PWBA), for the elastic processes, the form factor $F(q,\theta)$ can be further decomposed into longitudinal, $F_L(q)$, and transverse, $F_T(q)$, components

$$\left|F(q,\theta)\right|^2 = \left|F_L(q)\right|^2 + \left(\frac{1}{2} + \tan^2\frac{\theta}{2}\right)\left|F_T(q)\right|^2, \tag{5.4}$$

both of which can be further expanded into pieces with definite angular momentum L

$$\left|F_L(q)\right|^2 = \sum_{L\,\text{even}\,\leq 2J} \left|ZF_L^{\text{ch}}(q)\right|^2, \qquad \left|F_T(q)\right|^2 = \sum_{L\,\text{odd}\,\leq 2J} \left|F_L^{\text{mag}}(q)\right|^2, \tag{5.5}$$

[1] See again also App. A.2 for easier reference of the kinematic notation.

where J is the spin of the nucleus.[2] In general, the transverse cross-section also involves an electric part, which, however, vanishes for elastic processes due to time-reversal invariance [147, 148]. Parity conservation then implies that only even (odd) partial waves contribute to the Coulomb (magnetic) multipoles, respectively. For the elastic scattering process thus the scattering cross section is given by the charge and magnetic form factors F_L^{ch} and F_L^{mag}, which are directly related to the charge densities ρ_L and magnetic currents $j_{LL'}$ via[3]

$$\begin{aligned} ZF_L^{\text{ch}}(q) &= 4\pi \int \mathrm{d}r\; r^2\, j_L(qr)\rho_L(r), \qquad & \rho_L(r) &= \frac{1}{2\pi^2}\int \mathrm{d}q\; q^2\, j_L(qr) ZF_L^{\text{ch}}(q), \\ F_L^{\text{mag}}(q) &= 4\pi \int \mathrm{d}r\; r^2\, j_L(qr) j_{LL}(r), \qquad & j_{LL}(r) &= \frac{1}{2\pi^2}\int \mathrm{d}q\; q^2\, j_L(qr) F_L^{\text{mag}}(q). \end{aligned} \tag{5.6}$$

In particular, the spherical symmetrical part of the charge density $\rho(r) = \rho_0(r)$, is given by the charge form factor for $L = 0$, which is generally the dominating contribution of the cross-section.

We may calculate these form factors also directly from the SM in terms of nuclear structure functions, in the same way we calculated the $\mu \to e$ conversion rate for the dipole. The SM matrix element for free $Me \to Me$ is given by

$$i\mathcal{M} = i\frac{e^2}{q^2}\bar{u}(k')\gamma^\mu u(k) \left\langle M(p')\right| j^\mu_{\text{em}} \left|M(p)\right\rangle, \tag{5.7}$$

in accordance with Fig. 5.1 and with j^μ_{em} as defined in Eq. (3.48). Carrying out the same procedure as for $\mu \to e$ conversion and matching to the cross-section in Eq. (5.1) results in

$$\begin{aligned} ZF_L^{\text{ch}} &= \left(F_1^N + \frac{-q^2(F_1^N + 2F_2^N)}{8m_N^2}\right)\mathcal{F}_L^{M_N} + \left(\frac{q^2(F_1^N + 2F_2^N)}{4m_N^2}\right)\mathcal{F}_L^{\Phi''_N} + \mathcal{O}\left(\frac{q^4}{m_N^4}\right), \\ F_L^{\text{mag}} &= \frac{-iq}{m_N}\Big(F_1^N \mathcal{F}_L^{\Delta_N} - \tfrac{1}{2}\big(F_1^N + F_2^N\big)\mathcal{F}_L^{\Sigma'_N}\Big) + \mathcal{O}\left(\frac{q^3}{m_N^3}\right), \end{aligned} \tag{5.8}$$

where the various multipoles $\mathcal{F}_L^{\mathcal{S}_N}$, $\mathcal{S} \in \{M, \Phi'', \Delta, \Sigma', \ldots\}$ are given by Eq. (2.47). Inserting the leading expansion of the proton and neutron form factors

$$\begin{aligned} F_1^p &= 1 - \tfrac{\langle r_p^2\rangle}{6}q^2 + \tfrac{\kappa_p}{4m_N^2}q^2 + \mathcal{O}(q^4), \qquad & F_1^n &= 0 - \tfrac{\langle r_n^2\rangle}{6}q^2 + \tfrac{\kappa_n}{4m_N^2}q^2 + \mathcal{O}(q^4), \\ F_2^p &= \kappa_p + \mathcal{O}(q^2), & F_2^n &= \kappa_n + \mathcal{O}(q^2), \end{aligned} \tag{5.9}$$

where we follow the conventions of Ref. [116], results in

$$\begin{aligned} ZF_L^{\text{ch}} &= \left(1 - \tfrac{\langle r_p^2\rangle}{6}q^2 - \tfrac{1}{8m_N^2}q^2\right)\mathcal{F}_L^{M_p} - \tfrac{\langle r_n^2\rangle}{6}q^2\mathcal{F}_L^{M_n} + \tfrac{1+2\kappa_p}{4m_N^2}q^2\mathcal{F}_L^{\Phi''_p} + \tfrac{2\kappa_n}{4m_N^2}q^2\mathcal{F}_L^{\Phi''_n} + \mathcal{O}(q^4), \\ F_L^{\text{mag}} &= \frac{-iq}{m_N}\Big(\mathcal{F}_L^{\Delta_p} - \tfrac{1+\kappa_p}{2}\mathcal{F}_L^{\Sigma'_p} - \tfrac{\kappa_n}{2}\mathcal{F}_L^{\Sigma'_n}\Big) + \mathcal{O}(q^3), \end{aligned} \tag{5.10}$$

[2] We keep the slightly unfortunate convention to denote the angular momentum components of the longitudinal form factor F_L again by L.

[3] For a derivation we refer to App. C

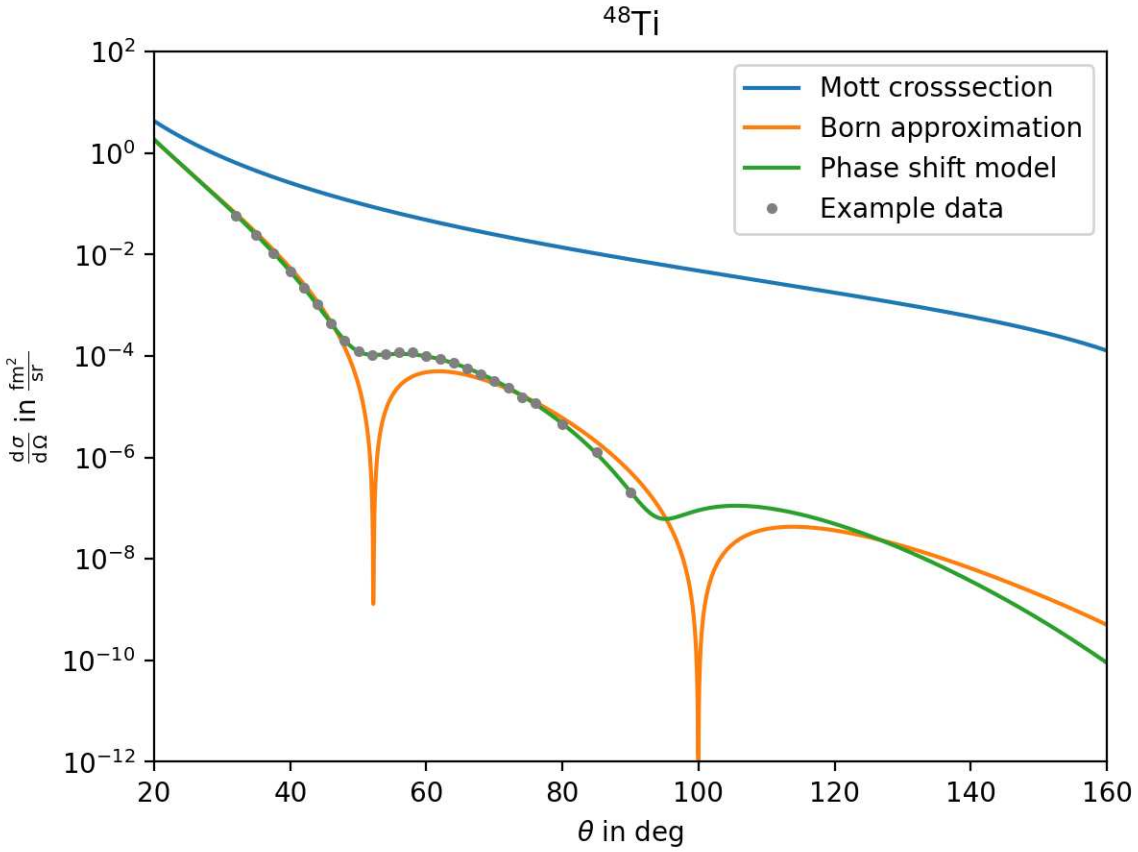

Figure 5.2: Comparison between cross sections for elastic electron-nucleus scattering at 249.5 MeV on ^{48}Ti as pure Mott, Born approximation, and including Coulomb corrections via the phase-shift model, as well as some example data points.

as commonly used. Note that for $J = 0$ only $L = 0$ contributes and thus the charge density is spherical symmetric with only F_0^{ch} respectively ρ_0 contributing.

Unfortunately, in practice, Eq. (5.1) is not sufficient for a reasonable description of elastic electron scattering data. Coulomb corrections, which fill up minima in the cross-section, need to be taken into account. These can be included rigorously by calculating the numerical wave functions for continuum electrons in the nucleus potential. An efficient procedure to do so for $L = 0$ is called the phase-shift model (see Sec. 5.4), while for $L > 0$ the so-called distorted wave Born approximation (DWBA) is employed (see Sec. 5.6). In Fig. 5.2 we illustrate for the example of ^{48}Ti how the inclusion of these Coulomb corrections fills out the minima and distorts the cross-section, and how only with these corrections a reasonable description of the example data can be achieved.

5.2 Charge Density, Electric Field, Potential

Since the charge density of the nucleus generates the electric field of the nucleus and thus dictates how charged particles are attracted by the nucleus charge potential, all these

quantities are related and the parameterization for the charge density directly determines the parameterization for the nucleus potential. In turn, a calculation of elastic electron-nucleus scattering, based on the potential, can be compared to experimental data to determine the charge density. The charge density predicts the electric field of the nucleus via

$$E(r) = \frac{\sqrt{4\pi\alpha_{\mathrm{el}}}}{r^2}\int_0^r \mathrm{d}r'\, r'^2\rho(r'), \qquad \rho(r) = \frac{1}{\sqrt{4\pi\alpha_{\mathrm{el}}}}\frac{1}{r^2}\frac{\mathrm{d}}{\mathrm{d}r}\big[r^2E(r)\big], \tag{5.11}$$

and the potential is then given by

$$V(r) = -\sqrt{4\pi\alpha_{\mathrm{el}}}\int_r^\infty \mathrm{d}r'\, E(r'), \qquad E(r) = \frac{1}{\sqrt{4\pi\alpha_{\mathrm{el}}}}\frac{\mathrm{d}}{\mathrm{d}r}[V(r)]. \tag{5.12}$$

Further, the total charge and charge radius are given by

$$Z = 4\pi\int_0^\infty \mathrm{d}r\, r^2\rho(r), \qquad \langle r^2\rangle = \frac{4\pi}{Z}\int_0^\infty \mathrm{d}r'\, r'^4\rho(r'). \tag{5.13}$$

Depending on the parameterization for the charge density, the electric field and the potential have different shapes. We consider a few toy models as well as the FB parameterization as a model-independent approach and will discuss them in the following.

In the following cases, we generally have for charge densities with a finite extent, such that $\exists\ R$ s.t. $\rho(r > R) = 0$:

$$E(r > R) = \sqrt{\frac{\alpha_{\mathrm{el}}}{4\pi}}\frac{Z}{r^2}, \qquad V(r > R) = -\frac{\alpha_{\mathrm{el}}Z}{r}, \tag{5.14}$$

meaning the potential behaves asymptotically like the Coulomb potential.

5.2.1 Toy Models

We first consider a selection of toy models. For the nucleus as a full sphere, with uniformly distributed charge, we have

$$\rho(r < R) = \frac{3Z}{4\pi R^3}, \quad E(r < R) = \sqrt{\frac{\alpha_{\mathrm{el}}}{4\pi}}\frac{Zr}{R^3}, \quad V(r < R) = -\frac{3}{2}\frac{\alpha_{\mathrm{el}}Z}{R}\left(1 - \frac{1}{3}\frac{r^2}{R^2}\right), \tag{5.15}$$

and a charge radius of $\sqrt{\langle r^2\rangle} = \sqrt{\frac{3}{5}}R$. This would be a quite naive model of a nucleus. Similarly, we find for the nucleus as an empty sphere

$$\rho(r) = \frac{Z}{4\pi R^2}\delta(r - R), \qquad E(r < R) = 0, \qquad V(r < R) = -\frac{\alpha_{\mathrm{el}}Z}{R}, \tag{5.16}$$

and a charge radius $\sqrt{\langle r^2\rangle} = R$. While this description might seem less natural in describing the charge density of a physical nucleus, we can combine several empty spheres

to build a more flexible toy model of the potential. One may use [149]

$$\rho(r) = \sum_{i=1}^{n} \frac{p_i}{R_i^2} \delta(r - R_i), \qquad Z = 4\pi \sum_{i=1}^{n} p_i, \tag{5.17}$$

with $0 = R_0 \leq R_1 \leq R_2 \leq \cdots \leq R_n = R$ the radii of the spheres and $p_i \geq 0$ dimensionless weights. One finds

$$E(R_j \leq r \leq R_{j+1}) = \sqrt{\frac{\alpha_{\mathrm{el}}}{4\pi}} \frac{Z_j}{r^2}, \qquad V(R_j \leq r \leq R_{j+1}) = V_j - \frac{Z_j \alpha_{\mathrm{el}}}{r}, \tag{5.18}$$

with

$$V_j = -4\pi\alpha_{\mathrm{el}} \sum_{i=1+j}^{n} \frac{p_i}{R_i}, \qquad Z_j = 4\pi \sum_{i=1}^{j} p_i, \tag{5.19}$$

and the charge radius and charge form factor (given by Eq. (5.6)) become

$$\langle r^2 \rangle = \frac{4\pi}{Z} \sum_{i=1}^{n} p_i R_i^2, \qquad F_0^{\mathrm{ch}}(q) = 4\pi \sum_{i=1}^{n} p_i \; j_0(qR_i). \tag{5.20}$$

With sufficiently large n, this model is quite flexible in describing any possible charge form factor $F_0^{\mathrm{ch}}(q)$ or potential $V(r)$, while at the same time still being solvable analytically, as the potential is given stepwise by a pure Coulomb potential Z_j with an energy offset V_j, which is known analytically (see Sec. 5.3.1). This strategy was for example employed in Ref. [150].

5.2.2 Fourier-Bessel Series

One option for a model-independent description of charge densities is in terms of a Fourier-Bessel (FB) series [149]. Such a series expansion takes the form

$$\rho(r) = \begin{cases} \sum_{n=1}^{N} a_n j_0(q_n r), & r \leq R \\ 0, & r > R \end{cases} \qquad \text{with} \qquad q_n = \frac{\pi n}{R}, \tag{5.21}$$

where N denotes the number of terms in the series, the cutoff radius $R > 0$ is related to the range of the charge distribution, and $a_n \in \mathbb{R}$ are the parameters. The quantities q_n are chosen in such a way that $j_0(q_n R) = 0 \; \forall n$, ensuring that the charge density $\rho(r)$ is continuous at $r = R$. Such a parameterization is very flexible and can with sufficiently many terms describe any possible shape. If the charge density is normalized to Z, it follows

$$Z = 4\pi R \sum_{n=1}^{N} (-1)^{n+1} \frac{a_n}{q_n^2}, \tag{5.22}$$

and in accordance with Eq. (5.6), the charge form factor is given by

$$F_0^{\rm ch}(q) = \frac{4\pi}{Z} R\ j_0(qR) \sum_{n=1}^{N} (-1)^n \frac{a_n}{q^2 - q_n^2}. \tag{5.23}$$

In particular, one has $F_0^{\rm ch}(q \to q_n) \to 2\pi R a_n/(Z q_n^2)$, which implies that the form factor in the vicinity of $q = q_n$ is mainly determined by a_n. A nucleus with the electric charge density of Eq. (5.21) possesses the following electric field and potential

$$E(r \le R) = \sqrt{4\pi\alpha_{\rm el}} \sum_{n=1}^{N} \frac{a_n}{q_n} j_1(q_n r), \quad V(r \le R) = -\frac{\alpha_{\rm el} Z}{R} - 4\pi\alpha_{\rm el} \sum_{n=1}^{N} \frac{a_n}{q_n^2} j_0(q_n r), \tag{5.24}$$

and for $r > R$ again like the Coulomb potential according to Eq. (5.14), due to the finite extent of the nucleus. To later also incorporate inputs from transition energies from muonic atoms, we also consider the so-called Barrett momentum

$$\left\langle r^k e^{-\alpha_{\rm el} r} \right\rangle = \frac{4\pi}{Z} \int_0^\infty {\rm d}r' r'^{2+k} e^{-\alpha r} \rho(r'), \tag{5.25}$$

which with empirically determined values for k and α, are a relatively model-independent way to classify this additional input. The charge radius and Barrett moments for the FB parameterization are given by

$$\begin{aligned} \left\langle r^2 \right\rangle &= \frac{4\pi}{Z} R^2 \sum_{n=1}^{N} (-1)^{n+1} \Big(\pi n - \frac{6}{\pi n} \Big) \frac{a_n}{q_n^3}, \\ \left\langle r^k e^{-\alpha r} \right\rangle &= \frac{4\pi}{Z} \sum_{n=1}^{N} \frac{a_n}{q_n} {\rm Im} \left[\frac{\Gamma\big(2+k, 0, R(\alpha - i q_n)\big)}{(\alpha - i q_n)^{k+2}} \right], \end{aligned} \tag{5.26}$$

where the generalized incomplete Γ function is defined by

$$\Gamma(z, a, b) = \Gamma(z, a) - \Gamma(z, b), \qquad \Gamma(z, a) = \int_a^\infty {\rm d}t\ t^{z-1} e^{-t}, \tag{5.27}$$

as well as the appropriate analytic continuation for complex arguments. In the limit $\alpha \to 0$, $k \to 2$ one indeed recovers the expression for $\langle r^2 \rangle$.

5.3 Dirac Equation

To precisely describe relativistic lepton physics in the vicinity of a nucleus potential, it is necessary to numerically solve the Dirac equation. To this end, we will summarize in the following section the basics of solving the Dirac equation with a radial symmetric potential. This introduction will also serve as the groundwork for the phase-shift model described in the subsequent section. For more details on the topic we refer to Refs. [123, 151].

The well-known free Dirac equation is given by[4]

$$(-i\hbar c\partial_\mu \gamma^\mu + mc^2)\psi = (i\partial\!\!\!/ - m) = 0, \tag{5.28}$$

with m the mass of the lepton. The time-independent Dirac equation becomes

$$(-i\partial_k \gamma^k + m)\psi = E\gamma^0\psi \quad \Leftrightarrow \quad (-i\gamma^0(\vec{\nabla}\cdot\vec{\gamma}) + \gamma^0 m)\psi = E\psi, \tag{5.29}$$

with E the energy of the particle. Under the influence of a potential $V(\vec{r})$ this becomes

$$(-i\gamma^0(\vec{\nabla}\cdot\vec{\gamma}) + \gamma^0 m + V(\vec{r}))\psi = E\psi. \tag{5.30}$$

We may project out the radial component by using the identity

$$\vec{\nabla} = \hat{\vec{r}}(\hat{\vec{r}}\cdot\nabla) - \hat{\vec{r}}\times(\hat{\vec{r}}\times\vec{\nabla}) = \hat{\vec{r}}\partial_r - i\frac{1}{r}\,\hat{\vec{r}}\times\vec{L}, \tag{5.31}$$

with $\vec{L} = -i\vec{r}\times\vec{\nabla}$ the orbital angular momentum. Inserting the gamma matrices in the Dirac representation

$$\gamma^0 = \begin{pmatrix} \mathbb{1}_2 & \\ & -\mathbb{1}_2 \end{pmatrix}, \qquad \gamma^i = \begin{pmatrix} & \sigma_i \\ -\sigma_i & \end{pmatrix}, \qquad \gamma^5 = \begin{pmatrix} & \mathbb{1}_2 \\ \mathbb{1}_2 & \end{pmatrix}, \tag{5.32}$$

with σ_i the Pauli matrices and using

$$(\hat{\vec{r}}\cdot\vec{\sigma})(\vec{L}\cdot\vec{\sigma}) = \underbrace{(\hat{\vec{r}}\cdot\vec{L})}_{=0} + i\vec{\sigma}\cdot(\hat{\vec{r}}\times\vec{L}), \tag{5.33}$$

we then find

$$-i\gamma^0(\vec{\nabla}\cdot\vec{\gamma}) = -i\left(\begin{pmatrix} & \sigma_r \\ \sigma_r & \end{pmatrix}\partial_r - \frac{1}{r}\begin{pmatrix} & \sigma_r(\vec{L}\cdot\vec{\sigma}) \\ \sigma_r(\vec{L}\cdot\vec{\sigma}) & \end{pmatrix}\right), \tag{5.34}$$

with $\sigma_r = \vec{\sigma}\cdot\hat{\vec{r}}$. We define

$$\Sigma_r = \begin{pmatrix} \sigma_r & \\ & \sigma_r \end{pmatrix}, \qquad K = \begin{pmatrix} (1+\vec{L}\cdot\vec{\sigma}) & \\ & -(1+\vec{L}\cdot\vec{\sigma}) \end{pmatrix}, \tag{5.35}$$

and get

$$-i\gamma^0(\vec{\nabla}\cdot\vec{\gamma}) = -i\gamma^5\Sigma_r\left(\partial_r + \frac{1}{r} - \frac{\gamma^0}{r}K\right), \tag{5.36}$$

such that the Dirac equation in spherical form becomes the usually used form of

$$\left(-i\gamma^5\Sigma_r\left(-\partial_r - \frac{1}{r} + \frac{\gamma^0}{r}K\right) + m\gamma^0 + V(\vec{r})\right)\psi = E\psi. \tag{5.37}$$

[4]We use $\hbar = c = 1$.

For a radial symmetrical potential $V(\vec{r}) = V(r)$, the angular dependencies of $\psi(\vec{r})$ are the same as for the free solution and are given by

$$\phi_\kappa^\mu(\hat{r}) = \sum_{m,m'=\pm\frac{1}{2}} \left\langle lm, \tfrac{1}{2}m' \middle| j\mu \right\rangle Y_{lm}(\hat{r})\chi_{m'}, \tag{5.38}$$

with

$$\begin{aligned} (1 + \vec{L}\cdot\vec{\sigma})\phi_\kappa^\mu(\hat{r}) &= -\kappa\phi_\kappa^\mu(\hat{r}), & J_z\phi_\kappa^\mu(\hat{r}) &= \mu\phi_\kappa^\mu(\hat{r}), \\ J^2\phi_\kappa^\mu(\hat{r}) &= j(j+1)\phi_\kappa^\mu(\hat{r}), & (\hat{r}\cdot\vec{\sigma})\phi_\kappa^\mu(\hat{r}) &= -\phi_{-\kappa}^\mu(\hat{r}), \end{aligned} \tag{5.39}$$

which are eigenfunctions to the total spin J^2, J_z and K and all commute with the Hamiltonian. Y_{lm} are the spherical harmonics and χ_m are the two-component Pauli spinors given by

$$\begin{aligned} \chi_+ := \chi_{+\frac{1}{2}} &= \begin{pmatrix} \cos\frac{\theta}{2} \\ e^{i\phi}\sin\frac{\theta}{2} \end{pmatrix}, & \chi_- := \chi_{-\frac{1}{2}} &= \begin{pmatrix} -e^{-i\phi}\sin\frac{\theta}{2} \\ \cos\frac{\theta}{2} \end{pmatrix}, \\ \chi_\pm^\dagger\chi_\pm &= 1, & \vec{\sigma}\hat{\vec{p}}\chi_\pm &= \pm\chi_\pm, \end{aligned} \tag{5.40}$$

with θ, ϕ the angles of $\hat{r}$. For a spin $\frac{1}{2}$ particle the introduction of κ makes it possible to instead of considering two values of $j = l \pm \frac{1}{2}$ with each $l \geq 0$, to combine these into one quantum number $\kappa \gtrless 0$. The association is according to

$$j = |\kappa| - \frac{1}{2}, \qquad l = \begin{cases} \kappa & , \quad \kappa > 0 \\ -\kappa - 1 & , \quad \kappa < 0 \end{cases}, \qquad \mu = j_z. \tag{5.41}$$

Hence, for example the $1s^{1/2}$ ground state with $l = 0$ and $j = \frac{1}{2}$ is the $\kappa = -1$ state. The angular wave functions fulfill the following orthogonality relation

$$\int \mathrm{d}\Omega\, \phi_\kappa^\mu(\hat{r})^* \phi_{\kappa'}^{\mu'}(\hat{r}) = \delta_{\kappa\kappa'}\delta_{\mu\mu'}. \tag{5.42}$$

Using theses wave functions we can parameterize the general solution for Eq. (5.37) as

$$\psi = \psi_\kappa^\mu(\vec{r}) = \frac{1}{r}\begin{pmatrix} g_\kappa(r)\phi_\kappa^\mu(\hat{r}) \\ i f_\kappa(r)\phi_{-\kappa}^\mu(\hat{r}) \end{pmatrix}, \tag{5.43}$$

as already used in Eq. (3.35). We may choose the free global phase such that $f_\kappa(r)$ and $g_\kappa(r)$ are real. Note that historically usually g_κ and f_κ are defined with the factor of $1/r$ included. However, as we will see in the next line, the radial Dirac equation for g_κ and f_κ takes a more convenient form if this factor is excluded. This is usually done in a second line of definitions. We skip this intermediate step and directly separate the factor $1/r$. Inserting this definition results in the following coupled differential equation for the radial components

$$\frac{\partial}{\partial r}\begin{pmatrix} g_\kappa(r) \\ f_\kappa(r) \end{pmatrix} = \begin{pmatrix} g'_\kappa(r) \\ f'_\kappa(r) \end{pmatrix} = \begin{pmatrix} -\frac{\kappa}{r} & E - V(r) + m \\ -(E - V(r) - m) & \frac{\kappa}{r} \end{pmatrix}\begin{pmatrix} g_\kappa(r) \\ f_\kappa(r) \end{pmatrix}. \tag{5.44}$$

We note that in the limit of $m \to 0$, we have

$$\begin{pmatrix} g'_\kappa(r) \\ f'_\kappa(r) \end{pmatrix} = \begin{pmatrix} -\frac{\kappa}{r} & E - V(r) \\ -(E - V(r)) & \frac{\kappa}{r} \end{pmatrix} \begin{pmatrix} g_\kappa(r) \\ f_\kappa(r) \end{pmatrix}, \tag{5.45}$$

which for $\kappa \to -\kappa$ can be rewritten as

$$\begin{pmatrix} f'_{-\kappa}(r) \\ -g'_{-\kappa}(r) \end{pmatrix} = \begin{pmatrix} -\frac{\kappa}{r} & E - V(r) \\ -(E - V(r)) & \frac{\kappa}{r} \end{pmatrix} \begin{pmatrix} f_{-\kappa}(r) \\ -g_{-\kappa}(r) \end{pmatrix}. \tag{5.46}$$

Hence, in this limit, we have

$$\begin{pmatrix} g_\kappa(r) \\ f_\kappa(r) \end{pmatrix} = e^{i\varphi} \begin{pmatrix} f_{-\kappa}(r) \\ -g_{-\kappa}(r) \end{pmatrix}, \tag{5.47}$$

since they fulfill the same differential equation, and have the same normalization. Since we chose f_κ and g_κ to be real, we can set the phase φ such that we have for $\kappa > 0$

$$g_\kappa = f_{-\kappa}, \qquad\qquad f_\kappa = -g_{-\kappa}, \tag{5.48}$$

in the limit $m \to 0$, which is in line with the sign convention of the Coulomb solutions (see Eqs. (5.56) and (5.57)).

We distinguish between bound-state solutions with binding energy $E_{\text{bin}} = E - m$, and continuum solutions. For $\lim_{r\to\infty} V(r) = 0$, there exist potential bound-state solutions for $\max(-2m, V_{\min}) < E_{\text{bin}} < 0$, and continuum solutions for $E \geq m$. For a physical potential $V(r)$ the bound-state solutions are regular for $r \to \infty$, while the continuum solutions become asymptotically free. For bound-state solutions, the normalization condition is given by

$$\int \mathrm{d}^3 r \left[\psi_\kappa^\mu(\vec{r})\right]^* \psi_{\kappa'}^{\mu'}(\vec{r}) = \delta_{\kappa\kappa'}\delta_{\mu\mu'}, \tag{5.49}$$

so that, after separating the angular components via Eq. (5.42),

$$\int_0^\infty \mathrm{d}r \left(|g_\kappa(r)|^2 + |f_\kappa(r)|^2\right) = 1. \tag{5.50}$$

Similarly, one has for continuum solutions[5]

$$\int \mathrm{d}^3 r \left[\psi_\kappa^{\mu,E}(\vec{r})\right]^* \psi_{\kappa'}^{\mu',E'}(\vec{r}) = 2\pi\delta_{\kappa\kappa'}\delta_{\mu\mu'}\delta\big(E - E'\big), \tag{5.51}$$

and thus

$$\int_0^\infty \mathrm{d}r \left(g_\kappa^E(r) g_\kappa^{E'}(r) + f_\kappa^E(r) f_\kappa^{E'}(r)\right) = 2\pi\delta\big(E - E'\big). \tag{5.52}$$

[5]The factor 2π is a matter of convention, e.g., Ref. [152] uses a normalization without. We chose this normalization in agreement with Ref. [88], to facilitate the calculation of the $\mu \to e$ overlap integrals.

5.3.1 Coulomb Potential

In the following, we discuss the solutions of Eq. (5.44) for a pure Coulomb potential, namely

$$V(r) = -\frac{Z\alpha_{\mathrm{el}}}{r}. \tag{5.53}$$

For more details and derivations see Refs. [123, 152]. Solving for the bound-state solutions results in the energies

$$E_{n,\kappa}^{C,r/i} = \frac{m}{\sqrt{1+\left(\frac{\alpha_{\mathrm{el}}Z}{n-|\kappa|\pm\rho_\kappa}\right)^2}} = m\sqrt{1-\left(\lambda_{n,k}^{\pm}\right)^2}, \tag{5.54}$$

with

$$\rho_\kappa = \sqrt{\kappa^2-(\alpha_{\mathrm{el}}Z)^2}, \qquad \lambda_{n,\kappa}^{\pm} = \frac{1}{\sqrt{1+\left(\frac{n-|\kappa|\pm\rho_\kappa}{\alpha_{\mathrm{el}}Z}\right)^2}}, \tag{5.55}$$

where the main quantum number is $n = 1, 2, 3, \ldots$ and $l < n$, $j = l \pm \frac{1}{2}$ determine κ via Eq. (5.41).

As an example, the energy levels for $Z = 82$ until $n = 3$ are shown in Fig. 5.3. As the mass of the particle m is the only dimensionful scale, all energies are proportional to the particle mass. As Eq. (5.54) only depends on $|\kappa|$, we see a degeneracy for $\kappa \leftrightarrow -\kappa$. In particular, this means that, while we see the fine-structure corrections and a splitting between the $2p^{1/2}$ and $2p^{3/2}$ states, the $2s^{1/2}$ and $2p^{1/2}$ states are predicted by the Dirac equation to have the same energy. The challenge of this prediction, as well as the subsequent discovery of the Lamb shift, splitting up the two energy states, laid the foundation for quantum electrodynamics, which is then able to describe this observation. For our application the Dirac equation result is sufficient. Furthermore, as we consider the nucleus simply as a potential well, hyperfine-structure corrections are also neither included nor necessary in the scope of this work.

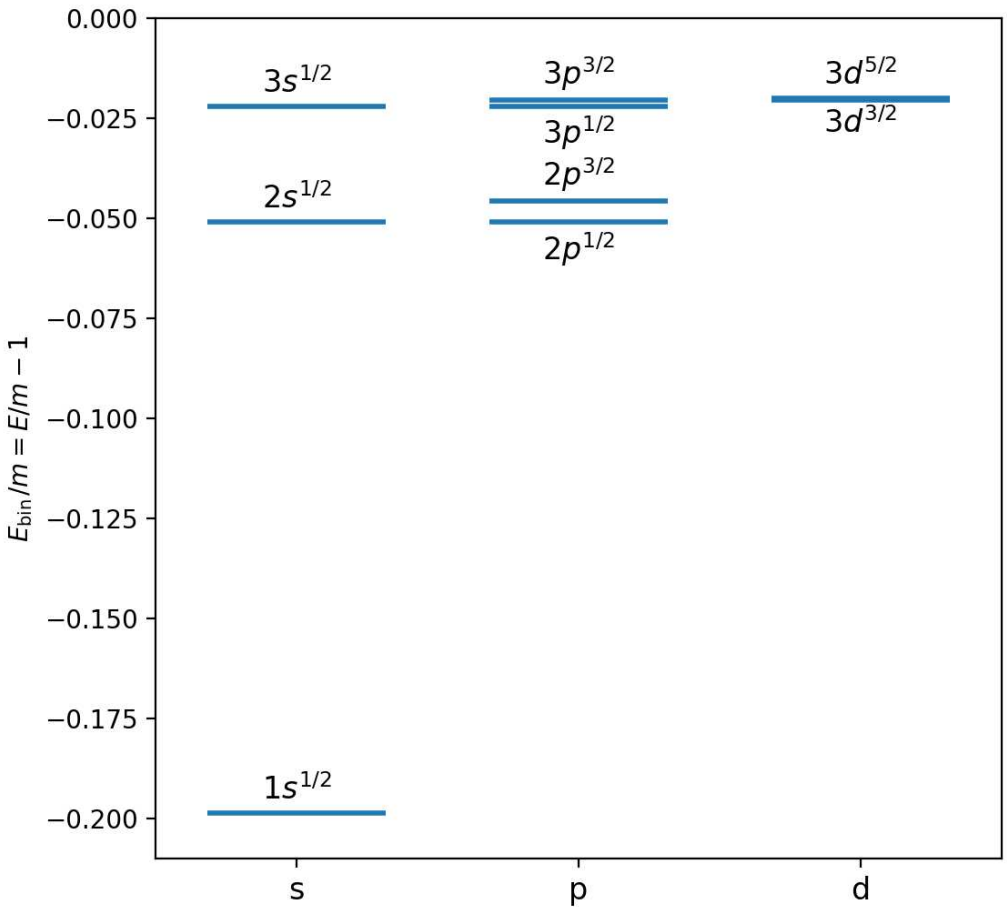

Figure 5.3: Energy levels until $n = 3$ for a pure Coulomb potential with $Z = 82$

Looking at the wave functions the explicit regular and irregular solutions for the bound states are given as

$$
\begin{aligned}
g^{C,r/i}_{n,\kappa}(r) = &\sqrt{\frac{\left(\lambda^{\pm}_{n,\kappa}\right)^3 (m + E^{C,r/i}_{n,\kappa})}{2\alpha_{\text{el}} Z(\alpha_{\text{el}} Z - \lambda^{\pm}_{n,\kappa}\kappa)}}\ (2\lambda^{\pm}_{n,\kappa} mr)^{\pm\rho_\kappa} \frac{\left|\sqrt{\Gamma(\pm 2\rho_\kappa + n - |\kappa| + 1)}\right|}{(n - |\kappa|)!\ \Gamma(\pm 2\rho_\kappa + 1)} e^{-\lambda^{\pm}_{n,\kappa} mr} \\
&\times \Big[(-n + |\kappa|) \times {}_1F_1(-n + |\kappa| + 1, \pm 2\rho_\kappa + 1, 2\lambda^{\pm}_{n,\kappa} mr) \\
&\quad + (\kappa - \alpha_{\text{el}} Z/\lambda^{\pm}_{n,\kappa}) \times {}_1F_1(-n + |\kappa|, \pm 2\rho_\kappa + 1, 2\lambda^{\pm}_{n,\kappa} mr)\Big], \\
f^{C,r/i}_{n,\kappa}(r) = -&\sqrt{\frac{\left(\lambda^{\pm}_{n,\kappa}\right)^3 (m - E^{C,r/i}_{n,\kappa})}{2\alpha_{\text{el}} Z(\alpha_{\text{el}} Z - \lambda^{\pm}_{n,\kappa}\kappa)}}\ (2\lambda^{\pm}_{n,\kappa} mr)^{\pm\rho_\kappa} \frac{\left|\sqrt{\Gamma(\pm 2\rho_\kappa + n - |\kappa| + 1)}\right|}{(n - |\kappa|)!\ \Gamma(\pm 2\rho_\kappa + 1)} e^{-\lambda^{\pm}_{n,\kappa} mr} \\
&\times \Big[(n - |\kappa|) \times {}_1F_1(-n + |\kappa| + 1, \pm 2\rho_\kappa + 1, 2\lambda^{\pm}_{n,\kappa} mr) \\
&\quad + (\kappa - \alpha_{\text{el}} Z/\lambda^{\pm}_{n,\kappa}) \times {}_1F_1(-n + |\kappa|, \pm 2\rho_\kappa + 1, 2\lambda^{\pm}_{n,\kappa} mr)\Big],
\end{aligned}
\tag{5.56}
$$

where the regular solutions to the first few states are shown in Fig. 5.4. Correspondingly,

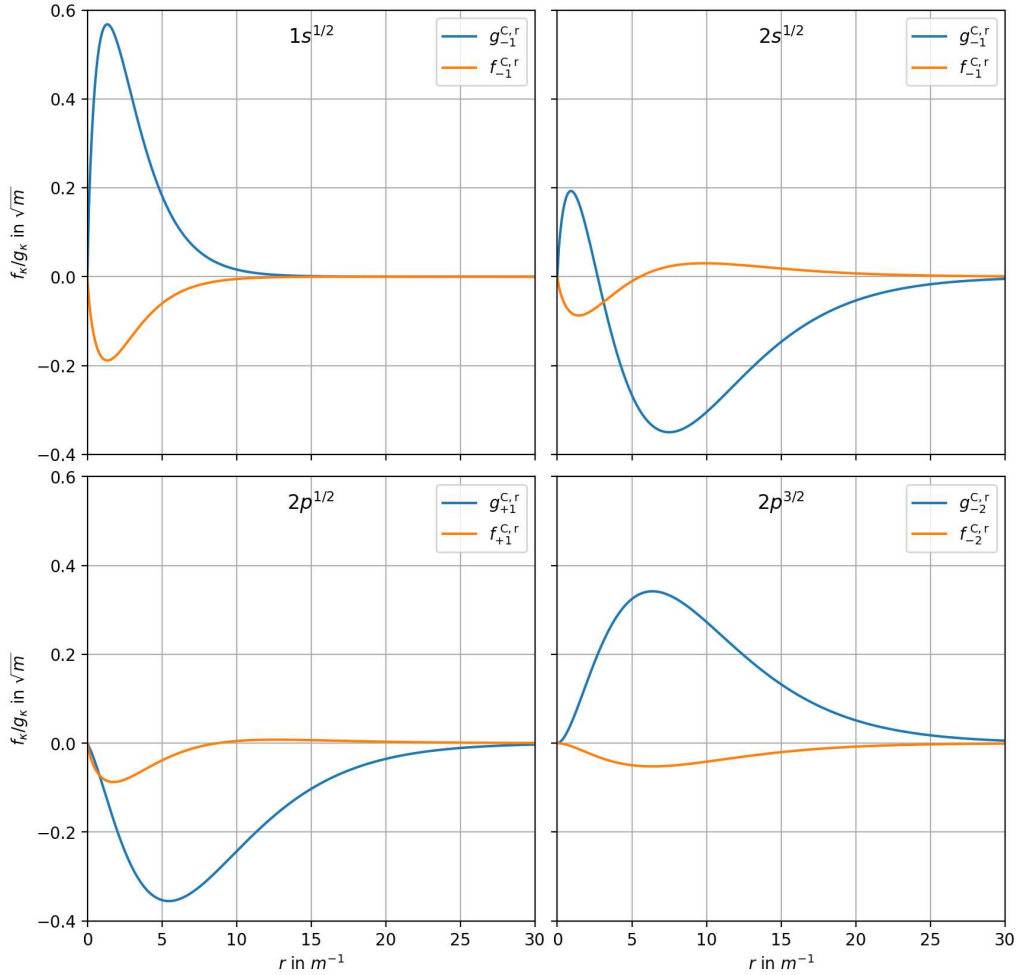

Figure 5.4: Bound-state solutions for a pure Coulomb potential with $Z = 82$.

the continuum solutions are given by

$$\begin{aligned} g_\kappa^{C,r/i}(r) &= -\text{sign}(\kappa)\sqrt{2\frac{E+m_e}{k}}(2kr)^{\pm\rho_\kappa}e^{\frac{\pi}{2}\gamma}\frac{|\Gamma(\pm\rho_\kappa+i\gamma)|}{\Gamma(\pm 2\rho_\kappa+1)} \\ &\quad\times \text{Re}\left[e^{-ikr+i\eta_\kappa^{r/i}}(\pm\rho_\kappa+i\gamma)\,{}_1F_1(\pm\rho_\kappa+1+i\gamma,\pm 2\rho_\kappa+1,2ikr)\right], \\ f_\kappa^{C,r/i}(r) &= \text{sign}(\kappa)\sqrt{2\frac{E-m_e}{k}}(2kr)^{\pm\rho_\kappa}e^{\frac{\pi}{2}\gamma}\frac{|\Gamma(\pm\rho_\kappa+i\gamma)|}{\Gamma(\pm 2\rho_\kappa+1)} \\ &\quad\times \text{Im}\left[e^{-ikr+i\eta_\kappa^{r/i}}(\pm\rho_\kappa+i\gamma)\,{}_1F_1(\pm\rho_\kappa+1+i\gamma,\pm 2\rho_\kappa+1,2ikr)\right], \end{aligned} \tag{5.57}$$

with $k = \left|\vec{k}\right|$ and where we further introduced

$$\begin{aligned} \eta_\kappa^r &= -\frac{\pi}{2}\frac{1+\text{sign}(\kappa)}{2} - \frac{1}{2}\arg\left[\rho_\kappa - \frac{\gamma^2 m_e}{\kappa E} + i\gamma\left(1+\frac{\rho_\kappa m_e}{\kappa E}\right)\right], \qquad \gamma = \alpha_{\text{el}}Z\frac{E}{k} \\ \eta_\kappa^i &= \eta_\kappa^r - \pi - (\eta_\kappa^r + \eta_{-\kappa}^r) = -\eta_{-\kappa}^r - \pi, \end{aligned} \tag{5.58}$$

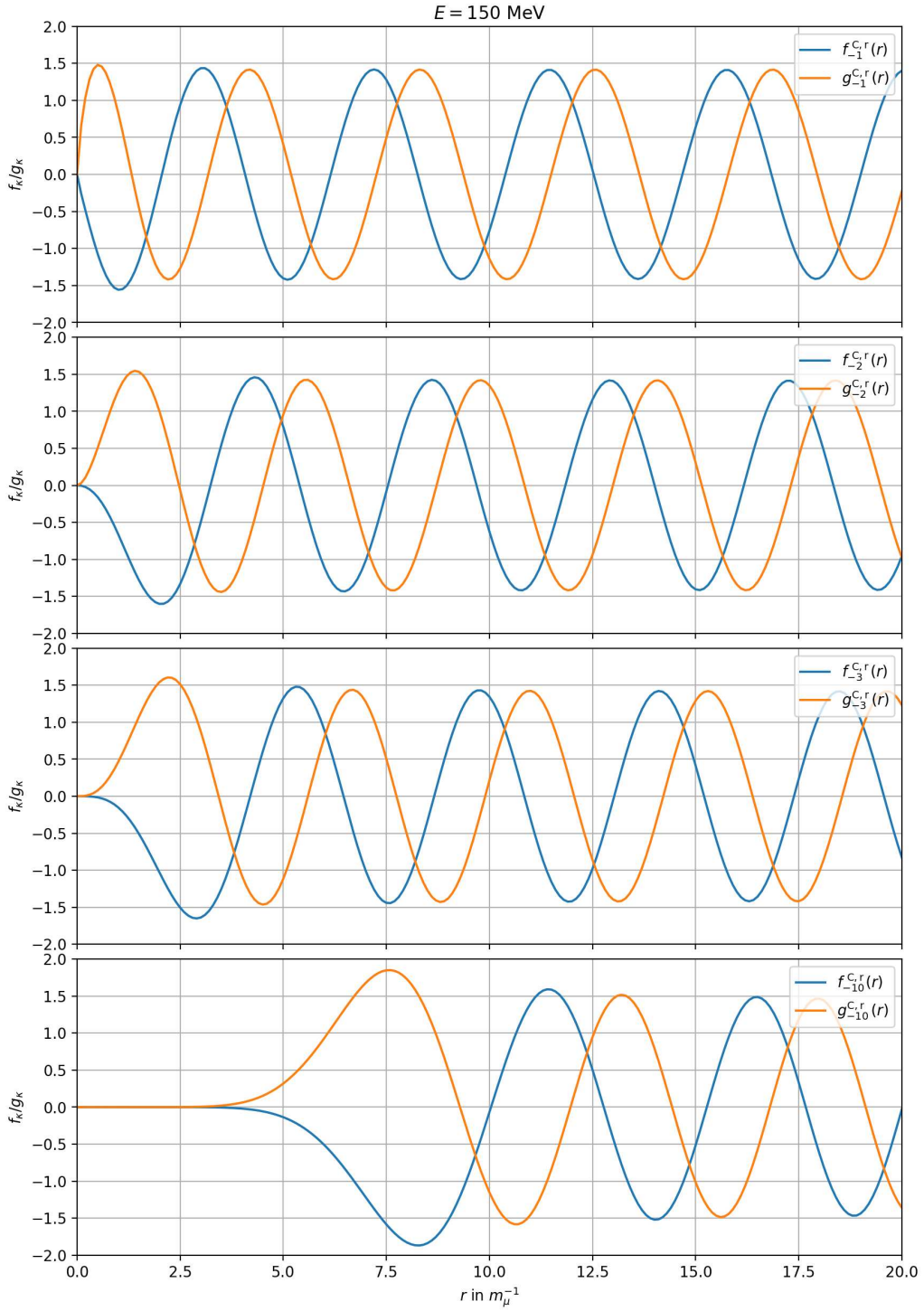

Figure 5.5: Continuum state solutions for $\kappa = -1, -2, -3, -10$ at $E = 150$ MeV for a pure Coulomb potential with $Z = 82$.

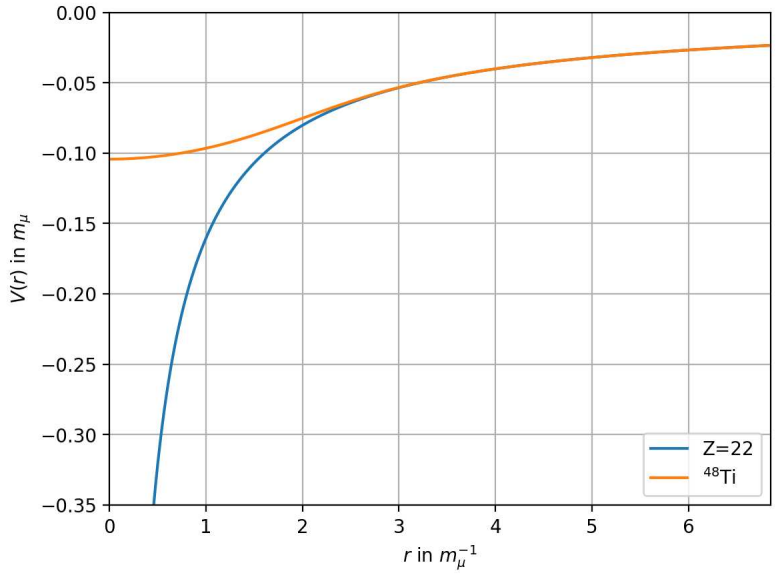

Figure 5.6: Potential for ^{48}Ti in comparison to a pure Coulomb potential with $Z = 22$.

For the continuum solutions the confluent hypergeometric function

$$ {}_1F_1(a, c, z) = \sum_{m=0}^{\infty} \frac{\Gamma(a+m)\Gamma(c)}{\Gamma(c+m)\Gamma(a)} \frac{z^m}{m!} = \frac{\Gamma(c)}{\Gamma(a)\Gamma(c-a)} \int_0^1 dt\, t^{a-1}(1-t)^{c-a-1} e^{zt}, \tag{5.59} $$

needs to be analytically continued to complex arguments, implementations for which in `python` can be found for example in the `mpmath` package.

Continuum solutions for an electron at an energy of $E = 150$ MeV, for $Z = 82$ and for $\kappa = -1, -2, -3$ and -10 can be seen in Fig. 5.5. As shown, far away from the central region of the potential, the plane waves oscillate freely with a fixed amplitude of $\sqrt{2\frac{E+m}{k}} \approx \sqrt{2}$ in line with the normalization condition of Eq. (5.52). The wave function always starts at $r = 0$ with $f_\kappa(r) = g_\kappa(r) = 0$, which with increasing κ rise more and more shallowly, probing less and less of the central region of the potential.

5.3.2 Physical Potential

While, as discussed in the previous subsection, for a pure Coulomb potential Eq. (5.44) is still solvable analytically, for a general physical potential $V(r)$, numerical methods need to be employed. We define a physical potential to fulfill the following boundary conditions

$$ V(r \to 0) = V_0, \qquad V'(r \to 0) = 0, \qquad V(r \to \infty) \to \frac{-Z\alpha_{\text{el}}}{r}, \tag{5.60} $$

hence, asymptotically becoming the Coulomb potential and for $r \to 0$ going flat to a constant (for an example see Fig. 5.6). Besides these conditions, how these two boundary cases are connected, is completely arbitrary. For such a general potential we can use

numerical methods and input for the wave functions at a specific position to stepwise predict the wave function at adjacent locations, using the differential equation. There exists a large number of numerical procedures to solve such initial value problems. We employ either an explicit RUNGE-KUTTA method of order 8 [153] (called `'DOP853'`) or a backwards differentiation formula (BDF) [154] (called `'LSODA'`), both from the `scipy` routine `scipy.integrate.solve_ivp` [155], as lower level procedures emerged to have insufficient accuracy. The second method is significantly fast as it is a wrapper of the `fortran` solver from `odepack` [156].

Since we can fix the normalization after the fact it is sufficient to supply as initial conditions unnormalized functions for $f_\kappa(r)$ and $g_\kappa(r)$ for $r \to 0$. These can be determined by solving Eq. (5.44) in the limit $r \to 0$ analytically. This limit will be different for the Coulomb potential, which even for $r \to 0$ goes like $1/r$, or a physical potential, which will go to a constant $V(r \to 0) = V_0$. For the Coulomb function we find[6]

$$g_\kappa^C(r) = -c\ \frac{\kappa - \rho_\kappa}{Z\alpha_{\text{el}}} r^{\rho_\kappa}, \qquad\qquad f_\kappa^C(r) = -c\ r^{\rho_\kappa}, \tag{5.61}$$

with c the global normalization. The sign is chosen such that for $c > 0$ the "large" component $g_\kappa^C(r)$ is positive in the ground state ($\kappa = -1$) in line with Fig. 5.4.

For a physical potential we have $V(r \to 0) = V_0 = \text{const}$. This results in[7]

$$g_\kappa(r) = c \begin{cases} -\sqrt{\frac{\bar{E}'}{\bar{E}}} r\ j_\kappa(k_0 r) & , \quad \kappa > 0 \\ r\ j_{-\kappa-1}(k_0 r) & , \quad \kappa < 0 \end{cases}, \qquad f_\kappa(r) = c \begin{cases} -r\ j_{\kappa-1}(k_0 r) & , \quad \kappa > 0 \\ -\sqrt{\frac{\bar{E}}{\bar{E}'}} r\ j_{-\kappa}(k_0 r) & , \quad \kappa < 0 \end{cases}, \tag{5.62}$$

where

$$k_0 = \sqrt{(E - V_0)^2 - m^2} = \sqrt{\bar{E}\bar{E}'}, \qquad \bar{E} = E - V_0 - m, \qquad \bar{E}' = E - V_0 + m, \tag{5.63}$$

and $j_\kappa(x)$ denotes the spherical Bessel function. $c > 0$ is again the global normalization factor, with the same choice for the sign as for the Coulomb potential. Since in both cases these functions tend to zero for $r \to 0$, we need to start our evaluation at an infinitesimal $r = \epsilon \cdot (\alpha_{\text{el}} m_\mu)^{-1}$. For low partial waves we achieved good results employing $\epsilon = 10^{-12}$, however as one can see for example in Fig. 5.5, higher partial waves start extremely close to zero. This results in very large fractions between the wave functions at ϵ and asymptotically. For example, in Fig. 5.5 the fraction $\frac{g_{-10}^{C,r}(7.5 m_\mu^{-1})}{g_{-10}^{C,r}(10^{-12}(\alpha_{\text{el}} m_\mu)^{-1})}$ is of order 10^{100}. To retain the necessary information in a numerical procedure that can span such large numerical ranges, it becomes necessary to increase ϵ and to adjust c such that all evaluated numbers stay within the range of the precision of the programming language. Finally, even with fine-tuning these numbers, this limits the number of partial waves that can be calculated numerically, without additional tricks (see also Sec. 5.4).

For the continuum state solutions, for a finitely ranged potential, the wave functions are asymptotically free. This is, apart from an additional r-dependent phase shift (see

[6] For a derivation we refer to App. B.2

[7] For a derivation we refer to App. B.2

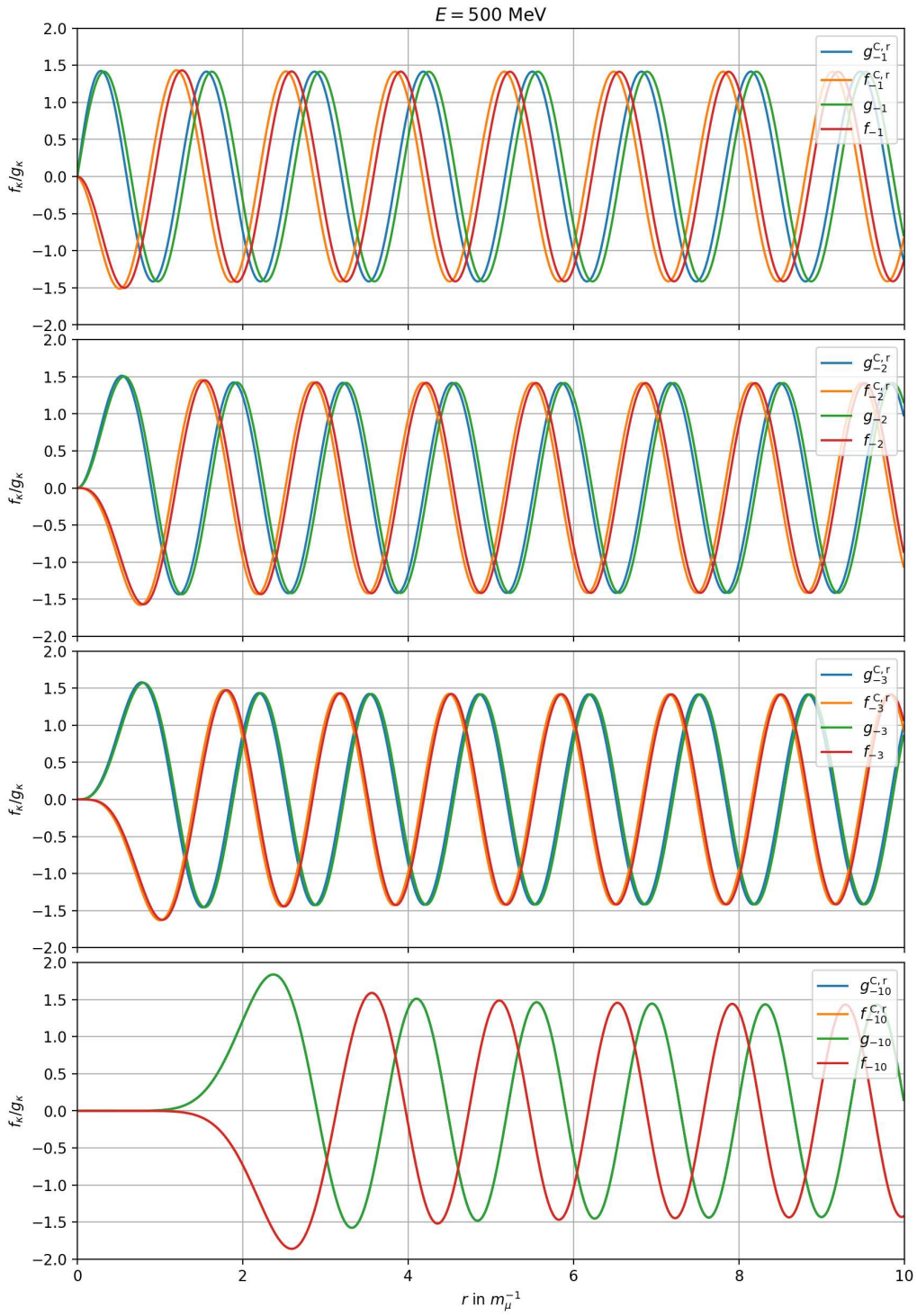

Figure 5.7: Continuum state solutions for $\kappa = -1, -2, -3, -10$ at $E = 500$ MeV for ^{48}Ti and a pure Coulomb potential with $Z = 22$.

$\kappa = -1$					$\kappa = +1$					$\kappa = -2$				
#	n	l	j	name	#	n	l	j	name	#	n	l	j	name
1.	1	0	$\frac{1}{2}$	$1s^{\frac{1}{2}}$	1.	2	1	$\frac{1}{2}$	$2p^{\frac{1}{2}}$	1.	2	1	$\frac{3}{2}$	$2p^{\frac{3}{2}}$
2.	2	0	$\frac{1}{2}$	$2s^{\frac{1}{2}}$	2.	3	1	$\frac{1}{2}$	$3p^{\frac{1}{2}}$	2.	3	1	$\frac{3}{2}$	$3p^{\frac{3}{2}}$
3.	3	0	$\frac{1}{2}$	$3s^{\frac{1}{2}}$	3.	4	1	$\frac{1}{2}$	$4p^{\frac{1}{2}}$	3.	4	1	$\frac{3}{2}$	$4p^{\frac{3}{2}}$

Table 5.1: Associating the found bound states with quantum numbers. # refers to the ordering by energy for each κ.

Eq. (5.72)), also true for potentials, which go asymptotically like the Coulomb potential. Thus, except for a phase shift, the asymptotic behavior is the same between a Coulomb potential and a physical one. This phase shift, and in particular its difference to the Coulomb one, contains a lot of information about the interaction of the particle with the nucleus. In Fig. 5.7 the Coulomb solution is shown in comparison to a ^{48}Ti parameterization from Ref. [134] at $E = 500$ MeV for $\kappa = -1, -2, -3$ and -10. One sees clearly, that the main difference is in the phase shifts, and how its difference to the Coulomb solution gets smaller with higher partial waves, nicely illustrating that with increasing $|\kappa|$ the wave function probes less and less of the inner structure of the nucleus. At some point r_c outside the nucleus, where we may assume $V(r > r_c) = \frac{-\alpha_{\text{el}} Z}{r}$, we can match a linear combination of regular and irregular solutions of the Coulomb potential for a valid high-energy continuation. Based on these we can also find the global normalization as elucidated in App. B.2. In practice, r_c can be chosen quite low, which then also limits the amount of numerical calculations that need to be done to reach r_c. It is usually sufficient to choose $r_c \sim 5 m_\mu^{-1}$ as can be seen in Fig. 5.6.

While for the continuum solutions, we can simply solve the differential equation system for a given energy E, for the bound-state solutions we first need to identify existing energy values. Instead of solving the (potentially) infinitely dimensional eigenvalue problem by numerically diagonalizing the corresponding infinite-dimensional matrix, we can scan over energy values starting from $E - m = V_0 < 0$ going up. For energies that are not eigenvalues, the resulting wave functions will asymptotically diverge. However, sign flips in this divergent behavior indicate bound-state solutions in between, which then can be systematically enclosed. Ordering the found bound states by energy makes it possible to associate the corresponding atomic states, which is shown exemplarily for the first few states in Tab. 5.1. Furthermore, Fig. 5.8 shows the first few energy levels for a ^{48}Ti parameterization from Ref. [134] in comparison to the Coulomb potential. One sees clearly how the s-orbitals see the biggest difference in energy, as they probe the central region of the potential a lot more than higher partial waves. Even with the most precise energy value sooner or later the wave functions will diverge for numerical reasons. To get a solution that is integrable until $r \to \infty$, we match an asymptotic exponential decay at $r = r_c \sim 2000/(Zm)$ onto our solution. This is deemed sufficient for these low-lying states but might need to be adjusted for higher energy states. Since it is not trivial to

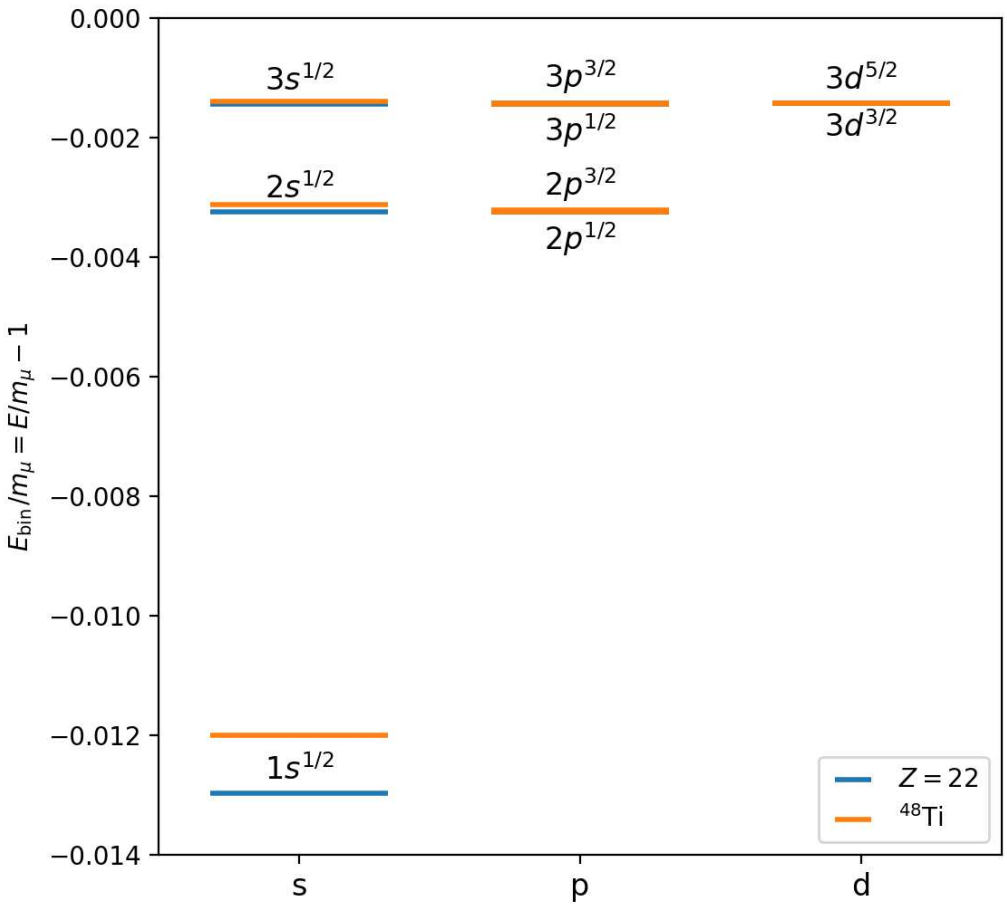

Figure 5.8: Energy levels for ^{48}Ti until $n = 3$ and for a pure Coulomb potential with $Z = 22$.

choose the increments in which one scans across the energies, as well as at which point to evaluate $f_\kappa(r)$ and $g_\kappa(r)$ which is sufficiently asymptotic to indicate the sign of the asymptotic behavior, it makes sense to benchmark this behavior comparing to the pure Coulomb potential. For the ground state, we usually choose $\sim 50 - 100$ increments and $r_{\text{inf}} \sim 100000/(Zm)$, but for higher partial waves these might need to be adjusted. If we compare our explicit numerical calculation of the Coulomb potential with the analytical one, the two plots are indistinguishable with differences below 10^{-6}. For light nuclei one can expect, the bound-state wave functions to be quite similar to the Coulomb ones. Comparing the ^{48}Ti parameterization, with the pure Coulomb potential at $Z = 20$ results in Fig. 5.9, where one can see how close these solutions are together and that the sign conventions are in line with Eq. (5.48).

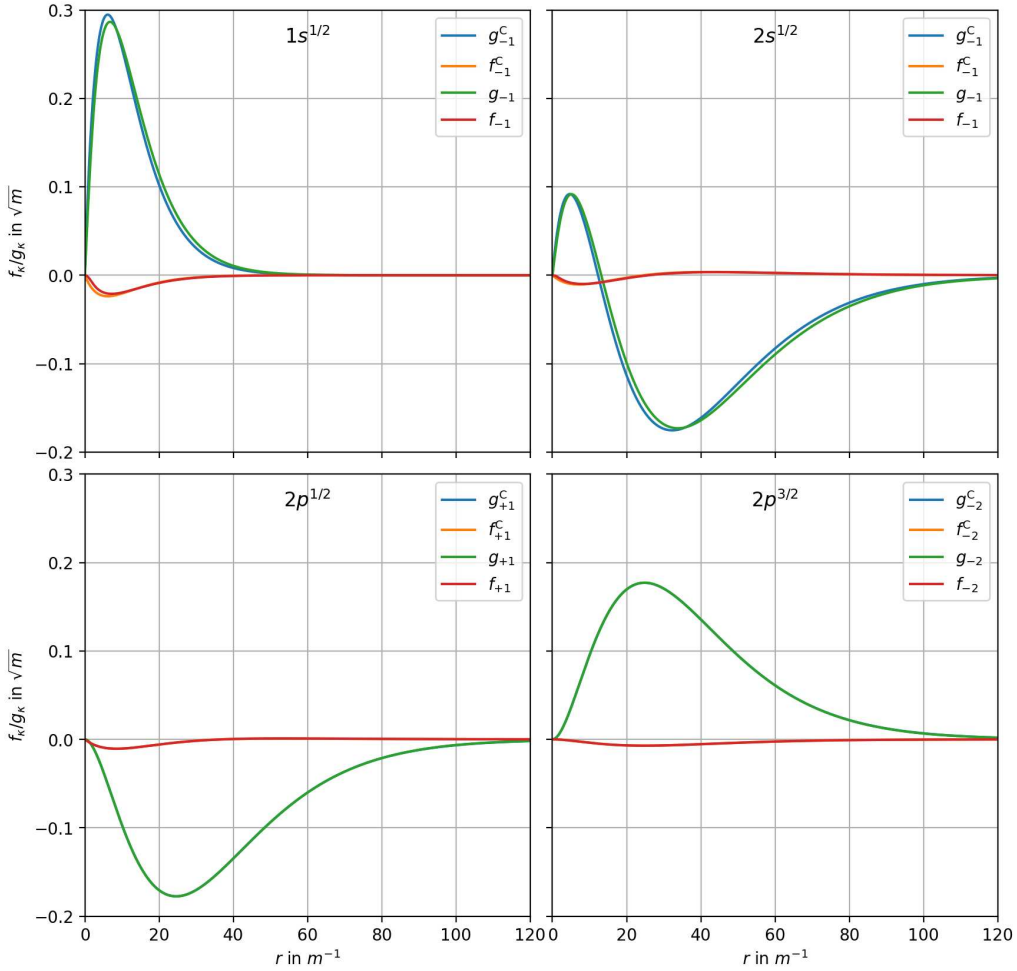

Figure 5.9: Bound-state solutions for ^{48}Ti and a pure Coulomb potential with $Z = 22$.

5.4 Phase-Shift Model

As already seen in the previous section, the phase shift of the continuum solution contains information about the nucleus potential. In fact, the elastic scattering cross section for electron-nucleus scattering can be deduced solely from these phase shifts. This procedure falls under the name of "phase-shift model". As this utilizes the numerically calculated wave functions in the vicinity of the nucleus, this goes beyond the PWBA as described in Sec. 5.1, and includes Coulomb distortion effects. In the following, we will review the main features and challenges of implementing the phase-shift model. The following remarks closely follow the conventions and discussions of Ref. [152], while some adjustments for consistency and readability were made. Crosschecks were performed and further inputs were taken in particular from Refs. [88,123,157–159]. Note that while some of the equations are quoted with explicit m_e dependence, in practice we set $m_e = 0$ in the calculations.

The phase-shift model describes the elastic scattering cross section for a spherically symmetric nucleus in terms of the phase shifts of the different partial waves, which can be deduced numerically using the solutions of the Dirac equation found in the previous

section. In the relativistic limit ($m_e \to 0$) the cross-section takes the form

$$\frac{\mathrm{d}\sigma}{\mathrm{d}\Omega} = \big|A_\mathrm{s}(\theta)\big|^2 + \big|A_\mathrm{sf}(\theta)\big|^2 \overset{m_e=0}{=} \Big(1 + \tan^2\frac{\theta}{2}\Big)\big|A_\mathrm{s}(\theta)\big|^2, \tag{5.64}$$

with

$$\begin{aligned} A_\mathrm{s}(\theta) &= \frac{1}{2ik}\sum_{\kappa>0} \kappa\big[e^{2i\delta_\kappa}P_\kappa(\cos\theta) + e^{2i\delta_{-\kappa}}P_{\kappa-1}(\cos\theta)\big], \\ A_\mathrm{sf}(\theta) &= -\frac{\sin\theta}{2ik}\sum_{\kappa>0} \big[e^{2i\delta_\kappa}P'_\kappa(\cos\theta) - e^{2i\delta_{-\kappa}}P'_{\kappa-1}(\cos\theta)\big], \end{aligned} \tag{5.65}$$

where P_κ are the Legendre polynomials, δ_κ the phase shifts, obtained from the solution of the Dirac equation (fulfilling $\delta_\kappa = \delta_{-\kappa}$ in the $m_e = 0$ limit), and $k = |\vec{k}|$ denotes the electron momentum. We may rewrite Eq. (5.65) as

$$A_\mathrm{s} = \frac{1}{2ik}\sum_{\kappa\geq 0} a_\kappa P_\kappa(\cos\theta), \qquad a_\kappa = \kappa e^{2i\delta_\kappa} + (\kappa+1)e^{2i\delta_{-(\kappa+1)}} =: a_\kappa^{(0)}. \tag{5.66}$$

This series does not converge easily and would generally require an infinite amount of partial waves. However, we may improve convergence by factoring out poles of $(1-\cos\theta)^{-1}$ responsible for the poor convergence by redefining

$$(1-\cos\theta)^m 2ikA_\mathrm{s}(\theta) = \sum_{\kappa\geq 0} a_\kappa^{(m)} P_\kappa(\cos\theta), \tag{5.67}$$

which implies

$$a_\kappa^{(i+1)} = a_\kappa^{(i)} - \frac{\kappa+1}{2\kappa+3}a_{\kappa+1}^{(i)} - \frac{\kappa}{2\kappa-1}a_{\kappa-1}^{(i)}. \tag{5.68}$$

In the large-κ limit, δ_κ reduces to the Coulomb phase shift, which behaves according to

$$\delta_\kappa^C \to -\gamma\log|\kappa|, \qquad \gamma = \alpha_\mathrm{el} Z\frac{E}{k}. \tag{5.69}$$

Based on this expression, one can show that

$$\left|\frac{a_\kappa^{(1)}}{a_\kappa^{(0)}}\right| = \frac{2\gamma^2}{\kappa^2} + \mathcal{O}\big(\kappa^{-3}\big), \tag{5.70}$$

and additional steps further improve the convergence, so that after a few reductions the series converges rapidly. We choose $m = 3$, in which case it is sufficient to calculate between 10 to 20 partial waves, as nicely illustrated in Fig. 5.10. Note that in the limit of $m_e = 0$ it follows that $\delta_\kappa = \delta_{-\kappa}$, which cuts the number of phase extractions that need to be performed in half.

The phase shifts δ_κ are extracted from the asymptotic behavior of the numerical solutions of the Dirac equation. For a potential that asymptotically approaches the Coulomb potential

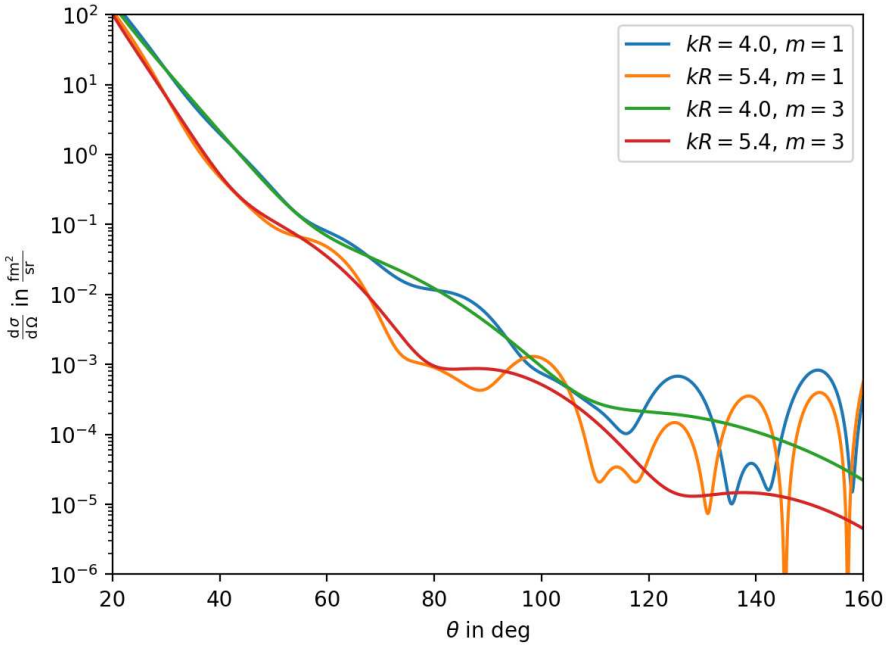

Figure 5.10: Cross section comparison for reductions with $m = 1$ and $m = 3$ including partial waves for $|\kappa| \leq 15$ for two uniform charge densities (see Eq. (5.15)) for Gold ($Z = 79$) [157] at 150 MeV.

$V(r) \to -\alpha_{\mathrm{el}} Z/r$, we have the following asymptotic plane-wave solutions

$$\begin{aligned} g_\kappa(r) &\to -\mathrm{sign}(\kappa)\sqrt{2\frac{E+m_e}{k}}\cos\left[kr + \tilde{\delta}_\kappa(r)\right], \\ f_\kappa(r) &\to \quad \mathrm{sign}(\kappa)\sqrt{2\frac{E-m_e}{k}}\sin\left[kr + \tilde{\delta}_\kappa(r)\right]. \end{aligned} \tag{5.71}$$

Since electromagnetic interactions are long-ranged, the potential never goes exactly to zero, and the remaining asymptotic $1/r$ behavior of the potential results in an r-dependent phase $\tilde{\delta}_\kappa(r)$. Since for a physical potential, this asymptotic behavior is always Coulombic, the r-dependent part of $\tilde{\delta}_\kappa$ is known analytically and given by

$$\tilde{\delta}_\kappa(r) = \delta_\kappa^{1/r}(r) + \delta_\kappa, \qquad \delta_\kappa^{1/r}(r) = \gamma\log(2kr) - (l+1)\frac{\pi}{2}, \tag{5.72}$$

which also defines δ_κ as used in Eq. (5.65). As already pointed out using Fig. 5.7, for high κ the phase shifts become the Coulomb phase shifts, which can be calculated analytically by considering Eq. (5.57) for large r. Hence, it makes sense to further separate the phase shift into several components based on the analytically known solution for a pure Coulomb potential according to

$$\delta_\kappa = \delta_\kappa^{C,r} + \bar{\delta}_\kappa. \tag{5.73}$$

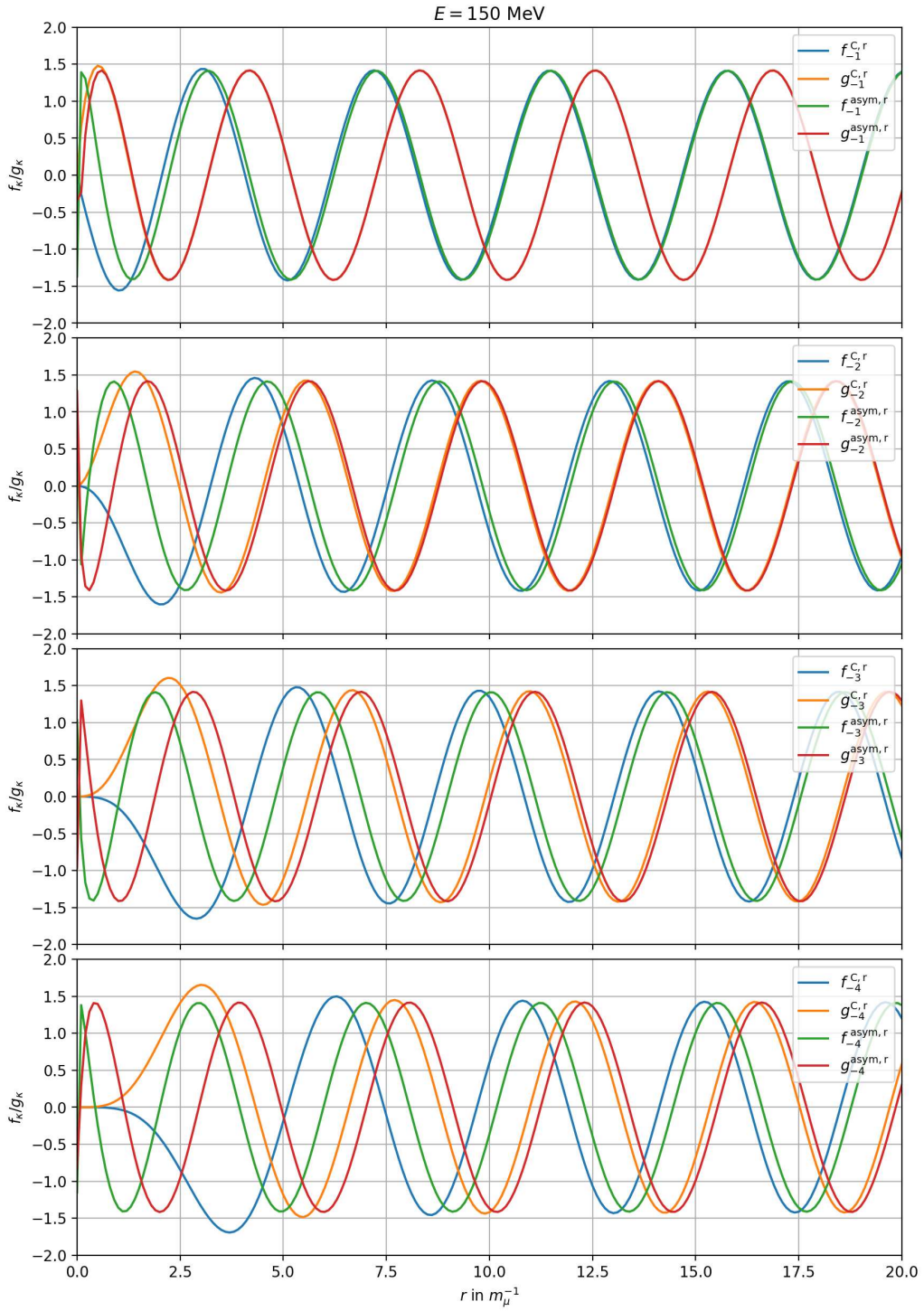

Figure 5.11: Continuum state solutions for $\kappa = -1, -2, -3, -4$ at $E = 150$ MeV for a pure Coulomb potential with $Z = 82$, in comparison to the expected asymptotic, according to Eq. (5.71).

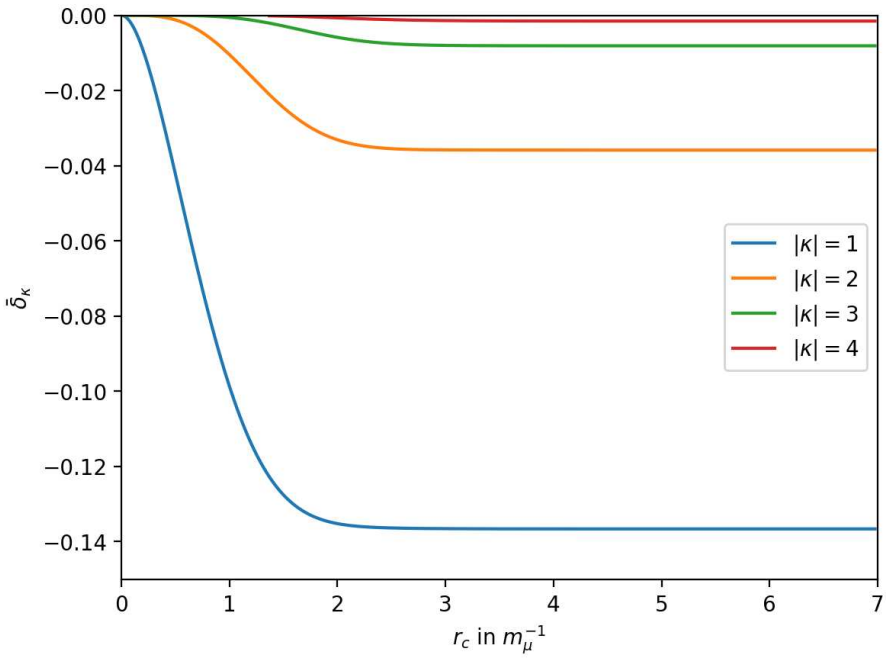

Figure 5.12: Cutoff dependence of $\bar{\delta}_\kappa$ for the first few partial waves for ^{48}Ti at 150 MeV.

The Coulomb phase shifts corresponding to the regular (r) and irregular (i) solutions are given as

$$\delta_\kappa^{C,r/i} = (l+1)\frac{\pi}{2} - \arg\Gamma(\pm\rho_\kappa + i\gamma) + \eta_\kappa^{r/i} \mp \frac{\pi}{2}\rho_\kappa, \tag{5.74}$$

with $\eta_\kappa^{r,i}$ as defined in Eq. (5.58), $\Gamma(x)$ is the Euler Γ function and r/i correspond to upper/lower signs, respectively. The difference between regular and irregular phase shifts takes the form

$$\begin{aligned}\theta_\kappa &= \tilde{\delta}_\kappa^{C,i} - \tilde{\delta}_\kappa^{C,r} = \delta_\kappa^{C,i} - \delta_\kappa^{C,r} \\ &= \pi\big(\rho_\kappa - |\kappa|\big) - \arctan\Big[\tan\Big(\pi\big(|\kappa| - \rho_\kappa\big)\Big)\coth(\pi\gamma)\Big] - \frac{\pi}{2} - \arg(\rho_\kappa + i\gamma) - (\eta_\kappa^r + \eta_{-\kappa}^r).\end{aligned} \tag{5.75}$$

The phase-shift difference $\bar{\delta}_\kappa$ tends to zero for large κ, as with increasing partial waves less of the central region of the potential is probed. Thus, it is usually sufficient to extract $\bar{\delta}_\kappa$ for a dozen partial waves. In theory, it would be enough to numerically calculate the wave functions until we reach the asymptotic regime and Eq. (5.71) is a good approximation. Then the phase δ_κ could be extracted by simply fitting a parameterization according to Eq. (5.71). Unfortunately, this becomes more difficult with higher partial waves, as the region where the wave function becomes asymptotic moves to higher radii. Even with very precise numerical methods one quickly reaches the point where numerical uncertainties dominate the extracted phase with this procedure. How fast the asymptotic region moves to large r is nicely illustrated in Fig. 5.11, where we show the asymptotic solutions for the analytically known Coulomb potential.

Fortunately, we can also extract the phase at a much earlier κ-independent point by employing the analytically known solutions for a pure Coulomb potential. Once we are at

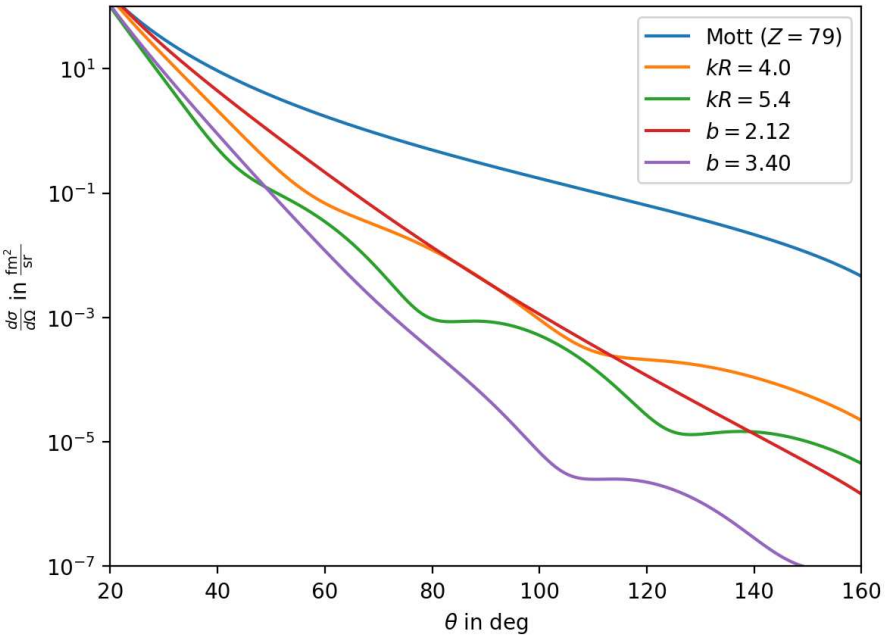

Figure 5.13: Cross section, calculated with the phase-shift model for a selection of toy model charge density parameterizations for Gold from Ref. [157] in comparison to the pure Mott cross section at 150 MeV.

a large enough r that the potential becomes the Coulomb potential, $V(r \geq r_c) = -\alpha_{\text{el}} Z/r$, the wave function is given by a linear combination of the regular and irregular solutions, and we can match

$$\begin{aligned} g_\kappa(r \geq r_c) &= A_\kappa g_\kappa^{C,r}(r \geq r_c) + B_\kappa g_\kappa^{C,i}(r \geq r_c), \\ f_\kappa(r \geq r_c) &= A_\kappa f_\kappa^{C,r}(r \geq r_c) + B_\kappa f_\kappa^{C,i}(r \geq r_c), \end{aligned} \tag{5.76}$$

where $g_\kappa^{C,r/i}(r)$ are the explicit regular and irregular analytical solutions to the Dirac equation for a pure Coulomb potential as given in Eq. (5.57). It follows

$$\frac{A_\kappa}{B_\kappa} = -\frac{f_\kappa^{C,i}(r_c) - g_\kappa^{C,i}(a)\frac{f_\kappa(r_c)}{g_\kappa(r_c)}}{f_\kappa^{C,r}(r_c) - g_\kappa^{C,r}(r_c)\frac{f_\kappa(r_c)}{g_\kappa(r_c)}}, \tag{5.77}$$

which is independent of r and independent of the (global) normalization c of f_κ and g_κ. We may use this knowledge to extract $\bar{\delta}_\kappa$ in the following way

$$\tan\left(\bar{\delta}_\kappa + \Delta_\kappa^{r_c}\right) = \frac{\frac{A_\kappa}{B_\kappa}\sin(\Delta_\kappa^{r_c}) + \sin(\theta_\kappa + \Delta_\kappa^{r_c})}{\frac{A_\kappa}{B_\kappa}\cos(\Delta_\kappa^{r_c}) + \cos(\theta_\kappa + \Delta_\kappa^{r_c})}, \qquad \Delta_\kappa^{r_c} = kr_c + \tilde{\delta}_\kappa^{C,r}, \tag{5.78}$$

which follows by inserting Eq. (5.71) into Eq. (5.76) and solving for $\bar{\delta}_\kappa$. Moreover, while Eq. (5.71) is only valid when f_κ and g_κ become asymptotic, we may extract A_κ/B_κ at the a lot smaller and κ-independent point $r = r_c$. As already illustrated in Fig. 5.6, this happens quite early and an examination of the dependence of $\bar{\delta}_\kappa$ on r_c as shown in Fig. 5.12, confirms this. We choose usually $r_c \approx 5m_\mu$, except for the FB parameterization which has

			this work			Ref. [157]	
$\lvert\kappa\rvert$	δ_c	θ_c	$\bar{\delta}^1_\kappa$	$\bar{\delta}^2_\kappa$	$\bar{\delta}^c_\kappa$	$\bar{\delta}^1_\kappa$	$\bar{\delta}^2_\kappa$
1	0.40734	−1.17382	−0.85814	−0.71689	$-1.3 \cdot 10^{-8}$	−0.85820	−0.71683
2	−0.23797	−0.54727	−0.27138	−0.18790	$-7.4 \cdot 10^{-10}$	−0.27143	−0.18795
3	−0.53303	−0.36073	−0.07631	−0.04845	$-5.9 \cdot 10^{-10}$	−0.07633	−0.04846
4	−0.72658	−0.26951	−0.01495	−0.01065	$-5.9 \cdot 10^{-10}$	−0.01494	−0.01064
5	−0.87096	−0.21522	−0.00199	−0.00199	$-5.8 \cdot 10^{-10}$	−0.00199	−0.00199
6	−0.98622	−0.17918	−0.00019	−0.00032	$-3.4 \cdot 10^{-10}$	−0.00017	−0.00030
7	−1.08216	−0.15349	−0.00001	−0.00005	$-1.6 \cdot 10^{-10}$	−0.00001	−0.00004
8	−1.16436	−0.13426	−0.00000	−0.00001	$-1.7 \cdot 10^{-13}$	−0.00000	−0.00000
9	−1.23627	−0.11931	−0.00000	−0.00000	$-8.9 \cdot 10^{-16}$	−0.00000	−0.00000

Table 5.2: Phase-shift differences at 150 MeV in comparison to Ref. [157].

a natural cutoff, where the charge density becomes zero and where Eq. (5.76) becomes exact.

As an example for the resulting cross sections of such a procedure, we show in Fig. 5.13, these for a selection of toy model charge density parameterizations for Gold from Ref. [157].

5.4.1 Benchmarking

For the sum in Eq. (5.65) to properly converge and result in a precise scattering cross section, δ_κ needs to be extracted with high precision and in particular $\bar{\delta}_\kappa$ needs to vanish for $\kappa \to \infty$. This would be quite difficult to do numerically exactly, in particular, if we tried to extract δ_κ directly since higher partial waves get increasingly expensive and become asymptotic for larger r. Hence, considering $\bar{\delta}_\kappa$ as the difference to the Coulomb phase shift is already a huge improvement in precision. In practice, this means that only the first few partial waves, where on numerical level $\bar{\delta}_\kappa > 0$, need to be calculated, and the rest can be filled up with the analytical solutions for the Coulomb potential. Moreover, extracting the phase at r_c instead of the asymptotic region further improves the quality of the extracted phases and the speed of the numerical calculation. Finally, the necessary precision of the numerical algorithm for solving the initial value problem needs to be assessed. We set the tolerance for the numerical precision on `atol` $= 10^{-12}$, `rtol` $= 10^{-10}$ for the absolute and relative precision, respectively. For lower partial waves we start with $c = 1$ in Eq. (5.62), where for $\kappa > 7$ we enlarge c by $10^{(\kappa-7)(\kappa-7+1)}$. We also incorporate the option to reduce `atol`, `rtol` by the same value,[8] however, this makes higher partial waves increasingly expensive and is not necessary if the number of partial waves that are calculated is limited enough. We further set $\epsilon = \sqrt[|\kappa|]{10^{-12}}$, in accordance with the fact that the initial values scale with $\epsilon^{|\kappa|}$, such that they do not become too small. This is capped at $\epsilon = 10^{-3}$, such that $V(\epsilon) \approx V(0) = V_0$ remains a good approximation.

As a benchmark for our phase extraction, we can numerically extract the phases for the

[8] From the routine, `rtol` is capped at a minimum of $3 \cdot 10^{-14}$.

κ	$\mathrm{Re}\,(a_\kappa)$	$\mathrm{Im}\,(a_\kappa)$	$\mathrm{Re}\,(a_\kappa^{(3)})$	$\mathrm{Im}\,(a_\kappa^{(3)})$
0	0.62036	−0.78432	−0.00818	−0.00296
1	1.66933	−2.48715	−0.02188	0.01262
2	2.08364	−4.51877	0.04463	0.03160
3	1.38516	−6.80055	0.04522	−0.02999
4	−0.52058	−8.90815	−0.05041	−0.04458
5	−3.21872	−10.44519	−0.03354	0.01648
6	−6.26281	−11.32436	0.01122	0.01748
7	−9.41450	−11.61282	0.00957	0.00188
8	−12.55896	−11.39237	0.00256	−0.00094
9	−15.63034	−10.73425	0.00056	−0.00060
10	−18.58666	−9.69959	0.00017	−0.00033
11	−21.40064	−8.34089	0.00007	−0.00020
12	−24.05481	−6.70323	0.00003	−0.00013
13	−26.53847	−4.82547	0.00001	−0.00009
14	−28.84560	−2.74118	0.00000	−0.00006
15	−30.97351	−0.47945	−0.00000	−0.00004
16	−32.92191	1.93438	−0.00000	−0.00003
17	−34.69214	4.47816	−0.00000	−0.00002
18	−36.28677	7.13251	−0.00000	−0.00002
19	−37.70921	9.88036	−0.00000	−0.00001
20	−38.96345	12.70664	−0.00000	−0.00001
21	−40.05388	15.59805	−0.00000	−0.00001
22	−40.98512	18.54278	−0.00000	−0.00001
23	−41.76198	21.53032	−0.00000	−0.00000
24	−42.38929	24.55133	−0.00000	−0.00000
25	−42.87192	27.59746	−0.00000	−0.00000
26	−43.21471	30.66125	−0.00000	−0.00000
27	−43.42242	33.73602		
28	−43.49973	36.81577		
29	−43.45120	39.89513		

Table 5.3: Prefactors a_κ and $a_\kappa^{(3)}$ for a uniform parameterization (see Eq. (5.15)) with $kR = 4.0$ of Gold ($Z = 79$) [157] at 150 MeV.

Coulomb potential, which should result in $\bar{\delta}_\kappa = 0$. Furthermore, we compare exemplary values for $\bar{\delta}_\kappa$ from Ref. [157] for two example parameterizations for the charge densities parameterizations of Gold as Uniform ($kR = 4.0$) and Gaussian ($b = 2.12$). The calculated phase-shift differences are shown in Tab. 5.2, and are quite consistent with the results from Ref. [157]. The remaining Coulomb phase-shift differences are at most at 10^{-8}, which gives an upper bound on what precision in principle can be expected for these values. In the final calculation, we set $\bar{\delta}_\kappa = 0$ and do not proceed to calculate further values numerically, once we hit $\delta_\kappa < 10^{-7}$, which usually happens within the first 15 partial waves.

Doing these calculations for $m_e \neq 0$ can be a lot more expensive and a lot less precise, among other reasons, since now $\delta_\kappa \neq \delta_{-\kappa}$. In this context, it makes sense to calculate the

phase-shift differences always also for a pure Coulomb potential and subtract this value to reduce systematic effects. As shown, for $m_e = 0$ however, this is not necessary.

For illustrative purposes and as a further benchmark for others, we list the values for a_κ and $a_\kappa^{(3)}$ for the uniform parameterization of Gold ($kR = 4.0$) from Ref. [157] in Tab. 5.3. One sees how the prefactors a_κ without any subtraction do not converge while for $m = 3$ they go to zero within the first 15 to 20 partial waves.

In Chap. 6 we also demonstrate our successful utilization of the phase-shift model to describe elastic scattering data for several nuclei and in turn extract their charge densities.

5.5 Recoil Effects

We can incorporate the leading (kinematic) recoil effects by boosting our reference frame from the Lab frame into the CMS frame, then doing our calculation, and finally transforming our result back into the Lab frame as discussed in Ref. [160]. For a nucleus of mass M this means in practice that we transform our energies E and angles θ to the CMS frame via

$$E_{\mathrm{CMS}} = E\left[1 - \frac{E}{m_M} + \mathcal{O}\left(\frac{E^2}{m_M^2}\right)\right], \qquad \theta_{\mathrm{CMS}} = \theta + \frac{E}{m_M}\sin\theta + \mathcal{O}\left(\frac{E^2}{m_M^2}\right), \tag{5.79}$$

before employing the phase-shift model. The resulting cross section is then transformed back to the Lab frame via

$$\left(\frac{\mathrm{d}\sigma}{\mathrm{d}\Omega}\right)_{\mathrm{Lab}} = \left(\frac{\mathrm{d}\sigma}{\mathrm{d}\Omega}\right)_{\mathrm{CMS}}\left[1 + 2\frac{E}{M}\cos\theta + \mathcal{O}\left(\frac{E_e^2}{M^2}\right)\right]. \tag{5.80}$$

In the end, the effect of the recoil correction proves rather small, with E/M for the considered nuclei at most of the percent order. Furthermore, dynamic recoil effects have been shown to be even more suppressed [160].

5.6 Distorted-Wave Born Approximation

For nuclei with non-zero spin J, the elastic scattering cross section also depends on higher (non-spherical) multipole contributions to the charge density as well as magnetic interactions. While these are generally suppressed in comparison to the leading spherically symmetric contributions from the charge density, such higher-order corrections do become relevant in the vicinity of the minima of the $L = 0$ charge form factor. To include these higher multipoles one may use the DWBA, which amounts to a generalization of the phase-shift model to arbitrary spin, and has found applications primarily to inelastic scattering. The main assumption is that Coulomb-distortion effects are restricted to the spherically symmetric charge density, which still defines the potential that enters the solution of the Dirac equation, however, the resulting Coulomb corrections then affect all

multipoles, not just the $L = 0$ ones. The interaction can be characterized by the following Hamiltonian[9]

$$H = \frac{e}{4\pi} \int \mathrm{d}^3 r \int \mathrm{d}^3 r' \, \frac{\rho(\vec{r})\rho_e(\vec{r'}) - \vec{j}(\vec{r}) \cdot \vec{j}_e(\vec{r'})}{|\vec{r} - \vec{r'}|}, \tag{5.81}$$

where $\vec{j}$ ($\vec{j}_e$) and $\vec{j}$ ($\vec{j}_e$) are the charge density and current of the nucleus (electron). The wave functions of the incoming and outgoing electron ψ_i and ψ_f enter via

$$\rho_e(\vec{r}) = -e\psi_f^\dagger \psi_i, \qquad \vec{j}_e(\vec{r}) = -e\psi_f^\dagger \gamma^0 \vec{\gamma} \psi_i. \tag{5.82}$$

The expectation value of the Hamiltonian interacting with a nucleus of total spin J and initial (final) spin state M_i (M_f) is given by

$$\langle JM_i | \, H \, | JM_f \rangle = \sum_{LM} \frac{\sqrt{2L+1}}{\sqrt{2J+1}} \langle JM_i, LM | JM_f \rangle \, H_{LM}. \tag{5.83}$$

To derive the CMS cross-section, we write

$$\begin{aligned} \frac{\mathrm{d}\sigma}{\mathrm{d}\Omega} &= \frac{k'}{k} \frac{|\overline{\mathcal{M}}_{\mathrm{rel}}|^2}{64\pi^2 M^2} = \frac{k'}{k} \frac{(2m_e 2M)^2}{64\pi^2 M^2} \frac{1}{2(2J+1)} \sum_{m,m'} \sum_{M_i, M_f} \left| \langle JM_i | \, H \, | JM_f \rangle \right|^2 \\ &= \frac{1}{4\pi^2} \frac{m_e^2}{2J+1} \frac{k'}{k} \frac{1}{2} \sum_{m,m'} \sum_{L,M} |H_{LM}|^2, \end{aligned} \tag{5.84}$$

where the first identity gives the cross-section in the standard relativistic normalization of states, $\langle \vec{p'} | \vec{p} \rangle = (2\pi)^3 2E_p \delta^{(3)}(\vec{p} - \vec{p'})$, with spin-averaged squared matrix element $|\overline{\mathcal{M}}_{\mathrm{rel}}|^2$ and initial (final) CMS momentum $k = |\vec{k}|$ ($k' = |\vec{k'}|$). We neglected corrections to the CMS squared energy $s = M^2$, and, by the same reasoning, the second step amounts to a non-relativistic normalization for the nuclear states, $\langle \vec{p'} | \vec{p} \rangle = (2\pi)^3 \delta^{(3)}(\vec{p} - \vec{p'})$, while the electron states are normalized to $\langle \vec{p'} | \vec{p} \rangle = (2\pi)^3 \delta^{(3)}(\vec{p} - \vec{p'}) E/m_e$. The spin average extends over the spin projections of the electron $m, m' = \pm 1/2$ and the nuclear spins $-J \leq M_i, M_f \leq J$, where the simplification in the last line follows from the orthogonality of the Clebsch-Gordan coefficients $\langle JM_i, LM | JM_f \rangle$.

Employing for ψ_i and ψ_f the wave functions numerically found by solving the Dirac equation and separating radial and angular components of the integral, the cross-section for elastic electron-nucleus scattering can be written as

$$\frac{\mathrm{d}\sigma}{\mathrm{d}\Omega} = \frac{1}{2} \sum_{m,m'=\pm\frac{1}{2}} \sum_{L=0}^{2J} \sum_{M=-L}^{L} \left| \sum_{\tau=\mathrm{ch,mag}} A_{LM}^{\tau,mm'} \right|^2, \tag{5.85}$$

$$A_{LM}^{\tau,mm'} = \frac{(4\pi)^{\frac{3}{2}} \alpha_{\mathrm{el}}}{2ik} \sum_{\kappa,\kappa'} (-1)^{l+|\kappa'|} \; i^{l-l'} e^{i(\delta_\kappa + \delta_{\kappa'})} \times \mathrm{CG}_0^{\kappa\kappa'} \times \mathrm{CG}_\tau^{\kappa\kappa'} \times R_{\tau,L}^{\kappa\kappa'} \times Y_{l'm-m'-M}(\theta, \phi),$$

[9]Note that the analog equation in Ref. [152] is given for $\alpha_{\mathrm{el}} = e^2$ and thus differs by $1/(4\pi)$.

where

$$\begin{aligned}
\mathrm{CG}_0^{\kappa\kappa'} &= \frac{2l+1}{2L+1}\sqrt{2j+1}\,\langle l0, \tfrac{1}{2}m\big|jm\rangle\,\langle jm, L-M|j'm-M\rangle \\
&\quad\times\big\langle l'm-m'-M, \tfrac{1}{2}m'\big|j'm-M\big\rangle\,, \\
\mathrm{CG}_{\mathrm{ch}}^{\kappa\kappa'} &= \langle l0, L0|l'0\rangle\, W(j'l'jl;\tfrac{1}{2}L), \quad \mathrm{CG}_{\mathrm{mag}}^{\kappa\kappa'} = \big\langle l0, L0\big|\bar{l}'0\big\rangle\, W(j'\bar{l}'jl;\tfrac{1}{2}L).
\end{aligned} \tag{5.86}$$

Moreover, the quantities $\mathrm{CG}_\tau^{\kappa\kappa'}$ are typically expressed in terms of the Racah coefficients $W(abcd;ef)$ [152, 158], which can be expanded in terms of Clebsch-Gordan coefficients via

$$W(abcd;ef)\delta_{cc'}\delta_{\gamma\gamma'} = \sum_{\alpha\beta\delta\epsilon\phi} \frac{\langle a\alpha, b\beta|e\epsilon\rangle\,\langle e\epsilon, d\delta|c\gamma\rangle\,\langle b\beta, d\delta|f\phi\rangle\,\langle a\alpha, f\phi|c'\gamma'\rangle}{\sqrt{(2e+1)(2f+1)}}, \tag{5.87}$$

in particular,

$$\langle l0, L0|l'0\rangle\, W(j'l'jl;\tfrac{1}{2}L) = (-1)^l \frac{\big\langle j'\tfrac{1}{2}, j-\tfrac{1}{2}\big|L0\big\rangle}{\sqrt{(2l+1)(2L+1)}}\frac{1}{2}\Big[1+(-1)^{L+l'+l}\Big]. \tag{5.88}$$

Finally, one has[10]

$$\begin{aligned}
R_{\mathrm{ch},\,L}^{\kappa\kappa'} &= \int \mathrm{d}r\,\mathrm{d}r'\,r'^2\Big[f_\kappa(r)f_{\kappa'}(r)+g_\kappa(r)g_{\kappa'}(r)\Big]\frac{r_<^L}{r_>^{L+1}}\;\rho_L(r'), \\
R_{\mathrm{mag},\,L}^{\kappa\kappa'} &= \tfrac{-i(\kappa+\kappa')}{\sqrt{L(L+1)}}\int \mathrm{d}r\,\mathrm{d}r'\,r'^2\Big[f_\kappa(r)g_{\kappa'}(r)+g_\kappa(r)f_{\kappa'}(r)\Big]\frac{r_<^L}{r_>^{L+1}}\;j_{LL}(r'),
\end{aligned} \tag{5.89}$$

with $r_> = \max(r,r')$, $r_< = \min(r,r')$, and f_κ, g_κ are the radial wave functions found by solving the Dirac equation. Here, ρ_L and j_{LL} are the charge density and current contributions to the expectation values of charge density and current with the given angular momentum according to

$$\begin{aligned}
\langle JM_i|\,\rho(\vec{r})\,|JM_f\rangle &= \sqrt{4\pi}\sum_{LM}\langle JM_i, LM|JM_f\rangle\,\rho_L(r)Y_{LM}^*(\hat{\vec{r}}), \\
\langle JM_i|\,\vec{j}(\vec{r})\,|JM_f\rangle &= \sqrt{4\pi}\sum_{LL'M}\langle JM_i, LM|JM_f\rangle\,j_{LL'}(r)\vec{Y}_{LL'M}^*(\hat{\vec{r}}),
\end{aligned} \tag{5.90}$$

where $\vec{Y}_{LL'M}$ are the vector spherical harmonics defined as in Eq. (2.38). In the special case, $L'=L$ one has

$$\vec{Y}_{LLM}(\hat{\vec{r}}) = \frac{\vec{L}}{\sqrt{L(L+1)}}Y_{LM}(\hat{\vec{r}}), \tag{5.91}$$

with the angular-momentum operator $\vec{L} = -i\vec{r}\times\vec{\nabla}$.

[10] The charges ρ_L are normalized according to $\sqrt{4\pi(2J+1)}\,\rho_L\big|_{\text{this work}} = \rho_L\big|_{\,[152]}$, the radial wave functions g_κ according to $-\mathrm{sgn}(\kappa)\,g_\kappa(r)\big|_{\text{this work}} = \sqrt{2k(E+m_e)}\,rg_\kappa(r)\big|_{\,[152]}$, and likewise for j_{LL} and f_κ, respectively.

For improved convergence, we may write again

$$(1-\cos\theta)^{\tilde{m}} 2ikA_{LM}^{\tau,mm'}(\theta) = \sum_{\kappa'\geq 0} a_{\kappa'}^{(\tilde{m})} Y_{\kappa' m-m'-M}(\theta,0), \tag{5.92}$$

where we set $\phi = 0$ as the absolute value removes any phase from the spherical harmonics. We obtain the series coefficients

$$\begin{aligned} a_{\kappa'}^{(0)} = \sum_{\kappa\neq 0} (-i)^{l-\kappa'} \Big[& e^{i(\delta_\kappa+\delta_{\kappa'})} \times \mathrm{CG}_0^{\kappa\kappa'} \times \mathrm{CG}_\tau^{\kappa\kappa'} \times R_{\tau,L}^{\kappa\kappa'} \times \left(1-\delta_{\kappa' 0}\right) \\ & - e^{i(\delta_\kappa+\delta_{-(\kappa'+1)})} \times \mathrm{CG}_0^{\kappa,-(\kappa'+1)} \times \mathrm{CG}_\tau^{\kappa,-(\kappa'+1)} \times R_{\tau,L}^{\kappa,-(\kappa'+1)} \Big], \end{aligned} \tag{5.93}$$

with the recursion relation [158]

$$\begin{aligned} a_{\kappa'}^{(\tilde{m})} = a_{\kappa'}^{(\tilde{m}-1)} & - \sqrt{\frac{(\kappa'+m-m'-M+1)(\kappa'-m+m'+M+1)}{(2\kappa'+1)(2\kappa'+3)}} a_{\kappa'+1}^{(\tilde{m}-1)} \\ & - \sqrt{\frac{(\kappa'+m-m'-M)(\kappa'-m+m'+M)}{(2\kappa'-1)(2\kappa'+1)}} a_{\kappa'-1}^{(\tilde{m}-1)}. \end{aligned} \tag{5.94}$$

Due to the coefficients $\langle l0, L0|l'0\rangle$, $\left\langle l0, L0\middle|\bar{l}'0\right\rangle$ in $\mathrm{CG}_\tau^{\kappa\kappa'}$, the summation in Eq. (5.93) only extends over finitely many values of κ, and half the terms vanish since $\langle l0, L0|l'0\rangle = 0$ for $l+L+l'$ odd. In addition to the convergence in κ also the integrals over Coulombic solutions in Eq. (5.89) become delicate, and methods have been developed to perform such integrals analytically [161–163]. In this work, we have not implemented Coulomb-distortion effects beyond $L = 0$, but such corrections could be taken into account along the lines described above if improved data sensitive to the $L > 1$ multipoles became available.

Chapter 6

Nuclear Charge Densities[1]

For proper discriminatory power, between the different effective operators contributing to $\mu \to e$ conversion, not only quantitative inputs for the hadronic matrix elements, are necessary, but also similarly precise inputs for the nuclear response and the bound-states physics are essential. Charge densities play an important role in classifying these nuclear responses as well as calculating the bound-state physics, as they directly dictate the electric potential of the nucleus, as already established in Chap. 5. Furthermore, the charge density is directly related to the charge form factor relevant for the dipole interaction and has a high overlap with the proton and neutron densities which are directly related to the M multipoles. In particular, direct model-independent access to neutron distributions is difficult to achieve and they have only recently been measured in PVES for only a few selected nuclei and momentum transfers [164–166]. A potential alternative could be to employ the strategy of Refs. [167, 168] by combining modern ab-initio methods to correlate charge densities with neutron densities, which we will discuss in a little more detail in Chap. 8. However, for such strategies to be successful, again quantitative inputs for the charge densities of the considered nuclei are crucial. Hence, for all these applications a quantitative extraction of the charge densities of the considered nuclei, including a systematic uncertainty estimation, is crucial for a meaningful description of $\mu \to e$ conversion. Similarly, the extracted charge densities and form factors can be used directly in other nuclear physics applications like neutrinos-nucleus scattering or PVES.

The charge densities of the nuclei can be extracted from elastic electron-nucleus scattering experiments, as these are strongly dependent on the charge form factor. In section 5.1 we have introduced the cross section for elastic electron-nucleus scattering in the PWBA. However, we have also seen, that in practice, a description using the PWBA expressions is not sufficient for a realistic description of the measured cross sections. This is because the potential of the nucleus distorts the electron's incoming and outgoing waves, resulting in substantial corrections in particular in the vicinity of the form factor minima. A strategy to include such effects, which fall under the name of Coulomb corrections, is the

[1] The contents of this chapter and the related App. D as well as Sec. 7.1 and substantial parts of the foundations laid in Chap. 5, were published in Ref. [2]

"phase-shift model" as introduced in Sec. 5.4. Using this method, a given charge density parameterization can be fit to elastic electron-nucleus scattering data.

Unfortunately, the commonly used FB parameterizations determined in Ref. [134] do not provide uncertainties at all, leading to the unsatisfactory situation that uncertainties can at best be guessed from nuclear charge radii or model-dependent fits. For this reason, we reanalyzed the original data for electron-nucleus scattering off a few selected isotopes most relevant for $\mu \to e$ conversion, to propagate the uncertainties profiting from modern statistical techniques and computational resources that were not available when the data was originally taken. To make matters worse, the data itself was often poorly documented, with minimal information on systematic uncertainties, only available in unpublished PhD theses, or even lost as private communication. We therefore spent considerable effort in Ref. [2] locating the original data wherever possible, collecting as complete a database as seems to be possible for ^{40,48}Ca [169–176], ^{48,50}Ti [171, 177–183], and ^{27}Al [184–193]. The latter two targets are directly motivated by the current limit for $\mu \to e$ conversion from Ref. [72] and future ones from Mu2e and COMET, respectively, while calcium is required as an intermediate step relative to which the titanium measurements were performed. Moreover, charge distributions for ^{27}Al [165] and ^{48}Ca [166] are also of direct interest for the analysis of PVES, providing further motivation to focus on this set of isotopes.

Consequently, we were able to successfully fit FB charge density parameterizations to the elastic electron scattering data, including a comprehensive investigation of uncertainties. In this chapter, we will discuss our results for the charge densities. For tabulations of the used data sets and explicit FB parameterizations including uncertainties and correlations, we refer to App. D. We furthermore provided a supplementary `python` notebook in Ref. [2], which makes the FB parameterizations for all charge distributions including uncertainties and complete covariance matrices available to the community.

6.1 Fitting Strategy and Constraints

According to Sec. 5.2.2, charge densities can be parameterized in terms of a FB series, which takes the form of Eq. (5.21). This parameterization was established in Ref. [149] as a model-independent method to describe charge densities, with a more direct relation to the available data than, e.g., for sums of Gaussians [194]. Already in Ref. [149], the main motivation to introduce the FB series was to extract charge densities from elastic electron–nucleus scattering in a model-independent way, including also the extraction of meaningful uncertainty estimates. Unfortunately, the strategies to derive such measures of uncertainty were not employed or at least not documented in subsequent reviews such as Ref. [134]. Furthermore, due to computational limitations, at the time the strategy involved the use of a toy model to transfer the cross-section data to form-factor pseudo-data, which could then be fit directly using the FB parameterization. In this toy model, the charge density was described as a sum of δ functions, under the assumption that for a sufficient density of δ functions, the result would become indistinguishable from the physical charge density, see, e.g., Ref. [150] and Sec. 5.2.1. Within this approach, the phase shifts can be calculated analytically, by solving the Dirac equation stepwise between each δ function,

which improved the speed of the calculation considerably, however, at the expense of introducing new systematic errors related to the convergence of the fit. Since with modern computational resources and optimizations to the code for the phase-shift solution, a direct fit using the FB parameterization becomes feasible, we fit directly to the cross-section data, avoiding the previous detour and the associated systematic uncertainties.

In the fit, we account for the statistical and systematic uncertainties from the measurements, including their correlations, wherever possible. Moreover, we employ a change of variables in which the conservation of the total charge becomes manifest, see Sec. 6.1.2. Recoil corrections are included by changing from the laboratory system (Lab) to the center-of-mass system (CMS), then performing the numerical calculation of the phase shifts, and finally transforming back into the Lab system, see Sec. 5.5.

Finally, to ensure robust control of statistical and systematic uncertainties, we employ the following fit strategies to scan over different combinations of N and R parameters, while fitting the FB coefficients a_n to the elastic scattering data of the considered nuclei, both with and without additional constraints from muonic atoms using Barrett moments. The range of these fits is then narrowed down to a selection with acceptable statistical quality and asymptotic behavior, to form the basis for our central solutions as well as statistical and systematic error bands. We divide the fitting strategy into the following steps:

1. Fit for a large grid of N and R pairs, beyond the expected range of validity of the FB expansion.
2. Use the statistical fit quality of all solutions in the grid to define a reasonable range of N and R pairs.
3. Redo the fits in the deduced range including the constraints to prevent unphysical oscillations, see App. 6.1.3.
4. Select fits that still display sufficient statistical quality and acceptable asymptotic behavior, see App. 6.1.4.
5. Select a central solution based on statistical fit quality, favoring lower values of N and R.
6. Deduce upper and lower systematic uncertainty bands based on the remaining solutions, see App. 6.1.6.
7. Redo steps 3–6 including the constraint from the Barrett moments.

Following this strategy, we end up with two solutions for each nucleus, enabling cross-checks of the consistency of electron scattering data and muonic-atom constraints. In each case, the fit is set up in such a way that we first allow for a wide range of values of N and R, to ensure that no admissible fits be overlooked. The maximal values are related to the largest momentum transfer for which measurements are available, essentially, because the charge form factor near the momentum transfer q_n is determined by the coefficient a_n in the FB series, see Sec. 5.2.2, leading to an initial guess of suitable ranges. The subsequent steps

then ensure that an overparameterization of the data is avoided, by giving precedence to lower values of N and R for comparable fit quality. More details on the intermediate results of the fit are provided in App. D.1.

We fit the charge-density parameterizations directly to the experimental cross-section data. As we need to solve the Dirac equation numerically for all partial waves in every iteration, calculation speed is of crucial importance for a working fit routine. We set the precision goals of the underlying numerical routines in such a way that further improvement in precision only marginally changes the resulting χ^2, verifying the latter for a representative set of cases.

As the data sets are generally not dominated by statistical uncertainties, systematic uncertainties need to be included in a robust manner, for which we follow the procedure established for fits to $e^+e^- \to$ hadrons cross-section data in Refs. [195–200]. Accordingly, our χ^2 function is defined by

$$\chi^2 = \sum_{i,j} (f(x_i) - y_i) X_{ij}^{-1} (f(x_j) - y_j), \tag{6.1}$$

with covariance matrix

$$X_{ij} = X_{ij}^{\text{stat}} + \frac{f(x_i) f(x_j)}{y_i y_j} X_{ij}^{\text{syst}}. \tag{6.2}$$

For the data sets used in this work, information on correlations is minimal, but most systematic effects concern normalizations, suggesting fully correlated errors, while for the statistical errors, no relevant correlations have been reported. Therefore, we assume

$$X_{ij}^{\text{stat}} = \delta_{ij} \sigma_i^2, \qquad X_{ij}^{\text{syst}} = \sigma_i \sigma_j. \tag{6.3}$$

Especially for correlations of the normalization type, care needs to be taken to avoid a D'Agostini bias [201, 202]. To this end, we calculate X_{ij} for our initial parameters once and only adjust it once the fit converges for that covariance matrix. Then we calculate a new covariance and restart the fit, iterating the procedure until the fit parameters do not change anymore.

In the cases for which an additional systematic uncertainty arises from the output of a previous fit of ours, we propagate the known correlations. This is particularly relevant for ^{46,50}Ti, as the available data were taken relative to ^{48}Ti, whose cross-section measurements involve sizable uncertainties themselves.

Regarding fit routines, due to the high correlation among the different FB parameters a standard gradient-descent approach proved insufficient. After benchmarking over different fit routines, we settled on the `'Powell'` method [203] as implemented in `scipy.optimize.minimize` [155] with interface `lmfit` [204], which consistently gave the best performance.

6.1.1 Normalization Constraint

To improve convergence and not scan unnecessarily over unphysical parameter space, we implement the charge-conservation constraint of Eq. (5.22) explicitly. Implementing such a condition for two parameters is trivial, but already with three parameters one may run into the scenario in which the first two parameters are chosen within reasonable bounds, while the third is forced to a highly unphysical value. To solve this problem, we employ the following strategy: By setting some conservative bounds for the FB parameters a_n, we can reparameterize them in such a way that they can only adopt values that (i) are still allowed by total charge conservation and (ii) no parameter needs to be chosen outside these bounds. In essence, instead of parameterizing a_n directly, we parameterize the position within the remaining parameter space which is left to still fulfill the normalization, after the $a_{n'}$ with $n' < n$ are chosen. To avoid introducing a fit bias, we choose a very generous limit of

$$\left|F_0^{\mathrm{ch}}(q_n)\right| \leq \pi\left(\frac{q_1}{q_n}\right)^3 = \frac{\pi}{n^3} \qquad \Leftrightarrow \qquad |a_n| \leq \frac{1}{n}\frac{\pi^2 Z}{2R^3} \equiv \tilde{a}_{n,\mathrm{lim}}, \tag{6.4}$$

which loosely reflects the expected asymptotic suppression of the form factor with q (one power less than the perturbative-QCD scaling [205, 206]). In particular, this is the minimal assumption to implement a suppression of $|a_n|$ for increasing values of n, while previous FB fits, e.g., in the compilation [134], typically imposed constraints on the asymptotic behavior of the FB coefficients that were much more stringent.

Next, to employ our reparameterization we define a version of the parameters without alternating signs via

$$\tilde{a}_n = -(-1)^n a_n, \tag{6.5}$$

for which the normalization condition of Eq. (5.22) becomes

$$\tilde{a}_n = \frac{Z}{4\pi R} q_n^2 - \sum_{\substack{n'\neq n \\ n'=1}}^{N} \tilde{a}_{n'} \frac{q_n^2}{q_{n'}^2}. \tag{6.6}$$

Initially, the parameter space for each parameter $\tilde{a}_n$ is given by $[-\tilde{a}_{n,\mathrm{lim}}, \tilde{a}_{n,\mathrm{lim}}]$. However, once $\tilde{a}_n$ have been chosen for some n, not the entire parameter space $[-\tilde{a}_{n,\mathrm{lim}}, \tilde{a}_{n,\mathrm{lim}}]$ may be available anymore, due to the normalization condition of Eq. (6.6). Hence, one can deduce which maximal and minimal value within $[-\tilde{a}_{n,\mathrm{lim}}, \tilde{a}_{n,\mathrm{lim}}]$ are still possible. Consequently, choosing the $\tilde{a}_n$ in ascending order starting at $n = 1$, we may assume that for any $\tilde{a}_n$ all the $\tilde{a}_{n'}$ with $n' < n$ are already set, while the ones with $n' > n$ are still to be determined.

Hence, the remaining parameter space for $\tilde{a}_n$ denoted by $\tilde{a}_n \in \left[\tilde{a}_{n,\overline{\min}}, \tilde{a}_{n,\overline{\max}}\right]$ is limited by

$$\tilde{a}_{n,\overline{\max}} = \min\left(\tilde{a}_{n,\lim}, \frac{Z}{4\pi R}q_n^2 + \sum_{\substack{n'>n \\ n'=1}}^{N} \tilde{a}_{n',\lim}\frac{q_n^2}{q_{n'}^2} - \sum_{\substack{n'<n \\ n'=1}}^{N} \tilde{a}_{n'}\frac{q_n^2}{q_{n'}^2}\right),$$
$$\tilde{a}_{n,\overline{\min}} = \max\left(-\tilde{a}_{n,\lim}, \frac{Z}{4\pi R}q_n^2 - \sum_{\substack{n'>n \\ n'=1}}^{N} \tilde{a}_{n',\lim}\frac{q_n^2}{q_{n'}^2} - \sum_{\substack{n'<n \\ n'=1}}^{N} \tilde{a}_{n'}\frac{q_n^2}{q_{n'}^2}\right). \tag{6.7}$$

Once the remaining parameter space has been constrained in this way, we can reparameterize the a_n in terms of $x_n \in [0,1]$ via

$$a_n(x_n) = -(-1)^n\Big[x_n(\tilde{a}_{n,\overline{\max}} - \tilde{a}_{n,\overline{\min}}) + \tilde{a}_{n,\overline{\min}}\Big]. \tag{6.8}$$

By fitting these x_n instead of the a_n parameters, we always make sure that the normalization constraint is exactly fulfilled and no unphysical parameter space is probed during the fit. Furthermore, in this way, the fit is encouraged to fix the parameters in ascending order, which projects the relative importance of the factors for the shape of the charge density and is in line with ascending momentum transfers in the form factor.

6.1.2 Constraints from Barrett Moments

Measurements of $2p \to 1s$ transition energies of muonic atoms can be used as an independent constraint on the charge radius and thus can be included as additional data points into our fits. These constraints are usually quoted in terms of the so-called Barrett moments [207], which can be extracted relatively model-independently from the measured transition energies, and can be easily calculated from a given charge density via

$$\left\langle r^k e^{-\alpha r}\right\rangle = \frac{4\pi}{Z}\int_0^\infty \mathrm{d}r\, r^{k+2}\rho(r)e^{-\alpha r}, \tag{6.9}$$

where k and α are chosen in a way that allows for the best extraction of the relevant information from the transition energies. We use the values from Refs. [208–210] as reproduced in Tab. 6.1, included in the χ^2 via

$$\chi^2 \to \chi^2 + \left(\frac{\left\langle r^k e^{-\alpha r}\right\rangle - \left\langle r^k e^{-\alpha r}\right\rangle_{\mathrm{ref}}}{\Delta\left\langle r^k e^{-\alpha r}\right\rangle_{\mathrm{ref}}}\right)^2. \tag{6.10}$$

Nucleus	k	α [fm^{-1}]	$\left\langle r^k e^{-\alpha r} \right\rangle_{\text{ref}}$ [fm^k]	Reference
^{27}Al	2.0573	0.0419	8.6616(17)(101)	[209]
^{40}Ca	2.0911	0.0596	10.7759(50)(81)	[210]
^{48}Ca	2.0912	0.0596	10.7809(50)(86)	[210]
^{46}Ti	2.1009	0.0640	11.4796(37)(110)	[210]
^{48}Ti	2.1007	0.0641	11.3877(37)(101)	[210]
^{50}Ti	2.1003	0.0642	11.2525(36)(91)	[210]

Table 6.1: Barrett moments as quoted in Ref. [208] via Barrett radii. The first error is statistical, the second one refers to a 30% uncertainty on the nuclear-polarization correction from Ref. [211].

6.1.3 Constraints to prevent Oscillations

To assess the systematic uncertainties of the fit, it is crucial to consider fit variants with a multitude of values for N and R. However, with increasing R and N, at some point energies are reached that are not constrained by the data anymore. Accordingly, the fit is enticed to add large contributions there, to balance minor improvements of the fit in the low-energy region and/or to accommodate additional constraints such as the Barrett moment. This results in unphysical oscillations in the shape of the charge density as well as unphysically large values for the form factor in the high-energy region. To counteract this behavior, we adopted the following strategy. For sufficiently large r (and relatively low Z), one expects a monotonically decreasing charge density to ensure a smooth transition to its asymptotic value zero, so that demanding the derivative to be negative, $\rho'(r) \leq 0$, suppresses oscillations. We implemented this idea by first performing an integration by parts in the sum rule for the charge radius, yielding

$$\begin{aligned}\left\langle r^2 \right\rangle &= \frac{4\pi}{Z} \int_0^\infty \mathrm{d}r\, r^4 \rho(r) = \frac{4\pi}{Z} \int_0^\infty \mathrm{d}r\, \frac{r^5}{5}\, (-\rho'(r)) \\ &= \underbrace{\frac{4\pi}{Z} \int_0^\infty \mathrm{d}r\, \frac{r^5}{5}\, (-\rho'(r))\, \theta(-\rho'(r))}_{\equiv \langle r^2 \rangle_+} + \underbrace{\frac{4\pi}{Z} \int_0^\infty \mathrm{d}r\, \frac{r^5}{5}\, (-\rho'(r))\, \theta(\rho'(r))}_{\equiv \langle r^2 \rangle_-} . \end{aligned} \tag{6.11}$$

If one strictly demanded $\rho'(r) \leq 0$, one would have $\langle r^2 \rangle_- = 0$ exactly, but of course this would constitute too strong a constraint. In practice, we impose $\left| \langle r^2 \rangle_- \right| \lesssim \Delta \langle r^2 \rangle$, where we choose $\Delta \langle r^2 \rangle = 0.04\,\mathrm{fm}^2$, as a rough upper limit on the typical statistical uncertainty of the charge radius, see Sec. 6.2. In particular, due to the r^5 weighting, this implementation only suppresses oscillations for large r, while the low-energy region remains essentially

unaffected. The additional term in the χ^2 is

$$\chi^2 \to \chi^2 + \left(\frac{\langle r^2 \rangle_-}{\Delta \langle r^2 \rangle} \right)^2 . \tag{6.12}$$

6.1.4 Veto on Asymptotics

Imposing the monotony constraint from Sec. 6.1.3 removes most of the unphysical oscillations, but some solutions in which the fit clearly exploits the lack of data in certain regions to produce implausible charge distributions remain, especially for fit variants in which large values of N are admitted. One could prevent such cases by simply restricting R and N to the range in which data are available, but we also considered another variant in which we impose a more stringent high-energy behavior. To this end, we estimate an upper limit on a reasonable asymptotic behavior of the form factor in the experimentally constrained region and exclude solutions that exceed this limit for higher energies. Assuming the form factor to decay asymptotically, we used the ansatz

$$|F_0^{\mathrm{ch}}(q)| < Aq^{-m}, \tag{6.13}$$

with $A > 0$, $m > 0$. Arguments from perturbative QCD [205, 206] suggest $m \geq 4$ while determining A and m by mapping this form onto the data-constrained part of the form factor tends to suggest even larger values of m. To arrive at such estimates, we took the maximal values between the last and second-to-last as well as second-to-last and third-to-last unambiguous minimum of the form factor to determine A and m. In fact, as the explicit fits in App. D.1 show, the real envelope tends to be even steeper. As we have a variety of R and N pairs for each scenario at our disposal, another way to relax the constraint is to use only the worst limit from all fits within that scenario. In the end, such considerations become most relevant for fit variants that already show signs of overparameterization, but with reasonable constraints on the asymptotic behavior, it is relatively straightforward to veto such cases, while minimizing the bias towards the selection of acceptable fits that form the basis for our uncertainty quantification.

6.1.5 Estimates of Systematic Uncertainties

In addition to the procedure already explained, with every set of fits we performed, we identified clear outliers (for example, cases in which $\chi^2(R, N+1) > \chi^2(R, N)$) and redid these fits with starting values based on adjacent solutions, to counteract the possibility of hitting local minima. Moreover, since a lot of the data are likely to be affected by systematic uncertainties not fully reflected by the quoted uncertainties, we follow the standard procedure to inflate the fit errors by scale factors $S = \sqrt{\chi^2/\mathrm{dof}}$. In practice, these scale factors mainly affect the fits to titanium and aluminum. In the documentation of the various fits, we provide the reduced χ^2 and corresponding p-values, from which the cases that require an error inflation can be inferred.

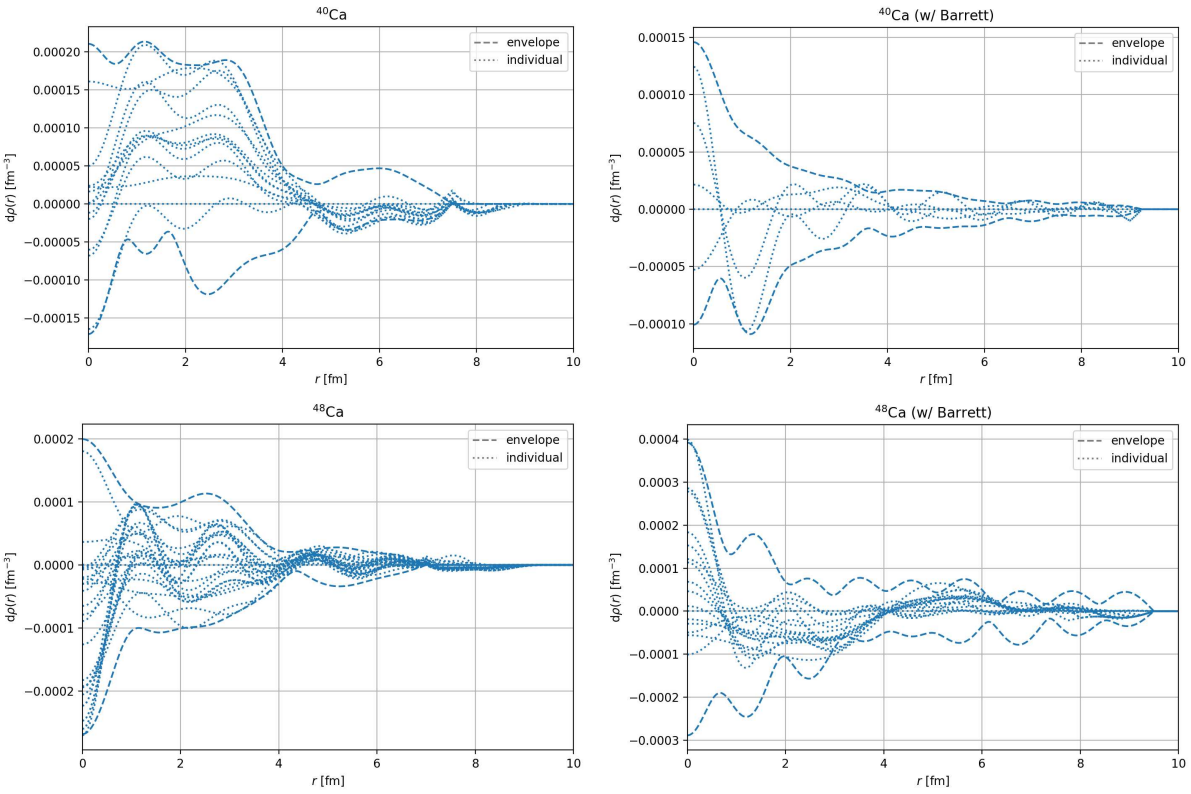

Figure 6.1: Deviations from central solution and fit uncertainty envelope for ^{40,48}Ca.

To assess the systematic uncertainties in our fits, we employ two main strategies. On the one hand, we parameterize the envelope of all acceptable fits again in terms of a FB series, and then propagate uncertainties for the quantities of interest such as the charge radii or overlap integrals. On the other hand, we can calculate these quantities of interest for all individual fits and then analyze the spread directly for the observable in question. The second strategy probably represents the systematic spread within this particular quantity more accurately, but requires one to keep track of a large set of parameterizations, necessitating the calculation of the observable for each one. The first strategy, therefore, is a lot more practical, requiring only a single parameterization. Furthermore, the implicit interpolation might represent the systematic uncertainty more accurately if the number of underlying fits is small. For the quantities considered in this work, we employed both strategies, allowing one to compare the outcome to be able to assess the stability of the uncertainty quantification. For the calcium and aluminum fits we observe reasonable agreement between the two strategies, while for titanium in some cases the envelope strategy tends to overestimate the uncertainties.

6.1.6 Fitting Systematic Uncertainty Bands

To fit a systematic uncertainty band, we take a set of solutions for the charge density $\rho(r)$ and calculate the maximum and minimum at 100 values between $r = 0$ and $r = 10\,\mathrm{fm}$. We call the upper/lower distance to the central value $\mathrm{d}\rho_{\mathrm{data}}^{\mathrm{syst},\pm}$. To define a conservative

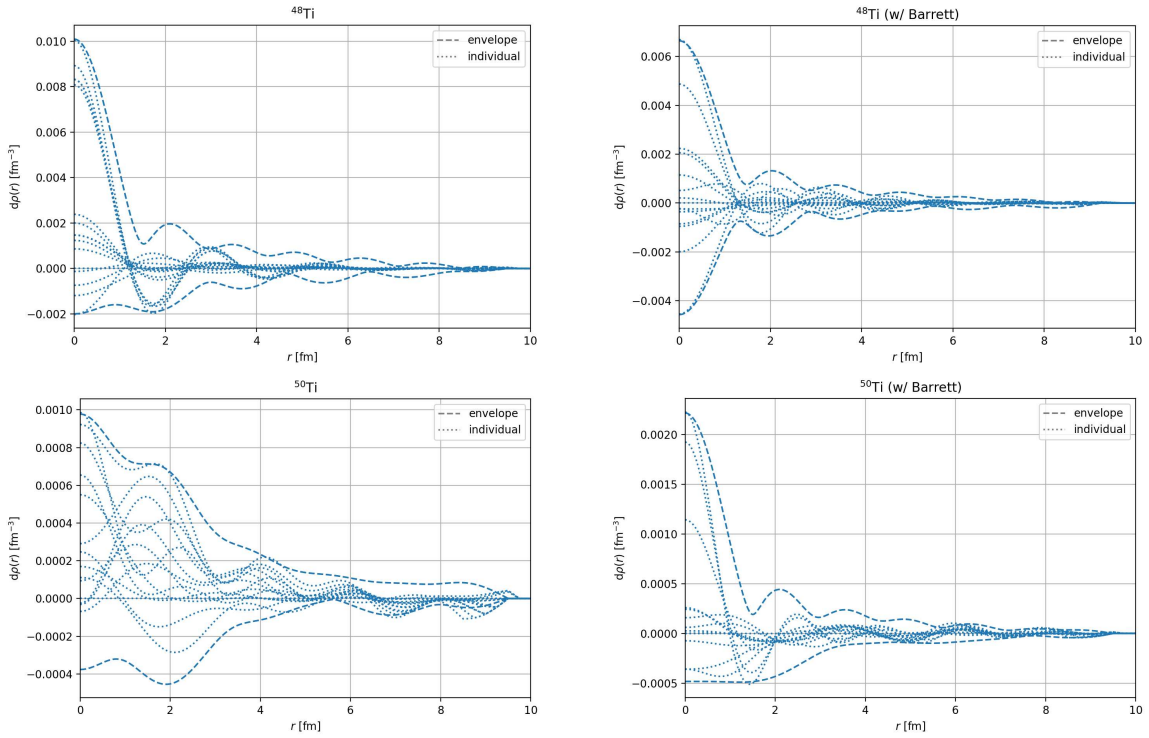

Figure 6.2: Deviations from central solution and fit uncertainty envelope for ^{48,50}Ti.

systematic uncertainty error band, we aim to construct an envelope around these limits, which is complicated by the fact that charge conservation should be fulfilled exactly. Accordingly, we choose to fit values of $\mathrm{d}x_i^{\mathrm{syst},\pm}$ that behave in the same way as the statistical uncertainties with the same correlations, and thus by construction fulfill charge conservation. Therefore, our model $\mathrm{d}\rho_{\mathrm{model}}^{\mathrm{syst},\pm}$ amounts to the Gaussian uncertainty propagation of $\mathrm{d}x_i^{\mathrm{syst},\pm}$ using the correlations of the statistical uncertainties. Since we want to fit an outer envelope, we penalize $\mathrm{d}\rho_{\mathrm{model}}^{\mathrm{syst},\pm} < \mathrm{d}\rho_{\mathrm{data}}^{\mathrm{syst},\pm}$ and write our loss function as

$$\chi^2 = \left(\mathrm{d}\rho_{\mathrm{model}}^{\mathrm{syst},\pm} - \mathrm{d}\rho_{\mathrm{data}}^{\mathrm{syst},\pm}\right)^2 \times \left(1 + \omega^2 \times \theta\left(\mathrm{d}\rho_{\mathrm{data}}^{\mathrm{syst},\pm} - \mathrm{d}\rho_{\mathrm{model}}^{\mathrm{syst},\pm}\right)\right), \tag{6.14}$$

which penalizes fits lying inside the uncertainty band a lot stronger than those outside. We find that $\omega = 10$ produces satisfactory fit results. Note that we are not able to describe any systematic effects for $r > R$, as by construction the charge density and also any propagated uncertainty goes to zero at $r = R$. On the other hand, we tend to overestimate systematic effects for $r \leq R$, as the envelope constructed in this way encompasses more parameter space than spanned by the individual fits. Finally, we round the values of $\mathrm{d}x_i^{\mathrm{syst},\pm}$ to their given uncertainty as extracted from the fit. We show the resulting envelope parameterizations of $\mathrm{d}\rho_{\mathrm{data}}^{\mathrm{syst},\pm}$ for all nuclei in Figs. 6.1–6.3 with all the individual deviations enclosed. In particular for ^{48}Ca, without the inclusion of the Barrett moment, the envelope sits very tight around the contributing solutions, while with the inclusion of the Barrett moment, the fit is forced to (strongly) overestimate the uncertainties. In general, we find that this description of the systematic errors gives a fair representation, with a tendency to overestimate the uncertainty in some cases, see also the discussion in Sec. 6.2.4.

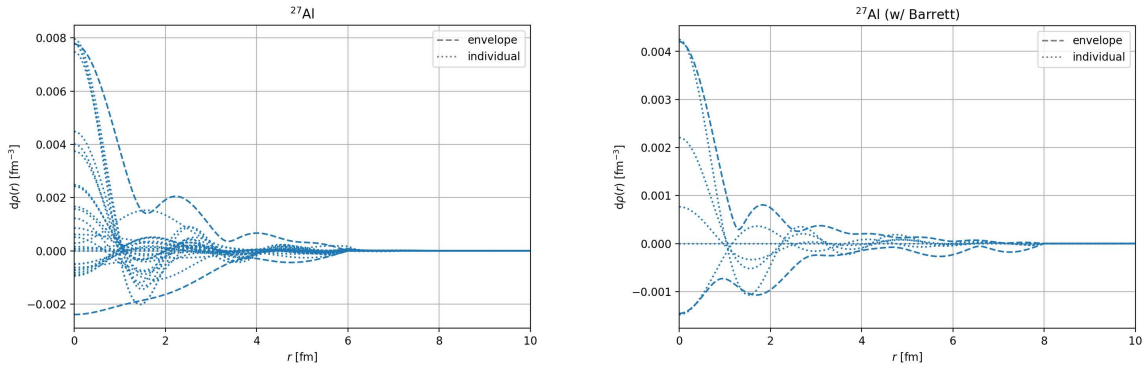

Figure 6.3: Deviations from central solution and fit uncertainty envelope for ^{27}Al.

6.1.7 Technical Details of the Fitting Program

For a clearer understanding of the fitting program and the documentation of some of the technical details we outline the core aspects of the fitting program. The program can be separated into three logical parts. One part describes the input quantities like charge densities and all directly related quantities like form factor, electric field, potential, radius, Barrett moment, and so on, one part carries out the phase-shift model calculation according to Sec. 5.4 and then calculates the cross section including recoil corrections and, finally, one part carries out the fit and compares the resulting cross-section result to experimental data.

Since for the FB parameterization, all input quantities can be given analytically, their implementation is mostly straightforward. Merely the analytical description of the Barrett moment requires an analytical continuation to complex values of the generalized incomplete gamma function. In `python` such an implementation can be found in the `mpmath` package. For different parameterizations, where not all quantities are known analytically, one might need to calculate some quantities numerically. In that case, it is important to allow sufficiently many subdivisions in the numerical integration routines (we use `scipy.integrate.quad`) and cut off the integral at some point adding a physical high-energy continuation at the end. As such a procedure will excessively increase the runtime of a fit, if these numerical integrations need to run for every iteration, we highly advise using an analytical description whenever possible.

In Sec. 5.4 we have already pointed out a few technical details about the implementation of the phase-shift model. Nevertheless, we will go over them again here with a few more details and focus on our application. First of all, the logic of the phase-shift model calculation runs in units of $[E] = [r^{-1}] = m_\mu \alpha_{\text{el}}$, which is an artifact of trying to make the energies for the bound-state solution more naturally sized (see Fig. 5.9). Changing to the continuum solutions, we kept this convention, despite being a factor of $\mathcal{O}(1\,\text{MeV})$, and the particle now being the electron. Hence, the first step for our calculation is to translate all input quantities into these units. We use

$$\alpha_{\text{el}} = \frac{1}{137.035999084}, \qquad \hbar c = 197.3269631\text{MeV fm}, \tag{6.15}$$

and for the lepton masses [130]

$$m_\mu = 105.6583745\,\text{MeV}, \qquad m_e = 0.5109989461\,\text{MeV}. \tag{6.16}$$

As we include recoil corrections according to Sec. 5.5, we need inputs for the masses of the nuclei. We use [212]

$$\begin{aligned} &m_{^{27}\text{Al}} = 26.981538408\,\text{u}, \quad m_{^{40}\text{Ca}} = 39.96259085\,\text{u}, \quad m_{^{48}\text{Ca}} = 47.952522654\,\text{u}, \\ &m_{^{46}\text{Ti}} = 45.952626356\,\text{u}, \quad m_{^{48}\text{Ti}} = 47.947940677\,\text{u}, \quad m_{^{50}\text{Ti}} = 49.944785622\,\text{u}, \end{aligned} \tag{6.17}$$

with $1\,\text{MeV} = 931.49410242\,\text{u}$. The cross-section is calculated using the phase-shift model as described in Sec. 5.4. Since the phase shifts are only energy and not angular dependent, we make sure to only calculate the phases once for every energy. We calculate for every energy the phase shift for a maximum of 20 partial waves, or until $\bar{\delta}_\kappa < 10^{-7}$, which usually happens within less than 15 partial waves. For the FB parameterization, the cutoff r_c is given by the cutoff of the parameterization R, which makes parameterizations with higher R more expensive to calculate. As in this context, we only require the phase shifts, we only propagate until r_c and omit tasks like normalizing the wave functions or defining high-energy continuations. For solving the initial value problem we use the method `LSODA` and set `atol`$= 10^{-12}$ and `rtol`$= 10^{-10}$ (see also Sec.5.4.1). As special input for the calculation, we use the confluent hypergeometric functions from the `mpmath` package, which we calculate with a working precision of 15 digits. We also make sure, to minimize the number of evaluations that are necessary of this quantity by evaluating it once at r_c and then passing this information forward, and similar for the Coulomb phases.

The fit itself is now run using the interface of `lmfit` with the `powell` method using the loss function of Eq. (6.1) and adding any potential additional constraints as discussed in the fitting strategy. To avoid D'Agostini bias we iterate over the covariance matrix until the changes in the parameters are below the level of 10^{-6}. We run multiple fits in parallel for different values of R and N, where a machine with many CPU cores is advantageous. To improve fit convergence it is important to have good initial values. For that reason the fits of step 1 are usually the most time-intensive ones, as one has to make a good initial guess. For the compatible value of R, one can take the parameters from Ref. [134] truncated to N terms, however a translation to other R is not trivial. We investigated different strategies, and found empirically that

$$a_i(R_2) = \frac{\int_0^{\min(R_1,R_2)} \mathrm{d}r\, j_0\big(\frac{i\pi}{R_1}r\big) j_0\big(\frac{i\pi}{R_2}r\big)}{\int_0^{R_2} \mathrm{d}r\, \big(j_0\big(\frac{i\pi}{R_2}r\big)\big)^2}\; a_i(R_1), \tag{6.18}$$

gives decent results, which is loosely motivated by trying to minimize the integrated quantity $\int \mathrm{d}r\, (\rho(a_i(R_2), r) - \rho(a_i(R_1), r))^2$ with respect to $a_i(R_2)$. To cover a grid of (R, N) value it makes sense to first branch out from the reference point to different values of R using Eq. (6.18), generating reference values for each R, and then based on this calculate for the different values of N at fixed R. As also arbitrary initial values tend to converge to the same solutions as the ones we find with this strategy, while taking a lot longer, we are confident that we do not introduce a bias with this strategy. In the later steps of the fitting strategy and generally, for other iterations of the same (N,R)

combination, it is always advantageous to use the already found solution as starting values for the new fit. For every fit, the found parameters and fit properties are saved in a file for later review and analysis. The best-fit results including all uncertainty estimates for each nucleus are included as supplementary material in Ref. [2] and can be read out with a supplementary `python` notebook.

6.2 Charge Distributions

In the following sections, we present our key results for the charge densities of the different nuclei, with tables of the resulting parameter sets, including uncertainties and correlations, given in App. D.2.

6.2.1 Calcium

We start our discussion with two calcium isotopes, ^{40,48}Ca, for the following reasons. First, both nuclei have spin $J = 0$, such that the simplest form of the DWBA, as given in Eq. (5.64), applies. Second, these isotopes are of interest either as reference points for Ti, as discussed in the subsequent section, or directly for phenomenological applications, e.g., in the context of PVES or neutrinoless double-β decay. Third, the data situation is exceptionally good, at least compared to other isotopes of interest for $\mu \to e$ conversion. We spent considerable effort going through the literature for electron scattering off calcium, including Refs. [169–176]. Unfortunately, most data sets are poorly documented, in many cases making it impossible to even access the original data, let alone retrieving information on uncertainties and correlations. Moreover, later surveys such as Ref. [213] heavily criticized especially early data sets, discarding a fair number of them due to suspected systematic effects. By these standards, the documentation in the PhD thesis [175] is exceptionally good, including complete data tables and a discussion of statistical and systematic uncertainties. In addition, data from Ref. [174] are made explicit, while only provided as a figure in the original reference. Taken together, these data sets then cover a wide range of momentum transfer, clearly superseding earlier measurements. We checked for possible tensions by comparing to the data from Ref. [171], a point to which we will return in the context of the charge distributions for titanium, while for the calcium fits the data provided in Ref. [175] were obviously superior. Since this reference is also not easily accessible, we provide the data as used in our fits in App. D.3.

The final results of our fits are shown in Fig. 6.4, where we display the extracted charge distributions for ^{40}Ca and ^{48}Ca including uncertainty bands containing statistical and systematic components. For ^{40}Ca one can see in the close-up that a tension between the electron-scattering-only fits and the variant including Barrett-moment constraints emerges for $r \to 0$, while for ^{48}Ca a more significant tension arises at larger distances. We return to this point in the context of charge radii in Sec. 6.2.4 and provide parameterizations for both solutions in App. D.2.

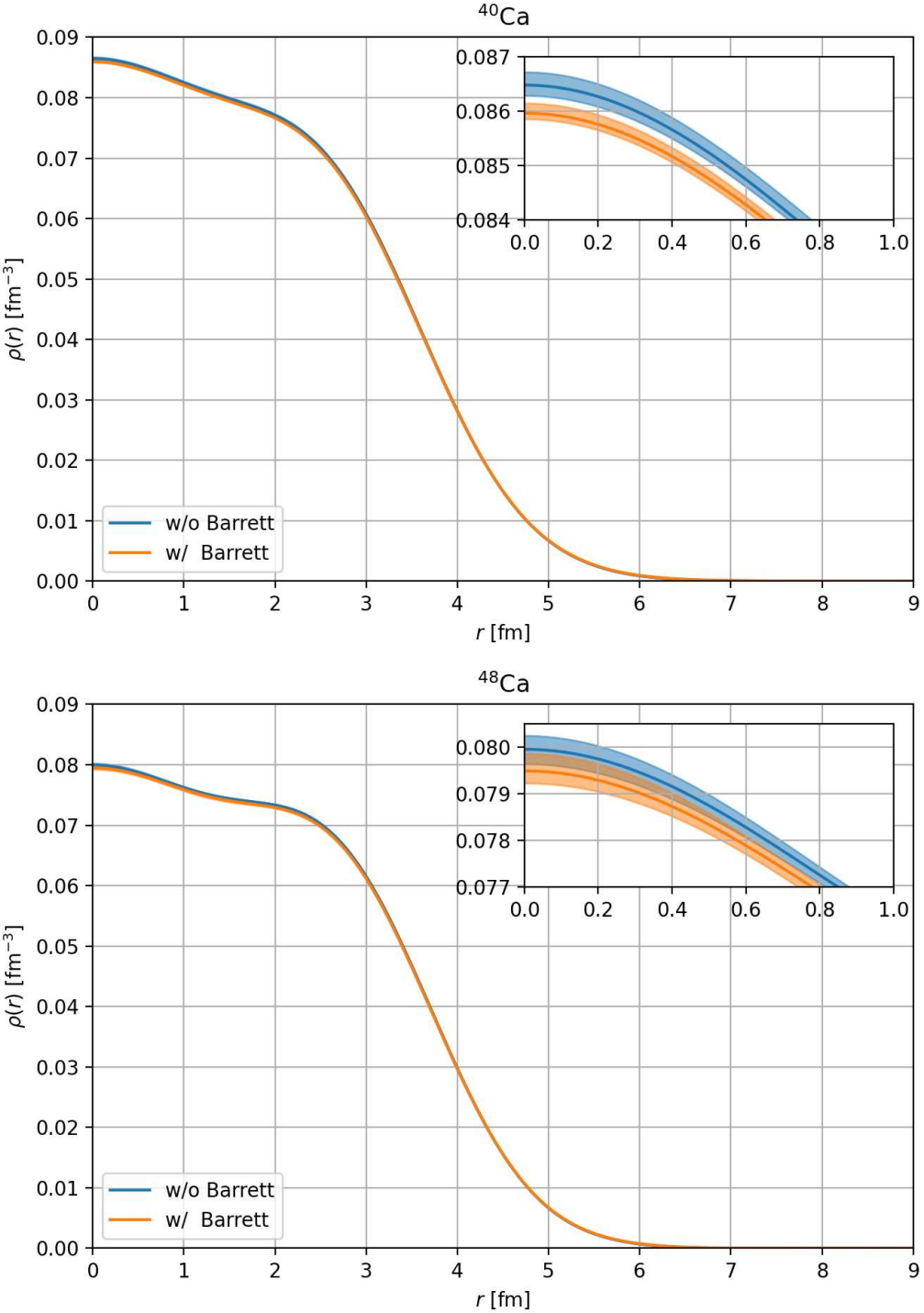

Figure 6.4: Charge densities of ^{40}Ca and ^{48}Ca. Two variants are shown, with (orange) or without (blue) the constraints from Barrett moments.

6.2.2 Titanium

For titanium the data situation is considerably worse than for the calcium isotopes discussed in the preceding section, see Refs. [171, 177–183]. In particular, the only reference from which the original data for the most abundant isotope ^{48}Ti could be retrieved is Ref. [171], in which a measurement relative to ^{48}Ca was performed. Unfortunately, Ref. [171] is among the works whose calcium results were criticized later due to inconsistencies with subsequent measurements, and we confirm the prevalence of such inconsistencies in comparison to the ^{40}Ca data of Ref. [175]. However, the ^{40}Ca data in Ref. [171] required an absolute calibration, involving a number of systematic effects that are absent in a relative measurement. Indeed, comparing the measurement of ^{48}Ca from Ref. [171] (taken relative to ^{40}Ca) with Ref. [175], the situation improves considerably, suggesting that the relative measurement of ^{48}Ti should also be less affected by the systematics observed for the absolute ^{40}Ca measurement. Accordingly, our ^{48}Ti fits are based on the relative measurement from Ref. [171], together with the ^{48}Ca results from the previous section.

A similar strategy was followed in Refs. [182, 183], in which their ^{48}Ti data set is compared to the relative measurement of Ref. [171], together with independent input for ^{48}Ca. While we were successful in retrieving the PhD thesis [182], the original data are not contained therein, so, unfortunately, the results from this measurement appear to be lost, too, leaving Ref. [171] as the only remaining source to extract the charge distribution for ^{48}Ti. Still, the analysis presented in Ref. [182] finds consistency with Ref. [171], increasing confidence that at least the relative measurement for ^{48}Ti therein should be reliable.

Similar difference measurements, relative to ^{48}Ti, are available for ^{46}Ti and ^{50}Ti [181], i.e., for the analysis of these charge distributions we could, in principle, use our previous results for ^{48}Ti as input. Unfortunately, the quality of these difference measurements is borderline, and for ^{46}Ti we were not able to extract meaningful uncertainty estimates. This conclusion is actually in line with the discussion of charge radii already given in Ref. [181], for which a tension to the previous measurement from Ref. [180] is observed, and indeed the isotope shift for ^{46}Ti compared to ^{48}Ti is compatible with zero instead of being slightly positive as found in spectroscopy measurements. More details on our fits for ^{46,48}Ti are discussed in App. D.1.1, the conclusion being that we only quote results for the case of ^{50}Ti. Apart from a more consistent data situation compared to ^{46}Ti, also a (qualitative) cross-check against Ref. [182] becomes possible, increasing confidence that the extracted charge distribution for ^{50}Ti is still useful despite the issues described in App. D.1.1.

For the remaining naturally occurring titanium isotopes, ^{47}Ti ($J = 5/2$) and ^{49}Ti ($J = 7/2$), we only found measurements of the magnetic part of the interaction in Refs. [214, 215], but not the main Coulomb contribution. The necessity of having reasonable control over the magnetic part of the cross-section for a robust extraction of the charge distribution in case of $J > 0$, see ^{27}Al in the next section, would complicate the extraction in either case, but since not even information on the Coulomb part could be retrieved, we do not see a way to extract charge distributions for these isotopes from electron-scattering data at present.

Our final results for ^{48}Ti and ^{50}Ti are shown in Fig. 6.5. The bands for the extracted charge distributions encompass statistical and systematic components, including the uncertainties propagated from the respective reference points as determined in our previous fits. The

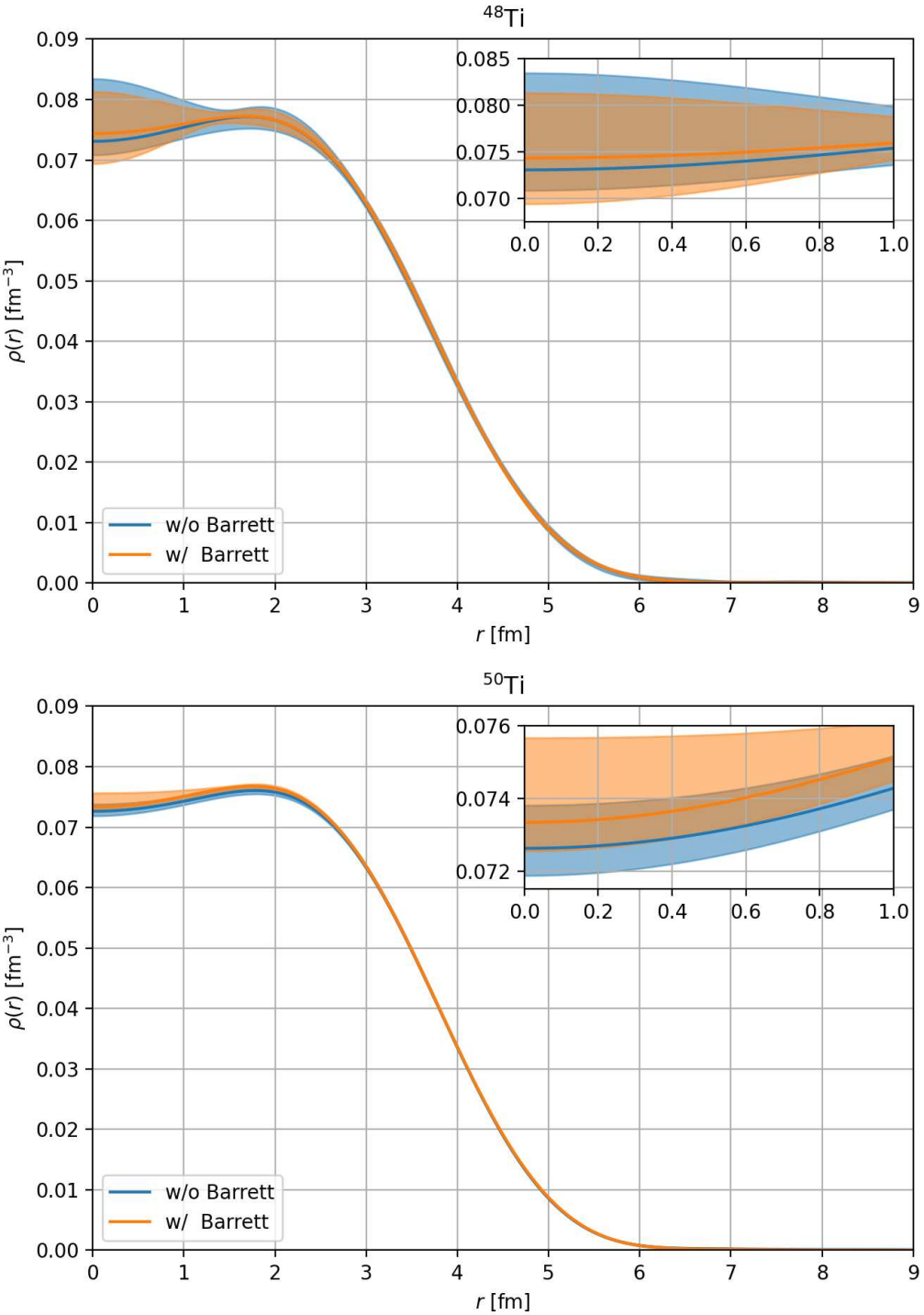

Figure 6.5: Charge densities of ^{48}Ti and ^{50}Ti. Two variants are shown, with (orange) or without (blue) the constraints from Barrett moments.

uncertainties are appreciably larger than for ^{40,48}Ca, as a direct consequence of the tenuous data situation. Accordingly, in this case, no significant tension with the Barrett moments arises.

6.2.3 Aluminum

For aluminum, we considered the scattering data taken in Refs. [184–193]. While, in principle, a fair number of measurements exists, only a few references documented the measured cross sections, so that in many cases at best a digitization of results on logarithmic plots would be possible. Even more disappointingly, the most precise scattering data off ^{27}Al ever taken, forming the basis for the FB fits given in Ref. [134], are not even published as a PhD thesis, but appear to be lost as "private communication." Given these restrictions, it is evident that the resulting uncertainties for ^{27}Al will again be more sizable than for our calcium fits.

Ultimately, we were able to track down the data from Refs. [185, 189, 192], where Ref. [189] shows the best coverage of momentum transfer. Reference [192] would allow one to add a few data points in the very low-energy region, but due to internal inconsistencies (likely reflecting an incomplete report of systematic uncertainties) as well as minor impact on the fit (since the total charge is conserved by construction), there was at best marginal gain by including these points in the fit. Likewise, the impact of the data from Ref. [185] proved negligible, given that the same range in momentum transfer was covered in Ref. [189] with much higher precision. Finally, we considered additional measurements in Ref. [189] at scattering angle 135° scanned over energy, but again the impact proved minimal due to the much higher contamination from higher multipoles compared to the main data set. Taken together with the significant cost of evaluating the DWBA for further energy values in the fit, we, therefore, concentrated on the main scans from Ref. [189] taken at $E = \{250, 500\}$ MeV.

A key point in the fit for ^{27}Al concerns the question of how to account for the non-zero spin $J = 5/2$, adding a new layer of complexity compared to the $J = 0$ nuclei considered in the previous sections. Two main effects complicate the extraction of the charge distribution. First, higher Coulomb multipoles, see Eqs. (5.5) and (5.6), contribute, filling out the minima that arise in the leading spherically symmetric charge form factor at $L = 0$. Second, magnetic contributions to the cross-section, see Eq. (5.4), need to be taken into account before conclusions on the charge distribution become possible. We address these corrections using estimates from the nuclear shell-model [1] (for the higher Coulomb multipoles) and ab-initio calculations using the in-medium similarity renormalization group (IMSRG) [100–102] (for both classes of corrections)[2]. We benchmarked the accuracy of these corrections by comparing to the elastic magnetic form factor as compiled in Ref. [216] using input from Refs. [187, 188, 191] (as well as further "private communication" sources), see Fig. 6.6. These data sets contain measurements beyond the 180° limit, in which only the magnetic contribution survives so that the interpretation again requires assumptions on the treatment of the Coulomb contribution as well. Especially in view of these caveats,

[2]We thank Matthias Heinz for providing these IMSRG results for the required M, Φ'', Σ', Δ multipoles.

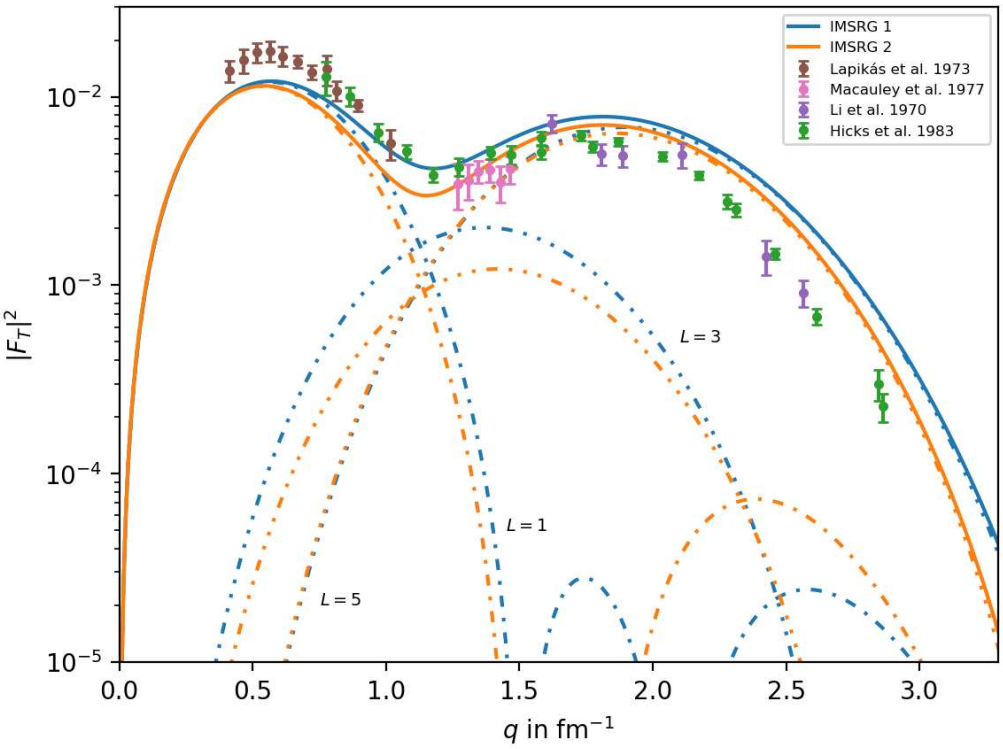

Figure 6.6: Results for the ^{27}Al transverse form factor F_T in comparison to the data given in Ref. [216], digitized and converted to our normalization convention. The data sets are Lapikás et al. 1973 [188], Li et al. 1970 [187], Macauley et al. 1977 (quoted in Ref. [191]), and Hicks et al. 1983 ("private communication"). In comparison, we show results from IMSRG calculations for two chiral Hamiltonians, as determined from the Σ'_L, Δ_L multipoles for $L = 1, 3, 5$ (dot-dashed curves, with the total given by the solid lines). IMSRG 1 and IMSRG 2 refer to two chiral Hamiltonians, ΔN2LO$_{\rm GO}$ [217] and N2LO$_{\rm sat}$ [218], respectively.

we observe that the IMSRG results, shown for two different chiral Hamiltonians, provide a very decent description of the data, justifying their use to subtract contributions beyond the $L = 0$ Coulomb multipole. We also show the $L > 0$ corrections to the longitudinal form factor, see Fig. 6.7, comparing the IMSRG results to nuclear shell-model calculations. Some differences are visible in the $L = 4$ contribution, leading to a slightly faster filling of the minimum of the $L = 0$ PWBA form factor in the case of the shell-model result.

Given that a purely data-driven determination of all the additional multipoles seems out of reach, we remove any data points that are clearly dominated by these corrections and only keep those points fulfilling the condition

$$\left(\frac{\mathrm{d}\sigma}{\mathrm{d}\Omega}\right)_{\rm data} - \left(\frac{\mathrm{d}\sigma}{\mathrm{d}\Omega}\right)_{L>0} > \Delta\left(\frac{\mathrm{d}\sigma}{\mathrm{d}\Omega}\right)_{\rm data}, \tag{6.19}$$

i.e., we include data points in the fit as long as the remainder after subtracting the $L > 0$ corrections is not consistent with zero. As input for $\left(\frac{\mathrm{d}\sigma}{\mathrm{d}\Omega}\right)_{L>0}$ we use the arithmetic mean of the two IMSRG calculations, while the spread between them (and to the shell-model

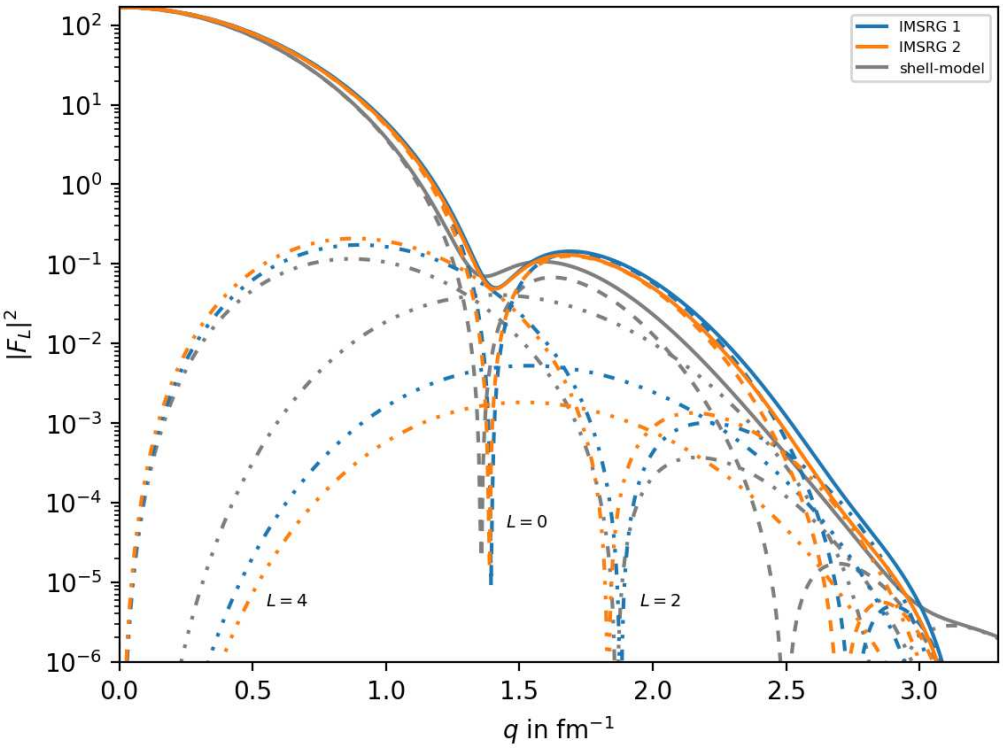

Figure 6.7: Results for the ^{27}Al longitudinal form factor F_L. IMSRG 1 and IMSRG 2 refer to the same two chiral Hamiltonians as for F_T, with F_L determined from the M_L, Φ''_L multipoles for $L = 0, 2, 4$ (dot-dashed curves, with the total given by the solid lines). Furthermore, we show results from the shell-model calculation from Ref. [1], based on Refs. [98, 99, 135, 137].

calculation) can serve as an estimate of the uncertainty. Given the sizable errors of the cross-section data themselves, we assume that for the data points that fulfill condition (6.19) the remaining systematic uncertainty is subdominant, or at least sufficiently covered by the scale factor. Fig. 6.8 shows the extracted $L = 0$ charge density for ^{27}Al, including uncertainty bands that comprise both statistical and systematic components.

6.2.4 Charge Radii and Discussion

To compare our results to previous work, it is instructive to consider the resulting charge radii, see Tab. 6.2, where we compare our determinations (with and without constraints from Barrett moments) to the ones from Refs. [134, 143]. The radii quoted in Ref. [143] are derived from spectroscopy measurements. Accordingly, these values agree well with our fits including Barrett moments, where the additional uncertainties in our case originate from the systematics of the combined fit. For ^{27}Al and ^{40,48}Ca the determinations from Ref. [134] are based on electron scattering data so that the resulting values largely agree with our fits excluding the Barrett-moment constraint. For ^{27}Al we do see a sizable difference, mainly due to the fact that we did not have access to the "private communication" data on which

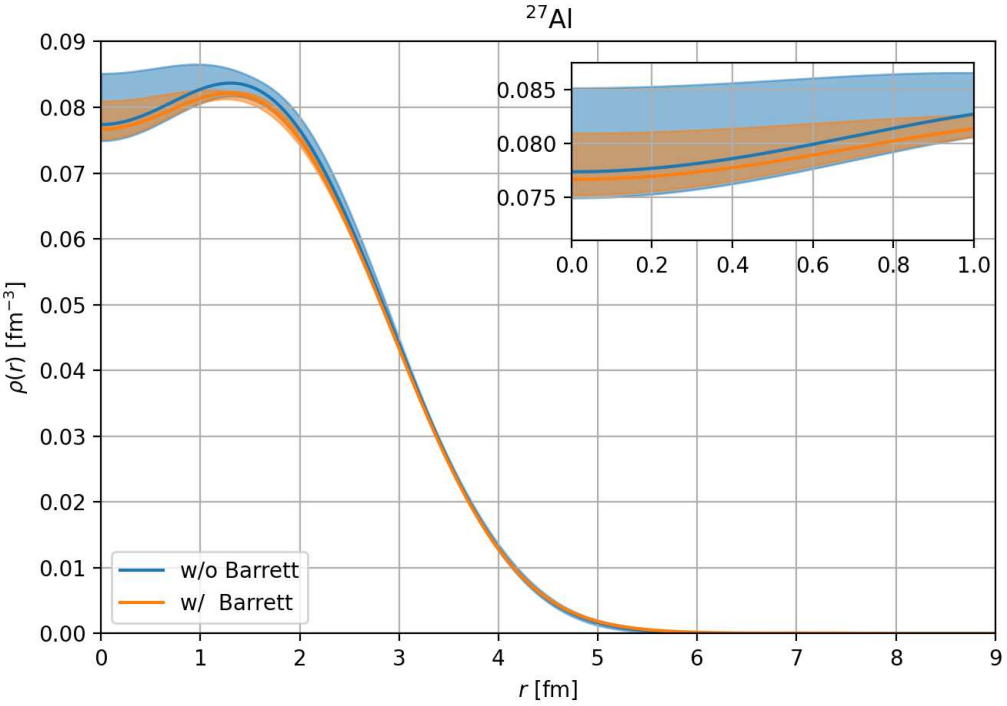

Figure 6.8: Charge density of ^{27}Al ($L = 0$). Two variants are shown, with (orange) or without (blue) the constraints from Barrett moments.

the FB fit from Ref. [134] is based. Comparing with our uncertainty estimates for ^{40}Ca, however, for which the data situation is exceptional in comparison, we believe that the uncertainty quoted in Ref. [134] for $\sqrt{\langle r^2 \rangle}$ is unrealistic, even if data of similar quality as for ^{40}Ca had been available at the time. Finally, for ^{48,50}Ti we do not have a direct comparison of electron-scattering-only determinations, since the FB fit from Ref. [134] already includes spectroscopic information, as confirmed by comparing with the FB fit in Ref. [182].

For each quoted charge radius, we show two variants of estimating the systematic uncertainty. The upper numbers are derived by propagating our systematic uncertainty band for the charge distribution, based on the final systematic covariance matrix for the FB parameters. In comparison, the lower numbers are deduced directly from the spread observed among the individual FB fits from which the systematic covariance matrix is constructed. In most cases, we observe reasonable agreement among the two estimates, with a few notable exceptions. First, the fits including Barrett moments essentially impose the spectroscopic value of the charge radius, in such a way that the spread among the individual fits is small. Accordingly, for these fits the systematic error propagated from the charge distribution tends to overestimate the true uncertainty (and potentially sizably so, as for ^{27}Al and ^{48}Ti). We emphasize, however, that this effect is special for the charge radius, and will become less pronounced the weaker a given quantity is correlated with the charge radius. Second, for ^{48}Ti also in the fit without Barrett moments the systematic uncertainties in the charge distribution appear overestimated, tracing back to the construction as an envelope of the individual fits. In this case, constructing a covariance matrix that encompasses all acceptable individual fits entails a large systematic uncertainty. This

behavior is ultimately caused by the poor data quality, e.g., for ^{40,48}Ca the different ways of estimating systematic errors show a higher degree of consistency.

Comparing the spectroscopy values from Ref. [143] with our electron-scattering-only fits, we can also quantify potential tensions between the two approaches. For ^{27}Al, we do see a deficit, but only at the level of 1.5σ, due to the sizable systematic uncertainty from the electron-scattering determination. Accordingly, the 7σ difference between Refs. [134, 143] very likely originates from underestimated uncertainties in Ref. [134]. For ^{40,48}Ca the tensions are more significant, particularly for ^{48}Ca. That is, in both cases the central values come out almost identical for both isotopes, in agreement with Refs. [134, 143], but we find that the systematic uncertainties in the ^{48}Ca are reduced compared to ^{40}Ca by almost a factor 2, increasing the tension in the charge radii from 2.5σ for ^{40}Ca to 4.3σ for ^{48}Ca. Interestingly, the systematic uncertainties hardly increase in the fits including Barrett moments, since the fit is able to accommodate a larger charge radius by modifications of the charge distribution at larger distances, see App. D.1. Finally, for ^{48,50}Ti we find charge radii larger than the spectroscopic values, but in these cases, the systematic uncertainties are large enough that no significant tension can be inferred.

All just presented results, including the full charge density parameterizations with uncertainties and correlations, are also made available in a supplementary `python` notebook provided in Ref. [2].

In view of the tensions for the calcium fits, one could worry about the impact of higher-order radiative corrections. Such two-photon effects, which are, in principle, sensitive to the possible excitations of the intermediate-state nucleus, go under the name of dispersive corrections. They become most relevant in the vicinity of the minima, contributing further to the filling of the zeros of the PWBA form factor. Such corrections have been studied in the literature, see, e.g., Refs. [219–229], but phenomenological estimates of their impact remain uncertain and model dependent. In Ref. [229] an upper bound on the impact of dispersive corrections on the charged radius is formulated in terms of

$$\Delta_{\text{disp}}\sqrt{\langle r^2\rangle} \simeq -\frac{3\sigma_{-1}}{4\pi Z\sqrt{\langle r^2\rangle}} \simeq -\frac{3a_0}{2\pi r_0} \simeq -7\times 10^{-3}\ \text{fm}, \tag{6.20}$$

with phenomenological parameters $\sqrt{\langle r^2\rangle} \simeq r_0 A^{1/3}$, $\sigma_{-1} \simeq a_0 A^{4/3}$, $r_0 \simeq 1.1$ fm, $a_0 \simeq 0.016$ fm^2 to try and estimate polarization effects. More realistic calculations tend to give smaller corrections [229, 230], so that while Eq. (6.20) slightly moves the ^{40,48}Ca radii from electron scattering towards the spectroscopy ones, one would suspect that the net effect is likely too small to make up the deficit. However, while in Ref. [229] it was concluded that the experimental evidence for dispersive corrections was scant, the calcium data are precise enough that their impact could potentially be detected. To improve our analysis along these lines, dedicated nuclear-structure calculations of polarization corrections would be required, to obtain a more realistic assessment of the impact of dispersive corrections beyond rough estimates such as Eq. (6.20).

	$\sqrt{\langle r^2 \rangle}$ [fm]		$\langle r^k e^{-\alpha r} \rangle$ [fm^k]	
Nucleus	Our fit	Refs. [134, 143]	Our fit	Ref. [208]
^{27}Al	$2.996(11)^{(43)[44]}_{(+26)(-33)[35]}$	3.035(2)	$8.32(6)^{(22)[23]}_{(+14)(-17)[18]}$	
	$3.063(3)^{(30)[31]}_{(+0)(-1)[3]}$	3.0610(31)	$8.66(1)^{(15)[15]}_{(+0)(-0)[1]}$	8.662(10)
^{40}Ca	$3.452(3)^{(8)[9]}_{(+1)(-9)[10]}$	3.450(10)	$10.637(18)^{(43)[47]}_{(+4)(-47)[50]}$	
	$3.4771(17)^{(17)[24]}_{(+0)(-5)[17]}$	3.4776(19)	$10.767(8)^{(8)[11]}_{(+0)(-2)[8]}$	10.776(10)
^{48}Ca	$3.4499(29)^{(31)[42]}_{(+42)(-52)[60]}$	3.451(9)	$10.645(16)^{(17)[23]}_{(+22)(-26)[31]}$	
	$3.475(2)^{(10)[10]}_{(+0)(-3)[4]}$	3.4771(20)	$10.772(9)^{(46)[47]}_{(+1)(-10)[14]}$	10.781(10)
^{48}Ti	$3.62(3)^{(8)[8]}_{(+2)(-3)[4]}$	3.597(1)	$11.50(14)^{(39)[41]}_{(+9)(-15)[21]}$	
	$3.596(3)^{(57)[57]}_{(+1)(-1)[3]}$	3.5921(17)	$11.39(1)^{(28)[28]}_{(+0)(-0)[1]}$	11.388(11)
^{50}Ti	$3.612(16)^{(42)[45]}_{(+19)(-48)[51]}$	3.572(2)	$11.45(8)^{(21)[23]}_{(+9)(-23)[25]}$	
	$3.572(3)^{(9)[9]}_{(+0)(-2)[3]}$	3.5704(22)	$11.254(12)^{(43)[45]}_{(+0)(-2)[12]}$	11.256(10)

Table 6.2: Extracted charge radii and Barrett moments. For each isotope, the upper/lower entries refer to the fits excluding/including the Barrett moments as constraint, with input values from Tab. 6.1 repeated in the last column. Moreover, for each entry, the common first error refers to the statistical uncertainty, while we show two variants of the systematic (and total, in square brackets) uncertainty, the upper one being propagated from the charge distribution, the lower one directly from the charge radii corresponding to the set of FB fits on which the systematic uncertainty band for the charge distribution is based. For comparison, we also quote the charge radii given in Ref. [134] (upper) and Ref. [143] (lower). Note that, while the radii given in Ref. [143] are derived from spectroscopy measurements, for Ref. [134] it is not always clear if spectroscopy constraints are included, but at least for ^{48,50}Ti Ref. [182] confirms that this is the case. The results for ^{50}Ti are separated by a dashed line, to indicate that the systematic uncertainties are harder to quantify than for the other isotopes, for the reasons spelled out in App. D.1.1.

Chapter 7

Towards a Correlation Analysis of Overlap Integrals

We have already seen in Sec. 3.8.1, that the decay rate for $\mu \to e$ conversion in nuclei is conventionally expressed in terms of the overlap integrals as introduced in Ref. [88] and shown in Eq. (3.92). In this chapter, we illustrate how uncertainties from the nuclear charge densities can be propagated to these overlap integrals. In particular, for the dipole interaction, this calculation is straightforward as the overlap integral is solely dependent on the charge density, which we extracted quantitatively in the previous chapter. The scalar and vector interactions on the other hand depend on the proton and neutron densities and need to be correlated to the charge density using nuclear structure calculations. These are carried out using ab-initio calculations. In contrast to the empirical shell-model calculations employed in Chap. 4, which are only assessed in comparison to experiments and are thus hard to test for experimentally hard-to-access quantities like the neutron charge density, the ab-initio calculations are based on QCD principles and facilitate a better assessment of the nuclear structure uncertainties.

7.1 Dipole Operators[1]

We first focus on the case of a dipole interaction. The part of the Lagrangian of Eq. (2.3) which describes this interaction is given by

$$\mathcal{L}_{\text{dipole}} = \frac{1}{\Lambda} \sum_{Y=L,R} C_Y^D \overline{e_Y} \sigma^{\mu\nu} \mu F_{\mu\nu} + \text{h.c.} = -\frac{4G_F}{\sqrt{2}} \frac{m_\mu}{\Lambda^2} \sum_{Y=L,R} A_Y \bar{\mu} \sigma^{\mu\nu} P_{\bar{Y}} e F_{\mu\nu} + \text{h.c.}, \quad (7.1)$$

where on the right-hand side, we followed the convention from Ref. [88] and counted the operator as dimension-6 with a chirality flip mediated by the muon mass, and the C_Y^D or

[1] This section was published as part of Ref. [2].

respectively the A_Y denote the corresponding Wilson coefficients. Since this operator leads to a long-range interaction, the response is determined by the charge form factor of the nucleus, and, accordingly, the respective overlap integral follows directly from the charge distribution without the need for any further nuclear corrections. With the definitions from Ref. [88], the overlap integrals from Eq. (3.84) take the explicitly form

$$\begin{aligned}\bar{D}_1 &= -\frac{4}{\sqrt{2}} m_\mu D_1 = -\frac{4}{\sqrt{2}} m_\mu \int_0^\infty \mathrm{d}r\, E(r) \left[g_{-1}^{(e)}(r)\, f_{-1}^{(\mu)}(r) + f_{-1}^{(e)}(r)\, g_{-1}^{(\mu)}(r) \right], \\ \bar{D}_2 &= -\frac{4}{\sqrt{2}} m_\mu D_2 = +\frac{4}{\sqrt{2}} m_\mu \int_0^\infty \mathrm{d}r\, E(r) \left[f_{+1}^{(e)}(r)\, f_{-1}^{(\mu)}(r) - g_{+1}^{(e)}(r)\, g_{-1}^{(\mu)}(r) \right], \end{aligned} \tag{7.2}$$

where $E(r)$ denotes the electric field and $f_\kappa^{(\ell)}(r)$, $g_\kappa^{(\ell)}(r)$, $\ell = e, \mu$, the muon and electron wave functions obtained by solving the Dirac equation. Following Eq. (5.48) in the limit $m_e = 0$ it follows $g_{+1}^{(e)} = f_{-1}^{(e)}$ and $f_{+1}^{(e)} = -g_{-1}^{(e)}$ and thus $D \equiv D_1 = D_2$, which is the limit considered in Ref. [88]. The electric field $E(r)$ follows from a given charge distribution $\rho(r)$ by virtue of Eq. (5.24), while the quantum numbers of the lepton wave functions, $\kappa = \mp 1$, are determined by the requirement that the initial-state muon occupy the $1s$ ground state. The total energy

$$E = \frac{(m_M + m_\mu + E_b^\mu)^2 - m_M^2 + m_e^2}{2(m_M + m_\mu + E_b^\mu)} \simeq m_\mu + E_b^\mu - \frac{m_\mu^2}{2m_M} + \ldots, \tag{7.3}$$

follows from the mass of the nucleus m_M including recoil effects [76] and the binding energy $E_b^\mu < 0$ via the ground-state solution, in line with Eq. (3.2). Going beyond the $m_e = 0$ limit, the decay rate changes according to Eqs. (3.83) and (3.86) and does only constitute interference terms via the superseded independence of the different helicity electrons, and not directly between terms with electron $\kappa = \mp 1$, as they correspond to real and imaginary part of the amplitude, respectively.

The uncertainty propagation from $E(r)$ is straightforward and can, in principle, be carried out analytically. However, to include also the uncertainty propagation from changes of the wave functions it is easiest to calculate the derivatives with respect to the FB parameters numerically. We calculate

$$\frac{\mathrm{d}D}{\mathrm{d}a_n} = \frac{D(\rho(a_1, \ldots, a_n + h, \ldots, a_N)) - D(\rho(a_1, \ldots, a_n, \ldots, a_N))}{h}, \tag{7.4}$$

with $h = a_i \cdot 10^{-6}$, which performs well since D turns out to be quite linear in local changes of a_i, as underlined by the fact, that including effects from the electron mass change only the central values, but not the uncertainties.

Using the FB parameters and their covariances provided in App. D.2, we obtain the results summarized in Tab. 7.1, where we also include the second variant to estimate systematic uncertainties based on the individual FB fits on which the construction of the systematic covariance matrix is based, in analogy to Tab. 6.2. First, we can check that our results are consistent with Ref. [88], in which the FB parameterizations from Ref. [134] were employed, see the comparison of the last two columns. In all cases, we observe a small deviation $\Delta\bar{D} = 1 \times 10^{-4}$, less than the effect of keeping m_e, as indicated by the difference

	This work				Ref. [88]	Ref. [134]
Nucleus	$\bar{D}_1$	$\bar{D}_2$	$\bar{D}$	$\Delta\bar{D}$	$\bar{D}$	
^{27}Al	0.03651	0.03668	0.03652	$(14)^{(55)[57]}_{(^{+41}_{-31})[44]}$	0.0362	0.03608*
	0.03586	0.03602	0.03587	$(2)^{(24)[24]}_{(^{+1}_{-3})[4]}$		
^{40}Ca	0.07584	0.07619	0.07587	$(10)^{(22)[24]}_{(^{+22}_{-2})[24]}$	0.0761	0.07595*
	0.075275	0.075625	0.075311	$(31)^{(33)[45]}_{(^{+14}_{-10})[34]}$		
^{48}Ca	0.07526	0.07561	0.07532	$(9)^{(10)[13]}_{(^{+10}_{-10})[13]}$		0.07531*
	0.07474	0.07508	0.07479	$(2)^{(10)[10]}_{(^{+1}_{-6})[7]}$		
^{48}Ti	0.0860	0.0864	0.0860	$(5)^{(16)[17]}_{(^{+5}_{-3})[7]}$	0.0864	0.08627*
	0.0863	0.0867	0.0864	$(1)^{(9)[9]}_{(^{+1}_{-1})[1]}$		
^{50}Ti	0.0862	0.0866	0.0863	$(3)^{(9)[9]}_{(^{+8}_{-3})[9]}$		0.08705*
	0.08696	0.08736	0.08702	$(12)^{(28)[31]}_{(^{+1}_{-12})[17]}$		

Table 7.1: Resulting dipole overlap integrals in units of $m_\mu^{5/2}$ in comparison to Ref. [88] and values calculated by us based on the parameterizations from Ref. [134]. The values for $\bar{D}$ are obtained assuming $m_e = 0$ and neglecting recoil corrections, in line with the conventions from Ref. [88]. $\bar{D}_{1,2}$ correspond to Eq. (7.2), with $m_e \neq 0$ and including recoil effects. The upper/lower values use the charge distributions from the fits excluding/including the Barrett moments. In each case, the systematic uncertainties are quoted in the two variants introduced in Tab. 6.2. The differences in the uncertainties $\Delta\bar{D}$ between $\bar{D}$, $\bar{D}_1$, and $\bar{D}_2$ are below the level quoted here.

between $\bar{D}_1$ and $\bar{D}_2$. In the last column, we have also produced reference values for the charge distributions from Ref. [134] for the remaining isotopes. As main results, we can now provide robust uncertainty estimates for D, directly propagated from the charge distributions. For ^{27}Al, this uncertainty is reduced appreciably once the Barrett-moment constraint for the charge radius is imposed, with a final value

$$\bar{D}\big(^{27}\mathrm{Al}\big) = 0.0359(2), \tag{7.5}$$

slightly lower than in Ref. [88], but consistent within uncertainties (the systematic error could be estimated more aggressively by looking at the individual FB fits). For ^{40,48}Ca, the tensions in the charge distributions are reflected at the (2–3)σ level for D, with best values including Barrett moments of

$$\bar{D}\big(^{40}\mathrm{Ca}\big) = 0.07531(5), \qquad \bar{D}\big(^{48}\mathrm{Ca}\big) = 0.07479(10). \tag{7.6}$$

Finally, for titanium we obtain

$$\bar{D}\big(^{48}\mathrm{Ti}\big) = 0.0864(1), \qquad \bar{D}\big(^{50}\mathrm{Ti}\big) = 0.0870(3), \tag{7.7}$$

where for ^{48}Ti we quote the systematic error based on the individual FB fits to avoid the overestimation discussed in Sec. 6.2.4. On the contrary, for ^{50}Ti the uncertainty might be slightly underestimated as a result of the rather indirect way, its charge distribution needs to be extracted from the data.

7.2 Prospects for Scalar and Vector Operators

We have already seen in the previous section how quantitative inputs for the dipole overlap integrals, as given in Eq. (7.2), can be derived based on the charge density parameterizations determined in the previous chapter, as they are directly related to the electric field of the nucleus. In this section, we demonstrate how similar results can be achieved for the scalar and vector overlap integrals, which are not directly accessible experimentally, with the help of ab-initio calculations of the nuclear response.

The parts of the Lagrangian of Eq. (2.3) which describes the scalar and vector interactions are given by

$$\begin{aligned}
\mathcal{L}_{\mathrm{scalar}} &= \frac{1}{\Lambda^2} \sum_{Y=L,R} C_Y^{S,q}\ \overline{e_Y}\mu\ \bar{q}q + \mathrm{h.c.} = -\frac{G_F}{\sqrt{2}} \frac{1}{\Lambda^2} \sum_{Y=L,R} g_{YS(q)}\ \overline{e_Y}\mu\ \bar{q}q + \mathrm{h.c.}, \\
\mathcal{L}_{\mathrm{vector}} &= \frac{1}{\Lambda^2} \sum_{Y=L,R} C_Y^{V,q}\ \overline{e_Y}\gamma^\mu\mu\ \bar{q}\gamma_\mu q + \mathrm{h.c.} = -\frac{G_F}{\sqrt{2}} \frac{1}{\Lambda^2} \sum_{Y=L,R} g_{YS(q)}\ \overline{e_Y}\gamma^\mu\mu\ \bar{q}\gamma_\mu q + \mathrm{h.c.},
\end{aligned} \tag{7.8}$$

where on the right-hand side, we again matched to the conventions from Ref. [88], and $C_Y^{S/V,q}$ or respectively the $g_{YS/V(q)}$ denote the Wilson coefficients. As derived in Chap. 3, considering only one-nucleon interactions, the point-like scalar and vector interactions lead to independent interactions with the protons and neutrons of the nucleus. According to

the derivations in Sec. 3.8.1 this leads to the scalar and vector overlap integrals, which are given for $N = n, p$ according to Eq. (3.90) as

$$\begin{aligned}\bar{S}^{(N)} &= \frac{1}{\sqrt{2}} S^{(N)} = \frac{1}{2\sqrt{2}} \int_0^\infty \mathrm{d}r \ (\#N)\rho_N(r) \left[g_{-1}^{(e)}(r) g_{-1}^{(\mu)}(r) - f_{-1}^{(e)}(r) f_{-1}^{(\mu)}(r) \right], \\ \bar{V}^{(N)} &= \frac{1}{\sqrt{2}} V^{(N)} = \frac{1}{2\sqrt{2}} \int_0^\infty \mathrm{d}r \ (\#N)\rho_N(r) \left[g_{-1}^{(e)}(r) g_{-1}^{(\mu)}(r) + f_{-1}^{(e)}(r) f_{-1}^{(\mu)}(r) \right], \end{aligned} \tag{7.9}$$

where we again changed to the conventions of Ref. [88]. In contrast to the dipole overlap integral, which depends directly on the charge density, these overlap integrals depend on the proton and neutron density which are directly related to the proton and neutron M responses. These are a lot harder to measure directly in an experiment than the full charge form factor. As we have seen in the previous chapter, the charge form factor can be extracted from elastic electron scattering and is given according to Eq. (5.10) as

$$\begin{aligned} Z F_L^{\mathrm{ch}}(q^2) = &\left(1 - \tfrac{\langle r_p^2 \rangle}{6} q^2 - \tfrac{1}{8m_N^2} q^2 \right) \mathcal{F}_L^{M_p}(q^2) - \tfrac{\langle r_n^2 \rangle}{6} q^2 \mathcal{F}_L^{M_n}(q^2) \\ &+ \tfrac{1+2\kappa_p}{4m_N^2} q^2 \mathcal{F}_L^{\Phi''_p}(q^2) + \tfrac{2\kappa_n}{4m_N^2} q^2 \mathcal{F}_L^{\Phi''_n}(q^2) + \mathcal{O}(q^4). \end{aligned} \tag{7.10}$$

While this is dominated by the M_p response, and thus the proton density ρ_p could at leading order be approximated by the charge density ρ_{ch}, the M_n response is only a $\mathcal{O}(q^2)$ correction and thus there is no clear way to extract the neutron density ρ_n without any further input. Furthermore, for a quantitative extraction, there is no clear way to remove the contamination from the Φ'' responses experimentally.

Only recently measurements of PVES made independent experimental inputs on the M_n response possible. In PVES the central observable is the left-right asymmetry, which can be derived in analogy to elastic electron scattering based on the quark-level interactions as

$$A_{\mathrm{PVES}} = \frac{(\frac{\mathrm{d}\sigma}{\mathrm{d}\Omega})_R - (\frac{\mathrm{d}\sigma}{\mathrm{d}\Omega})_L}{(\frac{\mathrm{d}\sigma}{\mathrm{d}\Omega})_R + (\frac{\mathrm{d}\sigma}{\mathrm{d}\Omega})_L} \approx -\frac{G_F q^2}{4\pi\alpha_{\mathrm{el}}\sqrt{2}} \frac{Q^{\mathrm{w}} F_0^{\mathrm{w}}(q^2)}{Z F_0^{\mathrm{ch}}(q^2)}, \tag{7.11}$$

where we only consider the leading $L = 0$ contributions, which will be the only terms for nuclei with total spin $J = 0$. This defines the weak form factor in analogy to the charge form factor as

$$\begin{aligned} Q^{\mathrm{w}} F_L^{\mathrm{w}}(q^2) = &\left(Q_p^{\mathrm{w}} \left(1 - \tfrac{\langle r_p^2 \rangle}{6} q^2 - \tfrac{1}{8m_N^2} q^2 \right) - Q_n^{\mathrm{w}} \tfrac{\langle r_n^2 \rangle + \langle r_{s,N}^2 \rangle}{6} q^2 \right) \mathcal{F}_L^{M_p}(q^2) \\ &+ \left(Q_n^{\mathrm{w}} \left(1 - \tfrac{\langle r_n^2 \rangle + \langle r_{s,N}^2 \rangle}{6} q^2 - \tfrac{1}{8m_N^2} q^2 \right) - Q_p^{\mathrm{w}} \tfrac{\langle r_n^2 \rangle}{6} q^2 \right) \mathcal{F}_L^{M_n}(q^2) \\ &+ \frac{Q_p^{\mathrm{w}}(1 + 2\kappa_p) + 2Q_n^{\mathrm{w}}(\kappa_n + \kappa_{s,N})}{4m_N^2} q^2 \mathcal{F}_L^{\Phi''_p}(q^2) \\ &+ \frac{Q_n^{\mathrm{w}}(1 + 2\kappa_p + 2\kappa_{s,N}) + 2Q_p^{\mathrm{w}} \kappa_n}{4m_N^2} q^2 \mathcal{F}_L^{\Phi''_n}(q^2) \end{aligned} \tag{7.12}$$

using the conventions of Ref. [116] with the proton and neutron weak charges given as [130, 231, 232]

$$Q_p^{\mathrm{w}} = 0.0710(4), \qquad Q_n^{\mathrm{w}} = -0.9891(3). \tag{7.13}$$

including radiative corrections, and the uncertainty reflecting the different renormalization schemes for $\sin^2\theta_W$. The weak form factor is thus dominated by the M_n response and the neutron density ρ_n can at leading order be approximated by the corresponding weak density ρ_{w}. In particular, combining inputs from the charge and the weak from factor the M_p and M_n responses can in principle be isolated, if the Φ'' responses are separately under control. Unfortunately, this is not the case yet, and PVES has only been measured for a few selected nuclei and momentum transfers [164–166]. Hence, for quantitative inputs of the proton and neutron densities, different strategies need to be employed.

One possible way around this limitation is to employ ab-initio calculations for the nuclear responses. While the central values of the predictions of nuclear structure observable via ab-initio calculations still strongly depend on the underlying interactions, indicating large systematic effects related to the implied chiral Hamiltonians, the correlations between different observables are significantly more stable. This enables robust predictions for quantities that are hard to access experimentally based on experimentally easily accessible ones [167, 168]. In this case, we predict the values of the overlap integrals depending on the proton or neutron densities, which are hard to access experimentally, based on the charge radius, which is easily accessible from the charge density and elastic electron scattering as shown in the previous chapter. In Fig. 7.1, we show the preliminary correlations between the charge radius squared and the overlap integrals for scalar and vector overlap integrals for ^{27}Al based on a selection of ab-initio calculations [217, 218, 233] using the IMSRG [100–102] as well as a shell-model calculation [98, 99, 137] for the proton, neutron and charge densities, which were carried out by our collaborators.[2] It directly becomes apparent, that while the central value of the different models varies, there is a clear linear dependence between the charge radius squared and the values of the overlap integrals, as nicely illustrated by the naively fitted lines. Using this strategy we can extract a more precise value for the overlap integral based on the experimentally extracted charge radii from Chap. 6, by calculating the intercept of the correlations and the experimental charge radius squared.

These results, here only shown qualitatively, will be presented in a future work, leading to quantitative inputs for the scalar and vector overlap integrals including a comprehensive uncertainty estimation, which we can propagate from our results for the charge radius from Chap. 6. For such a quantitative estimation, in particular, an extended discussion of statistical and systematic uncertainties needs to be conducted. First and foremost, an extended set of interactions should be studied going beyond the six results shown here. In that context, also systematic effects from the ab-initio calculations should be studied. In particular, the ab-initio calculations are carried out in a basis that breaks translational invariance. This results in a contamination of the calculated quantities with a center-of-mass motion, which needs to be accounted for [234].[3] Thus, systematic

[2] We thank Matthias Heinz for providing the ab-initio results and Javier Menéndez for the shell-model calculations.

[3] We thank Takayuki Miyagi (宮城宇志) and Matthias Heinz for useful discussions on this topic.

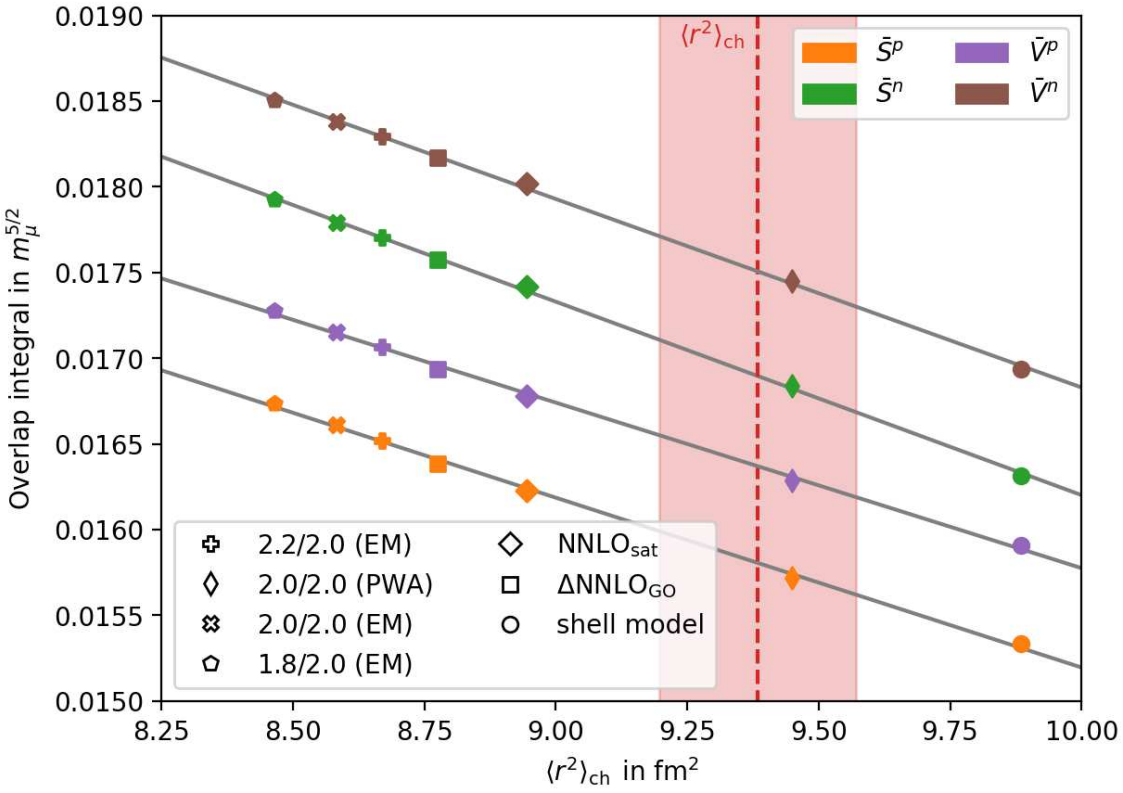

Figure 7.1: Preliminary correlation plots between the charge radius squared and overlap integrals for ^{27}Al for a set of ab-initio interactions [217,218,233] using the IMSRG [100–102] and the shell model [98, 99, 137]. The displayed value of the charge radius corresponds to the ^{27}Al result from Tab. 6.2 including the Barrett moment.

effects related to the way in which these center-of-mass effects are then resolved should be studied. Moreover, one can examine different alternatives to the charge radius squared as the integrated quantity based on the charge density. For example, one could consider as an alternative the integrals of Eq. (7.9) with $\rho_N \to \rho_{\rm ch}$, which would also be a scalar quantity based on the charge density, which could analogously be used for the correlation analysis. All these considerations should be systematically addressed and combined with the propagated uncertainties from the charge densities to combine into a comprehensive uncertainty estimation of the resulting scalar and vector overlap integrals.

In the long run, we would like to use similar methods to quantify uncertainty estimates also in subleading nuclear responses, where we first would need to study which nuclear structure observables are most suited to correlate to these responses. Employing such inputs would lead to a $\mu \to e$ conversion rate where all non-perturbative input quantities are systematically under control, whereas in the past, usually only uncertainties from hadronic matrix elements were considered. High precision in these predictions and quantifiable uncertainties also from the nuclear responses are crucial for a meaningful study of the diagnosing power of different $\mu \to e$ conversion target materials concerning disentangling the different contributing operators. While in principle the nuclear responses between any two different nuclei are distinct and thus put new constraints on the Wilson coefficients, it is advantageous to optimize for a combination of different nuclei, which combine

complementary sensitivities. Studying nuclei with significantly different numbers of neutrons N and protons Z can help separate underlying operators, as the coherent enhancement of the SI amplitude goes with the number of nucleons. For example, SD contributions have a bigger chance of competing against SI contributions in light nuclei and are, in comparison, more suppressed in heavy nuclei. Moreover, the individual overlap integrals, contributing to the SI amplitude, scale with either Z or N, depending on if they couple to protons or neutrons (see Eq. (7.9)). This means nuclei with different relative compositions of Z and N can help to disentangle couplings to protons and neutrons and subsequently between different quark flavors. However, for these strategies to work, the uncertainties of the $\mu \to e$ conversion description need to be under control. In particular, if SD contributions even for a lighter nucleus like aluminum are maybe at the $\sim 1\%$ level compared to the SI contributions, this means the uncertainties for the SI description need to be at a similar level to distinguish SD contributions from statistical fluctuations.[4] Similarly, predictions for the individual operators need to be precise enough that measurements with different compositions of Z and N can result in robust statements when assessing the sensitivity to different quark flavors. This strongly motivates an improvement in the precision of the nuclear structure inputs as well as a full quantification of nuclear uncertainties, as proposed in this section.

[4] As already pointed out in the discussion surrounding Eq. (4.25): Even if at BSM scales $\Lambda \gg m_W$ only SD operators exist, the RG running below the EW scale naturally produces SI operators, which may then dominate again due to the coherent enhancement of the SI responses.

Chapter 8

Conclusions and Outlook

Due to the several different scales involved, $\mu \to e$ conversion is a challenging process to describe, but at the same time provides stringent limits for studies of LFV. Thus, many works have already considered $\mu \to e$ conversion with EFT methods with versatile focal points, discussing bound-state physics, specific nuclear responses, two-nucleon interactions, RG corrections, or complementarity to other processes. The upcoming experiments Mu2e and COMET will now push the limits on $\mu \to e$ conversion by up to four orders of magnitude. This calls for a collaborative effort to combine all these facets of $\mu \to e$ conversion into a comprehensive EFT framework, which can describe all these aspects at the same time. In this work, we have performed the first steps in developing such a framework, by presenting a framework that includes a proper treatment of the nuclear response, and the bound-state physics at the same time. In particular, we rigorously include Coulomb distortion effects by employing the full numerical solutions for the lepton wave functions. For this framework, we list all amplitude-level terms, that are above pure $\mathcal{O}(q^2/m_N^2)$. Moreover, we could confirm consistency in the limit of the leading nuclear responses and a full bound-state physics description as well as simplified assumptions for the bound-state physics, but including subleading nuclear responses.

As the subleading nuclear responses for $\mu \to e$ conversion are mediated by the same effective operators as LFV decays of light pseudo-scalars, we can use these two processes to showcase how independent processes can lead to complementary constraints on the same LFV interactions. In particular, strict constraints on one process can lead to indirect constraints on the other process, with the same underlying operators. In this case, due to the stringent bounds on $\mu \to e$ conversion, we were able to find indirect limits on the LFV pseudo-scalar decays, which are several orders of magnitude stronger, than current experimental limits.

For a quantitative description of $\mu \to e$ conversion and proper discriminatory power among the different effective LFV operators, reliable inputs for the non-perturbative quantities, like the hadronic matrix elements or the nuclear response, are crucial. While inputs for the hadronic matrix elements are usually available from either phenomenological considerations or from LatticeQCD, the inputs for the nuclear response are harder to benchmark and

depend on complicated computationally expensive calculations of the nuclear structure, with different degrees of model dependence. Modern ab-initio methods to calculate nuclear structure are relatively model-independent and facilitate results that are grounded on QCD principles instead of empirical models. Especially, for quantities like the neutron charge density, which only recently became available experimentally in PVES, these calculations can generate inputs for nuclear responses, which are hard to disentangle experimentally. In particular, correlations with well-known quantities like the charge density, which is easily accessible via elastic electron nucleus scattering, can mitigate systematic effects and differences among different models for the nuclear responses.

For that reason, we reevaluated elastic electron-nucleus scattering data and extracted nuclear charge densities for a small selection of nuclei relevant to $\mu \to e$ conversion. We considered ^{27}Al, ^{48,50}Ti, and ^{40,48}Ca, since Mu3e and COMET are going to measure on aluminum, and the current best limits on $\mu \to e$ conversion are from titanium. The analysis of the calcium isotopes was necessary for the interpretation of the titanium data, due to a relative measurement, but also play an important role in the context of neutrinoless double-β decays and PVES. The latter one has seen recent developments with measurements on ^{27}Al, ^{48}Ca, and ^{208}Pb by the Qweak, CREX, and PREX-2 collaboration, respectively. In PVES reliable inputs for the charge form factor are crucial for a consistent experimental extraction of the weak form factor and the neutron density, which provides further motivation to focus on these isotopes. For that reason we presented as one main result of this work, the extracted charge densities of the above-mentioned nuclei, including a thorough study of statistical and systematical uncertainties as well as their correlations, which were not available in the literature up to that point. All results, including their uncertainties and correlations, were also made available to the community in a supplementary `python` notebook. Due to the quite dated, hard-to-retrieve, and in parts even lost elastic electron scattering data we advocate for data preservation measures as well as (re)measurements of elastic electron scattering, with modern methods and modern uncertainty management, for the nuclei most relevant for $\mu \to e$ conversion and PVES.

To demonstrate how the different uncertainty sources from the charge densities can be propagated, we calculated for the example of a dipole interaction, the overlap integrals that comprise the bound-state physics input for the leading nuclear responses. For the example of the dipole overlap integral, this quantity can be calculated solely based on the charge density, as on the one hand the bound-state physics is dictated by the nucleus potential, which is given by the charge density, and on the other hand the nuclear response for the dipole interaction is given in terms of the charge form factor, which also directly relates to the charge density. Furthermore, for scalar and vector interactions, we outline how ab-initio calculation can be employed to derive quantitative inputs for the related overlap integrals, using the correlations between different observables as well as our extracted charge densities.

Combining all these considerations, we developed a comprehensive framework for $\mu \to e$ conversion, which utilizes controlled inputs for bound-state physics and the nuclear responses at the same time, where we further demonstrated how these can be obtained. This is the first step toward phenomenological analyses of $\mu \to e$ conversion using this

framework, also in light of the upcoming experiments Mu2e and COMET, to facilitate a quantitative study of potential LFV interactions.

8.1 Outlook

Building upon the progress made in this thesis, we want to further improve our framework for $\mu \to e$ conversion. On the one hand, two-nucleon interactions are not part of the current consideration and could result in sizeable corrections, as well as necessary adjustments of the framework, having more kinematic degrees of freedom than the one-nucleon interactions. Similarly, corrections from RG evolution should be included, when studying BSM consequences. On the other hand, the nuclear structure aspects can further be refined in collaboration with experts in ab-initio theory.

In particular, in the already in Sec. 7.2 outlined future project, we will collaborate with experts on ab-initio calculations, to calculate overlap integrals for scalar and vector interactions, using the correlations between different nuclear structure observables. To that end, we will also propagate uncertainties from the charge densities onto the overlap integrals, which we have already demonstrated for the dipole overlap integral, which however for the scalar and vector integral additionally requires a study of the systematic effects from the correlations and nuclear structure calculations. Using this strategy we will then be able to provide quantitative inputs for scalar and vector overlap integrals, based on the charge densities already extracted.

In this context, we also plan to further improve our program, which fits charge density parameterizations to elastic electron scattering, and make it publicly available. This will make it possible for anyone to extract robust charge density parameterizations from elastic electron scattering data, using our implementation. In this way, if new data for the nuclei of interest for $\mu \to e$ conversion become available, they can be readily analyzed. Furthermore, for nuclei of interest in neutrino-nucleus scattering, neutrinoless double-β decays or PVES, this can also be utilized. In particular, given the complementarity of studying nuclei with different proton Z and neutron N content in all these processes, there may always be the consideration to study another nucleus, for which quantitative charge density parameterizations are not yet available.

In the case that really precise data becomes available, for nuclei with non-zero spin $J > 0$, Coulomb corrections for higher-order multipoles could become relevant and should be studied. This could potentially extend the existing `python` program to also include Coulomb corrections for higher-order multipoles. Moreover, in light of the slight tensions of the charge radii of the calcium isotopes between electron scattering and muon spectroscopy, higher-order radiative corrections to the charge densities could be studied.

More generally, $\mu \to e$ conversion remains a very promising probe for LFV operators, and with the experiments, Mu2e and COMET soon starting their measurements, we are excitedly looking forward to an improvement of up to four orders of magnitude in comparison to current $\mu \to e$ conversion limits. While a positive observation would clearly be spectacular and would allow for a detailed study of potential BSM scenarios, even just

this improvement of several orders of magnitude would further restrict potential LFV interactions substantially. In particular, in combination with the complementary limits from $\mu \to e\gamma$ and $\mu \to 3e$, which will also improve their limits in the next years via the experiments MEG2 and Mu3e respectively, this puts serious constraints onto LFV between electrons and muons. The proposed η/η' factories of JEF and REDTOP could also give complementary limits onto LFV decays of the η and η' meson, which however, as showed in Chap. 4, will not be able to supersede the indirect limits inferred from $\mu \to e$ conversion in nuclei. New limits for LFV Kaon decays could also become available via the planned upgrade of the KOTO experiment, which is after the cancellation of HIKE, now the only dedicated large-scale Kaon experiment. While flavor or CKM relations could potentially be used to relate these processes to other LFV processes, in itself the necessary LFV operators for these processes are independent and do complement the landscape of LFV searches. With the recent launch of Belle II, also more stringent limits on LFV τ-decays are to be expected in the near future, which will yet again give insights into complementary LFV interactions including τ leptons. Here in particular hadronic final states need to be systematically controlled.

With all these prospective experimental advances, it is timely to develop quantitative frameworks for these processes, which go beyond the leading qualitative features, to study the complementarity of different probes of LFV.

Appendix A

Notations and Abbreviations

In this appendix, we summarize the used abbreviations and some of the notations for easier reference.

A.1 Abbreviations

SM	Standard Model of particle physics
BSM	Beyond the SM
EFT	Effective field theory
SMEFT	SM EFT
LEFT	Low-energy effective field theory below the electroweak scale
QCD	Quantum Chromo Dynamics
ChPT	Chiral perturbation theory
LF	Lepton Flavor
LFV	LF Violation
NLFV	neutral LFV
CLFV	charged LFV
UV	Ultra violet
DIO	Decay in orbit
SD	Spin dependent
SI	Spin independent
FB	Fourier Bessel
PWBA	plane-wave Born approximation
DWBA	distorted-wave Born approximation
PVES	Parity violating electron scattering
IMSRG	In-medium similarity renormalization group
ODE	Ordinary differential equation
RG	Renormalization group

A.2 Kinematic and other notation

Z	Nuclear charge number
$\alpha_{\text{el}} = \frac{e^2}{4\pi}$	Fine structure constant
m_e	Electron mass
m_μ	Muon mass
m_N	Nucleon mass
m_M	Nucleus mass
$\vec{k}$	Initial lepton 3-momentum
$\vec{k'}$	Final lepton 3-momentum
$\vec{p}$	Initial nucleon 3-momentum
$\vec{p'}$	Final nucleon 3-momentum
$\vec{q}$	Transferred 3-momentum ($\vec{q} = \vec{k'} - \vec{k} = \vec{p} - \vec{p'}$)
E	Initial lepton energy ($E = k_{\mu=0}$)
E'	Final lepton energy ($E' = k'_{\mu=0}$)
k	Absolute value of the 3-momentum $\vec{k}$ ($k = \lvert\vec{k}\rvert$)
k'	Absolute value of the 3-momentum $\vec{k'}$ ($k' = \lvert\vec{k'}\rvert$)
q	Absolute value of the 3-momentum $\vec{q}$ ($q = \lvert\vec{q}\rvert$)
$1/2, t$	Initial lepton spin
$1/2, t'$	Final lepton spin
$1/2, s$	Initial nucleon spin
$1/2, s'$	Final nucleon spin
J	Total nucleus spin
J, M_i	Initial nucleus spin
J, M_f	Final nucleus spin

A.3 Labels

S	Scalar
P	Pseudo-scalar
V	Vector
A	Axial vector
T	Tensor
D	Dipole
GG	Gluonic (symmetric contraction: $G^a_{\alpha\beta}G^{\alpha\beta}_a$)
$G\tilde{G}$	Gluonic (antisymmetric contraction: $G^a_{\alpha\beta}\tilde{G}^{\alpha\beta}_a = \frac{1}{2}\epsilon^{\alpha\beta\gamma\delta}G^a_{\alpha\beta}G_{a,\gamma\delta}$))
X, X'	Type of current out of S, P, V, A, T, D, GG, $G\tilde{G}$
S	Type of nuclear structure out of Eq. (2.46), i.e. $M, \Phi'', \Sigma', \Sigma'', \ldots$
$Y = L, R$	Helicity of the electron
$N = n, p$	Proton or Neutron
M	Nucleus, i.e. $M = {}^{27}\text{Al}, {}^{48}\text{Ti}, \ldots$
$\mu(1s)$	Bound muon in the $1s$ ground state of a nucleus
$\tilde{e}$	Free electron distorted by a nucleus potential

Appendix B

Dirac Equation: Limiting Cases

In this appendix, we look at results for the ordinary differential equation (ODE) of Eq. (5.44), namely again

$$\frac{\partial}{\partial r}\begin{pmatrix} g_\kappa(r) \\ f_\kappa(r) \end{pmatrix} = \begin{pmatrix} g'_\kappa(r) \\ f'_\kappa(r) \end{pmatrix} = \begin{pmatrix} -\frac{\kappa}{r} & E - V(r) + m \\ -(E - V(r) - m) & \frac{\kappa}{r} \end{pmatrix} \begin{pmatrix} g_\kappa(r) \\ f_\kappa(r) \end{pmatrix}, \tag{B.1}$$

in different limiting cases, as deemed useful for the numerical procedures of solving this ODE for a general physical radial symmetric potential $V(r)$.

B.1 Dirac Equation for $r \to \infty$

If $V(r \to \infty) \to -\frac{Z\alpha_{\text{el}}}{r}$, the leading term to the ODE of Eq. (B.1) becomes

$$\begin{pmatrix} g'_\kappa \\ f'_\kappa \end{pmatrix} = \begin{pmatrix} 0 & (E+m) \\ -(E-m) & 0 \end{pmatrix} \begin{pmatrix} g'_\kappa \\ f'_\kappa \end{pmatrix}. \tag{B.2}$$

We can decouple this ODE by differentiating and find

$$\begin{pmatrix} g''_\kappa \\ f''_\kappa \end{pmatrix} = -\underbrace{(E-m)(E+m)}_{=E^2-m^2=:k_E^2} \begin{pmatrix} g'_\kappa \\ f'_\kappa \end{pmatrix}. \tag{B.3}$$

Hence, it is solved by

$$g_\kappa = c_g \sin\Big(k_E r + \tilde{\delta}_g\Big), \qquad f_\kappa = c_f \sin\Big(k_E r + \tilde{\delta}_f\Big), \tag{B.4}$$

with the normalization $c_{g,f}$ and the phase $\delta_{g,f}$. Inserting this back into the first-order differential equation results in

$$\begin{aligned}
\cos(k_E r + \delta_g) = \sin\Big(k_E r + \tilde{\delta}_f\Big) \qquad & \Rightarrow \tilde{\delta}_g + \frac{\pi}{2} = \tilde{\delta}_f, \\
c_g k_E = (E+m) c_f \qquad & \Rightarrow \tfrac{c_g}{c_f} = \tfrac{E+m}{k_E} = \sqrt{\tfrac{E+m}{E-m}}, \\
c_f k_E = (E-m) c_g \qquad & \Rightarrow \tfrac{c_g}{c_f} = \tfrac{k_E}{E-m} = \sqrt{\tfrac{E+m}{E-m}},
\end{aligned}$$

such that we may write

$$g_\kappa = -c\,\sqrt{E+m}\cos\Big(k_E r + \tilde{\delta}_\kappa\Big), \qquad f_\kappa = c\,\sqrt{E-m}\sin\Big(k_E r + \tilde{\delta}_\kappa\Big). \tag{B.5}$$

The normalization condition of Eq. (5.52) states

$$\int_0^\infty \mathrm{d}r\,\Big(g_\kappa^E g_\kappa^{E'} + f_\kappa^E f_\kappa^{E'}\Big) = 2\pi\delta\big(E-E'\big). \tag{B.6}$$

We find

$$\begin{aligned}
g_\kappa^E g_\kappa^{E'} + f_\kappa^E f_\kappa^{E'} = {} & \tfrac{c_g^E c_g^{E'} + c_f^E c_f^{E'}}{2}\cos\Big(k_E r - k_{E'} r + \tilde{\delta}_\kappa^E - \tilde{\delta}_\kappa^{E'}\Big) \\
& + \tfrac{c_f^E c_f^{E'} - c_g^E c_g^{E'}}{2}\cos\Big(k_E r + k_{E'} r + \tilde{\delta}_\kappa^E + \tilde{\delta}_\kappa^{E'}\Big),
\end{aligned} \tag{B.7}$$

where we can use

$$\delta(E-E') = \frac{1}{2\pi}\int_{-\infty}^{\infty}\mathrm{d}r\cos(Er - E'r + \delta) = \frac{1}{\pi}\int_0^\infty \mathrm{d}r\cos(Er - E'r + \delta), \tag{B.8}$$

where the phase δ is arbitrary and can be absorbed by redefinition of r. We get

$$\int_0^\infty \mathrm{d}r\,\Big(g_\kappa^E g_\kappa^{E'} + f_\kappa^E f_\kappa^{E'}\Big) = \tfrac{c_g^E c_g^{E'} + c_f^E c_f^{E'}}{2}\pi\delta(k_E - k'_E) = \tfrac{(c_g^E)^2 + (c_f^E)^2}{2}\pi\frac{k_E}{E}\delta(E-E'), \tag{B.9}$$

from which follows comparing to Eq. (B.6)

$$(c_g^E)^2 + (c_f^E)^2 = 4\frac{E}{k_E} = (c^E)^2(E+m+E-m) \Rightarrow c^E = \pm\sqrt{\frac{2}{k_E}}, \tag{B.10}$$

resulting in

$$g_\kappa = \mp\sqrt{2\frac{E+m}{k_E}}\cos\Big(k_E r + \tilde{\delta}_\kappa\Big), \qquad f_\kappa = \pm\sqrt{2\frac{E-m}{k_E}}\sin\Big(k_E r + \tilde{\delta}_\kappa\Big), \tag{B.11}$$

where the global sign is conventional. This is in line with Eq. (5.71), where we have seen that if one does keep terms with $1/r$, the phase $\tilde{\delta}$ becomes r-dependent.

If we want to fix our normalization for the numerical solutions, we can do so by considering

the found values of A, B, when matching according to Eq. (5.76). If we calculate here

$$\begin{aligned}
&\int_0^\infty \mathrm{d}r \left(g_\kappa^E g_\kappa^{E'} + f_\kappa^E f_\kappa^{E'} \right) \\
&\quad = \int_0^\infty \mathrm{d}r \Big((A^E g_\kappa^{C,r,E} + B^E g_\kappa^{C,i,E})(A^{E'} g_\kappa^{C,r,E'} + B^{E'} g_\kappa^{C,i,E'}) \\
&\qquad + (A^E f_\kappa^{C,r,E} + B^E f_\kappa^{C,i,E})(A^{E'} f_\kappa^{C,r,E'} + B^{E'} f_\kappa^{C,i,E'}) \Big) \\
&\quad = (A^E A^{E'} + B^E B^{E'}) 2\pi\delta(E - E') \qquad \text{(B.12)} \\
&\qquad + \int_0^\infty \mathrm{d}r \Big(A^E B^{E'} (g_\kappa^{C,r,E} g_\kappa^{C,i,E'} + f_\kappa^{C,r,E} f_\kappa^{C,i,E'}) + (E \leftrightarrow E') \Big). \qquad \text{(B.13)}
\end{aligned}$$

Using the asymptotic phase-shift difference θ_κ between regular and irregular solutions, see Eq. (5.75), we can write the irregular solutions in terms of the regular ones according to

$$\begin{aligned}
g_\kappa^{C,i,E} &= g_\kappa^{C,r,E} \cos\theta_\kappa + f_\kappa^{C,r,E} \sqrt{\frac{E+m}{E-m}} \sin\theta_\kappa, \\
f_\kappa^{C,i,E} &= f_\kappa^{C,r,E} \cos\theta_\kappa - g_\kappa^{C,r,E} \sqrt{\frac{E-m}{E+m}} \sin\theta_\kappa. \qquad \text{(B.14)}
\end{aligned}$$

We find

$$\begin{aligned}
&\int_0^\infty \mathrm{d}r \, (g_\kappa^{C,r,E} g_\kappa^{C,i,E'} + f_\kappa^{C,r,E} f_\kappa^{C,i,E'}) \\
&\quad = \int_0^\infty \mathrm{d}r \left(g_\kappa^{C,r,E} \left(g_\kappa^{C,r,E'} \cos\theta_\kappa + f_\kappa^{C,r,E'} \sqrt{\frac{E'+m}{E'-m}} \right) \right. \\
&\qquad \left. + f_\kappa^{C,r,E} \left(f_\kappa^{C,r,E'} \cos\theta_\kappa - g_\kappa^{C,r,E'} \sqrt{\frac{E'-m}{E'+m}} \sin\theta_\kappa \right) \right) \\
&\quad = 2\pi\delta(E - E') \cos\theta \\
&\qquad + \sin\theta_\kappa \int_0^\infty \mathrm{d}r \left(\sqrt{\frac{E'+m}{E'-m}} g_\kappa^{C,r,E} f_\kappa^{C,r,E'} - \sqrt{\frac{E'-m}{E'+m}} f_\kappa^{C,r,E} g_\kappa^{C,r,E'} \right). \qquad \text{(B.15)}
\end{aligned}$$

Using the asymptotic solutions for the Coulomb potential we can show that

$$\int_0^\infty \mathrm{d}r \, g_\kappa^{C,r,E} f_\kappa^{C,r,E'} = \frac{k_E}{2E} 2\pi\delta(E - E'), \qquad \text{(B.16)}$$

such that

$$\int_0^\infty \mathrm{d}r \, (g_\kappa^{C,r,E} g_\kappa^{C,i,E'} + f_\kappa^{C,r,E} f_\kappa^{C,i,E'}) = 2\pi\delta(E - E') \Big(\cos\theta + \frac{m}{E} \sin\theta \Big), \qquad \text{(B.17)}$$

and we find

$$\int_0^\infty \mathrm{d}r \left(g_\kappa^E g_\kappa^{E'} + f_\kappa^E f_\kappa^{E'}\right) = 2\pi\delta(E-E')\Big((A^E)^2 + (B^E)^2 + 2A^E B^E\Big(\cos\theta + \frac{m}{E}\sin\theta\Big)\Big), \tag{B.18}$$

such that the normalization condition is

$$1 = (A^E)^2 + (B^E)^2 + 2A^E B^E\Big(\cos\theta + \frac{m}{E}\sin\theta\Big), \tag{B.19}$$

which can be used in the numerical procedure.

B.2 Dirac Equation for $r \to 0$

For the initial values, we need to consider the limit $r \to 0$. This will be different for a pure Coulomb potential and a realistic potential. A pure Coulomb potential goes like $1/r$ even for $r \to 0$, while a realistic potential will approach a constant $V(0) = V_0 = \text{const}$.

For the Coulomb potential, the ODE of Eq. (B.1) becomes

$$\begin{pmatrix} g'_\kappa \\ f'_\kappa \end{pmatrix} = \begin{pmatrix} -\kappa/r & Z\alpha_{\mathrm{el}}/r \\ -Z\alpha_{\mathrm{el}}/r & \kappa/r \end{pmatrix} \begin{pmatrix} g_\kappa \\ f_\kappa \end{pmatrix} \qquad \Leftrightarrow y'(r) = Mr^{-1}y(r). \tag{B.20}$$

The matrix M does not have any r dependence anymore. Thus, we can solve the ODE by simply diagonalizing M. We define the basis change

$$y = Sx\,, \qquad S = \begin{pmatrix} \frac{\kappa-\rho_\kappa}{Z\alpha_{\mathrm{el}}} & \frac{\kappa+\rho_\kappa}{Z\alpha_{\mathrm{el}}} \\ 1 & 1 \end{pmatrix}, \tag{B.21}$$

which diagonalizes M such that

$$S^{-1}MS = \begin{pmatrix} \rho_\kappa & 0 \\ 0 & -\rho_\kappa \end{pmatrix} := M_D, \tag{B.22}$$

with eigenvalues $\pm\rho_\kappa = \pm\sqrt{\kappa^2 - (Z\alpha_{\mathrm{el}})^2}$. We solve

$$x' = M_D r^{-1} x, \tag{B.23}$$

which decouples and solves to

$$x_{1,2}(r) := c_{1,2}\; r^{\pm\rho_\kappa}, \tag{B.24}$$

with only x_1 regular for $r \to 0$.[1] Hence, we need $c_2 = 0$ and with Eq. (B.21) one gets

$$g_\kappa(r) = c\frac{\kappa - \rho_\kappa}{Z\alpha_{\text{el}}} r^{\rho_\kappa}, \qquad f_\kappa(r) = cr^{\rho_\kappa}, \tag{B.25}$$

with $c = c_1$ up to a global sign, in line with Eq. (5.61).

For a realistic potential, on the other hand, the ODE of Eq. (B.1) becomes

$$\begin{pmatrix} g'_\kappa \\ f'_\kappa \end{pmatrix} = \begin{pmatrix} -\kappa/r & \bar{E}' \\ -\bar{E} & \kappa/r \end{pmatrix} \begin{pmatrix} g_\kappa \\ f_\kappa \end{pmatrix}. \tag{B.26}$$

Where we call $\bar{E} = E - V_0 - m$ and $\bar{E}' = E - V_0 + m$. In principle, the leading term here is just the $\pm\kappa/r$ terms, which would directly decouple the ODE. However, in this limit, we also forfeit any information about the relation between g_κ and f_κ and cannot extract the relative normalization between the two. We can decouple the full ODE by differentiating, which results in

$$g''_\kappa = \left(\frac{\kappa(\kappa+1)}{r^2} - k_0^2\right) g_\kappa, \qquad f''_\kappa = \left(\frac{\kappa(\kappa-1)}{r^2} - k_0^2\right) f_\kappa, \tag{B.27}$$

where we introduced

$$k_0 = \sqrt{\bar{E}\bar{E}'} = \sqrt{(E - V_0)^2 - m^2}. \tag{B.28}$$

The general solutions to these ODEs are given in terms of the spherical Bessel functions j_κ, namely

$$g_\kappa(r) = \begin{cases} c_1^\kappa \; r \; j_\kappa(k_0 r) & ,\kappa > 0 \\ c_1^\kappa \; r \; j_{-\kappa-1}(k_0 r) & ,\kappa < 0 \end{cases}, \qquad f_\kappa(r) = \begin{cases} c_2^\kappa \; r \; j_{\kappa-1}(k_0 r) & ,\kappa > 0 \\ c_2^\kappa \; r \; j_{-\kappa}(k_0 r) & ,\kappa < 0 \end{cases}, \tag{B.29}$$

where we only consider the spherical Bessel functions of the first kind, such that the solutions are regular for $r \to 0$. Inserting these back into Eq. (B.26) we find

$$\frac{c_1^{\kappa>0}}{c_2^{\kappa>0}} = \sqrt{\frac{\bar{E}'}{\bar{E}}}, \qquad \frac{c_2^{\kappa<0}}{c_1^{\kappa<0}} = -\sqrt{\frac{\bar{E}}{\bar{E}'}}, \tag{B.30}$$

where we used the following identities for spherical Bessel functions

$$j'_n(x) = \frac{1}{2}\left(j_{n-1}(x) - j_{n+1}(x) - \frac{j_n(x)}{x}\right) = \frac{n j_n(x)}{x} - j_{n+1}(x) = -\frac{(n+1) j_n(x)}{x} + j_{n-1}(x), \tag{B.31}$$

[1] This also motivates the naming for the full solution for the Coulomb potential, with the main difference between regular and irregular solution being the sign of $\pm\rho_\kappa$

resulting in

$$
\begin{aligned}
g_\kappa(r) &= c \begin{cases} \sqrt{\frac{\bar{E}'}{\bar{E}}} r \; j_\kappa(k_0 r) & , \kappa > 0 \\ r \; j_{-\kappa-1}(k_0 r) & , \kappa < 0 \end{cases} \\
f_\kappa(r) &= c \begin{cases} r \; j_{\kappa-1}(k_0 r) & , \kappa > 0 \\ -\sqrt{\frac{\bar{E}}{\bar{E}'}} r \; j_{-\kappa}(k_0 r) & , \kappa < 0 \end{cases} ,
\end{aligned}
\tag{B.32}
$$

where c is the global normalization up to a sign, in line with Eq. (5.62).

Appendix C

Higher-order Charge Densities and Currents in relation to Charge and Magnetic Form Factors

We want to derive the relation of Eq. (5.6). Taking the cross section for the DWBA of Eq. (5.84), namely

$$\frac{\mathrm{d}\sigma}{\mathrm{d}\Omega} = \frac{1}{4\pi^2}\frac{m_e^2}{2J+1}\frac{k'}{k}\frac{1}{2}\sum_{m,m'}\sum_{L,M}|H_{LM}|^2 := \frac{\mathrm{d}\sigma}{\mathrm{d}\Omega}^{\mathrm{ch}} + \frac{\mathrm{d}\sigma}{\mathrm{d}\Omega}^{\mathrm{mag}}, \tag{C.1}$$

where we separated charged and magnetic components, as they cleanly separate in the plane wave limit. H_{LM} is defined via Eq. (5.83),

$$\langle JM_i|\, H\, |JM_f\rangle = \sum_{LM}\frac{\sqrt{2L+1}}{\sqrt{2J+1}}\langle JM_i, LM|JM_f\rangle\, H_{LM}, \tag{C.2}$$

with the interaction Hamiltonian of Eq. (5.81),

$$H = \frac{e}{4\pi}\int \mathrm{d}^3r \int \mathrm{d}^3r'\, \frac{\rho(\vec{r})\rho_e(\vec{r'}) - \vec{j}(\vec{r})\cdot\vec{j}_e(\vec{r'})}{|\vec{r}-\vec{r'}|} =: H^{\mathrm{ch}} + H^{\mathrm{mag}}, \tag{C.3}$$

with

$$\rho_e(\vec{r}) = -e\psi_f^\dagger\psi_i, \qquad \vec{j}_e(\vec{r}) = -e\psi_f^\dagger\gamma^0\vec{\gamma}\psi_i. \tag{C.4}$$

We can match this to the Born cross section of Eq. (5.1), by inserting plane waves for the electron wave functions, which are given by

$$\psi_m = u_m(\vec{p})e^{i(\vec{p}\cdot\vec{r}-p_0t)}, \tag{C.5}$$

such that we get

$$\rho_e(\vec{r}) = -e\ u^\dagger_{m'}(\vec{k}')u_m(\vec{k})\ e^{i(\vec{k}-\vec{k}')\cdot\vec{r}}, \qquad \vec{j}_e(\vec{r}) = -e\ u^\dagger_{m'}(\vec{k}')\gamma^0\vec{\gamma}u_m(\vec{k})\ e^{i(\vec{k}-\vec{k}')\cdot\vec{r}}. \tag{C.6}$$

We will separate the calculation for H^{ch} and H^{mag} from here on.

C.1 Charge Form Factors from Charge Densities

We can rewrite the interaction Hamiltonian of Eq. (C.3) using the Fourier transform as

$$\begin{aligned} H^{\text{ch}} &= \frac{e}{4\pi}\int \mathrm{d}^3r \int \mathrm{d}^3r'\,\rho(\vec{r})\frac{\rho_e(\vec{r'})}{|\vec{r}-\vec{r'}|} = \frac{e}{4\pi}\int\frac{\mathrm{d}^3q}{(2\pi)^3}\int\frac{\mathrm{d}^3q'}{(2\pi)^3}\tilde{\rho}(\vec{q})\tilde{\rho}_e(\vec{q'})\int\mathrm{d}^3r\int\mathrm{d}^3r'\,\frac{e^{i\vec{q}\cdot\vec{r}}e^{i\vec{q'}\cdot\vec{r'}}}{|\vec{r}-\vec{r'}|} \\ &= \frac{e}{4\pi}\int\frac{\mathrm{d}^3q}{(2\pi)^3}\int\frac{\mathrm{d}^3q'}{(2\pi)^3}\tilde{\rho}(\vec{q})\tilde{\rho}_e(\vec{q'})(2\pi)^3\delta^{(3)}(\vec{q}+\vec{q'})\frac{4\pi}{q^2} = e\int\frac{\mathrm{d}^3q}{(2\pi)^3}\tilde{\rho}(\vec{q})\frac{\tilde{\rho}_e(-\vec{q})}{q^2}. \end{aligned} \tag{C.7}$$

According to Eq. (C.6) we have

$$\rho_e(\vec{r}) = -e\ u^\dagger_{m'}(\vec{k}')u_m(\vec{k})\ e^{i(\vec{k}-\vec{k}')\cdot\vec{r}}. \tag{C.8}$$

For this formula, the spinors are given in the normalization of

$$u_m(\vec{k}) = \sqrt{\frac{E+m_e}{2m_e}}\begin{pmatrix}\mathbb{1}\chi_m \\ \frac{(\vec{\sigma}\cdot\vec{k})}{E+m_e}\chi_m\end{pmatrix}, \tag{C.9}$$

with the Pauli spinors χ_m as in Eq. (5.40), given by

$$\chi_+ = \begin{pmatrix}\cos\frac{\theta}{2} \\ e^{i\phi}\sin\frac{\theta}{2}\end{pmatrix}, \qquad \chi_- = \begin{pmatrix}-e^{-i\phi}\sin\frac{\theta}{2} \\ \cos\frac{\theta}{2}\end{pmatrix}, \qquad \chi^\dagger_\pm\chi_\pm = 1, \qquad \hat{\vec{\sigma}}\hat{\vec{k}}\chi_\pm = \pm\chi_\pm, \tag{C.10}$$

From this follows

$$u_m(\vec{k}) = \sqrt{\frac{E+m_e}{2m_e}}\begin{pmatrix}\mathbb{1}\chi_m \\ \mathrm{sgn}(m)\frac{|\vec{p}|}{E+m_e}\mathbb{1}\chi_m\end{pmatrix} \approx \sqrt{\frac{E}{2m_e}}\begin{pmatrix}\mathbb{1}\chi_m \\ \mathrm{sgn}(m)\mathbb{1}\chi_m\end{pmatrix}, \tag{C.11}$$

where we neglect higher terms in m_e. We then find

$$u^\dagger_{m'}(\vec{k}')u_m(\vec{k}) = \frac{E}{2m_e}(1+\mathrm{sgn}(m)\mathrm{sgn}(m'))\chi^\dagger_{m'}(\hat{p}_f)\chi_m(\hat{p}_i) = \frac{E}{m_e}\delta_{mm'}\cos\left(\tfrac{\theta}{2}\right), \tag{C.12}$$

where θ is the angle between $\vec{k}$ and $\vec{k}'$. This can be easily verified if $\vec{k}$ points in $\hat{e}_z$ direction and is in a plane with $\vec{k}'$, such that $\theta(\hat{k}) = \phi(\hat{k}) = \phi(\hat{k}') = 0$ and $\theta(\hat{k}') := \theta$. We get

$$\begin{aligned}\tilde{\rho_e}(\vec{q}) &= \int \mathrm{d}^3r\, e^{-i\vec{q}\cdot\vec{r}}\rho_e(\vec{r}) = -e\,\frac{E}{m_e}\cos\!\left(\tfrac{\theta}{2}\right)\delta_{mm'}\int \mathrm{d}^3r\, e^{i(\vec{k}-\vec{k}'-\vec{q})\cdot\vec{r}} \\ &= -e\,\frac{E}{m_e}\cos\!\left(\tfrac{\theta}{2}\right)(2\pi)^3\delta^{(3)}(\vec{k}-\vec{k}'-\vec{q})\delta_{mm'}, \end{aligned} \tag{C.13}$$

and thus

$$\begin{aligned} H^{\mathrm{ch}} &= -e^2\frac{E}{m_e}\cos\!\left(\tfrac{\theta}{2}\right)\delta_{mm'}\int \mathrm{d}^3q\,\frac{\tilde{\rho}(\vec{q})}{q}\delta^{(3)}(\vec{q}-(\vec{k}'-\vec{k})) \\ &:= -(4\pi\alpha_{\mathrm{el}})\,\frac{E}{m_e}\cos\!\left(\tfrac{\theta}{2}\right)\frac{\tilde{\rho}(\vec{q})}{q^2}\delta_{mm'}, \end{aligned} \tag{C.14}$$

where we defined $\vec{q} := \vec{k}' - \vec{k}$ and $\alpha_{\mathrm{el}} = e^2/(4\pi)$. The expectation value between nucleus states becomes

$$\begin{aligned}\langle JM_i|\, H^{\mathrm{ch}}\,|JM_f\rangle &= -(4\pi\alpha_{\mathrm{el}})\frac{E}{m_e}\frac{\cos\!\left(\frac{\theta}{2}\right)}{q^2}\delta_{mm'}\int \mathrm{d}^3r\, e^{-i\vec{q}\cdot\vec{r}}\,\langle JM_i|\,\rho(\vec{r})\,|JM_f\rangle \\ &= -\alpha_{\mathrm{el}}(4\pi)^{3/2}\frac{E}{m_e}\frac{\cos\!\left(\frac{\theta}{2}\right)}{q^2}\delta_{mm'} \\ &\quad\times\sum_{LM}\langle JM_i, LM|JM_f\rangle\int \mathrm{d}^3r\, e^{-i\vec{q}\cdot\vec{r}}\rho_L(r)Y^*_{LM}(\hat{r}), \end{aligned} \tag{C.15}$$

where we entered in the second line the definition of ρ_L according to

$$\langle JM_i|\rho(\vec{r})\,|JM_f\rangle = \sqrt{4\pi}\sum_{LM}\langle JM_i, LM|JM_f\rangle\,\rho_L(r)Y^*_{LM}(\hat{r}). \tag{C.16}$$

By the means of Eq. (C.2) this defines

$$H^{\mathrm{ch}}_{LM} = -\alpha_{\mathrm{el}}(4\pi)^{3/2}\frac{E}{m_e}\frac{\cos\!\left(\frac{\theta}{2}\right)}{q^2}\delta_{mm'}\frac{\sqrt{2J+1}}{\sqrt{2L+1}}\int \mathrm{d}^3r\, e^{-i\vec{q}\cdot\vec{r}}\rho_L(r)Y^*_{LM}(\hat{r}), \tag{C.17}$$

and the cross section of Eq. (C.3) becomes

$$\begin{aligned}\frac{\mathrm{d}\sigma}{\mathrm{d}\Omega}^{\mathrm{ch}} &= \frac{1}{2}\frac{m_e^2}{(2\pi)^2}\frac{k'}{k}\frac{1}{2J+1}\sum_{m,m'}\sum_{L,M}\left|H^{\mathrm{ch}}_{LM}\right|^2 \\ &= 16\pi\alpha_{\mathrm{el}}^2E^2\frac{k'}{k}\frac{\cos^2\!\left(\frac{\theta}{2}\right)}{q^4}\underbrace{\left(\frac{1}{2}\sum_{m,m'}\delta^2_{mm'}\right)}_{=1}\sum_{L,M}\left|\frac{1}{\sqrt{2L+1}}\int \mathrm{d}^3r\, e^{-i\vec{q}\cdot\vec{r}}\rho_L(r)Y^*_{LM}(\hat{r})\right|^2. \end{aligned} \tag{C.18}$$

Looking at the last part we have

$$\sum_{L,M}\left|\frac{1}{\sqrt{2L+1}}\int \mathrm{d}^3r\, e^{-i\vec{q}\cdot\vec{r}}\rho_L(r)Y^*_{LM}(\hat{r})\right|^2$$
$$=\frac{1}{4\pi}\sum_L\int \mathrm{d}^3r\int \mathrm{d}^3r'\, e^{-i\vec{q}\cdot\vec{r}}e^{i\vec{q}\cdot\vec{r'}}\rho_L(r)\rho_L(r')P_L(\hat{r}\cdot\hat{r}'), \tag{C.19}$$

using

$$\sum_M Y^*_{LM}(\hat{r})Y_{LM}(\hat{r'})=\frac{2L+1}{4\pi}P_L(\hat{r}\cdot\hat{r}'). \tag{C.20}$$

We may expand the plane waves to separate radial and angular parts according to

$$e^{i\vec{k}\cdot\vec{x}}=\sum_{l=0}^{\infty}(2l+1)i^l j_l(kx)P_l(\hat{k}\cdot\hat{x}), \tag{C.21}$$

which gives us

$$\sum_{L,M}\left|\frac{1}{\sqrt{2L+1}}\int \mathrm{d}^3r\, e^{-i\vec{q}\cdot\vec{r}}\rho_L(r)Y^*_{LM}(\hat{r})\right|^2$$
$$=\frac{1}{4\pi}\sum_{L,l,l'}\int \mathrm{d}^3r\int \mathrm{d}^3r'\,(2l+1)(2l'+1)i^{l'-l}\rho_L(r)\rho_L(r')j_l(qr)j_{l'}(qr')P^*_l(\hat{q}\cdot\hat{r})P_{l'}(\hat{q}\cdot\hat{r}')P_L(\hat{r}\cdot\hat{r}')$$
$$=\frac{1}{4\pi}\sum_{L,l,l'}(2l+1)(2l'+1)i^{l'-l}\int \mathrm{d}r\, r^2\rho_L(r)j_l(qr)\int \mathrm{d}r'\, r'^2\rho_L(r')j_{l'}(qr')$$
$$\times\iint \mathrm{d}\Omega\,\mathrm{d}\Omega'\,P^*_l(\hat{q}\cdot\hat{r})P_{l'}(\hat{q}\cdot\hat{r}')P_L(\hat{r}\cdot\hat{r}'). \tag{C.22}$$

We can employ

$$\iint \mathrm{d}\Omega\,\mathrm{d}\Omega'\,P^*_l(\hat{q}\cdot\hat{r})P_{l'}(\hat{q}\cdot\hat{r'})P_L(\hat{r}\cdot\hat{r'})=\frac{(4\pi)^2}{(2L+1)^2}\delta_{lL}\delta_{l'L}, \tag{C.23}$$

which can be proven by using the orthogonality relations for the spherical harmonics in combination with

$$P_L(\cos(\gamma))=\frac{4\pi}{2L+1}\sum_M Y_{LM}(\theta,\phi)Y^*_{LM}(\theta',\phi'),\quad P_l(\cos(\theta))=\sqrt{\frac{4\pi}{2l+1}}Y_{l0}(\theta,\phi), \tag{C.24}$$

where $\cos(\gamma)=\cos(\theta)\cos(\theta')+\sin(\theta)\sin(\theta')\cos(\phi-\phi')$. We get

$$\sum_{L,M}\left|\frac{1}{\sqrt{2L+1}}\int \mathrm{d}^3r\, e^{-i\vec{q}\cdot\vec{r}}\rho_L(r)Y^*_{LM}(\hat{r})\right|^2=4\pi\sum_L\left|\int \mathrm{d}r\, r^2\rho_L(r)j_L(qr)\right|^2, \tag{C.25}$$

and the cross section becomes

$$\frac{\mathrm{d}\sigma}{\mathrm{d}\Omega}^{\mathrm{ch}} = 4\alpha_{\mathrm{el}}^2 \frac{k'}{k} \frac{\cos^2\left(\frac{\theta}{2}\right) E^2}{q^4} (4\pi)^2 \sum_L \left| \int \mathrm{d}r\, r^2 \rho_L(r) j_L(qr) \right|^2 . \tag{C.26}$$

With our conventions $k \approx E$, $k' \approx E'$ and $q^4 \approx 16E^4 \sin^4\left(\frac{\theta}{2}\right)$, which gives

$$\frac{\mathrm{d}\sigma}{\mathrm{d}\Omega}^{\mathrm{ch}} \approx \frac{\alpha_{\mathrm{el}}^2}{4E^2} \frac{E'}{E} \frac{\cos^2\left(\frac{\theta}{2}\right)}{\sin^4\left(\frac{\theta}{2}\right)} \sum_L \left| 4\pi \int \mathrm{d}r\, r^2 \rho_L(r) j_L(qr) \right|^2 , \tag{C.27}$$

such that comparing to the cross section of Eq. (5.1) leads to

$$Z F_L^{\mathrm{ch}}(q) = 4\pi \int \mathrm{d}r\, r^2 \rho_L(r) j_L(qr), \tag{C.28}$$

in accordance with Eq. (5.6).

C.2 Magnetic Form Factors from Charge Currents

Analogously to H^{ch} we write H^{mag} via the Fourier transforms as

$$H^{\mathrm{mag}} = -\frac{e}{4\pi} \int \mathrm{d}^3 r \int \mathrm{d}^3 r' \, \frac{\vec{j}(\vec{r}) \cdot \vec{j}_e(\vec{r'})}{|\vec{r} - \vec{r'}|} = -e \int \frac{\mathrm{d}^3 q}{(2\pi)^3} \frac{\tilde{\vec{j}}(\vec{q}) \cdot \tilde{\vec{j}}_e(-\vec{q})}{q}. \tag{C.29}$$

According to Eq. (C.6) we have

$$\vec{j}_e(\vec{r}) = -e \, \frac{1}{(2\pi)^3} u_{m'}^\dagger(\vec{k'}) \gamma^0 \vec{\gamma} u_m(\vec{k}) \; e^{i(\vec{k} - \vec{k'}) \cdot \vec{r}}. \tag{C.30}$$

Here we find

$$u_{m'}^\dagger(\vec{k'}) \gamma^0 \vec{\gamma} u_m(\vec{k}) = \frac{E}{2m_e} (\mathrm{sgn}(m) + \mathrm{sgn}(m')) \chi_{m'}^\dagger(\hat{p}_f) \vec{\sigma} \chi_m(\hat{p}_i) = \frac{E}{m_e} \delta_{m,m'} \vec{\xi}_m, \tag{C.31}$$

with

$$\vec{\xi}_m := \mathrm{sgn}(m) \chi_m^\dagger(\hat{p}_f) \vec{\sigma} \chi_m(\hat{p}_i) = \begin{pmatrix} 1 \\ -i \; \mathrm{sign}(m) \sin\frac{\theta}{2} \\ 0 \end{pmatrix}, \tag{C.32}$$

with θ as before the angle between $\vec{k}$ and $\vec{k'}$. This representation is dependent on the choice of the coordinate system. This result is given for $\vec{k} - \vec{k'}$ in $\hat{e}_z$ direction and $\vec{k}$, $\vec{k'}$ in the $\hat{e}_x \times \hat{e}_z$ plane. One way to confirm this is to calculate $\vec{\xi}_m$ for $\vec{k}$ in $\hat{e}_z$ direction as we have done for ρ_L, and then rotate the coordinate system by $\frac{\theta}{2} - \frac{\pi}{2}$, such that $\vec{k} - \vec{k'}$ points

in $\hat{e}_z$ direction. We get

$$\begin{aligned}\tilde{\vec{j}}_e(\vec{q}) &= \int \mathrm{d}^3r\, e^{-i\vec{q}\cdot\vec{r}}\vec{j}_e(\vec{r}) = -e\,\frac{E}{m_e}\vec{\xi}_m\delta_{m,m'}\int \mathrm{d}^3r\, e^{i(\vec{k}-\vec{k}'-\vec{q})\cdot\vec{r}},\\ &= -e\,\frac{E}{m_e}\vec{\xi}_m(2\pi)^3\delta^{(3)}(\vec{k}-\vec{k}'-\vec{q})\delta_{m,m'},\end{aligned} \tag{C.33}$$

and thus

$$\begin{aligned}H^{\mathrm{mag}} &= e^2\frac{E}{m_e}\delta_{m,m'}\int\frac{\mathrm{d}^3q}{(2\pi)^3}\vec{\xi}_m\cdot\tilde{\vec{j}}(\vec{q})\delta^{(3)}(\vec{q}-(\vec{k}'-\vec{k}))\frac{4\pi}{q^2},\\ &:= (4\pi\alpha_{\mathrm{el}})\,\frac{E}{m_e}\frac{\vec{\xi}_m\cdot\tilde{\vec{j}}(\vec{q})}{q^2}\delta_{m,m'},\end{aligned} \tag{C.34}$$

where we defined again $\vec{q} := \vec{k}' - \vec{k}$ and $\alpha_{\mathrm{el}} = e^2/(4\pi)$. The expectation value between nucleus states becomes

$$\begin{aligned}\langle JM_i|\,H^{\mathrm{mag}}\,|JM_f\rangle &= (4\pi\alpha_{\mathrm{el}})\frac{E}{m_e}\frac{\delta_{m,m'}}{q^2}\int \mathrm{d}^3r\, e^{-i\vec{q}\cdot\vec{r}}\vec{\xi}_m\cdot\langle JM_i|\,\vec{j}(\vec{r})\,|JM_f\rangle \\ &= \alpha_{\mathrm{el}}(4\pi)^{3/2}\frac{E}{m_e}\frac{\delta_{m,m'}}{q^2}\\ &\quad\times\sum_{LL'M}\frac{\sqrt{2L+1}}{\sqrt{2J+1}}\frac{\langle JM_i, LM|JM_f\rangle}{\sqrt{2L+1}}\int \mathrm{d}^3r\, e^{-i\vec{q}\cdot\vec{r}}j_{LL'}(r)\;\vec{\xi}_m\cdot\vec{Y}^*_{LL'M}(\hat{r}),\end{aligned} \tag{C.35}$$

where we used the definition of $\vec{j}_{LL}$ according to

$$\langle JM_i|\vec{j}(\vec{r})\,|JM_f\rangle = \sqrt{4\pi}\sum_{LL'M}\langle JM_i, LM|JM_f\rangle\, j_{LL'}(r)\vec{Y}^*_{LL'M}(\hat{r}).$$

By means of Eq. (C.2) this defines

$$H^{\mathrm{mag}}_{LM} = \alpha_{\mathrm{el}}(4\pi)^{3/2}\frac{E}{m_e}\frac{\delta_{m,m'}}{q^2}\frac{\sqrt{2J+1}}{\sqrt{2L+1}}\int \mathrm{d}^3r\, e^{-i\vec{q}\cdot\vec{r}}\sum_{L'}j_{LL'}(r)\;\vec{\xi}_m\cdot\vec{Y}^*_{LL'M}(\hat{r}), \tag{C.36}$$

and the cross section becomes

$$\begin{aligned}\frac{\mathrm{d}\sigma}{\mathrm{d}\Omega}^{\mathrm{mag}} &= \frac{1}{2}\frac{m_e^2}{(2\pi)^2}\frac{k'}{k}\frac{1}{2J+1}\sum_{m,m'}\sum_{L,M}|H^{\mathrm{mag}}_{LM}|^2 \\ &= 16\pi\alpha_{\mathrm{el}}^2E^2\frac{k'}{k}\frac{1}{q^4}\frac{1}{2}\sum_m\sum_{L,M}\left|\frac{1}{\sqrt{2L+1}}\int \mathrm{d}^3r\, e^{-i\vec{q}\cdot\vec{r}}\sum_{L'}j_{LL'}(r)\;\vec{\xi}_m\cdot\vec{Y}^*_{LL'M}(\hat{r})\right|^2.\end{aligned} \tag{C.37}$$

Looking at the last part we have

$$\frac{1}{2}\sum_m\sum_{L,M}\left|\frac{1}{\sqrt{2L+1}}\int \mathrm{d}^3r\, e^{-i\vec{q}\cdot\vec{r}}\sum_{L'} j_{LL'}(r)\ \vec{\xi}_m\cdot\vec{Y}^*_{LL'M}(\hat{r})\right|^2$$
$$=\frac{1}{2}\sum_{L,M,m}\frac{\xi^i_m\xi^{j*}_m}{2L+1}\int \mathrm{d}^3r\int \mathrm{d}^3r'\, e^{-i\vec{q}\cdot\vec{r}}e^{i\vec{q}\vec{r'}}j_{LL}(r)j^*_{LL}(r')Y^{i*}_{LLM}(\hat{r})Y^j_{LLM}(\hat{r}') \tag{C.38}$$
$$+\frac{1}{2}\sum_{L,M,m}\sum_{L,'L''\neq L}\frac{\xi^i_m\xi^{j*}_m}{2L+1}\int \mathrm{d}^3r\int \mathrm{d}^3r'\, e^{-i\vec{q}\cdot\vec{r}}e^{i\vec{q}\vec{r'}}j_{LL'}(r)j^*_{LL''}(r')Y^{i*}_{LL'M}(\hat{r})Y^j_{LL''M}(\hat{r}'),$$

In the plane wave born approximation of Eq. (5.1), for elastic scattering only ρ_L and j_{LL} contribute. Hence, the terms in the second line, dependent on $j_{LL'}$ with $L\neq L'$, may only contribute going beyond this. Thus, for the matter of matching j_{LL}, we can drop these, and just consider the first line. For these terms, we can use

$$\vec{Y}_{LLM}(\hat{r})=\frac{\vec{L}}{\sqrt{L(L+1)}}Y_{LM}(\hat{r}),\qquad\qquad \vec{L}=-i\vec{r}\times\vec{\nabla}, \tag{C.39}$$

which gives us

$$\begin{aligned}\int \mathrm{d}^3r\, e^{-i\vec{q}\cdot\vec{r}}j_{LL}(r)\vec{Y}^*_{LLM}(\hat{r}) &= \int \mathrm{d}^3r\, e^{-i\vec{q}\cdot\vec{r}}j_{LL}(r)\frac{\vec{L}}{\sqrt{L(L+1)}}Y^*_{LM}(\hat{r})\\ &= \int \mathrm{d}^3r\,\frac{\vec{r}\times\vec{q}}{\sqrt{L(L+1)}}e^{-i\vec{q}\cdot\vec{r}}j_{LL}(r)Y^*_{LM}(\hat{r}),\end{aligned} \tag{C.40}$$

using partial integration to act with $\vec{\nabla}$ on $e^{-i\vec{q}\cdot\vec{r}}$.

$$\frac{1}{2}\sum_{L,M,m}\left|\frac{1}{\sqrt{2L+1}}\int \mathrm{d}^3r\, e^{-i\vec{q}\cdot\vec{r}}j_{LL}(r)\ \vec{\xi}_m\cdot\vec{Y}^*_{LLM}(\hat{r})\right|^2 \tag{C.41}$$
$$=\frac{1}{2}\sum_{L,M,m}\int \mathrm{d}^3r\int \mathrm{d}^3r'\,\frac{(\vec{\xi}_m\cdot(\vec{r}\times\vec{q}))(\vec{\xi}_m\cdot(\vec{r'}\times\vec{q}))^*}{(2L+1)L(L+1)}e^{-i\vec{q}\cdot\vec{r}}e^{i\vec{q}\vec{r'}}j_{LL}(r)j^*_{LL}(r')Y^*_{LM}(\hat{r})Y_{LM}(\hat{r}').$$

In the coordinate system where $\vec{q}$ goes in $\hat{e}_z$ direction. We have

$$\begin{aligned}\vec{\xi}_m\cdot(\vec{r}\times\vec{q}) &= qr(\sin\theta_r\sin\phi_r+i\mathrm{sgn}(m)\sin\tfrac{\theta}{2}\sin\theta_r\cos\phi_r)\\ &= iqr\sqrt{\frac{2\pi}{3}}\big((Y_{1+1}(\hat{r})+Y_{1-1}(\hat{r}))-\mathrm{sgn}(m)\sin\tfrac{\theta}{2}(Y_{1+1}(\hat{r})-Y_{1-1}(\hat{r}))\big),\end{aligned} \tag{C.42}$$

with $\hat{r} = (\theta_r, \phi_r)$ and where we inserted the explicit form of the spherical harmonics for $Y_{1\pm1}$ in the second line. Hence

$$\begin{aligned}
&\frac{1}{2}\sum_m (\vec{\xi}_m \cdot (\vec{r} \times \vec{q}))(\vec{\xi}_m \cdot (\vec{r} \times \vec{q}))^* \\
&\quad = q^2 r r' \frac{2\pi}{3}\Big[(Y_{1+1} + Y_{1-1})(Y'_{1+1} + Y'_{1-1}) + \sin^2\tfrac{\theta}{2}(Y_{1+1} - Y_{1-1})(Y'_{1+1} - Y'_{1-1})\Big], \qquad \text{(C.43)}
\end{aligned}$$

where we introduced the shorthand notation of $Y_{1,\pm1} = Y_{1,\pm1}(\hat{r})$ and $Y'_{1,\pm1} = Y_{1,\pm1}(\hat{r}')$. We find

$$\begin{aligned}
&\frac{1}{2}\sum_{L,M,m}\left|\frac{1}{\sqrt{2L+1}}\int \mathrm{d}^3 r\, e^{-i\vec{q}\cdot\vec{r}} j_{LL}(r)\ \vec{\xi}_m \cdot \vec{Y}^*_{LLM}(\hat{r})\right|^2 \\
&\quad = \frac{2\pi}{3}\sum_{L,M}\int \mathrm{d}^3 r \int \mathrm{d}^3 r'\, \frac{q^2 r r'}{(2L+1)L(L+1)}\ e^{-i\vec{q}\cdot\vec{r}} e^{i\vec{q}\cdot\vec{r}'} j_{LL}(r) j^*_{LL}(r') Y^*_{LM}(\hat{r}) Y_{LM}(\hat{r}') \\
&\qquad \times \Big[(Y_{1+1} + Y_{1-1})(Y'_{1+1} + Y'_{1-1}) + \sin^2\tfrac{\theta}{2}(Y_{1+1} - Y_{1-1})(Y'_{1+1} - Y'_{1-1})\Big]. \qquad \text{(C.44)}
\end{aligned}$$

We may use again

$$e^{i\vec{k}\cdot\vec{x}} = \sum_{l=0}^{\infty}(2l+1) i^l j_l(kx) P_l(\hat{k}\hat{x}), \qquad P_l(\cos(\theta)) = \sqrt{\frac{4\pi}{2l+1}} Y_{l0}(\theta, \phi), \qquad \text{(C.45)}$$

such that we get

$$\begin{aligned}
&\frac{1}{2}\sum_{L,M,m}\left|\frac{1}{\sqrt{2L+1}}\int \mathrm{d}^3 r\, e^{-i\vec{q}\cdot\vec{r}} j_{LL}(r)\ \vec{\xi}_m \cdot \vec{Y}^*_{LLM}(\hat{r})\right|^2 \qquad \text{(C.46)} \\
&\quad = \frac{2\pi}{3}\sum_{L,M}\int \mathrm{d}^3 r \int \mathrm{d}^3 r'\, q^2 r r' \sum_{l,l'} \frac{4\pi\sqrt{(2l+1)(2l'+1)}}{(2L+1)L(L+1)} i^{l'-l} j_l(kr)^* j_{l'}(kr') j_{LL}(r) j^*_{LL}(r') \\
&\qquad \times Y^*_{l0} Y'_{l'0} Y^*_{LM} Y'_{LM}\Big[(Y_{1+1} + Y_{1-1})(Y'_{1+1} + Y'_{1-1}) + \sin^2\tfrac{\theta}{2}(Y_{1+1} - Y_{1-1})(Y'_{1+1} - Y'_{1-1})\Big],
\end{aligned}$$

such that the angular integrals that need to be performed are

$$\begin{aligned}
&\int \mathrm{d}\Omega\,(Y_{1+1}(\theta,\phi) \pm Y_{1-1}(\theta,\phi)) Y^*_{l0}(\theta,\phi) Y_{LM}(\theta,\phi) \\
&\quad = -\sqrt{\frac{3}{4\pi}}\sqrt{\frac{L(L+1)}{2(2l+1)(2L+1)}}(\delta_{L,l+1} - \delta_{L,l-1})(\delta_{M,-1} \pm \delta_{M,+1}), \qquad \text{(C.47)}
\end{aligned}$$

which can be derived using the condition

$$\int \mathrm{d}\Omega\, Y_{l_1 m_1}(\theta,\phi) Y_{l_2 m_2}(\theta,\phi) Y_{l_2 m_3}(\theta,\phi)$$
$$= \sqrt{\frac{(2l_1+1)(2l_2+1)(2l_3+1)}{4\pi}} \begin{pmatrix} l_1 & l_2 & l_3 \\ 0 & 0 & 0 \end{pmatrix} \begin{pmatrix} l_1 & l_2 & l_3 \\ m_1 & m_2 & m_3 \end{pmatrix}$$
$$Y^*_{LM}(\theta,\phi) = (-1)^M Y_{L-M}(\theta,\phi), \tag{C.48}$$

with the Wigner-3j symbols given in terms of Clebsch–Gordan coefficients as

$$\begin{pmatrix} l_1 & l_2 & l_3 \\ m_1 & m_2 & m_3 \end{pmatrix} = \frac{(-1)^{l_1-l_2-m_3}}{\sqrt{2l_3+1}} \langle l_1 m_1; l_2 m_2 | l_3 - m_3 \rangle\,, \tag{C.49}$$

and the explicit values for the Clebsch–Gordan coefficients of [235]

$$\langle 10, l0 | L0 \rangle = \frac{(-1)^{l+1-L}}{\sqrt{2l+1}} \begin{cases} \sqrt{l+1} & , L = l+1 \\ -\sqrt{l} & , L = l-1 \\ 0 & , \text{else} \end{cases},$$
$$\langle 1\pm 1, l0 | L \pm 1 \rangle = \frac{(-1)^{l+1-L}}{\sqrt{2l+1}} \begin{cases} \sqrt{\frac{l+2}{2}} & , L = l+1 \\ \pm\frac{1}{\sqrt{2}} & , L = l \\ \sqrt{\frac{l-1}{2}} & , L = l-1 \\ 0 & , \text{else} \end{cases}, \tag{C.50}$$

Using

$$\sum_M (\delta_{M,-1} \pm \delta_{M,+1})(\delta_{M,-1} \pm \delta_{M,+1}) = 2\delta_{L>0}, \tag{C.51}$$

we find

$$\frac{1}{2} \sum_{L,M,m} \left| \frac{1}{\sqrt{2L+1}} \int \mathrm{d}^3 r\, e^{-i\vec{q}\cdot\vec{r}} j_{LL}(r)\; \vec{\xi}_m \cdot \vec{Y}^*_{LLM}(\hat{r}) \right|^2$$
$$= (1+\sin^2\tfrac{\theta}{2}) \sum_{L>0} \frac{2\pi}{(2L+1)^2}$$
$$\times \sum_{l,l'} \int \mathrm{d}r \int \mathrm{d}r'\, q^2 r^3 r'^3 i^{l'-l} j_l(qr)^* j_{l'}(qr') j_{LL}(r) j^*_{LL}(r') (\delta_{L,l+1} - \delta_{L,l-1})(\delta_{L,l'+1} - \delta_{L,l'-1})$$
$$= (1+\sin^2\tfrac{\theta}{2}) \sum_{L>0} \frac{2\pi}{(2L+1)^2} \left| \sum_l (\delta_{L,l+1} - \delta_{L,l-1}) i^{-l} \int \mathrm{d}r\, r^2 qr\, j_l(qr) j_{LL}(r) \right|^2, \tag{C.52}$$

where

$$\begin{aligned}
&\sum_l (\delta_{L,l+1} - \delta_{L,l-1}) i^{-l} \int \mathrm{d}r\, r^2 qr j_l(qr) j_{LL}(r) \\
&\quad = i^{-L+1} \int \mathrm{d}r\, r^2 qr j_{LL}(r)(j_{L-1}(qr) + j_{L+1}(qr)) \\
&\quad = i^{-L+1}(2L+1) \int \mathrm{d}r\, r^2 j_{LL}(r) j_L(qr),
\end{aligned} \tag{C.53}$$

using the identity for spherical Bessel functions

$$x(j_{n-1}(x) + j_{n+1}(x)) = (2n+1) j_n(x), \tag{C.54}$$

such that

$$\begin{aligned}
&\frac{1}{2} \sum_{L,M,m} \left| \frac{1}{\sqrt{2L+1}} \int \mathrm{d}^3 r\, e^{-i\vec{q}\cdot\vec{r}} j_{LL}(r)\ \vec{\xi}_m \cdot \vec{Y}^*_{LLM}(\hat{r}) \right|^2 \\
&\quad = 4\pi \frac{1}{2} (1 + \sin^2 \tfrac{\theta}{2}) \sum_{L>0} \left| \int \mathrm{d}r\, r^2 j_l(qr) j_{LL}(r) \right|^2,
\end{aligned} \tag{C.55}$$

and the cross section becomes

$$\begin{aligned}
\frac{\mathrm{d}\sigma}{\mathrm{d}\Omega}^{\mathrm{mag}} &= 4\alpha_{\mathrm{el}}^2 E^2 \frac{k'}{k} \frac{(4\pi)^2}{q^4} \frac{1}{2} \big(1 + \sin^2 \tfrac{\theta}{2}\big) \sum_{L>0} \left| \int \mathrm{d}r\, r^2 j_l(qr) j_{LL}(r) \right|^2, \\
&= \frac{\alpha_{\mathrm{el}}^2}{4E^2} \frac{E'}{E} \frac{\cos^2\big(\frac{\theta}{2}\big)}{\sin^4\big(\frac{\theta}{2}\big)} \left(\frac{1}{2} + \tan^2 \tfrac{\theta}{2} \right) \sum_{L>0} \left| 4\pi \int \mathrm{d}r\, r^2 j_l(qr) j_{LL}(r) \right|^2,
\end{aligned} \tag{C.56}$$

where we used again $k \approx E$, $k' \approx E'$ and $q^4 \approx 16E^4 \sin^4\big(\frac{\theta}{2}\big)$. Comparing to Eq. (5.1) then results in

$$F_L^{\mathrm{mag}}(q) = 4\pi \int \mathrm{d}r\, r^2 j_l(qr) j_{LL}(r), \tag{C.57}$$

in accordance with Eq. (5.6).

Appendix D

Further Documentation and Tables for the Charge Density Extractions[1]

D.1 Documentation of the intermediate Steps of the Fitting Strategy

For each nucleus we show the reduced χ^2 and electron scattering cross sections after steps 1 and 2 in Sec. 6.1, excluding fits based on the p-value (p_{val}), see Figs. D.1–D.3. One sees how with the chosen limits all remaining fits describe the data points reasonably well, while beyond the data points the shape of the cross section becomes largely unconstrained. In particular for ^{40,48}Ca a quite large set of reasonable fits can be selected with a wide range of R and N combinations, reflecting the high quality of the data without any major inconsistencies. For the other nuclei, the data situation is markedly worse, which is reflected by the smaller set of reasonable fits that could be found.

Next, we show the resulting charge density, form factor, and reduced χ^2 values after steps 3 and 4, either with or without the inclusion of the corresponding Barrett moment. Here we again exclude fits based on the p-value, but, in addition, remove fits based on their asymptotic behavior. The results are shown in Figs. D.4–D.8. As one can see, the limiting asymptotic behavior is crucial to suppress an extreme increase in the form factor for large momentum transfer, which otherwise results in extreme variations in the charge density for $r \to 0$. The remaining solutions are the foundation for the central solutions and systematic uncertainty bands as presented in Sec. 6.2.

On a more general note, one can see that the limiting factor in precision is generally the highest measured momentum transfer, as beyond this point without further external input the fit remains largely unconstrained. This then results in uncertainties for small and large distances. In particular for ^{40,48}Ca, for which we observe significant tension between the input from muonic atoms in terms of Barrett moments and the pure electron scattering

[1] This appendix was published as part of Ref. [2].

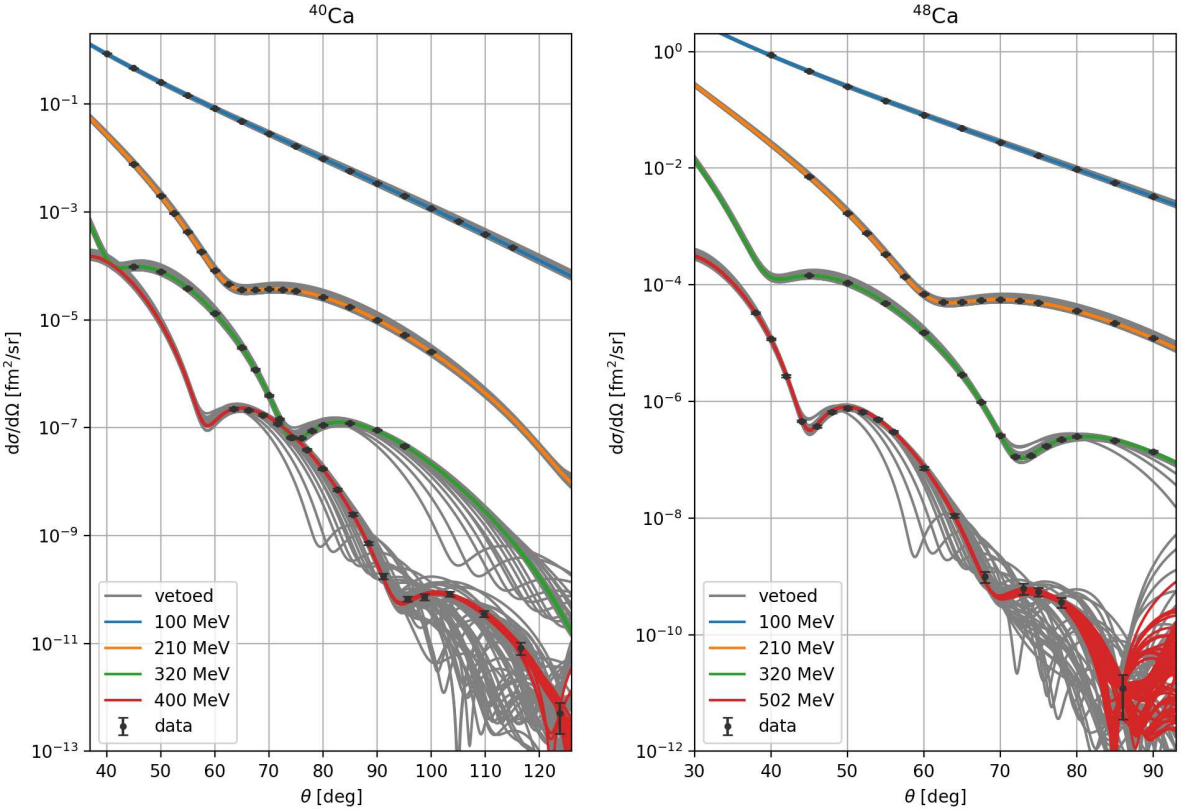

^{40}Ca

$R\backslash N_x$	3	4	5	6	7	8	9	10	11	12	13	14
6.00	125.7	27.4	25.8	20.8	8.3	6.1	5.1					
6.25		12.0	9.9	9.5	5.1	2.1	1.8	1.7				
6.50		39.6	6.8	4.5	3.3	1.8	1.8	1.2				
6.75		62.0	4.0	2.7	2.3	1.2	1.1	1.1				
7.00		72.0	4.1	2.3	1.6	1.1	1.1	1.1				
7.25			2.7	2.7	1.3	1.1	1.1	1.1	1.1			
7.50			13.1	3.6	1.1	1.1	1.1	1.1	1.1			
7.75			29.8	4.5	1.2	1.1	1.1	1.1	1.1			
8.00				4.1	1.8	1.2	1.1	1.1	1.1	1.1		
8.25				2.8	2.8	1.2	1.1	1.1	1.1	1.1		
8.50				8.7	3.7	1.1	1.1	1.1	1.1	1.1		
8.75				19.6	4.5	1.3	1.1	1.1	1.1	1.1		
9.00					4.1	1.9	1.1	1.1	1.1	1.1	1.2	
9.25					2.8	2.7	1.1	1.1	1.2	1.1	1.1	
9.50					6.6	3.7	1.2	1.2	1.2	1.1	1.2	
9.75						11.8	8.0	8.1	8.0	7.6	7.6	7.7

^{48}Ca

$R\backslash N_x$	3	4	5	6	7	8	9	10	11	12	13
6.00	74.9	13.0	12.1	5.5	2.2	1.8	1.6				
6.25	118.2	3.6	2.8	2.2	1.4	1.3	1.3				
6.50		1.4	1.3	1.3	1.2	1.2	1.2	1.2			
6.75		6.9	2.0	1.2	1.2	1.2	1.2	1.2			
7.00		21.0	2.3	1.1	1.2	1.2	1.2	1.2			
7.25			1.9	1.2	1.2	1.2	1.2	1.2	1.2		
7.50			1.5	1.5	1.2	1.2	1.2	1.2	1.2		
7.75			3.4	2.1	1.2	1.2	1.2	1.2	1.2		
8.00			8.7	2.2	1.2	1.2	1.2	1.1	1.2		
8.25				2.0	1.3	1.2	1.1	1.1	1.1	1.2	
8.50				1.9	1.8	1.1	1.1	1.1	1.1	1.2	
8.75				2.9	2.2	1.1	1.1	1.1	1.1	1.2	
9.00				5.6	2.3	1.1	1.1	1.1	1.1	1.2	
9.25					2.0	1.3	1.2	1.2	1.1	1.2	1.2
9.50					1.9	1.8	1.1	1.2	1.1	1.2	1.2
9.75					7.3	6.8	5.6	5.6	5.5	5.5	5.6

Figure D.1: Steps 1 and 2 of the fits for ^{40}Ca and ^{48}Ca. The plots show the cross-section data and the fit solutions, while the accompanying tables show the χ^2/dof (dof $= 65 - N_x$). Solutions in gray are excluded for $p_{\text{val}} < 15\%$ for ^{40}Ca and $p_{\text{val}} < 12\%$ for ^{48}Ca.

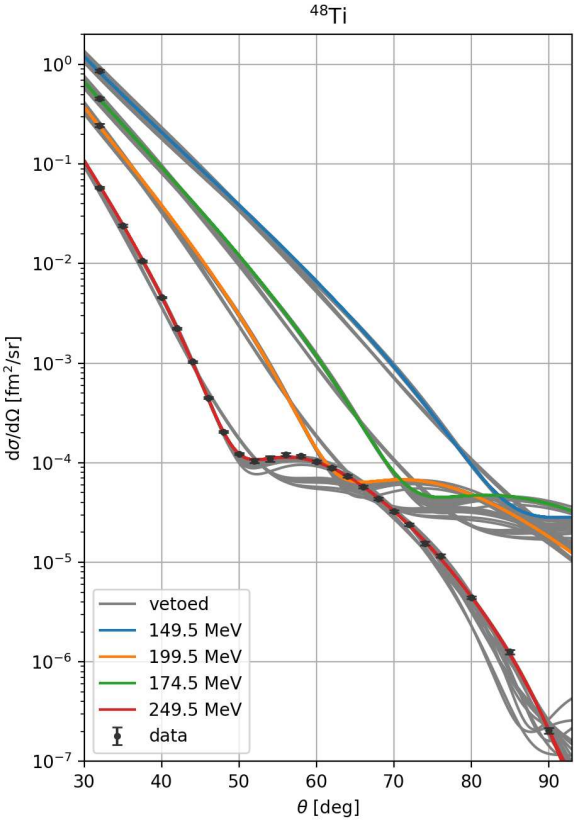

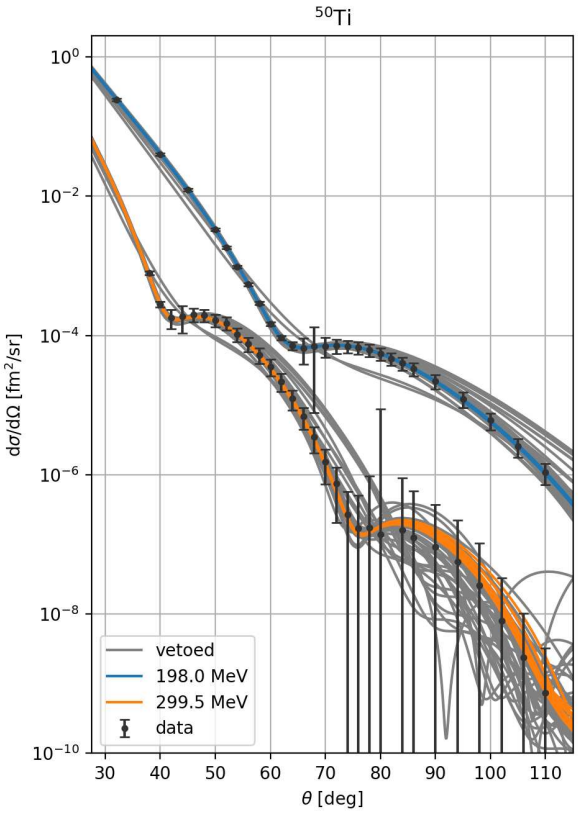

^{48}Ti

$R\backslash N_x$	3	4	5	6	7	8	9
8.50	119.7	117.5	102.2	99.8	101.8	105.9	
8.75	32.2	1.8	1.7	1.4	1.4	1.5	
9.00		1.9	1.7	1.4	1.5	1.5	1.6
9.25		1.8	1.7	1.4	1.5	1.5	1.6
9.50		1.7	1.7	1.4	1.5	1.5	1.6
9.75		2.6	1.8	1.5	1.5	1.5	1.6
10.00		7.9	2.6	2.0	2.0	2.1	2.2
10.25		37.4	18.0	16.6	17.2	18.0	18.8

^{50}Ti

$R\backslash N_x$	2	3	4	5	6	7	8	9
6.25	4.9	3.6	2.6	1.9	1.7			
6.50			110.7	56.6				
6.75		9.7	1.8	1.8	1.7	1.7		
7.00		6.7	1.7	1.7	1.7	1.7		
7.25		4.9	1.6	1.7	1.7	1.7		
7.50		4.2	2.2	1.6	1.6	1.7		
7.75			5.4	1.6	1.6	1.7	1.7	
8.00			7.7	1.6	1.6	1.7	1.6	
8.25			8.9	1.6	4.2	1.6	1.6	
8.50			6.1	1.7	1.6	1.6	1.6	
8.75			5.7	2.4	1.6	1.7	1.5	
9.00				4.7	1.6		1.5	1.5
9.25				7.0	1.6	1.5	1.5	1.5
9.50				8.3	1.5	1.5	1.5	1.5
9.75				11.3	6.4	1.5	1.5	1.5
10.00				11.0	5.4	1.8		
10.25					8.2	6.6	5.0	

Figure D.2: Steps 1 and 2 of the fits for ^{48}Ti and ^{50}Ti. The plots show the cross-section data and the fit solutions, while the accompanying tables show the χ^2/dof (dof $= 28 - N_x$ for ^{48}Ti, dof $= 57 - N_x$ for ^{50}Ti). Solutions in gray are excluded for $p_{\text{val}} < 3\%$ for ^{48}Ti and $p_{\text{val}} < 0.5\%$ for ^{50}Ti.

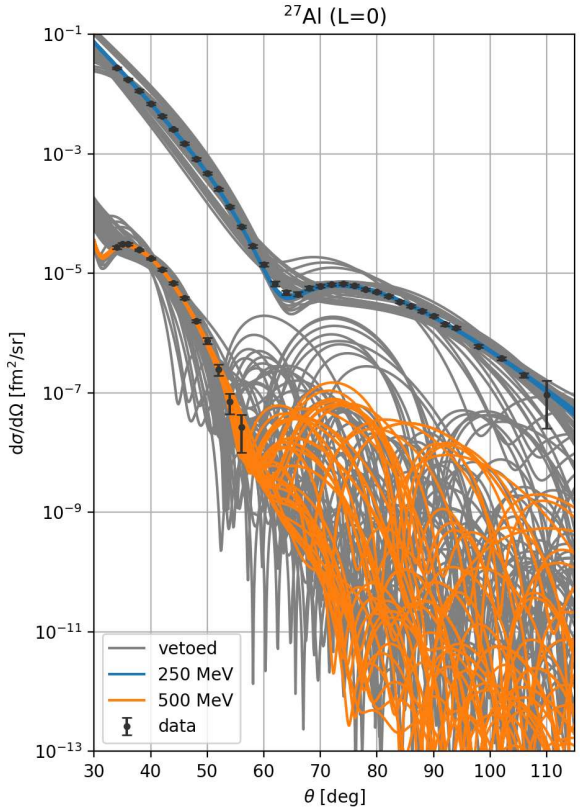

	^{27}Al								
$R\backslash N_x$	2	3	4	5	6	7	8	9	10
5.50	74.4	76.0	73.4	71.7	70.8	70.8	72.8		
5.75	122.2	74.9	72.3	70.8	70.1	69.8	71.3		
6.00	93.4	2.0	2.0	2.0	2.0	2.1	2.1		
6.25	149.2	2.1	2.1	2.0	2.1	2.1	2.1		
6.50	201.5	3.1	2.1	2.0	2.0	2.1	2.1		
6.75		6.6	2.1	2.0	2.0	2.1	2.1	2.2	
7.00		17.0	2.0	2.0	2.0	2.1	2.1	2.2	
7.25		41.3	2.0	2.0	2.0	2.1	2.1	2.2	
7.50		82.2	2.1	2.0	2.0	2.1	2.1	2.2	
7.75		132.8	2.8	2.1	2.0	1.9	1.9	1.9	
8.00			5.1	2.1	1.9	1.8	1.9	1.9	2.0
8.25			42.5	29.1	21.2	16.6	14.3	13.6	13.0
8.50			43.1	16.3	11.1	10.4	9.5	9.0	8.9
8.75			61.2	11.9	10.9	10.0	9.9	9.9	10.0

Figure D.3: Steps 1 and 2 of the fits for ^{27}Al. The plot shows the cross-section data and the fit solutions, while the table shows the χ^2/dof (dof $= 48 - N_x$). Solutions in gray are excluded for $p_{\text{val}} < 10^{-5}$.

data, one sees that the fits including the Barrett moments modify the tail of the charge density to increase the value of the charge radius. In these cases, the charge density first decreases in a similar fashion as without the additional constraint, but then hovers just slightly above zero until the larger charge radius is reached. In this way, the shape of the charge density is not altered significantly, at least not in a way that would contradict the measured cross sections or any of the other constraints we imposed, while at the same time adjusting integrated quantities such as the charge radius or the Barrett moment.

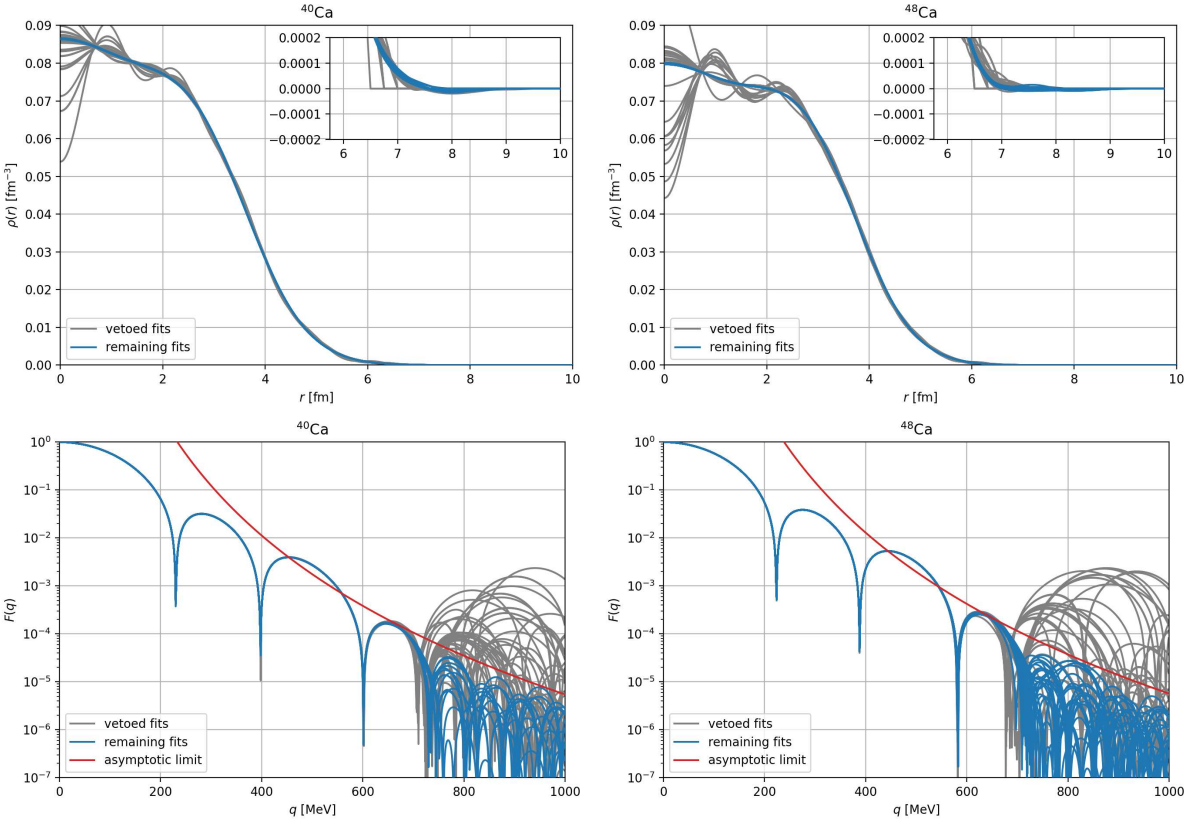

^{40}Ca								^{48}Ca							
$R\backslash N_x$	7	8	9	10	11	12	13	$R\backslash N_x$	6	7	8	9	10	11	12	13
6.50				1.416				6.50			1.168	1.177	1.197			
6.75		1.153	1.109	1.129				6.75	1.135	1.154	1.162	1.167	1.186			
7.00		1.101	1.077	1.096				7.00	1.124	1.140	1.155	1.163	1.183			
7.25		1.071	1.082	1.099	1.119			7.25		1.145	1.154	1.168	1.186	1.206		
7.50	1.107	1.085	1.087	1.101	1.121			7.50		1.155	1.152	1.164	1.185	1.206		
7.75		1.123	1.085	1.103	1.117			7.75		1.140	1.155	1.164	1.185	1.206		
8.00			1.087	1.104	1.120	1.141		8.00		1.171	1.167	1.167	1.184	1.205		
8.25		1.140	1.096	1.105	1.121	1.139		8.25			1.180	1.172	1.181	1.203	1.224	
8.50		1.107	1.111	1.128	1.119	1.137		8.50			1.137	1.152	1.168	1.189	1.211	
8.75			1.135	1.113	1.113	1.131		8.75			1.162	1.149	1.169	1.187	1.209	
9.00			1.139	1.122	1.107	1.127	1.148	9.00			1.244	1.151	1.170	1.188	1.210	
9.25			1.208	1.150	1.135	1.149	1.171	9.25				1.189	1.190	1.206	1.228	1.252
9.50						1.196	1.186	9.50				1.192	1.212	1.219	1.241	1.264

Figure D.4: Resulting charge densities and form factors after steps 3 and 4 for ^{40}Ca and ^{48}Ca. The tables show χ^2/dof (dof $= 65 + 1 - N_x$). Solutions in gray are excluded for $p_{\text{val}} < 17\%$ for ^{40}Ca and $p_{\text{val}} < 12\%$ for ^{48}Ca or when violating the asymptotic limit (indicated in red).

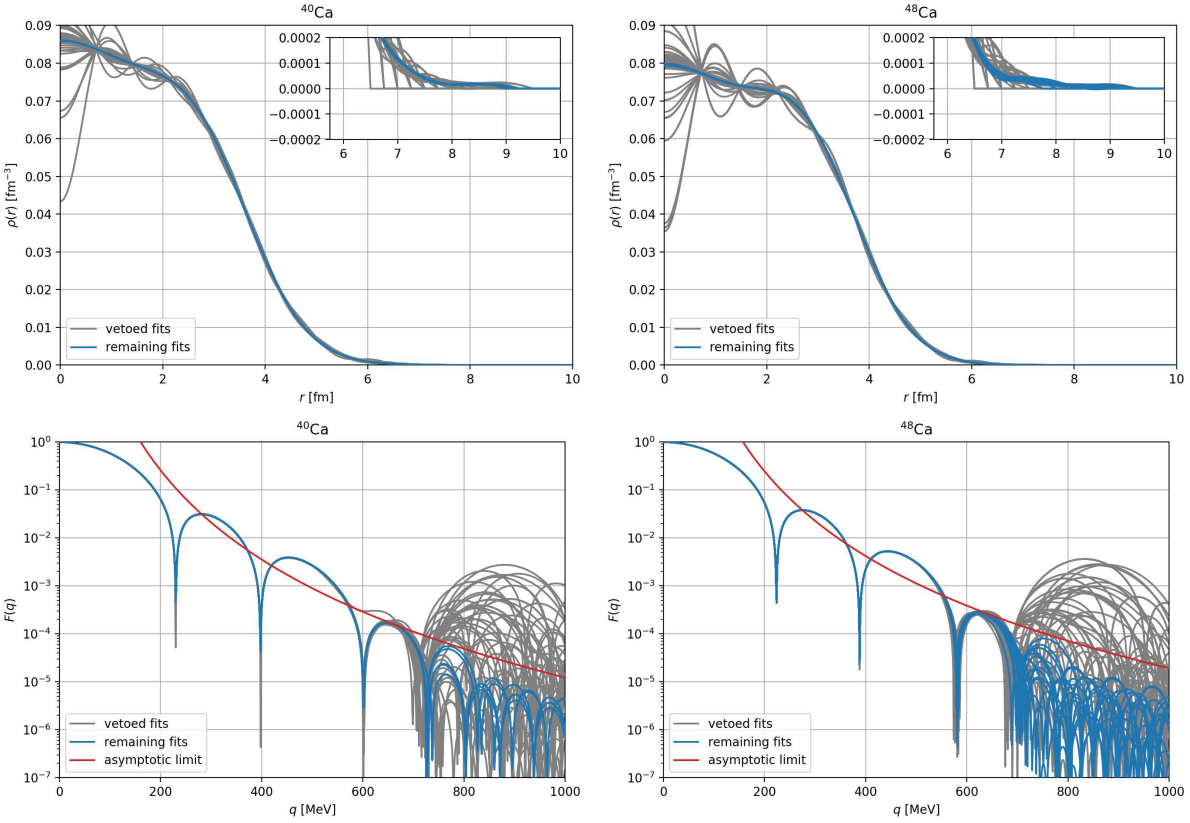

^{40}Ca							
$R\backslash N_x$	7	8	9	10	11	12	13
6.50				3.950			
6.75		3.190	2.720	2.764			
7.00		2.300	1.948	1.953			
7.25		1.875	1.740	1.769	1.784		
7.50	1.992	1.936	1.672	1.671	1.701		
7.75		1.611	1.632	1.623	1.648		
8.00			1.612	1.594	1.622	1.651	
8.25		1.580	1.599	1.571	1.599	1.628	
8.50		1.608	1.601	1.550	1.576	1.604	
8.75			1.867	1.530	1.553	1.579	
9.00			1.862	1.505	1.531	1.551	1.577
9.25			1.453	1.459	1.485	1.510	1.528
9.50						1.533	1.488

^{48}Ca								
$R\backslash N_x$	6	7	8	9	10	11	12	13
6.50			1.985	2.019	2.055			
6.75	2.256	2.164	1.721	1.731	1.761			
7.00	1.929	1.886	1.658	1.626	1.644			
7.25		1.762	1.592	1.563	1.573	1.598		
7.50		1.679	1.502	1.516	1.537	1.565		
7.75		1.535	1.472	1.497	1.521	1.547		
8.00		1.453	1.476	1.489	1.514	1.541		
8.25			1.463	1.486	1.508	1.535	1.563	
8.50			1.460	1.485	1.500	1.527	1.554	
8.75			1.459	1.481	1.498	1.522	1.544	
9.00			1.540	1.481	1.481	1.505	1.528	
9.25				1.474	1.454	1.472	1.492	1.511
9.50				1.407	1.422	1.446	1.472	1.485

Figure D.5: Same as Fig. D.4, but including the Barrett moment as an additional constraint. The tables show χ^2/dof (dof $= 65+1+1-N_x$). Solutions in gray are excluded for $p_{\text{val}} < 0.3\%$ for ^{40}Ca and $p_{\text{val}} < 0.25\%$ for ^{48}Ca or when violating the asymptotic limit (indicated in red).

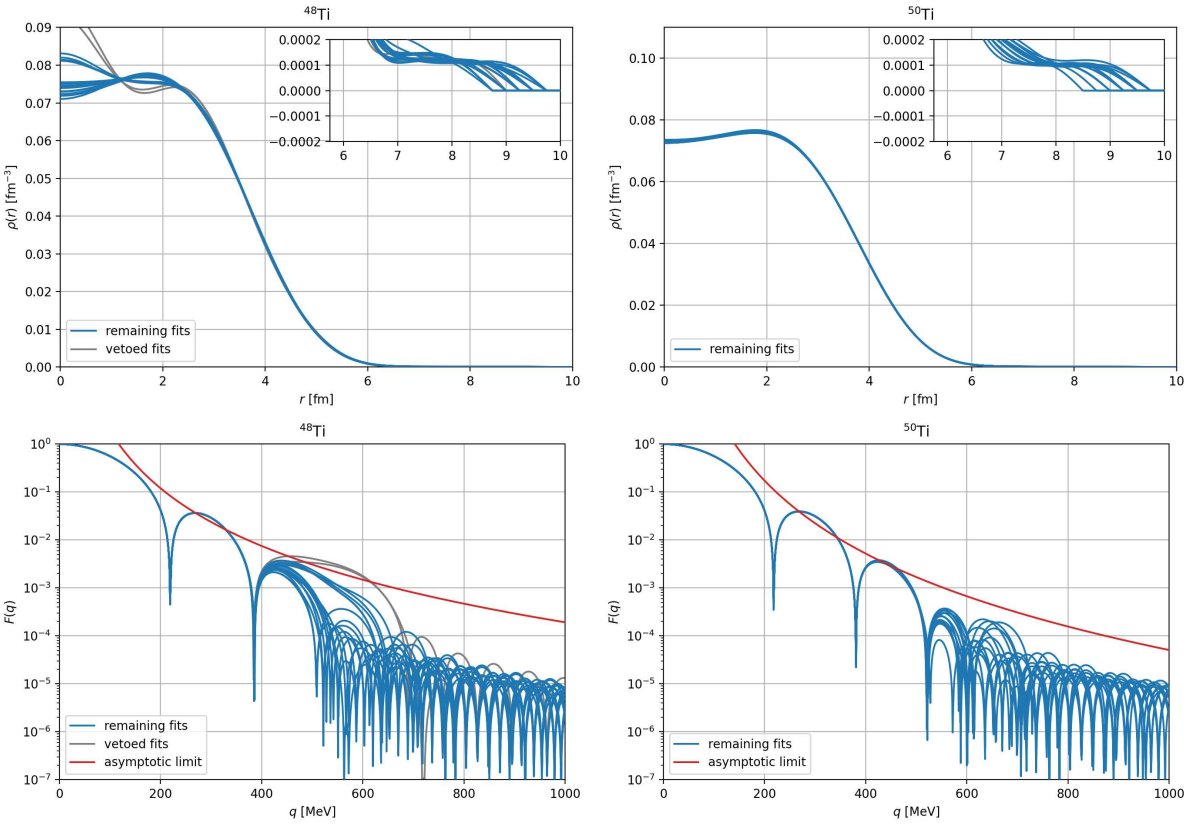

^{48}Ti				
$R\backslash N_x$	6	7	8	9
8.75	1.659	1.729	1.809	
9.00	1.623	1.694	1.737	
9.25	1.587	1.659	1.716	1.792
9.50	1.565	1.625	1.669	1.747
9.75	1.568	1.598	1.639	1.721

^{50}Ti				
$R\backslash N_x$	6	7	8	9
8.50			1.627	
8.75			1.606	
9.00			1.584	1.617
9.25		1.532	1.562	1.594
9.50	1.486	1.514	1.543	1.574
9.75		1.500	1.528	1.557

Figure D.6: Resulting charge densities and form factors after steps 3 and 4 for ^{48}Ti and ^{50}Ti. The tables show χ^2/dof (dof $= 28 + 1 - N_x$ for ^{48}Ti, dof $= 57 + 1 - N_x$ for ^{50}Ti). Solutions in gray are excluded for $p_{\text{val}} < 1\%$ for ^{48}Ti and $p_{\text{val}} < 0.1\%$ for ^{50}Ti or when violating the asymptotic limit (indicated in red).

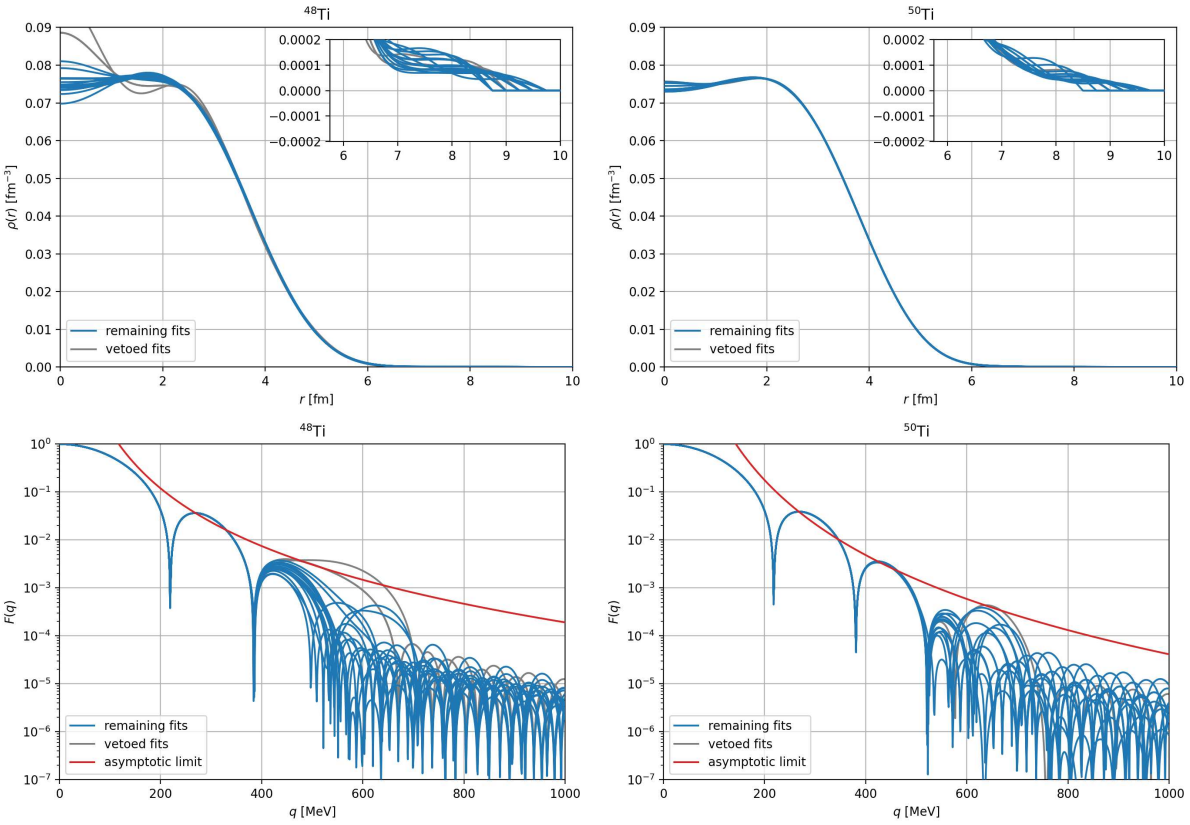

^{48}Ti

$R\backslash N_x$	6	7	8	9
8.75	1.601	1.657	1.727	
9.00	1.556	1.621	1.693	1.742
9.25	1.532	1.596	1.640	1.718
9.50	1.530	1.581	1.652	1.722
9.75	1.542	1.576	1.633	

^{50}Ti

$R\backslash N_x$	6	7	8	9
8.50			1.601	
8.75			1.575	
9.00			1.562	1.591
9.25		1.526	1.556	1.584
9.50	1.500	1.527	1.556	1.582
9.75		1.538	1.560	1.586

Figure D.7: Same as Fig. D.6, but including the Barrett moment as an additional constraint. The tables show χ^2/dof (dof $= 28 + 1 + 1 - N_x$ for ^{48}Ti, dof $= 57 + 1 + 1 - N_x$ for ^{50}Ti). Solutions in gray are excluded for $p_{\text{val}} < 0.25\%$ for ^{48}Ti and $p_{\text{val}} < 0.1\%$ for ^{50}Ti or when violating the asymptotic limit (indicated in red).

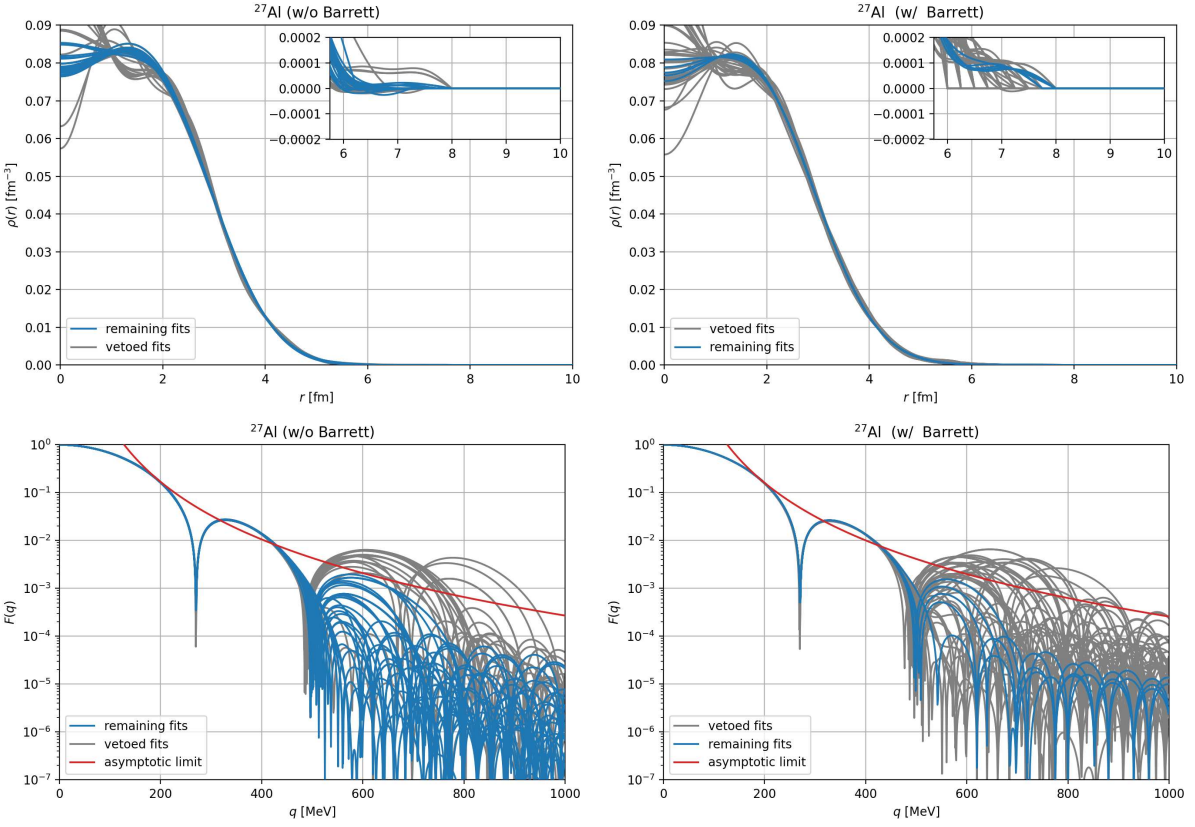

^{27}Al (w/o Barrett)								
$R\backslash N_x$	3	4	5	6	7	8	9	10
6.00	1.951	1.994	1.994	2.031	2.079	2.130		
6.25	2.103	2.019	2.013	2.032	2.080	2.129		
6.50		2.026	2.032	2.039	2.081	2.131		
6.75		2.021	2.048	2.054	2.084	2.133	2.186	
7.00		2.013	2.059	2.070	2.067	2.117	2.169	
7.25		2.113	2.069	2.092	2.110	2.108	2.161	
7.50		2.544	2.080	2.104	2.131	2.183	2.238	
7.75			2.175	2.109	2.149	2.196	2.251	
8.00			2.237	2.121	2.154	2.180	2.207	2.263

^{27}Al (w/ Barrett)								
$R\backslash N_x$	3	4	5	6	7	8	9	10
6.00	3.764	2.660	2.536	2.575	2.626	2.688		
6.25	2.504	2.496	2.477	2.496	2.553	2.611		
6.50		2.398	2.429	2.441	2.496	2.556		
6.75		2.344	2.394	2.403	2.448	2.506	2.567	
7.00		2.314	2.365	2.370	2.416	2.474	2.534	
7.25		2.310	2.344	2.334	2.383	2.439	2.471	
7.50		2.530	2.322	2.289	2.330	2.385	2.417	
7.75			2.291	2.230	2.270	2.266	2.320	
8.00			2.214	2.158	2.197	2.152	2.204	2.259

Figure D.8: Resulting charge densities and form factors after steps 3 and 4 for ^{27}Al with and without Barrett moment. The tables show χ^2/dof (dof $= 48 + 1 - N_x$ without Barrett moment, dof $= 48 + 1 + 1 - N_x$ wit Barrett moment). Solutions in gray are excluded for $p_{\text{val}} < 10^{-5}$ for fits without Barrett moment and $p_{\text{val}} < 3 \times 10^{-6}$ for fits with Barrett moment or when violating the asymptotic limit (indicated in red).

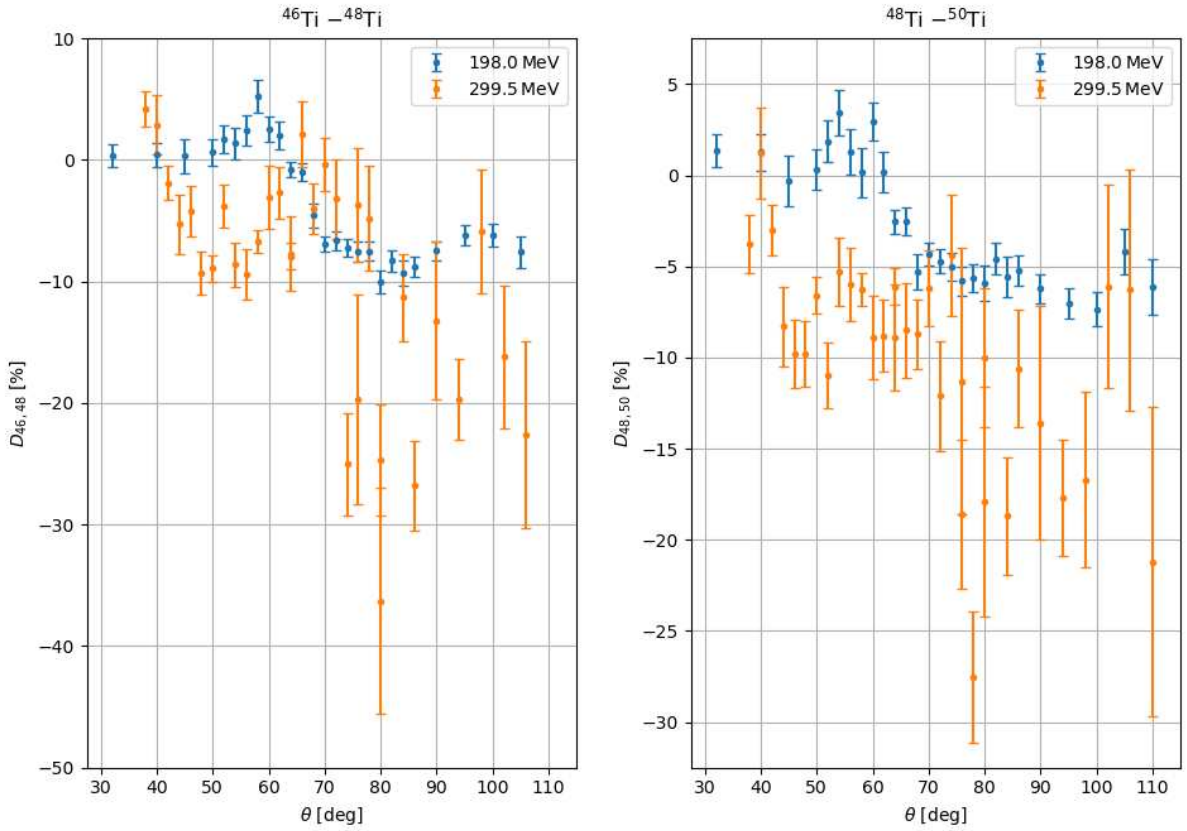

Figure D.9: Data of Ref. [181] for the differential-cross-section differences $D_{A,B}$ off target nuclei A and B (normalized to the sum).

D.1.1 Remarks on ^{46,50}Ti Data

Using the data of Ref. [181], we attempted to also extract charge densities for both ^{46}Ti and ^{50}Ti. However, ultimately we had to conclude that at least for ^{46}Ti inconsistencies in this data set were so severe that no meaningful charge distribution could be determined. Since the situation for ^{50}Ti was still significantly better than for ^{46}Ti, we included these results in this work, with the caveat that not all systematic tensions might be fully reflected by our uncertainty estimates. In Fig. D.9 we reproduce the original data from Ref. [181], illustrating the inconsistencies alluded to above. In particular, for $D_{46,48}$ there exist two (supposedly) identical measurements at 299.5 MeV and 76°, which are inconsistent at $> 1.5\sigma$. Furthermore, the measurements at 299.5 MeV do not convey a clear structure that our fit could be expected to describe, as measurements very close in angular distance can deviate drastically.

Moreover, the extracted charge density of ^{48}Ti, necessary as input to calculate the cross sections of ^{46,50}Ti, by itself is already afflicted with sizable uncertainties, which need to be propagated into the fit. Despite the large absolute value of these propagated uncertainties, surpassing the direct statistical ones, due to the strong correlations among cross sections at different angles, the direct statistical uncertainties appear to dominate the fit. This results in a fit with artificially small uncertainties, which are also not sufficiently enhanced by

scale factors. Comparing uncertainties from ^{48}Ti and ^{50}Ti, it should be expected that the precision with which ^{48}Ti can be extracted serves as a rough upper limit for the precision that can be achieved for ^{46,50}Ti. This condition is, however, only approximately fulfilled for ^{50}Ti, and strongly violated for ^{46}Ti. Finally, the p-value for the best fits for ^{46}Ti was at the 10^{-5} level, while for ^{50}Ti we could reach p-values above 1%. This led to the conclusion that even if we could scale errors to better reflect the intrinsic uncertainties, for ^{46}Ti we did not see a way to extract meaningful information beyond the ^{48}Ti charge density, while for ^{50}Ti the separate fits should still encode useful information.

D.2 Fourier-Bessel Parameter Sets

We tabulate the parameters for all our charge densities including statistic and systematic uncertainties as well as their correlations. All values listed here are also available in the supplementary `python` notebook of Ref. [2]. We list the x_i parameters including a statistical as well as an upper and lower systematic bound. The upper and lower bounds hereby refer to the side of the error band of the charge density they parameterize and do not necessarily refer to a direction in which the parameter itself may deviate. For easy accessibility, we also list the a_i parameters with a single uncertainty, defined by the combination of the individual components. We list these parameters in Tables D.1–D.3, with the corresponding correlations provided in Tables D.4–D.6. Note that by construction all uncertainty components of the x_i have the same correlation, which would however not be the case anymore if we quoted individual uncertainty components for the a_i.

^{40}Ca				
	w/o Barrett		w/ Barrett	
n	a_n	x_n	a_n	x_n
1	0.052028(85)	$0.66089(36)(^{+85}_{-50})$	0.0313412(76)	$0.73243(11)(^{+9}_{-11})$
2	0.05896(30)	$0.46506(57)(^{+101}_{-24})$	0.058045(48)	$0.08136(60)(^{+41}_{-66})$
3	−0.01332(18)	$0.41163(34)(^{+50}_{-15})$	0.022084(92)	$0.64635(87)(^{+70}_{-70})$
4	−0.02320(15)	$0.66804(53)(^{+80}_{-70})$	−0.019018(69)	$0.80501(76)(^{+70}_{-80})$
5	0.003893(49)	$0.54160(33)(^{+20}_{-40})$	−0.017467(65)	$0.15359(83)(^{+90}_{-60})$
6	0.00770(20)	$0.40127(65)(^{+250}_{-0})$	0.000966(57)	$0.47675(68)(^{+0}_{-120})$
7	0.001045(35)	$0.51564(53)(^{+0}_{-0})$	0.007210(48)	$0.70235(89)(^{+100}_{-100})$
8	−0.00075(20)	$0.4977(12)(^{+20}_{-10})$	0.003362(68)	$0.39217(90)(^{+0}_{-200})$
9	0.00012(12)		−0.000043(39)	$0.49845(98)(^{+0}_{-100})$
10			−0.00057(12)	$0.4976(13)(^{+20}_{-20})$
11			0.000055(54)	

^{48}Ca				
	w/o Barrett		w/ Barrett	
n	a_n	x_n	a_n	x_n
1	0.060470(58)	$0.63198(35)(^{+37}_{-38})$	0.029287(26)	$0.74113(12)(^{+57}_{-50})$
2	0.05005(18)	$0.55505(29)(^{+24}_{-30})$	0.056123(56)	$0.03046(35)(^{+10}_{-110})$
3	−0.03108(18)	$0.41244(47)(^{+60}_{-70})$	0.02222(17)	$0.66040(67)(^{+260}_{-250})$
4	−0.01544(14)	$0.53997(33)(^{+80}_{-20})$	−0.021143(69)	$0.86326(61)(^{+40}_{-0})$
5	0.012265(89)	$0.56299(54)(^{+40}_{-0})$	−0.02059(36)	$0.06244(47)(^{+400}_{-900})$
6	0.00493(20)	$0.5151(11)(^{+10}_{-16})$	0.000919(48)	$0.47604(74)(^{+100}_{-100})$
7	−0.00125(16)		0.009187(36)	$0.7793(11)(^{+0}_{-0})$
8			0.00448(32)	$0.3571(10)(^{+0}_{-0})$
9			−0.00019(75)	$0.46486(86)(^{+0}_{-0})$
10			−0.000809(20)	

Table D.1: FB parameters for ^{40}Ca and ^{48}Ca.

^{48}Ti				
w/o Barrett			w/ Barrett	
n	a_n	x_n	a_n	x_n
1	0.03166(28)	$0.7351(20)(^{+0}_{-54})$	0.03392(20)	$0.72798(19)(^{+0}_{-380})$
2	0.0579(10)	$0.1043(51)(^{+0}_{-170})$	0.05913(54)	$0.1639(19)(^{+0}_{-80})$
3	0.01966(48)	$0.5576(28)(^{+0}_{-30})$	0.01547(77)	$0.4950(26)(^{+0}_{-0})$
4	−0.0232(24)	$0.8333(46)(^{+100}_{-460})$	−0.02550(92)	$0.8333(43)(^{+160}_{-90})$
5	−0.0178(31)	$0.2312(58)(^{+800}_{-0})$	−0.0152(17)	$0.3217(51)(^{+380}_{-100})$
6	0.0011(51)	$0.395(14)(^{+160}_{-21})$	0.0029(37)	$0.406(23)(^{+92}_{-68})$
7	0.0038(58)		0.0037(37)	

^{50}Ti				
w/o Barrett			w/ Barrett	
n	a_n	x_n	a_n	x_n
1	0.03168(15)	$0.7356(11)(^{+29}_{-15})$	0.031816(31)	$0.73837(17)(^{+60}_{-20})$
2	0.05810(58)	$0.1008(38)(^{+94}_{-64})$	0.05854(30)	$0.0933(25)(^{+0}_{-52})$
3	0.01934(46)	$0.5497(27)(^{+27}_{-0})$	0.01935(48)	$0.5518(29)(^{+0}_{-40})$
4	−0.02511(53)	$0.8681(39)(^{+90}_{-0})$	−0.02471(41)	$0.8612(38)(^{+0}_{-63})$
5	−0.01908(25)	$0.2008(58)(^{+0}_{-0})$	−0.01882(57)	$0.2090(61)(^{+160}_{-20})$
6	0.00245(64)	$0.3552(73)(^{+140}_{-40})$	0.00243(96)	$0.3692(70)(^{+340}_{-10})$
7	0.00524(57)		0.0047(13)	

Table D.2: FB parameters for ^{48}Ti and ^{50}Ti.

^{27}Al				
w/o Barrett			w/ Barrett	
n	a_n	x_n	a_n	x_n
1	0.06189(74)	$0.6386(17)(^{+54}_{-68})$	0.03125(11)	$0.73357(22)(^{+0}_{-230})$
2	0.0531(25)	$0.5427(10)(^{+50}_{-71})$	0.05727(73)	$0.1042(12)(^{+0}_{-137})$
3	−0.0212(33)	$0.3895(17)(^{+370}_{-70})$	0.02301(71)	$0.6235(14)(^{+0}_{-40})$
4	−0.0164(55)		−0.01565(49)	$0.7163(19)(^{+0}_{-0})$
5			−0.0163(11)	$0.2457(19)(^{+270}_{-0})$
6			−0.0039(26)	$0.4723(19)(^{+530}_{-150})$
7			0.0010(19)	

Table D.3: FB parameters for ^{27}Al.

^{40}Ca; w/o Barrett									
$a_i \backslash x_i$	1	2	3	4	5	6	7	8	
1	1.000	−0.933	−0.560	0.777	0.202	−0.460	0.023	0.295	–
2	0.984	1.000	0.683	−0.765	−0.284	0.338	−0.087	−0.153	–
3	−0.839	−0.751	1.000	−0.755	−0.434	0.005	−0.247	0.194	–
4	−0.746	−0.776	0.699	1.000	0.138	−0.466	−0.015	0.255	–
5	0.202	0.245	−0.153	−0.252	1.000	−0.138	0.020	−0.017	–
6	0.460	0.409	−0.426	−0.329	0.138	1.000	−0.041	−0.369	–
7	0.023	0.055	−0.013	−0.077	0.020	0.041	1.000	−0.211	–
8	−0.407	−0.380	0.369	0.327	−0.232	−0.915	−0.272	1.000	–
9	−0.295	−0.231	0.293	0.110	0.017	−0.369	0.211	0.264	1.000

^{40}Ca; w/ Barrett											
$a_i \backslash x_i$	1	2	3	4	5	6	7	8	9	10	
1	1.000	−0.376	−0.217	0.054	−0.180	0.063	0.083	0.051	0.110	0.340	–
2	0.420	1.000	−0.622	−0.294	0.496	−0.180	−0.320	−0.178	−0.485	−0.243	–
3	−0.233	0.703	1.000	−0.278	−0.371	−0.074	0.011	0.050	0.297	0.092	–
4	−0.054	−0.291	0.079	1.000	−0.409	0.171	0.302	0.215	0.237	−0.078	–
5	−0.189	−0.431	−0.352	0.397	1.000	−0.173	−0.191	−0.352	−0.403	−0.027	–
6	−0.063	−0.180	−0.009	0.171	0.107	1.000	−0.010	−0.053	−0.018	−0.139	–
7	0.083	0.318	0.117	−0.302	−0.134	0.010	1.000	−0.022	0.337	0.372	–
8	−0.051	−0.177	−0.094	0.215	0.330	−0.053	0.022	1.000	0.046	−0.046	–
9	0.110	0.480	0.368	−0.237	−0.360	0.018	0.337	−0.046	1.000	0.280	–
10	0.036	−0.499	−0.714	−0.250	0.182	−0.368	−0.093	−0.237	−0.322	1.000	–
11	−0.340	−0.255	−0.078	−0.078	0.023	−0.139	−0.372	−0.046	−0.280	0.253	1.000

^{48}Ca; w/o Barrett							
$a_i \backslash x_i$	1	2	3	4	5	6	
1	1.000	0.776	−0.775	0.625	0.443	0.071	–
2	0.975	1.000	−0.714	0.608	0.426	0.129	–
3	−0.828	−0.731	1.000	−0.534	−0.344	0.021	–
4	−0.672	−0.662	0.759	1.000	0.492	0.216	–
5	0.099	0.159	−0.226	−0.098	1.000	0.295	–
6	0.374	0.296	−0.242	−0.340	−0.282	1.000	–
7	−0.071	−0.043	0.028	0.082	0.048	0.202	1.000

^{48}Ca; w/ Barrett										
$a_i \backslash x_i$	1	2	3	4	5	6	7	8	9	
1	1.000	−0.453	−0.157	−0.352	−0.088	0.005	−0.350	0.141	0.059	–
2	0.499	1.000	−0.466	0.247	0.172	−0.309	0.486	−0.344	−0.151	–
3	−0.465	0.345	1.000	−0.513	−0.350	0.128	−0.414	0.287	0.224	–
4	0.547	0.338	0.226	1.000	0.031	−0.273	0.479	−0.368	−0.167	–
5	−0.123	−0.188	−0.262	−0.214	1.000	0.158	0.042	0.020	−0.066	–
6	−0.005	−0.301	−0.168	−0.133	−0.161	1.000	−0.310	0.369	0.078	–
7	−0.350	−0.493	−0.266	−0.519	0.064	0.310	1.000	−0.499	−0.083	–
8	0.433	0.089	−0.219	0.429	0.701	−0.107	−0.238	1.000	0.046	–
9	−0.443	−0.131	0.187	−0.461	−0.692	0.153	0.299	−0.991	1.000	–
10	0.059	0.150	0.176	0.188	−0.074	−0.078	−0.083	0.067	−0.051	1.000

Table D.4: Correlations for ^{40}Ca and ^{48}Ca for x_i (upper triangle) and a_i (lower triangle).

^{48}Ti; w/o Barrett							
$a_i \backslash x_i$	1	2	3	4	5	6	
1	1.000	−0.932	0.096	−0.429	0.151	−0.075	–
2	0.947	1.000	−0.235	0.423	−0.285	−0.038	–
3	−0.272	0.025	1.000	−0.660	0.196	−0.127	–
4	0.444	0.427	0.162	1.000	−0.389	−0.004	–
5	0.211	0.333	0.371	0.551	1.000	0.303	–
6	−0.060	−0.112	−0.206	−0.397	−0.004	1.000	–
7	0.075	−0.025	−0.174	0.017	−0.288	0.695	1.000

^{48}Ti; w/ Barrett							
$a_i \backslash x_i$	1	2	3	4	5	6	
1	1.000	−0.424	0.021	−0.037	0.089	0.098	–
2	0.614	1.000	−0.271	0.108	−0.324	−0.382	–
3	−0.696	0.119	1.000	−0.708	0.159	−0.251	–
4	0.205	0.093	−0.035	1.000	−0.266	−0.029	–
5	−0.143	0.287	0.460	0.336	1.000	0.169	–
6	0.289	−0.138	−0.449	−0.061	0.053	1.000	–
7	−0.098	−0.357	−0.120	0.026	−0.219	0.752	1.000

^{50}Ti; w/o Barrett							
$a_i \backslash x_i$	1	2	3	4	5	6	
1	1.000	−0.846	0.158	−0.262	0.040	0.402	–
2	0.875	1.000	−0.540	0.060	0.117	−0.281	–
3	−0.166	0.314	1.000	−0.242	−0.165	−0.042	–
4	0.310	0.095	−0.214	1.000	−0.522	−0.032	–
5	−0.121	−0.109	0.076	0.573	1.000	0.027	–
6	0.091	−0.155	−0.572	−0.307	−0.362	1.000	–
7	−0.402	−0.298	0.182	−0.066	0.120	0.329	1.000

^{50}Ti; w/ Barrett							
$a_i \backslash x_i$	1	2	3	4	5	6	
1	1.000	−0.460	0.207	0.076	−0.077	−0.082	–
2	0.489	1.000	−0.746	−0.321	0.313	0.389	–
3	0.159	0.887	1.000	−0.195	−0.253	−0.215	–
4	−0.056	−0.355	−0.115	1.000	−0.470	−0.229	–
5	−0.106	−0.256	−0.238	0.477	1.000	0.236	–
6	0.130	0.019	−0.079	−0.085	0.337	1.000	–
7	0.082	0.385	0.332	−0.253	−0.200	0.714	1.000

Table D.5: Correlations for ^{48}Ti and ^{50}Ti for x_i (upper triangle) and a_i (lower triangle).

^{27}Al; w/o Barrett				
$a_i \backslash x_i$	1	2	3	
1	1.000	0.655	−0.202	–
2	0.961	1.000	0.235	–
3	−0.595	−0.570	1.000	–
4	−0.202	−0.328	0.800	1.000

^{27}Al; w/ Barrett							
$a_i \backslash x_i$	1	2	3	4	5	6	
1	1.000	−0.335	−0.052	0.017	−0.010	−0.001	–
2	0.391	1.000	−0.460	−0.323	−0.205	−0.031	–
3	−0.209	0.787	1.000	−0.033	0.397	−0.127	–
4	0.221	−0.766	−0.861	1.000	−0.020	0.586	–
5	−0.106	0.463	0.595	−0.471	1.000	−0.088	–
6	0.176	−0.449	−0.467	0.704	0.172	1.000	–
7	0.001	−0.030	0.011	0.184	0.072	0.586	1.000

Table D.6: Correlations for ^{27}Al for x_i (upper triangle) and a_i (lower triangle).

D.3 Data Tables

Due to the complications of retrieving the original cross sections, we tabulate in this appendix the data we used in our analysis. Tab. D.7 shows the data for calcium, Tab. D.8 the data for titanium, and Tab. D.9 the data for aluminum.

^{40}Ca					
E [MeV]	θ [deg]	dσ/dΩ	(stat)	(sys)	[fm^2/sr]
100	40	8.698	(74)	(107)	$\times 10^{-1}$
	45	4.673	(40)	(58)	$\times 10^{-1}$
	50	2.542	(17)	(31)	$\times 10^{-1}$
	55	1.462	(13)	(18)	$\times 10^{-1}$
	60	8.317	(58)	(103)	$\times 10^{-2}$
	65	4.873	(34)	(60)	$\times 10^{-2}$
	70	2.840	(20)	(35)	$\times 10^{-2}$
	75	1.679	(11)	(21)	$\times 10^{-2}$
	80	9.856	(67)	(122)	$\times 10^{-3}$
	85	5.846	(40)	(72)	$\times 10^{-3}$
	90	3.433	(29)	(42)	$\times 10^{-3}$
	95	2.007	(14)	(25)	$\times 10^{-3}$
	100	1.173	(10)	(14)	$\times 10^{-3}$
	105	6.776	(58)	(84)	$\times 10^{-4}$
	110	3.897	(33)	(48)	$\times 10^{-4}$
	115	2.223	(19)	(27)	$\times 10^{-4}$
210	45	7.703	(73)	(182)	$\times 10^{-3}$
	50	1.976	(18)	(47)	$\times 10^{-3}$
	52.5	9.434	(85)	(223)	$\times 10^{-4}$
	55	4.274	(39)	(101)	$\times 10^{-4}$
	57.5	1.847	(17)	(44)	$\times 10^{-4}$
	60	8.293	(77)	(196)	$\times 10^{-5}$
	62.5	4.571	(39)	(108)	$\times 10^{-5}$
	65	3.644	(31)	(86)	$\times 10^{-5}$
	67.5	3.599	(31)	(85)	$\times 10^{-5}$
	70	3.731	(32)	(88)	$\times 10^{-5}$
	72.5	3.675	(32)	(87)	$\times 10^{-5}$
	75	3.468	(29)	(82)	$\times 10^{-5}$
	80	2.658	(22)	(63)	$\times 10^{-5}$
	85	1.748	(15)	(41)	$\times 10^{-5}$
	90	9.997	(90)	(236)	$\times 10^{-6}$
	95	5.250	(52)	(124)	$\times 10^{-6}$
	100	2.565	(28)	(61)	$\times 10^{-6}$
320	45	9.678	(93)	(267)	$\times 10^{-5}$
	50	7.860	(76)	(217)	$\times 10^{-5}$
	55	3.872	(38)	(107)	$\times 10^{-5}$
	60	1.339	(13)	(37)	$\times 10^{-5}$
	65	3.056	(32)	(84)	$\times 10^{-6}$
	67.5	1.206	(14)	(33)	$\times 10^{-6}$
	70	3.983	(58)	(110)	$\times 10^{-7}$
	72	1.449	(27)	(40)	$\times 10^{-7}$
	74	6.653	(136)	(184)	$\times 10^{-8}$
	76	6.423	(133)	(177)	$\times 10^{-8}$
	78	8.751	(157)	(242)	$\times 10^{-8}$
	80	1.133	(14)	(31)	$\times 10^{-7}$
	85	1.218	(22)	(34)	$\times 10^{-7}$
	90	9.064	(172)	(250)	$\times 10^{-8}$
	95	4.596	(123)	(127)	$\times 10^{-8}$
400*	63.528	2.240	(79)	(55)	$\times 10^{-7}$
	66.196	2.110	(75)	(52)	$\times 10^{-7}$
	68.882	1.740	(62)	(43)	$\times 10^{-7}$
	71.588	1.200	(48)	(30)	$\times 10^{-7}$
	74.316	6.640	(281)	(163)	$\times 10^{-8}$
	77.067	3.940	(139)	(97)	$\times 10^{-8}$
	79.845	1.750	(62)	(43)	$\times 10^{-8}$
	82.65	7.110	(360)	(175)	$\times 10^{-9}$
	85.485	2.480	(151)	(61)	$\times 10^{-9}$
	88.355	7.210	(488)	(177)	$\times 10^{-10}$
	91.189	1.770	(191)	(44)	$\times 10^{-10}$
	95.671	6.680	(660)	(164)	$\times 10^{-11}$
	98.72	7.330	(977)	(180)	$\times 10^{-11}$
	103.398	8.280	(842)	(204)	$\times 10^{-11}$
	109.758	3.570	(434)	(88)	$\times 10^{-11}$
	116.507	8.360	(2154)	(206)	$\times 10^{-12}$
	123.719	5.110	(2991)	(126)	$\times 10^{-13}$

^{48}Ca					
E [MeV]	θ [deg]	dσ/dΩ	(stat)	(sys)	[fm^2/sr]
100	40	8.694	(75)	(97)	$\times 10^{-1}$
	45	4.636	(40)	(52)	$\times 10^{-1}$
	50	2.515	(17)	(28)	$\times 10^{-1}$
	55	1.441	(12)	(16)	$\times 10^{-1}$
	60	8.220	(57)	(92)	$\times 10^{-2}$
	65	4.828	(33)	(54)	$\times 10^{-2}$
	70	2.783	(19)	(31)	$\times 10^{-2}$
	75	1.645	(11)	(18)	$\times 10^{-2}$
	80	9.552	(65)	(106)	$\times 10^{-3}$
	85	5.635	(37)	(63)	$\times 10^{-3}$
	90	3.266	(26)	(36)	$\times 10^{-3}$
	95	1.888	(13)	(21)	$\times 10^{-3}$
	100	1.081	(9)	(12)	$\times 10^{-3}$
	105	6.170	(52)	(69)	$\times 10^{-4}$
	110	3.480	(29)	(39)	$\times 10^{-4}$
	115	1.945	(17)	(22)	$\times 10^{-4}$
210	45	7.138	(67)	(156)	$\times 10^{-3}$
	50	1.707	(16)	(37)	$\times 10^{-3}$
	52.5	7.744	(72)	(170)	$\times 10^{-4}$
	55	3.312	(31)	(73)	$\times 10^{-4}$
	57.5	1.401	(13)	(31)	$\times 10^{-4}$
	60	6.975	(65)	(153)	$\times 10^{-5}$
	62.5	5.034	(42)	(110)	$\times 10^{-5}$
	65	5.085	(41)	(111)	$\times 10^{-5}$
	67.5	5.437	(43)	(119)	$\times 10^{-5}$
	70	5.599	(45)	(123)	$\times 10^{-5}$
	72.5	5.352	(43)	(117)	$\times 10^{-5}$
	75	4.904	(39)	(107)	$\times 10^{-5}$
	80	3.565	(28)	(78)	$\times 10^{-5}$
	85	2.219	(17)	(49)	$\times 10^{-5}$
	90	1.210	(10)	(26)	$\times 10^{-5}$
	95	6.124	(59)	(134)	$\times 10^{-6}$
	100	2.732	(27)	(60)	$\times 10^{-6}$
320	45	1.450	(14)	(39)	$\times 10^{-4}$
	50	1.076	(10)	(29)	$\times 10^{-4}$
	55	4.837	(46)	(130)	$\times 10^{-5}$
	60	1.512	(15)	(41)	$\times 10^{-5}$
	65	2.866	(30)	(77)	$\times 10^{-6}$
	67.5	9.757	(108)	(262)	$\times 10^{-7}$
	70	2.618	(39)	(70)	$\times 10^{-7}$
	72	1.137	(20)	(31)	$\times 10^{-7}$
	74	1.182	(26)	(32)	$\times 10^{-7}$
	76	1.732	(34)	(47)	$\times 10^{-7}$
	78	2.232	(39)	(60)	$\times 10^{-7}$
	80	2.513	(48)	(68)	$\times 10^{-7}$
	85	2.139	(37)	(58)	$\times 10^{-7}$
	90	1.385	(26)	(37)	$\times 10^{-7}$
	95	6.482	(169)	(174)	$\times 10^{-8}$
502	38	3.321	(114)	(56)	$\times 10^{-5}$
	40	1.183	(41)	(20)	$\times 10^{-5}$
	42	2.759	(111)	(46)	$\times 10^{-6}$
	44	4.614	(188)	(78)	$\times 10^{-7}$
	46	3.797	(173)	(64)	$\times 10^{-7}$
	48	6.558	(289)	(110)	$\times 10^{-7}$
	50	7.631	(298)	(128)	$\times 10^{-7}$
	52	6.586	(253)	(111)	$\times 10^{-7}$
	54	4.972	(186)	(84)	$\times 10^{-7}$
	56	3.040	(111)	(51)	$\times 10^{-7}$
	60	7.259	(408)	(122)	$\times 10^{-8}$
	64	1.102	(81)	(19)	$\times 10^{-8}$
	68	9.921	(2049)	(167)	$\times 10^{-10}$
	73	6.231	(1342)	(105)	$\times 10^{-10}$
	75	5.457	(966)	(92)	$\times 10^{-10}$
	78	3.607	(681)	(61)	$\times 10^{-10}$
	86	1.217	(865)	(20)	$\times 10^{-11}$

Table D.7: Electron scattering off ^{40}Ca and ^{48}Ca cross-section data from Ref. [175]. The 400* MeV data for ^{40}Ca are adjusted (initially measured at 502 MeV) from Ref. [174], as used in Ref. [175].

^{48}Ti − ^{50}Ti				
E [MeV]	θ [deg]	$D_{48,50}$	(stat)	
198	32	1.36	(92)	%
	40	1.26	(100)	%
	45	-0.32	(140)	%
	50	0.32	(110)	%
	52	1.86	(115)	%
	54	3.45	(125)	%
	56	1.27	(125)	%
	58	0.17	(135)	%
	60	2.96	(105)	%
	62	0.16	(110)	%
	64	−2.55	(65)	%
	66	−2.51	(75)	%
	68	−5.30	(100)	%
	70	−4.33	(65)	%
	72	−4.72	(65)	%
	74	−5.00	(77)	%
	76	−5.81	(79)	%
	78	−5.63	(76)	%
	80	−5.91	(98)	%
	82	−4.60	(86)	%
	84	−5.56	(111)	%
	86	−5.24	(81)	%
	90	−6.22	(80)	%
	95	−7.02	(82)	%
	100	−7.35	(95)	%
	105	−4.21	(124)	%
	110	−6.14	(150)	%
299.5	38	−3.8	(16)	%
	40	1.2	(25)	%
	42	−3.0	(14)	%
	44	−8.3	(22)	%
	46	−9.8	(19)	%
	48	−9.8	(18)	%
	50	−6.6	(10)	%
	52	−11.0	(18)	%
	54	−5.3	(19)	%
	56	−6.0	(20)	%
	58	−6.3	(9)	%
	60	−8.9	(23)	%
	62	−8.8	(20)	%
	64	−7.5	(29)	%
	66	−8.5	(26)	%
	68	−8.7	(19)	%
	70	−6.2	(21)	%
	72	−12.1	(30)	%
	74	−4.4	(33)	%
	76	−15.0	(73)	%
	78	−27.5	(36)	%
	80	−14.0	(63)	%
	84	−18.7	(32)	%
	86	−10.6	(32)	%
	90	−13.6	(64)	%
	94	−17.7	(32)	%
	98	−16.7	(48)	%
	102	−6.1	(56)	%
	106	−6.3	(66)	%
	110	−21.2	(85)	%

^{46}Ti − ^{48}Ti				
E [MeV]	θ [deg]	$D_{46,48}$	(stat)	
198	32	0.33	(92)	%
	40	0.44	(100)	%
	45	0.32	(140)	%
	50	0.63	(110)	%
	52	1.75	(115)	%
	54	1.35	(125)	%
	56	2.46	(125)	%
	58	5.20	(135)	%
	60	2.51	(105)	%
	62	2.02	(110)	%
	64	−0.76	(65)	%
	66	−0.99	(75)	%
	68	−4.57	(100)	%
	70	−6.90	(65)	%
	72	−6.63	(75)	%
	74	−7.23	(71)	%
	76	−7.56	(82)	%
	78	−7.50	(75)	%
	80	−10.00	(94)	%
	82	−8.30	(86)	%
	84	−9.30	(104)	%
	86	−8.80	(86)	%
	90	−7.45	(78)	%
	95	−6.20	(84)	%
	100	−6.20	(97)	%
	105	−7.58	(129)	%
299.5	38	4.2	(15)	%
	40	2.9	(24)	%
	42	−1.9	(14)	%
	44	−5.3	(24)	%
	46	−4.2	(21)	%
	48	−9.3	(18)	%
	50	−8.9	(11)	%
	52	−3.8	(18)	%
	54	−8.6	(18)	%
	56	−9.4	(21)	%
	58	−6.7	(9)	%
	60	−3.1	(26)	%
	62	−2.7	(21)	%
	64	−7.8	(31)	%
	66	2.1	(27)	%
	68	−4.0	(21)	%
	70	−0.4	(22)	%
	72	−3.2	(33)	%
	74	−25.0	(42)	%
	76	−11.7	(86)	%
	78	−4.8	(43)	%
	80	−30.5	(93)	%
	84	−11.3	(36)	%
	86	−26.8	(37)	%
	90	−13.2	(65)	%
	94	−19.7	(33)	%
	98	−5.9	(51)	%
	102	−16.2	(59)	%
	106	−22.6	(77)	%

^{48}Ca − ^{48}Ti				
E [MeV]	θ [deg]	$D_{\mathrm{Ca,Ti}}$	(stat)	
149.5	32	−7.9	(12)	%
174.5	32	−5.7	(16)	%
199.5	32	−5.2	(18)	%
249.5	32	0.9	(12)	%
	35	1.2	(15)	%
	37.5	3.8	(10)	%
	40	4.3	(7)	%
	42	5.0	(10)	%
	44	5.4	(8)	%
	46	6.1	(10)	%
	48	3.4	(10)	%
	50	−7.2	(7)	%
	52	−16.1	(15)	%
	54	−19.3	(15)	%
	56	−19.9	(15)	%
	58	−16.1	(14)	%
	60	−10.5	(12)	%
	62	−7.4	(12)	%
	64	−4.8	(12)	%
	66	−1.1	(15)	%
	68	1.8	(14)	%
	70	4.0	(14)	%
	72	5.5	(14)	%
	74	11.4	(20)	%
	76	8.6	(14)	%
	80	17.5	(14)	%
	85	20.9	(24)	%
	90	34.9	(30)	%

Table D.8: Electron scattering cross-section differences $D_{A,B}$ between ^{48}Ca, ^{48}Ti, ^{50}Ti, and ^{46}Ti from Refs. [171, 181].

^{27}Al					
E [MeV]	θ [deg]	dσ/dΩ	(stat)	(sys)	[fm^2/sr]
250	34	2.78	(8)	(8)	$\times 10^{-2}$
	36	1.79	(5)	(5)	$\times 10^{-2}$
	38	1.16	(3)	(3)	$\times 10^{-2}$
	40	7.05	(21)	(21)	$\times 10^{-3}$
	42	4.37	(13)	(13)	$\times 10^{-3}$
	44	2.65	(8)	(8)	$\times 10^{-3}$
	46	1.55	(5)	(5)	$\times 10^{-3}$
	48	8.76	(26)	(26)	$\times 10^{-4}$
	50	5.15	(15)	(15)	$\times 10^{-4}$
	52	2.86	(9)	(9)	$\times 10^{-4}$
	54	1.53	(5)	(5)	$\times 10^{-4}$
	56	7.70	(23)	(23)	$\times 10^{-5}$
	58	4.12	(12)	(12)	$\times 10^{-5}$
	60	2.36	(7)	(7)	$\times 10^{-5}$
	62	1.39	(4)	(4)	$\times 10^{-5}$
	64	1.01	(3)	(3)	$\times 10^{-5}$
	66	8.50	(26)	(26)	$\times 10^{-6}$
	68	8.62	(26)	(26)	$\times 10^{-6}$
	70	8.35	(25)	(25)	$\times 10^{-6}$
	72	8.20	(25)	(25)	$\times 10^{-6}$
	74	7.95	(24)	(24)	$\times 10^{-6}$
	76	7.10	(21)	(21)	$\times 10^{-6}$
	78	6.13	(18)	(18)	$\times 10^{-6}$
	80	5.42	(16)	(16)	$\times 10^{-6}$
	82	4.64	(14)	(14)	$\times 10^{-6}$
	84	3.74	(12)	(11)	$\times 10^{-6}$
	86	3.14	(9)	(9)	$\times 10^{-6}$
	88	2.60	(8)	(8)	$\times 10^{-6}$
	90	2.19	(7)	(7)	$\times 10^{-6}$
	92	1.62	(5)	(5)	$\times 10^{-6}$
	94	1.44	(4)	(4)	$\times 10^{-6}$
	98	7.76	(23)	(23)	$\times 10^{-7}$
	102	5.26	(16)	(16)	$\times 10^{-7}$
	106	3.26	(11)	(10)	$\times 10^{-7}$
	110	2.04	(67)	(6)	$\times 10^{-7}$
	114	1.24	(38)	(4)	$\times 10^{-7}$
	118	8.03	(32)	(24)	$\times 10^{-8}$
	122	6.55	(34)	(20)	$\times 10^{-8}$
	126	4.00	(19)	(12)	$\times 10^{-8}$
500	34	3.64	(12)	(11)	$\times 10^{-5}$
	35	3.75	(11)	(11)	$\times 10^{-5}$
	36	3.54	(11)	(11)	$\times 10^{-5}$
	38	2.70	(8)	(8)	$\times 10^{-5}$
	40	1.90	(6)	(6)	$\times 10^{-5}$
	42	1.25	(4)	(4)	$\times 10^{-5}$
	44	7.52	(20)	(23)	$\times 10^{-6}$
	46	4.45	(13)	(13)	$\times 10^{-6}$
	48	2.04	(6)	(6)	$\times 10^{-6}$
	50	1.08	(8)	(3)	$\times 10^{-6}$
	52	4.99	(49)	(15)	$\times 10^{-7}$
	54	2.55	(26)	(8)	$\times 10^{-7}$
	56	1.56	(16)	(5)	$\times 10^{-7}$
	58	8.87	(89)	(27)	$\times 10^{-8}$
	60	5.10	(51)	(15)	$\times 10^{-8}$
	62	3.26	(33)	(10)	$\times 10^{-8}$
	64	1.73	(17)	(5)	$\times 10^{-8}$
	66	1.60	(16)	(5)	$\times 10^{-8}$
	68	7.78	(78)	(23)	$\times 10^{-9}$
	70	2.85	(41)	(9)	$\times 10^{-9}$

^{27}Al					
E [MeV]	θ [deg]	dσ/dΩ	(stat)	(sys)	[fm^2/sr]
170	135	8.05	(80)	(24)	$\cdot 10^{-7}$
188.5	135	4.50	(45)	(13)	$\cdot 10^{-7}$
195	135	3.32	(20)	(10)	$\cdot 10^{-7}$
221	135	9.15	(92)	(27)	$\cdot 10^{-8}$
254	135	2.00	(20)	(6)	$\cdot 10^{-8}$
270	135	1.14	(11)	(3)	$\cdot 10^{-8}$
285.5	135	1.28	(13)	(4)	$\cdot 10^{-8}$

^{27}Al					
E [MeV]	θ [deg]	dσ/dΩ	(stat)	(sys)	[fm^2/sr]
47.34	70	20.71	(50)	–	$\times 10^{-2}$
61.45	70	9.87	(22)	–	$\times 10^{-2}$
72.34	70	6.06	(12)	–	$\times 10^{-2}$
53.86	90	3.97	(8)	–	$\times 10^{-2}$
75.31	90	1.14	(3)	–	$\times 10^{-2}$
79.08	90	1.020	(28)	–	$\times 10^{-2}$
28.7	110	7.32	(17)	–	$\times 10^{-2}$
37.35	110	3.60	(8)	–	$\times 10^{-2}$
55.24	110	1.050	(28)	–	$\times 10^{-2}$

Table D.9: Electron scattering off ^{27}Al from Ref. [189] including measurements at large angles, without fixed energy and Ref. [192] for low momentum transfer; the systematic error from Ref. [189] corresponds to 3% of the cross section.

Bibliography

[1] M. Hoferichter, J. Menéndez and F. Noël, *Improved Limits on Lepton-Flavor-Violating Decays of Light Pseudoscalars via Spin-Dependent $\mu \to e$ Conversion in Nuclei*, *Phys. Rev. Lett.* **130** (4, 2023) 131902, [2204.06005].

[2] F. Noël and M. Hoferichter, *Uncertainty quantification for $\mu \to e$ conversion in nuclei: charge distributions*, *JHEP* **08** (2024) 052, [2406.06677].

[3] S. Weinberg, *A Model of Leptons*, *Phys. Rev. Lett.* **19** (1967) 1264–1266.

[4] M. Gell-Mann, *A Schematic Model of Baryons and Mesons*, *Phys. Lett.* **8** (1964) 214–215.

[5] D. J. Gross and F. Wilczek, *Asymptotically Free Gauge Theories - I*, *Phys. Rev. D* **8** (1973) 3633–3652.

[6] S. Weinberg, *Nonabelian Gauge Theories of the Strong Interactions*, *Phys. Rev. Lett.* **31** (1973) 494–497.

[7] S. L. Glashow, *Partial Symmetries of Weak Interactions*, *Nucl. Phys.* **22** (1961) 579–588.

[8] A. Salam, *Weak and Electromagnetic Interactions*, *Conf. Proc. C* **680519** (1968) 367–377.

[9] P. W. Higgs, *Broken symmetries, massless particles and gauge fields*, *Phys. Lett.* **12** (1964) 132–133.

[10] P. W. Higgs, *Broken Symmetries and the Masses of Gauge Bosons*, *Phys. Rev. Lett.* **13** (1964) 508–509.

[11] F. Englert and R. Brout, *Broken Symmetry and the Mass of Gauge Vector Mesons*, *Phys. Rev. Lett.* **13** (1964) 321–323.

[12] CDF collaboration, F. Abe et al., *Observation of top quark production in $\bar{p}p$ collisions*, *Phys. Rev. Lett.* **74** (1995) 2626–2631, [hep-ex/9503002].

[13] D0 collaboration, S. Abachi et al., *Observation of the top quark*, *Phys. Rev. Lett.* **74** (1995) 2632–2637, [hep-ex/9503003].

[14] DONUT collaboration, K. Kodama et al., *Observation of tau neutrino interactions*, *Phys. Lett. B* **504** (2001) 218–224, [hep-ex/0012035].

[15] ATLAS collaboration, G. Aad et al., *Observation of a new particle in the search for the Standard Model Higgs boson with the ATLAS detector at the LHC*, *Phys. Lett. B* **716** (2012) 1–29, [1207.7214].

[16] CMS collaboration, S. Chatrchyan et al., *Observation of a New Boson at a Mass of 125 GeV with the CMS Experiment at the LHC*, *Phys. Lett. B* **716** (2012) 30–61, [1207.7235].

[17] T. Aoyama, T. Kinoshita and M. Nio, *Theory of the Anomalous Magnetic Moment of the Electron*, *Atoms* **7** (2019) 28.

[18] X. Fan, T. G. Myers, B. A. D. Sukra and G. Gabrielse, *Measurement of the Electron Magnetic Moment*, *Phys. Rev. Lett.* **130** (2023) 071801, [2209.13084].

[19] F. Zwicky, *Die Rotverschiebung von extragalaktischen Nebeln*, *Helv. Phys. Acta* **6** (1933) 110–127.

[20] V. C. Rubin and W. K. Ford, Jr., *Rotation of the Andromeda Nebula from a Spectroscopic Survey of Emission Regions*, *Astrophys. J.* **159** (1970) 379–403.

[21] S. M. Faber and R. E. Jackson, *Velocity dispersions and mass to light ratios for elliptical galaxies*, *Astrophys. J.* **204** (1976) 668.

[22] D. Clowe, M. Bradac, A. H. Gonzalez, M. Markevitch, S. W. Randall, C. Jones et al., *A direct empirical proof of the existence of dark matter*, *Astrophys. J. Lett.* **648** (2006) L109–L113, [astro-ph/0608407].

[23] Supernova Cosmology Project collaboration, S. Perlmutter et al., *Measurements of* Ω *and* Λ *from 42 High Redshift Supernovae*, *Astrophys. J.* **517** (1999) 565–586, [astro-ph/9812133].

[24] Supernova Search Team collaboration, A. G. Riess et al., *Observational evidence from supernovae for an accelerating universe and a cosmological constant*, *Astron. J.* **116** (1998) 1009–1038, [astro-ph/9805201].

[25] SDSS collaboration, D. J. Eisenstein et al., *Detection of the Baryon Acoustic Peak in the Large-Scale Correlation Function of SDSS Luminous Red Galaxies*, *Astrophys. J.* **633** (2005) 560–574, [astro-ph/0501171].

[26] WMAP collaboration, G. Hinshaw et al., *Nine-Year Wilkinson Microwave Anisotropy Probe (WMAP) Observations: Cosmological Parameter Results*, *Astrophys. J. Suppl.* **208** (2013) 19, [1212.5226].

[27] DES collaboration, T. Abbott et al., *The Dark Energy Survey: more than dark energy – an overview*, *Mon. Not. Roy. Astron. Soc.* **460** (2016) 1270–1299, [1601.00329].

[28] A. D. Sakharov, *Violation of CP Invariance, C asymmetry, and baryon asymmetry of the universe*, *Pisma Zh. Eksp. Teor. Fiz.* **5** (1967) 32–35.

[29] M. Kobayashi and T. Maskawa, *CP Violation in the Renormalizable Theory of Weak Interaction*, *Prog. Theor. Phys.* **49** (1973) 652–657.

[30] C. Jarlskog, *Commutator of the Quark Mass Matrices in the Standard Electroweak Model and a Measure of Maximal CP Nonconservation*, *Phys. Rev. Lett.* **55** (1985) 1039.

[31] G. R. Farrar and M. E. Shaposhnikov, *Baryon asymmetry of the universe in the standard electroweak theory*, *Phys. Rev. D* **50** (1994) 774, [hep-ph/9305275].

[32] M. B. Gavela, P. Hernandez, J. Orloff and O. Pene, *Standard model CP violation and baryon asymmetry*, *Mod. Phys. Lett. A* **9** (1994) 795–810, [hep-ph/9312215].

[33] M. B. Gavela, P. Hernandez, J. Orloff, O. Pene and C. Quimbay, *Standard model CP violation and baryon asymmetry. Part 2: Finite temperature*, *Nucl. Phys. B* **430** (1994) 382–426, [hep-ph/9406289].

[34] T. Aoyama et al., *The anomalous magnetic moment of the muon in the Standard Model*, *Phys. Rept.* **887** (2020) 1–166, [2006.04822].

[35] Muon g-2 collaboration, B. Abi et al., *Measurement of the Positive Muon Anomalous Magnetic Moment to 0.46 ppm*, *Phys. Rev. Lett.* **126** (2021) 141801, [2104.03281].

[36] Super-Kamiokande collaboration, Y. Fukuda et al., *Evidence for oscillation of atmospheric neutrinos*, *Phys. Rev. Lett.* **81** (1998) 1562–1567, [hep-ex/9807003].

[37] S. T. Petcov, *The Processes $\mu \to e + \gamma$, $\mu \to e + \overline{e}$, $\nu' \to \nu + \gamma$ in the Weinberg-Salam Model with Neutrino Mixing*, *Sov. J. Nucl. Phys.* **25** (1977) 340.

[38] W. J. Marciano and A. I. Sanda, *Exotic Decays of the Muon and Heavy Leptons in Gauge Theories*, *Phys. Lett. B* **67** (1977) 303–305.

[39] W. J. Marciano and A. I. Sanda, *The Reaction μ^-+ Nucleus $\to e^-$+ Nucleus in Gauge Theories*, *Phys. Rev. Lett.* **38** (1977) 1512.

[40] B. W. Lee, S. Pakvasa, R. E. Shrock and H. Sugawara, *Muon and Electron Number Nonconservation in a V-A Gauge Model*, *Phys. Rev. Lett.* **38** (1977) 937.

[41] B. W. Lee and R. E. Shrock, *Natural Suppression of Symmetry Violation in Gauge Theories: Muon- and Electron-lepton-number Nonconservation*, *Phys. Rev. D* **16** (1977) 1444.

[42] P. Minkowski, *$\mu \to e\gamma$ at a Rate of One Out of 10^9 Muon Decays?*, *Phys. Lett. B* **67** (1977) 421–428.

[43] MEG collaboration, A. M. Baldini et al., *Search for the lepton flavour violating decay $\mu^+ \to e^+\gamma$ with the full dataset of the MEG experiment*, *Eur. Phys. J. C* **76** (2016) 434, [1605.05081].

[44] SINDRUM collaboration, U. Bellgardt et al., *Search for the Decay $\mu^+ \to e^+e^+e^-$*, *Nucl. Phys. B* **299** (1988) 1–6.

[45] MEG II collaboration, A. M. Baldini et al., *The design of the MEG II experiment*, *Eur. Phys. J. C* **78** (2018) 380, [1801.04688].

[46] Mu3e collaboration, K. Arndt et al., *Technical design of the phase I Mu3e experiment*, *Nucl. Instrum. Meth. A* **1014** (2021) 165679, [2009.11690].

[47] M. Aiba et al., *Science Case for the new High-Intensity Muon Beams HIMB at PSI*, 2111.05788.

[48] Mu2e collaboration, L. Bartoszek et al., *Mu2e Technical Design Report*, 1501.05241.

[49] COMET collaboration, R. Abramishvili et al., *COMET Phase-I Technical Design Report*, *PTEP* **2020** (2020) 033C01, [1812.09018].

[50] L. Gan et al., "Eta Decays with Emphasis on Rare Neutral Modes: The JLab Eta Factory (JEF) Experiment, JLab proposal." https://www.jlab.org/exp_prog/proposals/14/PR12-14-004.pdf.

[51] REDTOP collaboration, J. Elam et al., *The REDTOP experiment: Rare η/η' Decays To Probe New Physics*, 2203.07651.

[52] BaBar collaboration, B. Aubert et al., *Search for Lepton Flavor Violating Decays $\tau^\pm \to \ell^\pm\pi^0$, $\ell^\pm\eta$, $\ell^\pm\eta'$*, *Phys. Rev. Lett.* **98** (2007) 061803, [hep-ex/0610067].

[53] Belle collaboration, Y. Miyazaki et al., *Search for lepton flavor violating τ^- decays into $\ell^-\eta$, $\ell^-\eta'$ and $\ell^-\pi^0$*, *Phys. Lett. B* **648** (2007) 341–350, [hep-ex/0703009].

[54] BaBar collaboration, B. Aubert et al., *Searches for Lepton Flavor Violation in the Decays $\tau^\pm \to e^\pm\gamma$ and $\tau^\pm \to \mu^\pm\gamma$*, *Phys. Rev. Lett.* **104** (2010) 021802, [0908.2381].

[55] K. Hayasaka et al., *Search for Lepton Flavor Violating τ Decays into Three Leptons with 719 Million Produced $\tau^+\tau^-$ Pairs*, *Phys. Lett. B* **687** (2010) 139–143, [1001.3221].

[56] Belle collaboration, Y. Miyazaki et al., *Search for Lepton Flavor Violating tau-Decays into $\ell^- K^0_S$ and $\ell^- K^0_S K^0_S$*, *Phys. Lett. B* **692** (2010) 4–9, [1003.1183].

[57] Belle collaboration, Y. Miyazaki et al., *Search for Lepton-Flavor-Violating and Lepton-Number-Violating $\tau \to \ell hh'$ Decay Modes*, *Phys. Lett. B* **719** (2013) 346–353, [1206.5595].

[58] Belle collaboration, A. Abdesselam et al., *Search for lepton-flavor-violating tau-lepton decays to $\ell\gamma$ at Belle*, *JHEP* **10** (2021) 19, [2103.12994].

[59] Belle collaboration, N. Tsuzuki et al., *Search for lepton-flavor-violating τ decays into a lepton and a vector meson using the full Belle data sample*, *JHEP* **06** (2023) 118, [2301.03768].

[60] Belle-II collaboration, W. Altmannshofer et al., *The Belle II Physics Book*, *PTEP* **2019** (2019) 123C01, [1808.10567].

[61] BNL collaboration, D. Ambrose et al., *New limit on muon and electron lepton number violation from $K^0_L \to \mu^\pm e^\mp$ decay*, *Phys. Rev. Lett.* **81** (1998) 5734–5737, [hep-ex/9811038].

[62] A. Sher et al., *An Improved upper limit on the decay $K^+ \to \pi^+ \mu^+ e^-$*, *Phys. Rev. D* **72** (2005) 012005, [hep-ex/0502020].

[63] KTeV collaboration, E. Abouzaid et al., *Search for lepton flavor violating decays of the neutral kaon*, *Phys. Rev. Lett.* **100** (2008) 131803, [0711.3472].

[64] NA62 collaboration, E. Cortina Gil et al., *Search for Lepton Number and Flavor Violation in K^+ and π^0 Decays*, *Phys. Rev. Lett.* **127** (2021) 131802, [2105.06759].

[65] K. Aoki et al., *Extension of the J-PARC Hadron Experimental Facility: Third White Paper*, 2110.04462.

[66] G. Anzivino et al., *Workshop summary: Kaons@CERN 2023*, *Eur. Phys. J. C* **84** (2024) 377, [2311.02923].

[67] R. Appel et al., *An Improved limit on the rate of decay $K^+ \to \pi^+ \mu^+ e^-$*, *Phys. Rev. Lett.* **85** (2000) 2450–2453, [hep-ex/0005016].

[68] R. Appel et al., *Search for lepton flavor violation in K^+ decays*, *Phys. Rev. Lett.* **85** (2000) 2877–2880, [hep-ex/0006003].

[69] D. B. White et al., *Search for the decays $\eta \to \mu e$ and $\eta \to e^+ e^-$*, *Phys. Rev. D* **53** (1996) 6658–6661.

[70] CLEO collaboration, R. A. Briere et al., *Rare decays of the η'*, *Phys. Rev. Lett.* **84** (2000) 26–30, [hep-ex/9907046].

[71] SINDRUM II collaboration, W. H. Bertl et al., *A Search for muon to electron conversion in muonic gold*, *Eur. Phys. J. C* **47** (2006) 337–346.

[72] P. Wintz, *Results of the SINDRUM-II experiment*, *Conf. Proc. C* **980420** (1998) 534–546.

[73] T. Suzuki, D. F. Measday and J. P. Roalsvig, *Total Nuclear Capture Rates for Negative Muons*, *Phys. Rev. C* **35** (1987) 2212.

[74] HIKE collaboration, E. Cortina Gil et al., *HIKE, High Intensity Kaon Experiments at the CERN SPS: Letter of Intent*, 2211.16586.

[75] J. Heeck, R. Szafron and Y. Uesaka, *Isotope dependence of muon-to-electron conversion*, *Nucl. Phys. B* **980** (2022) 115833, [2203.00702].

[76] A. Czarnecki, X. Garcia i Tormo and W. J. Marciano, *Muon decay in orbit: spectrum of high-energy electrons*, *Phys. Rev. D* **84** (2011) 013006, [1106.4756].

[77] Mu2e collaboration, E. Diociaiuti, *Status and perspectives of cLFV at Mu2e*, *PoS* **WIFAI2023** (2024) 017.

[78] S. Weinberg and G. Feinberg, *Electromagnetic Transitions Between mu Meson and Electron*, *Phys. Rev. Lett.* **3** (1959) 111–114.

[79] O. U. Shanker, *Z Dependence of Coherent μe Conversion Rate in Anomalous Neutrinoless Muon Capture*, *Phys. Rev. D* **20** (1979) 1608.

[80] V. Cirigliano, R. Kitano, Y. Okada and P. Tuzon, *On the model discriminating power of $\mu \to e$ conversion in nuclei*, *Phys. Rev. D* **80** (2009) 013002, [0904.0957].

[81] A. A. Petrov and D. V. Zhuridov, *Lepton flavor-violating transitions in effective field theory and gluonic operators*, *Phys. Rev. D* **89** (2014) 033005, [1308.6561].

[82] A. Crivellin, S. Najjari and J. Rosiek, *Lepton Flavor Violation in the Standard Model with general Dimension-Six Operators*, *JHEP* **04** (2014) 167, [1312.0634].

[83] A. Crivellin, M. Hoferichter and M. Procura, *Improved predictions for $\mu \to e$ conversion in nuclei and Higgs-induced lepton flavor violation*, *Phys. Rev. D* **89** (2014) 093024, [1404.7134].

[84] S. Davidson, Y. Kuno and M. Yamanaka, *Selecting $\mu \to e$ conversion targets to distinguish lepton flavour-changing operators*, *Phys. Lett. B* **790** (2019) 380–388, [1810.01884].

[85] S. Davidson, *Completeness and complementarity for $\mu \to e\gamma$, $\mu \to e\bar{e}e$ and $\mu A \to eA$*, *JHEP* **02** (2021) 172, [2010.00317].

[86] S. Davidson and B. Echenard, *Reach and complementarity of $\mu \to e$ searches*, *Eur. Phys. J. C* **82** (2022) 836, [2204.00564].

[87] M. Ardu, S. Davidson and S. Lavignac, *Distinguishing models with $\mu \to e$ observables*, *JHEP* **11** (2023) 101, [2308.16897].

[88] R. Kitano, M. Koike and Y. Okada, *Detailed calculation of lepton flavor violating muon electron conversion rate for various nuclei*, *Phys. Rev. D* **66** (2002) 096002, [hep-ph/0203110].

[89] V. Cirigliano, S. Davidson and Y. Kuno, *Spin-dependent $\mu \to e$ conversion*, *Phys. Lett. B* **771** (2017) 242–246, [1703.02057].

[90] S. Davidson, Y. Kuno and A. Saporta, *"Spin-dependent" $\mu \to e$ conversion on light nuclei*, *Eur. Phys. J. C* **78** (2018) 109, [1710.06787].

[91] A. Crivellin, S. Davidson, G. M. Pruna and A. Signer, *Renormalisation-group improved analysis of $\mu \to e$ processes in a systematic effective-field-theory approach*, *JHEP* **05** (2017) 117, [1702.03020].

[92] V. Cirigliano, K. Fuyuto, M. J. Ramsey-Musolf and E. Rule, *Next-to-leading order scalar contributions to $\mu \to e$ conversion*, *Phys. Rev. C* **105** (2022) 055504, [2203.09547].

[93] A. Bartolotta and M. J. Ramsey-Musolf, *Coherent $\mu - e$ conversion at next-to-leading order*, *Phys. Rev. C* **98** (2018) 015208, [1710.02129].

[94] E. Rule, W. C. Haxton and K. McElvain, *Nuclear-Level Effective Theory of $\mu \to e$ Conversion*, *Phys. Rev. Lett.* **130** (9, 2023) 131901, [2109.13503].

[95] W. C. Haxton, E. Rule, K. McElvain and M. J. Ramsey-Musolf, *Nuclear-level effective theory of $\mu \to e$ conversion: Formalism and applications*, *Phys. Rev. C* **107** (8, 2023) 035504, [2208.07945].

[96] W. Haxton, K. McElvain, T. Menzo, E. Rule and J. Zupan, *Effective theory tower for $\mu \to e$ conversion*, 2406.13818.

[97] K. G. Wilson, *Confinement of Quarks*, *Phys. Rev. D* **10** (1974) 2445–2459.

[98] E. Caurier, G. Martínez-Pinedo, F. Nowacki, A. Poves and A. P. Zuker, *The Shell Model as Unified View of Nuclear Structure*, *Rev. Mod. Phys.* **77** (2005) 427–488, [nucl-th/0402046].

[99] T. Otsuka, A. Gade, O. Sorlin, T. Suzuki and Y. Utsuno, *Evolution of shell structure in exotic nuclei*, *Rev. Mod. Phys.* **92** (2020) 015002, [1805.06501].

[100] S. R. Stroberg, A. Calci, H. Hergert, J. D. Holt, S. K. Bogner, R. Roth et al., *A nucleus-dependent valence-space approach to nuclear structure*, *Phys. Rev. Lett.* **118** (2017) 032502, [1607.03229].

[101] S. R. Stroberg, J. D. Holt, A. Schwenk and J. Simonis, *Ab Initio Limits of Atomic Nuclei*, *Phys. Rev. Lett.* **126** (2021) 022501, [1905.10475].

[102] S. R. Stroberg, S. K. Bogner, H. Hergert and J. D. Holt, *Nonempirical Interactions for the Nuclear Shell Model: An Update*, *Ann. Rev. Nucl. Part. Sci.* **69** (2019) 307–362, [1902.06154].

[103] W. Buchmuller and D. Wyler, *Effective Lagrangian Analysis of New Interactions and Flavor Conservation*, *Nucl. Phys. B* **268** (1986) 621–653.

[104] B. Grzadkowski, M. Iskrzynski, M. Misiak and J. Rosiek, *Dimension-Six Terms in the Standard Model Lagrangian*, *JHEP* **10** (aug, 2010) 085, [1008.4884].

[105] I. Brivio and M. Trott, *The Standard Model as an Effective Field Theory*, *Phys. Rept.* **793** (2019) 1–98, [1706.08945].

[106] E. Fermi, *An attempt of a theory of beta radiation. 1.*, *Z. Phys.* **88** (1934) 161–177.

[107] F. L. Wilson, *Fermi's Theory of Beta Decay*, *Am. J. Phys.* **36** (1968) 1150–1160.

[108] J. Gasser and H. Leutwyler, *Chiral Perturbation Theory to One Loop*, *Annals Phys.* **158** (1984) 142.

[109] H. Fritzsch, M. Gell-Mann and H. Leutwyler, *Advantages of the Color Octet Gluon Picture*, *Phys. Lett. B* **47** (1973) 365–368.

[110] D. J. Gross and F. Wilczek, *Ultraviolet Behavior of Nonabelian Gauge Theories*, *Phys. Rev. Lett.* **30** (1973) 1343–1346.

[111] H. D. Politzer, *Reliable Perturbative Results for Strong Interactions?*, *Phys. Rev. Lett.* **30** (1973) 1346–1349.

[112] Particle Data Group collaboration, S. Navas and Others, *Review of Particle Physics*, *Phys. Rev. D* **110** (2024) 030001.

[113] M. E. Peskin and D. V. Schroeder, *An Introduction to quantum field theory*. Addison-Wesley, Reading, USA, 1995.

[114] J. D. Walecka, *Theoretical nuclear and subnuclear physics*, vol. 16. 1995, 10.1142/5500.

[115] P. Klos, J. Menéndez, D. Gazit and A. Schwenk, *Large-scale nuclear structure calculations for spin-dependent WIMP scattering with chiral effective field theory currents*, *Phys. Rev. D* **88** (2013) 083516, [1304.7684].

[116] M. Hoferichter, J. Menéndez and A. Schwenk, *Coherent elastic neutrino-nucleus scattering: EFT analysis and nuclear responses*, *Phys. Rev. D* **102** (2020) 074018, [2007.08529].

[117] A. L. Fitzpatrick, W. Haxton, E. Katz, N. Lubbers and Y. Xu, *The Effective Field Theory of Dark Matter Direct Detection*, *JCAP* **02** (2013) 004, [1203.3542].

[118] A. R. Edmonds, *Angular momentum in quantum mechanics*, .

[119] B. D. Serot, *Semileptonic Weak and Electromagnetic Interactions with Nuclei: Nuclear Current Operators Through Order $(v/c)^2_{nucleon}$*, *Nucl. Phys. A* **308** (1978) 457–499.

[120] W. Bertozzi, J. Friar, J. Heisenberg and J. W. Negele, *Contributions of neutrons to elastic electron scattering from nuclei*, *Phys. Lett. B* **41** (1972) 408–414.

[121] V. Cirigliano, W. Dekens, J. de Vries, S. Gandolfi, M. Hoferichter and E. Mereghetti, *Ab-initio electroweak corrections to superallowed β decays and their impact on V_{ud}*, 2405.18464.

[122] J. C. Romao and J. P. Silva, *A resource for signs and Feynman diagrams of the Standard Model*, *Int. J. Mod. Phys. A* **27** (2012) 1230025, [1209.6213].

[123] M. Rose, *Relativistic Electron Theory*. John Wiley & Sons, INC. New York, 1961.

[124] D. E. Hazard and A. A. Petrov, *Lepton flavor violating quarkonium decays*, *Phys. Rev. D* **94** (2016) 074023, [1607.00815].

[125] L. Gan, B. Kubis, E. Passemar and S. Tulin, *Precision tests of fundamental physics with η and η' mesons*, *Phys. Rept.* **945** (2022) 2191, [2007.00664].

[126] SINDRUM II collaboration, C. Dohmen et al., *Test of lepton flavor conservation in $\mu \to e$ conversion on titanium*, *Phys. Lett. B* **317** (1993) 631–636.

[127] R. Escribano, S. Gonzàlez-Solís, P. Masjuan and P. Sánchez-Puertas, *η' transition form factor from space- and timelike experimental data*, *Phys. Rev. D* **94** (2016) 054033, [1512.07520].

[128] RQCD collaboration, G. S. Bali, V. Braun, S. Collins, A. Schäfer and J. Simeth, *Masses and decay constants of the η and η' mesons from lattice QCD*, *JHEP* **08** (2021) 137, [2106.05398].

[129] T. Feldmann, P. Kroll and B. Stech, *Mixing and decay constants of pseudoscalar mesons*, *Phys. Rev. D* **58** (1998) 114006, [hep-ph/9802409].

[130] Particle Data Group collaboration, P. A. Zyla et al., *Review of Particle Physics*, *PTEP* **2020** (2020) 083C01.

[131] HERMES collaboration, A. Airapetian et al., *Precise determination of the spin structure function g(1) of the proton, deuteron and neutron*, *Phys. Rev. D* **75** (2007) 012007, [hep-ex/0609039].

[132] H.-W. Lin, R. Gupta, B. Yoon, Y.-C. Jang and T. Bhattacharya, *Quark contribution to the proton spin from $2+1+1$-flavor lattice QCD*, *Phys. Rev. D* **98** (2018) 094512, [1806.10604].

[133] J. Liang, Y.-B. Yang, T. Draper, M. Gong and K.-F. Liu, *Quark spins and Anomalous Ward Identity*, *Phys. Rev. D* **98** (2018) 074505, [1806.08366].

[134] H. de Vries, C. W. de Jager and C. de Vries, *Nuclear charge and magnetization density distribution parameters from elastic electron scattering*, *Atom. Data Nucl. Data Tabl.* **36** (1987) 495–536.

[135] E. Caurier and F. Nowacki, *Present Status of Shell Model Techniques*, *Acta Phys. Pol.* **30** (1999) 705.

[136] A. Poves, J. Sánchez-Solano, E. Caurier and F. Nowacki, *Shell model study of the isobaric chains $A = 50$, $A = 51$ and $A = 52$*, *Nucl. Phys. A* **694** (2001) 157–198, [nucl-th/0012077].

[137] B. A. Brown and W. A. Richter, *New 'USD' Hamiltonians for the sd shell*, *Phys. Rev. C* **74** (2006) 034315.

[138] https://www.nndc.bnl.gov/ensdf/.

[139] W. A. Richter, S. Mkhize and B. A. Brown, *sd-shell observables for the USDA and USDB Hamiltonians*, *Phys. Rev. C* **78** (Dec, 2008) 064302.

[140] V. Kumar, P. C. Srivastava and J. G. Hirsch, *Shell model description of Gamow-Teller strengths in pf-shell nuclei*, *Eur. Phys. J. A* **52** (2016) 181, [1511.03887].

[141] H. Matsubara et al., *Nonquenched Isoscalar Spin-$M1$ Excitations in sd-Shell Nuclei*, *Phys. Rev. Lett.* **115** (2015) 102501.

[142] G. Martínez-Pinedo, A. Poves, E. Caurier and A. P. Zuker, *Effective g_A in the pf shell*, *Phys. Rev. C* **53** (1996) R2602, [nucl-th/9603039].

[143] I. Angeli and K. P. Marinova, *Table of experimental nuclear ground state charge radii: An update*, *Atom. Data Nucl. Data Tabl.* **99** (2013) 69–95.

[144] T. W. Donnelly and W. C. Haxton, *Multipole operators in semileptonic weak and electromagnetic interactions with nuclei*, *Atom. Data Nucl. Data Tabl.* **23** (1979) 103–176.

[145] N. F. Mott, *The Scattering of Fast Electrons by Atomic Nuclei*, *Proc. Roy. Soc. Ser. A, 124, 426* **124** (1929) 425.

[146] N. F. Mott, *The polarisation of electrons by double scattering*, *Proc. Roy. Soc. A* **135** (mar, 1932) 429–458.

[147] T. de Forest, Jr. and J. D. Walecka, *Electron scattering and nuclear structure*, *Adv. Phys.* **15** (1966) 1–109.

[148] T. W. Donnelly and J. D. Walecka, *Semileptonic Weak and Electromagnetic Interactions with Nuclei: Isoelastic Processes*, *Nucl. Phys. A* **274** (1976) 368–412.

[149] B. Dreher, J. Friedrich, K. Merle, H. Rothhaas and G. Lührs, *The determination of the nuclear ground state and transition charge density from measured electron scattering data*, *Nucl. Phys. A* **235** (dec, 1974) 219–248.

[150] J. Friedrich and F. Lenz, *Elastic electron scattering from ^{208}Pb at moderate momentum transfers and model-independent description of the nuclear charge distribution*, *Nucl. Phys. A* **183** (apr, 1972) 523–544.

[151] F. Schwabl, *Quantenmechanik für Fortgeschrittene*. Springer-Verlag, Berlin, sep, 2008.

[152] H. Überall, *Electron Scattering from Complex Nuclei (Part A + B)*. Elsevier Science & Techn., dez, 1971.

[153] E. Hairer, S. Norsett and G. Wanner, *Solving Ordinary Differential Equations I: Nonstiff Problems*, vol. 8. 01, 1993, 10.1007/978-3-540-78862-1.

[154] L. Petzold, *Automatic Selection of Methods for Solving Stiff and Nonstiff Systems of Ordinary Differential Equations*, *SIAM Journal on Scientific and Statistical Computing* **4** (1983) 136–148.

[155] P. Virtanen et al., *SciPy 1.0–Fundamental Algorithms for Scientific Computing in Python*, *Nature Meth.* **17** (2020) 261, [1907.10121].

[156] A. Hindmarsh, *ODEPACK: A systematized collection of ODE solvers*, *IMACS Trans. Sci. Comput.* **1** (01, 1982) .

[157] D. R. Yennie, D. G. Ravenhall and R. N. Wilson, *Phase-Shift Calculation of High-Energy Electron Scattering*, *Phys. Rev.* **95** (jul, 1954) 500–512.

[158] S. Tuan, L. Wright and D. Onley, *A computer program for analysis of inelastic electron scattering from nuclei*, *Nuclear Instruments and Methods* **60** (mar, 1968) 70–76.

[159] J. Heisenberg, *Nuclear Transition Density Determinations from Inelastic Electron Scattering*, pp. 61–133. Springer US, Boston, MA, 1981. 10.1007/978-1-4613-9889-9.

[160] L. L. Foldy, K. W. Ford and D. R. Yennie, *Effect of Recoil on the Elastic Scattering of High-Energy Electrons by Zero-Spin Nuclei*, *Phys. Rev.* **113** (feb, 1959) 1147–1153.

[161] J. T. Reynolds, D. S. Onley and L. C. Biedenharn, *Some exact radial integrals for Dirac-Coulomb functions*, *J. Math. Phys.* **5** (1964) 411.

[162] K. Alder and T. H. Schucan, *Radial integrals for relativistic Coulomb functions*, *Nucl. Phys.* **76** (1966) 177.

[163] W. W. Gargaro and D. S. Onley, *Matrix elements of relativistic electrons in a Coulomb field*, *J. Math. Phys.* **11** (1970) 1191.

[164] PREX collaboration, D. Adhikari et al., *Accurate Determination of the Neutron Skin Thickness of ^{208}Pb through Parity-Violation in Electron Scattering*, *Phys. Rev. Lett.* **126** (2021) 172502, [2102.10767].

[165] Q_{WEAK} collaboration, D. Androić et al., *Determination of the ^{27}Al Neutron Distribution Radius from a Parity-Violating Electron Scattering Measurement*, *Phys. Rev. Lett.* **128** (apr, 2022) 132501, [2112.15412].

[166] CREX collaboration, D. Adhikari et al., *Precision Determination of the Neutral Weak Form Factor of ^{48}Ca*, *Phys. Rev. Lett.* **129** (May, 2022) 042501, [2205.11593].

[167] G. Hagen et al., *Neutron and weak-charge distributions of the ^{48}Ca nucleus*, *Nature Phys.* **12** (2016) 186–190, [1509.07169].

[168] C. G. Payne, S. Bacca, G. Hagen, W. Jiang and T. Papenbrock, *Coherent elastic neutrino-nucleus scattering on ^{40}Ar from first principles*, *Phys. Rev. C* **100** (2019) 061304, [1908.09739].

[169] M. Croissiaux, R. Hofstadter, A. E. Walker, M. R. Yearian, D. G. Ravenhali, B. C. Clark et al., *Electron Scattering by Calcium at 250 MeV*, *Phys. Rev.* **137** (Feb, 1965) B865–B873.

[170] J. B. Bellicard, P. Bounin, R. F. Frosch, R. Hofstadter, J. S. McCarthy, F. J. Uhrhane et al., *Scattering of 750 MeV Electrons by Calcium Isotopes*, *Phys. Rev. Lett.* **19** (Aug, 1967) 527–529.

[171] R. F. Frosch, R. Hofstadter, J. S. McCarthy, G. K. Noldeke, K. J. van Oostrum, M. R. Yearian et al., *Electron Scattering Studies of Calcium and Titanium Isotopes*, *Phys. Rev.* **174** (oct, 1968) 1380–1399.

[172] R. A. Eisenstein, D. W. Madsen, H. Theissen, l. S. Cardman and C. K. Bockelman, *Electron-Scattering Studies on ^{40}Ca and ^{48}Ca*, *Phys. Rev.* **188** (Dec, 1969) 1815–1830.

[173] B. B. P. Sinha, G. A. Peterson, R. R. Whitney, I. Sick and J. S. McCarthy, *Nuclear Charge Distributions of Isotone Pairs. II. ^{39}K and ^{40}Ca*, *Phys. Rev. C* **7** (May, 1973) 1930–1938.

[174] I. Sick, J. B. Bellicard, J. M. Cavedon, B. Frois, M. Huet, P. Leconte et al., *Charge density of ^{40}Ca*, *Phys. Lett. B* **88** (dec, 1979) 245–248.

[175] H. Emrich, *Elektronenstreuung an den doppeltmagischen Isotopen ^{40}Ca und ^{48}Ca als Beitrag zur Bestimmung der radialen Verteilung der Nukleonen.* PhD thesis, Johannes-Gutenberg-Universität Mainz, 1983.

[176] H. J. Emrich, G. Fricke, G. Mallot, H. Miska, H. G. Sieberling, J. M. Cavedon et al., *Radial distribution of nucleons in the isotopes $^{48,40}Ca$*, *Nucl. Phys. A* **396** (mar, 1983) 401C–408C.

[177] R. Engfer, *Elastische Elektronenstreuung an Titan bei 33 bis 58 MeV*, *Zeitschrift für Physik* **192** (feb, 1966) 29–50.

[178] H. Theissen, *Messung der Kernradiusdifferenzen von ^{46}Ti, ^{48}Ti und ^{50}Ti durch elastische Elektronenstreuung*, *Zeitschrift für Physik* **202** (dec, 1967) 190–213.

[179] J. Heisenberg, J. S. Mccarthy and I. Sick, *Inelastic electron scattering from several Ca, Ti and Fe isotopes*, *Nucl. Phys. A* **164** (mar, 1971) 353–366.

[180] E. F. Romberg, N. S. Wall, D. Blum, J. W. Lightbody and S. Penner, *Elastic scattering of 60-120 MeV electrons from $^{46,48,50}Ti$*, *Nucl. Phys. A* **173** (1971) 124–128.

[181] J. Heisenberg, R. Hofstadter, J. S. McCarthy, R. Herman, B. C. Clark and D. G. Ravenhall, *Electron-Scattering Determination of Isotopic Differences in the Charge Distributions of ^{46}Ti, ^{48}Ti, ^{50}Ti*, *Phys. Rev. C* **6** (jul, 1972) 381–384.

[182] A. M. Selig, *Effective electro-magnetic operators in the $1f2p$ shell investigated with (e, e') reactions.* PhD thesis, University of Amsterdam, 1985.

[183] A. M. Selig, C. de Vries, P. K. A. de Witt Huberts and I. E. Zacharov, *Effective electro-magnetic operators of ^{50}Ti investigated with the (e, e') reaction*, *Nucl. Phys. A* **476** (jan, 1988) 413–447.

[184] T. Stovall, D. Vinciguerra and M. Bernheim, *Study of ^{27}Al by elastic electron scattering*, *Nucl. Phys. A* **91** (feb, 1967) 513–520.

[185] R. M. Lombard and G. R. Bishop, *The scattering of high-energy electrons by ^{27}Al*, *Nucl. Phys. A* **101** (sep, 1967) 601–624.

[186] H. A. Bentz, M. Loewenhaupt and H. Theissen, *Nuclear Charge Radii of Al and Si from Elastic Electron Scattering between 25 and 60 MeV*, *Z. Physik* **231** (1970) 484–490.

[187] G. C. Li, I. Sick, J. D. Walecka and G. E. Walker, *$M5$ and higher magnetic moments in elastic electron scattering*, *Phys. Lett. B* **32** (aug, 1970) 317–320.

[188] L. Lapikás, A. E. L. Dieperink and G. Box, *Elastic electron scattering from the magnetization distribution of ^{27}Al*, *Nucl. Phys. A* **203** (mar, 1973) 609–626.

[189] G. C. Li, I. Sick and M. R. Yearian, *High-momentum-transfer electron scattering from ^{24}Mg, ^{27}Al, ^{28}Si, and ^{32}S*, *Phys. Rev. C* **9** (may, 1974) 1861–1877.

[190] R. P. Singhal, A. Johnston, W. A. Gillespie and E. W. Lees, *Inelastic scattering of electrons from ^{27}Al*, *Nucl. Phys. A* **279** (mar, 1977) 29–44.

[191] R. P. Singhal, A. Watt and R. R. Whitehead, *Elastic electron scattering from ^{23}Na, ^{25}Mg and ^{27}Al and a shell-model interpretation*, *J. Phys. G: Nucl. Phys.* **8** (aug, 1982) 1059–1083.

[192] B. S. Dolbilkin, Kondrat'ev, Kostin, Lisin, Ponomarev and Polonskil, *Measurement of the parameters of the ground state and low-lying excited states of ^{27}Al*, *Sov. J. Nucl. Phys.* **37** (1983) 157–160.

[193] P. J. Ryan, R. S. Hicks, A. Hotta, J. F. Dubach, G. A. Peterson and D. V. Webb, *Electroexcitation of even-parity states in ^{27}Al*, *Phys. Rev. C* **27** (jun, 1983) 2515–2528.

[194] I. Sick, *Model-independent nuclear charge densities from elastic electron scattering*, *Nucl. Phys. A* **218** (1974) 509–541.

[195] G. Colangelo, M. Hoferichter and P. Stoffer, *Two-pion contribution to hadronic vacuum polarization*, *JHEP* **02** (sep, 2019) 006, [1810.00007].

[196] M. Hoferichter, B.-L. Hoid and B. Kubis, *Three-pion contribution to hadronic vacuum polarization*, *JHEP* **08** (2019) 137, [1907.01556].

[197] B.-L. Hoid, M. Hoferichter and B. Kubis, *Hadronic vacuum polarization and vector-meson resonance parameters from $e^+e^- \to \pi^0\gamma$*, *Eur. Phys. J. C* **80** (2020) 988, [2007.12696].

[198] D. Stamen, D. Hariharan, M. Hoferichter, B. Kubis and P. Stoffer, *Kaon electromagnetic form factors in dispersion theory*, *Eur. Phys. J. C* **82** (2022) 432, [2202.11106].

[199] G. Colangelo, M. Hoferichter, B. Kubis and P. Stoffer, *Isospin-breaking effects in the two-pion contribution to hadronic vacuum polarization*, *JHEP* **10** (2022) 032, [2208.08993].

[200] M. Hoferichter, B.-L. Hoid, B. Kubis and D. Schuh, *Isospin-breaking effects in the three-pion contribution to hadronic vacuum polarization*, *JHEP* **08** (2023) 208, [2307.02546].

[201] G. D'Agostini, *On the use of the covariance matrix to fit correlated data*, *Nucl. Instrum. Meth. A* **346** (jul, 1994) 306–311.

[202] NNPDF collaboration, R. D. Ball, L. Del Debbio, S. Forte, A. Guffanti, J. I. Latorre, J. Rojo et al., *Fitting Parton Distribution Data with Multiplicative Normalization Uncertainties*, *JHEP* **05** (2010) 075, [0912.2276].

[203] M. J. D. Powell, *An efficient method for finding the minimum of a function of several variables without calculating derivatives*, *Comput. J.* **7** (1964) 155–162.

[204] M. Newville, T. Stensitzki, D. B. Allen and A. Ingargiola, *LMFIT: Non-Linear Least-Square Minimization and Curve-Fitting for Python*, oct, 2015. 10.5281/zenodo.11813.

[205] G. P. Lepage and S. J. Brodsky, *Exclusive Processes in Quantum Chromodynamics: Evolution Equations for Hadronic Wave Functions and the Form-Factors of Mesons*, *Phys. Lett. B* **87** (1979) 359–365.

[206] G. P. Lepage and S. J. Brodsky, *Exclusive Processes in Perturbative Quantum Chromodynamics*, *Phys. Rev. D* **22** (1980) 2157.

[207] R. C. Barrett, *Model-independent parameters of the nuclear charge distribution from muonic X-rays*, *Phys. Lett. B* **33** (nov, 1970) 388–390.

[208] G. Fricke, C. Bernhardt, K. Heilig, L. A. Schaller, L. Schellenberg, E. B. Shera et al., *Nuclear Ground State Charge Radii from Electromagnetic Interactions*, *Atom. Data Nucl. Data Tabl.* **60** (jul, 1995) 177–285.

[209] G. Fricke, J. Herberz, T. Hennemann, G. Mallot, L. A. Schaller, L. Schellenberg et al., *Behavior of the nuclear charge radii systematics in the s-d shell from muonic atom measurements*, *Phys. Rev. C* **45** (jan, 1992) 80–89.

[210] H. D. Wohlfahrt, E. B. Shera, M. V. Hoehn, Y. Yamazaki and R. M. Steffen, *Nuclear charge distributions in $1f_{\frac{7}{2}}$-shell nuclei from muonic x-ray measurements*, *Phys. Rev. C* **23** (jan, 1981) 533–548.

[211] G. A. Rinker and J. Speth, *Nuclear Polarization in Muonic Atoms*, *Nucl. Phys. A* **306** (1978) 397–405.

[212] IAEA - Nuclear Data Section, "Chart of Nuclides."

[213] I. Angeli, *Table of nuclear root mean square charge radii*, tech. rep., International Atomic Energy Agency, International Nuclear Data Committee, Vienna (Austria), 1999.

[214] V. P. Likhachev, N. G. Afanasev, A. A. Nemashkalo, G. A. Savitsky, V. M. Khvastunov, L. D. Yaroshevsky et al., *Investigation of Magnetization Distribution in the ^{49}Ti Nucleus by Means of Elastic electron Scattering*, *Sov. J. Nucl. Phys.* **23** (1976) 261.

[215] S. K. Platchkov, J. B. Bellicard, J. M. Cavedon, B. Frois, D. Goutte, M. Huet et al., *Magnetic electron scattering and valence nucleon radial wave functions*, *Phys. Rev. C* **25** (may, 1982) 2318–2352.

[216] T. W. Donnelly and I. Sick, *Elastic magnetic electron scattering from nuclei*, *Rev. Mod. Phys.* **56** (jul, 1984) 461–566.

[217] W. G. Jiang, A. Ekström, C. Forssén, G. Hagen, G. R. Jansen and T. Papenbrock, *Accurate bulk properties of nuclei from $A = 2$ to ∞ from potentials with Δ isobars*, *Phys. Rev. C* **102** (2020) 054301, [2006.16774].

[218] A. Ekström, B. D. Carlsson, K. A. Wendt, C. Forssén, M. Hjorth-Jensen, R. Machleidt et al., *Statistical uncertainties of a chiral interaction at next-to-next-to-leading-order*, *J. Phys. G* **42** (2015) 034003, [1406.6895].

[219] A. Bottino and G. Ciocchetti, *Nuclear dispersive contributions to low-energy elastic electron scattering*, *Nucl. Phys. A* **178** (1972) 593–611.

[220] J. L. Friar and M. Rosen, *Dispersion corrections to elastic electron scattering by O-16 and C-12*, *Phys. Lett. B* **39** (1972) 615–619.

[221] J. Knoll and R. Rosenfelder, *Longitudinal and transverse dispersion corrections in electron scattering*, *Nucl. Phys. A* **229** (1974) 333–345.

[222] J. L. Friar and M. Rosen, *Dispersion corrections to elastic electron scattering by C-12 and O-16. II. on the use of the closure approximation*, *Annals Phys.* **87** (oct, 1974) 289–326.

[223] R. L. Mercer and D. G. Ravenhall, *Coupled-channel calculations of electron scattering by samarium*, *Phys. Rev. C* **10** (1974) 2002–2014.

[224] T. de Forest, Jr. and J. L. Friar, *Dispersion Corrections to Elastic electron Scattering and the Closure Approximation*, *Phys. Lett. B* **58** (1975) 397–401.

[225] F. Hachenberg and R. Rosenfelder, *Eikonal Expansion in Electron Scattering. II. Inelastic Scattering*, *Z. Phys. A* **276** (1976) 309–316.

[226] J. L. Friar, *Unitarity, Breit-like amplitudes, and low-energy approximations to dispersion corrections*, *Nucl. Phys. A* **257** (feb, 1976) 403–412.

[227] D. G. Ravenhall and R. L. Mercer, *Electron scattering from oriented holmium*, *Phys. Rev. C* **13** (1976) 2324–2342.

[228] R. L. Mercer, *Coupled Channel Method for Nuclear Scattering of Dirac Particles: High-Energy Electrons on Calcium*, *Phys. Rev. C* **15** (1977) 1786–1800.

[229] J. L. Friar, *Corrections to the impulse approximation: 1. Dispersion and recoil effects in elastic electron scattering. 2. Meson exchange currents and relativistic effects*, in *International School on Electron and Pion Interactions with Nuclei at Intermediate Energies*, p. 143, 6, 1979.

[230] J. L. Friar and J. W. Negele, *The determination of the nuclear charge distribution of ^{12}C from elastic electron scattering*, *Nucl. Phys. A* **240** (1975) 301–333.

[231] J. Erler and S. Su, *The Weak Neutral Current*, *Prog. Part. Nucl. Phys.* **71** (2013) 119–149, [1303.5522].

[232] A. Crivellin, M. Hoferichter, M. Kirk, C. A. Manzari and L. Schnell, *First-generation new physics in simplified models: from low-energy parity violation to the LHC*, *JHEP* **10** (2021) 221, [2107.13569].

[233] K. Hebeler, S. K. Bogner, R. J. Furnstahl, A. Nogga and A. Schwenk, *Improved nuclear matter calculations from chiral low-momentum interactions*, *Phys. Rev. C* **83** (2011) 031301, [1012.3381].

[234] G. Hagen, T. Papenbrock and D. J. Dean, *Solution of the center-of-mass problem in nuclear structure calculations*, *Phys. Rev. Lett.* **103** (may, 2009) 062503, [0905.3167].

[235] M. Abramowitz and I. A. Stegun, *Handbook of Mathematical Functions with Formulas, Graphs, and Mathematical Tables*. 1964.

[236] K. Merle, *Elastische Elektronenstreuung an ^{12}C, ^{31}P, ^{32}S und die Ladungsstruktur dieser Kerne*. PhD thesis, Johannes-Gutenberg-Universität Mainz, 1976.

[237] L. Von Detten, F. Noël, C. Hanhart, M. Hoferichter and B. Kubis, *On the scalar πK form factor beyond the elastic region*, *Eur. Phys. J. C* **81** (mar, 2021) 420, [2103.01966].

Acknowledgments

First and foremost, I want to profusely thank Martin Hoferichter for giving me the opportunity to work with him as his Ph.D. student in these last nearly four years, on the here presented projects. It has been an amazing experience to work with someone with so much technical knowledge and experience, who at the same time does not restrain from getting his hands dirty and collaborates on equal footing. I have always felt valued and able to talk to him, and he always took time for discussions if necessary, for which I am very grateful. I am very proud of the projects we have achieved together and look forward to further collaboration. I am also very thankful for giving me the freedom for outreach projects and orientation possibilities as well as giving valuable inputs for postdoc applications. Moreover, he made it possible for me to attend several schools and conferences and was always financially supportive, which created a lot of rewarding experiences.

Furthermore, I would like to thank Vincenzo Cirigliano for taking over the role of external referee and getting up early to participate remotely in my defense despite the substantial time difference to the US. Similarly, I would like to thank Gilberto Colangelo for taking the role of chair for my defense.

I would also like to thank all our collaborators, without whose input the here presented works would not have been possible. I would like to thank Javier Menéndez for the collaboration on Ref. [1] and in particular for calculating the shell-model results as used in this work and Refs. [1, 2]. Moreover, I would like to thank Matthias Heinz, Takayuki Miyagi (宮城宇志) and Achim Schwenk for past and ongoing extended collaborative efforts in the project outlined in Chap. 7 as well as feedback on Ref. [2]. In particular, I would like to thank Matthias Heinz for providing the ab-initio calculations for ^{27}Al using the IMSRG, as used in this work and Ref. [2], despite the resulting strain on their computational resources. I also appreciated the possibility of visiting for a seminar in Darmstadt to kick-start our collaboration, and am grateful for the nice atmosphere and hospitality, I received there.

Furthermore, I would like to thank Peter Wintz for valuable communication on Ref. [72], T. William Donnelly for correspondence on Ref. [216], and Vincenzo Cirigliano, Andreas Crivellin, and Bastian Kubis for helpful discussions of Ref. [1]. In the effort to recover old electron scattering data, I would like to thank Sonia Bacca and Luca Doria [175], Franziska Hagelstein [236], and Jordy de Vries [182] for heroic efforts tracking down unpublished Ph.D. theses in the archives at JGU Mainz and the University of Amsterdam.

Additionally, I would like to thank Bastian Kubis, who after finishing my masters in Bonn put me in contact with Martin Hoferichter, and who took time for extended discussions in the postdoc orientation process. Further, I would like to thank Leon von Detten for proofreading parts of this thesis.

I would also like to thank Joël Gogniat[2], Bai Long Hoid, and Maximilian Zillinger[3], who were my office mates for quite some time now, just as Simon Holz, Martina Cottini and Nikolaos Kalntis, who where all always available for discussions (both on-topic or off-topic) and activities. In particular, I would like to thank Maximilian Zillinger for taking over my duties of correcting exams in the last week before handing in this thesis and proofreading parts of this thesis. Moreover, the whole community of the institute was very sociable and communicative and always open for collective activities like meeting in the evening, hiking, or skiing. I would like to thank all Professors of the ITP in particular Thomas Becher, Gilberto Colangelo, and Urs Wenger for promoting, organizing, and contributing to social events in the institute. Furthermore, I would like to thank Anders Eller Thomsen, Gurtej Kanwar, Sebastian Burri, and Philipp Klose for two amazing ski vacations and further activities and discussions.

Moreover, I would like to thank the administrative staff of the ITP, namely Binia Marti and Franziska Stämpfli, who did a heck of a job representing our interests toward the university administration and were always available for questions regarding formalities. I would also like to thank Markus Moser for taking care of the IT infrastructure and organizing modern monitors for the offices.

Finally, I would like to thank my friends in Bremen, Bonn, and all over Germany and Switzerland, who had to deal with a less reliable and available friend in particular in the last months before handing in this thesis but were nevertheless always supportive. Similarly, I would like to thank my family for their continuous support. In particular, my parents and my sister as well as my girlfriend Maren, were always supportive and on the one hand offered valued external assessments and on the other hand, could help take things off my mind.

Last but not least, I would like to thank the Swiss National Science Foundation for funding the project PCEFP2_181117 in which context this thesis [1,2] as well as finalizing touches on my Master's project [237] were created, and which financially supported me through the time of my Ph.D., as well as financing several travels to conferences, workshops, or for collaboration.

[2]according to the ITP poster now called Goignat

[3]according to the ITP poster until recently called Zollinger

Selbstständigkeitserklärung

gemäss Art. 18 PromR Phil.-nat. 2019

Name/Vorname: Noël / Frederic

Matrikelnummer: 20-143-343

Studiengang: Theoretische Physik, Doktorat
Bachelor ☐ Master ☐ Dissertation ☒

Titel der Arbeit: $\mu \to e$ conversion in nuclei: EFT description, charge densities, and pseudo-scalar decays

Leiter der Arbeit: Prof. Dr. Martin Hoferichter

Ich erkläre hiermit, dass ich diese Arbeit selbständig verfasst und keine anderen als die angegebenen Quellen benutzt habe. Alle Stellen, die wörtlich oder sinngemäss aus Quellen entnommen wurden, habe ich als solche gekennzeichnet. Mir ist bekannt, dass andernfalls der Senat gemäss Artikel 36 Absatz 1 Buchstabe r des Gesetzes über die Universität vom 5. September 1996 und Artikel 69 des Universitätsstatuts vom 7. Juni 2011 zum Entzug des Doktortitels berechtigt ist. Für die Zwecke der Begutachtung und der Überprüfung der Einhaltung der Selbständigkeitserklärung bzw. der Reglemente betreffend Plagiate erteile ich der Universität Bern das Recht, die dazu erforderlichen Personendaten zu bearbeiten und Nutzungshandlungen vorzunehmen, insbesondere die Doktorarbeit zu vervielfältigen und dauerhaft in einer Datenbank zu speichern sowie diese zur Überprüfung von Arbeiten Dritter zu verwenden oder hierzu zur Verfügung zu stellen.

Ort/Datum:
Bern/22.08.2024

Unterschrift:

Frederic Noël